ENHANCED OPTICAL SENSING VIA WAVEFRONT SHAPING AND

MICROSCOPIC INTERFACE ENGINEERING

A Dissertation

by

JONATHAN VERL THOMPSON

Submitted to the Office of Graduate and Professional Studies of
Texas A&M University
in partial fulfillment of the requirements for the degree of

DOCTOR OF PHILOSOPHY

Chair of Committee,	Marlan O. Scully
Co-Chair of Committee,	Vladislav V. Yakovlev
Committee Members,	Alexei V. Sokolov
	Aleksei M. Zheltikov
	Jaan Laane
Head of Department,	Peter McIntyre

May 2017

Major Subject: Physics

ABSTRACT

Optical methods have become an integral part of today's sensing and spectroscopic techniques. These techniques provide many tools that are used for research, security, safety and health. However, attenuation effects, like scattering, limit the effectiveness of these optical tools to situations when the attenuation is low. Through deeper understanding of the scattering interactions between light and matter, we show that these detrimental effects can be mitigated, thereby enhancing our optical detection range and sensitivity.

Here we investigate and demonstrate the application of advanced techniques in a way that enhances optical signal and sensitivity in the presence of optically dense, nonlinear, or highly scattering materials. In particular, we focus on situations when slight modifications to the light or optical interface geometry result in large signal enhancements. First, we demonstrate the generation of a backward and directional superfluorescent emission from a dense Sodium vapor. We then investigate the use of wavefront shaping technologies to focus light through scattering materials, and in particular, use this to enhance Raman scattering signal through the material. Wavefront shaping methods are also used to demonstrate second harmonic generation with an enhanced efficiency from a nonlinear crystal in both the forward and backward directions. Furthermore, phase modulation in the frequency domain (pulseshaping) is used to increase the amplitude of selected frequency components after a femtosecond pulse undergoes filamentation. Lastly, we demonstrate that by focusing light into a microscopic hole ablated into the surface of a highly scattering material, we can trap the light inside the material for a much longer period of time than if the light was merely focused onto the surface. This is especially useful for linear spectroscopic detection methods (such as Raman scattering and fluorescence) than benefit greatly from an increased optical interaction time. These techniques show that by utilization of

the interaction of light with matter, it is possible to overcome the current limits of sensing

and detection in the presence of scattering and other attenuation effects.

DEDICATION

To my wife, Elizabeth

ACKNOWLEDGMENTS

First and foremost I would like to thank my co-advisors Dr. Marlan Scully and Dr. Vladislav Yakovlev for their valuable guidance, support, and advice. They have given me a unique and wonderful opportunity to explore, discover, and learn among very bright scientists, using cutting-edge equipment and laboratories. I am also very grateful for the collaboration and direction given by my committee members, Dr. Alexei Sokolov, Dr. Aleksei Zheltikov, and Dr. Jaan Laane; thank you.

I next wish to express my heart-felt gratitude to my many mentors, collaborators, and friends; without whom, this work would probably not exist: Charles Ballmann, Brett Hokr, Matthew Springer, Andrew Traverso, Ben Strycker, John Mason, Frank Echeverria, Dawson Nodurft, Graham Throckmorton, Dawei Wang, Han Cai, Wihan Kim, Yujie Shen, Kai Wang, Zhenhuan Yi, Sasha Zhdanova, Peter Zhokhov, Gombojav Ariunbold, Georgi Petrov, Brian Applegate, Kim Chapin, Javier Jo, Alexey Yamilov, and Hui Cao. I also want to thank those at the Air Force research lab at JBSA-Fort Sam Houston for the opportunites they have given me to work on fascinating projects: Robert Thomas, Benjamin Rockwell, Gary Noojin, Joel Bixler, Hope Beier, Bennett Ibey. I have learned a lot working with them.

I must also express my appreciation for my undergraduate mentors and professors, who first taught me the skills I would need to succeed in a research environment: Vince Eccles, Jan Sojka, David Peak, Farrell Edwards and Karalee Ransom.

I do not think enough gratitude could be said or given to my wonderful parents, David & Nancy Thompson, who have taught me to be honest, think clearly, and work hard. They have provided me with constant encouragement and hope. My wife's parents, John & Jane Tschirhart, as well as her sister's family, have similarly impacted my life, providing me

with friendship and encouragement. The support of my siblings: Cary, Jason, Jeremy, Kisty, Katie, Jordon, and Cami, as well as their families has also been a valuable asset to me during this work. Lastly, I wish to express my heart-felt gratitude to my beautiful wife, Lizzy, and our son Ian. Their excitement, patience, and encouragement has carried me through many days. This work would certainly not exist without them. They make life better, and joyful.

Finally, I wish to acknowledge, and express my deepest gratitude that we are blessed to live in such a marvelous universe filled with mysteries to discover, questions to ponder, and the friendships that make it worthwhile.

CONTRIBUTORS AND FUNDING SOURCES

Contributors

This work was supported by a dissertation committee consisting of Professors Marlan Scully [co-advisor], Vladislav Yakovlev [co-advisor], Alexei Sokolov, and Aleksei Zheltikov of the Department of Physics and Professor Jaan Laane of the Department of Chemistry.

All work for the dissertation was completed by the student, in collaboration with Charles Ballmann, Brett Hokr, Matt Springer, Andrew Traverso, Peter Zhokhov, Gombojav Ariunbold, Han Cai, Zhenhuan Yi, Dawei Wang, Alexei Sokolov, Aleksei Zheltikov, Marlan Scully, and Vladislav Yakovlev of the Department of Physics, Phillip Hemmer of the Department of Electrical & Computer Engineering, Wihan Kim, Brian Applegate, Javier Jo of the Department of Biomedical Engineering, Yuri Rostovtsev from the University of North Texas, Graham Throckmorton from Baylor University, Alexey Yamilov from Missouri University of Science & Technology and Hui Cao from Yale University.

Funding Sources

TABLE OF CONTENTS

LIST OF FIGURES

xvii

xix

xxxii

1. INTRODUCTION

The world of sensing and detection was revolutionized with the advent of the laser [1–4], which made it possible to deliver coherent light with high intensity to targets far away. Optical sensing and imaging, including the ability to detect and measure chemicals and other materials from a distance without physical contact is widely used, ranging from everyday scanners at the supermarket to biomedical research and security applications. In many cases, the main limitations on using light as a diagnostic or measuring tool lies in the scattering of light by particles [5] or turbulence [6]. For example, Raman spectroscopy, which uses light to identify molecules via inelastic scattering off of vibrational energy levels, has the capability to map the chemical structure of bone for osteoporosis diagnosis [7, 8]. However, the large scattering cross section of the bone [9], as well as the tissue covering the bone, makes it difficult to reach the intensities required to realize this in practice. Countless other instances exist where tools like Raman scattering, second harmonic generation, and two-photon fluorescence could be much more useful if the loss of energy due to the elastic scattering of light could be overcome or mitigated. Some of these instances include applications like deep tissue chemical imaging [10, 11] and detection [12], detection and research of cancer [13], fibrosis, and connective tissue disorders [14–16], second harmonic imaging microscopy [14, 17], non-invasive detection of pharmaceutical products through packaging [18], and detection of explosives [19, 20]. However, because elastic scattering of light is a fundamental property of the materials themselves, it is extremely difficult to circumvent.

While scattering typically inhibits our ability to image and detect chemicals through or inside other materials, the clever use of scattering effects can actually contribute to the improvement of optical detection. For example, some detection systems utilize scattering

in order to achieve higher efficiencies and sensitivities. By placing a highly scattering material behind another, an enhancement in the Raman scattering signal detected can be observed [20]. Cavities built out of highly scattering powder have expanded the sensitivity limits of fluorescence spectroscopy [21, 22]. The working principle here is that by increasing the scattering of light, the path length and interaction time of light with the sample can be increased, yielding more optical signal [23, 24]. From these examples, it becomes evident that perhaps a more effective way to enhance optical spectroscopic signals in the presence of highly scattering media is by gaining control of the scattering process rather than attempting to removing it.

In this dissertation, I present the results from a number of experiments concerned with improving our ability to use scattering for the enhancement of optical sensing techniques. This is first approached from the relm of adaptive optics and wavefront shaping technologies. In chapter 2, the use of superfluorescence as a means of achieving a backward propagating beam of radiation is demonstrated. Such backward propagating light beams can be used for spectroscopy as well as for providing a guide star for adaptive optics. Chapters 3, 4, and 5 use adaptive optics to shape the wavefront of a laser beam and thereby control its propagation through scattering and nonlinear media. In chapter 6, adaptive optics are applied in the frequency domain of a laser pulse (i.e. pulse shaping) to control the spectral intensities of light after nonlinear absorption associated with femtosecond filamentation. Finally, in chapters 7 and 8 the use of microscopic optical interface engineering via laser ablation is shown to enhance the coupling of laser light into a highly scattering material. With enhanced coupling, the scattering of the material traps the light inside the medium for a longer period of time, allowing it to diffuse/penetrate deeper than it would without interface engineering.

For the remainder of this chapter, some of the basic concepts of optical elastic scattering will be introduced. This treatment will progress from the case of scattering by a single

particle to scattering from many particles in the single scattering regime. After that, the regime of multiple scattering from many particles will be discussed in both one dimension and three dimensions. Following this, the concepts of optical phase conjugation and wave-front shaping will be introduced. Lastly, a one dimensional model which demonstrates the enhanced transmittance of light through a multiply scattering medium by injection of light below the top layers of the material will be examined. This effect will be more thoroughly investigated with calculations and experimental results in chapter 7. Chapter 8 will also use this method to experimentally demonstrate substantial enhancements to Raman spectroscopy.

1.1 Scattering of light by a single particle

This section will introduce some of the basic concepts of the elastic scattering of light from a single particle, and will follow the treatment of [25]. Here, we consider a plane wave propagating in the z direction,

$$E_0(z,t) = e^{-ikz+i\omega t} \tag{1.1}$$

where k is the wave vector, $2\pi/\lambda$, and ω is the angular frequency. Light scattered off of a single particle becomes a spherical wave in the far field [25, 26], thus it can be described by

$$E_1(r,t) = S(\theta,\phi)\frac{e^{-ikr+i\omega t}}{ikr} \tag{1.2}$$

where $S(\theta,\phi)$ is a scattering amplitude function (complex) that determines the amplitude, isotropy, and phase offset of the scattered light. In the forward direction ($\theta = 0$), at some constant plane ($z \gg y, x$) the total field becomes

$$E_0 + E_1 = E_0\left[1 + \frac{S(0)}{ikz}e^{-ik(x^2+y^2)/2z}\right] \tag{1.3}$$

which has an intensity proportional to the square of the modulus

$$|E_0 + E_1|^2 = 1 + \frac{2}{kz}\text{Re}\left\{\frac{S(0)}{i}e^{-ik(x^2+y^2)/2z}\right\} + \frac{|S(0)|^2}{k^2z^2} \qquad (1.4)$$

Here, we note that the first term is the intensity of the unscattered wave. The third term can be resonably neglected when z is large. The second term is related to the extinction due to scattering, and this fact is made clear by integration of this term over x and y, which gives

$$\sigma_{ext} = -\frac{4\pi}{k^2}\text{Re}\left\{S(0)\right\} \qquad (1.5)$$

Thus we see that the total intensity of the wave propagating in the forward direction has been attenuated by an amount proportional to this extinction formula or cross section. It is as if some area σ_{ext} of the detection plane had been blocked. This extinction cross section, has units of area, and is typically related to the geometric cross-sectional area (σ_g) via

$$\sigma_{ext} = \sigma_g Q_{ext} \qquad (1.6)$$

where $Q_{ext} = Q_{sca} + Q_{abs}$, and is an extinction efficiency factor. It is the sum of the scattering efficiency and absorption efficiency. Therefore, if we assume very little or no absorption, this extinction cross section becomes the scattering cross section (σ_{sca}) of the particle, with a scattering efficiency that can be computed with Mie theory [25, 27].

Two important conclusions should be noted from the preceeding results of scattering from a single particle. The first is that scattering involves the interference of the incident wave with the scattered wave, and in fact, the attenuation from scattering from a single particle is not due to the blocking of light, but is actually a subtle interference phenomenon [25, 26]. This is because the attenuation comes from the cross term between E_0 and E_1 in Eq. 1.4, and is therefore an interference effect. The second conclusion is that

due to the superposition principle and this interference effect, the resulting wave after scattering has a wavefront which has been modified. This modification may not be large for a single small particle, but as the number of randomly placed scattering particles increases, so will this wavefront distortion. This is an important point for optical phase conjugation and wavefront shaping, which will be discussed in section 1.4.

1.2 Scattering of light by many particles (single scattering regime)

The introduction of more scattering particles into the field at this point is relatively simple as long as the particles remain independent of each other. This means that we only consider single scattering of light from the particles, or, in other words, photons are only scattered once before exiting the material. After establishing this foundation of single scattering from multiple particles, the introduction of multiple light scattering events will be addressed in section 1.3.

As previously shown, the scattering cross section denotes the attenuation of the intensity of a wave scattering off of a single particle. If we have N particles contained in a volume, V, then the total scattering coefficient, μ_s, of the medium is the sum of the cross sections from each particle per unit volume [25, 27]. Given a volume of identical particles,

$$\mu_s = \frac{N\sigma_{sca}}{V} = n\sigma_{sca} \tag{1.7}$$

where n is the number density of the scattering particles. The significance of the scattering coefficient, which has units of inverse length, is that as light propagates through a scattering medium of length L, it is attenuated by a value of $\mu_s L$ by scattering. By the inclusion of anisotropy in scattering and the absorption coefficient, μ_a, a total transport coefficient can written as

$$\mu_t = (1 - g)\mu_s + \mu_a \tag{1.8}$$

5

The scattering anisotropy is characterized here by an asymmetry parameter which is equal to the mean cosine of the scattering angle, $g = \langle\cos(\theta)\rangle$ [27]. This parameter g is equal to 0 for isotropic scattering, -1 for total backscattering, and 1 for total forward scattering. Therefore, if light propagates through a material which scatters only in the forward direction, attenuation from scattering is zero in the calculation of μ_t.

For singly scattered light, we can consider the scenario of an initial beam of light with intensity I_0 incident upon a volume of scatterers with total thickness L. As the light propagates through an infinitesimal slice of the volume, the intensity is attenuated by a factor of $\mu_t dz$. Thus,

$$dI(z) = I(z + dz) - I(z) = -\mu_t I(z)dz \tag{1.9}$$

Integration of this leads to the well known Beer–Lambert law [27]

$$I(z) = I_0 e^{-\mu_t z} \tag{1.10}$$

This law shows that as light propagates through a scattering medium it is attenuated exponentially in z with the attenuation coefficient, μ_t determining the rate of decay. It is worth noting here that the optical density of a medium with thickness L can be written as either $\mu_t L$ or L/l_t where $l_t = 1/\mu_t$ is the effective transport mean free path of the light [27].

1.3 Scattering of light by many particles (multiple scattering regime)

To this point, we have considered only regions with relatively few scattering particles, such that light is only scattered once from each particle before leaving the medium. However, as we move to the regime of more densely packed scattering materials, we reach the point when multiple scattering events become significant. In this regime, the Beer–Lambert law breaks down because light that was backscattered can be scattered again into

6
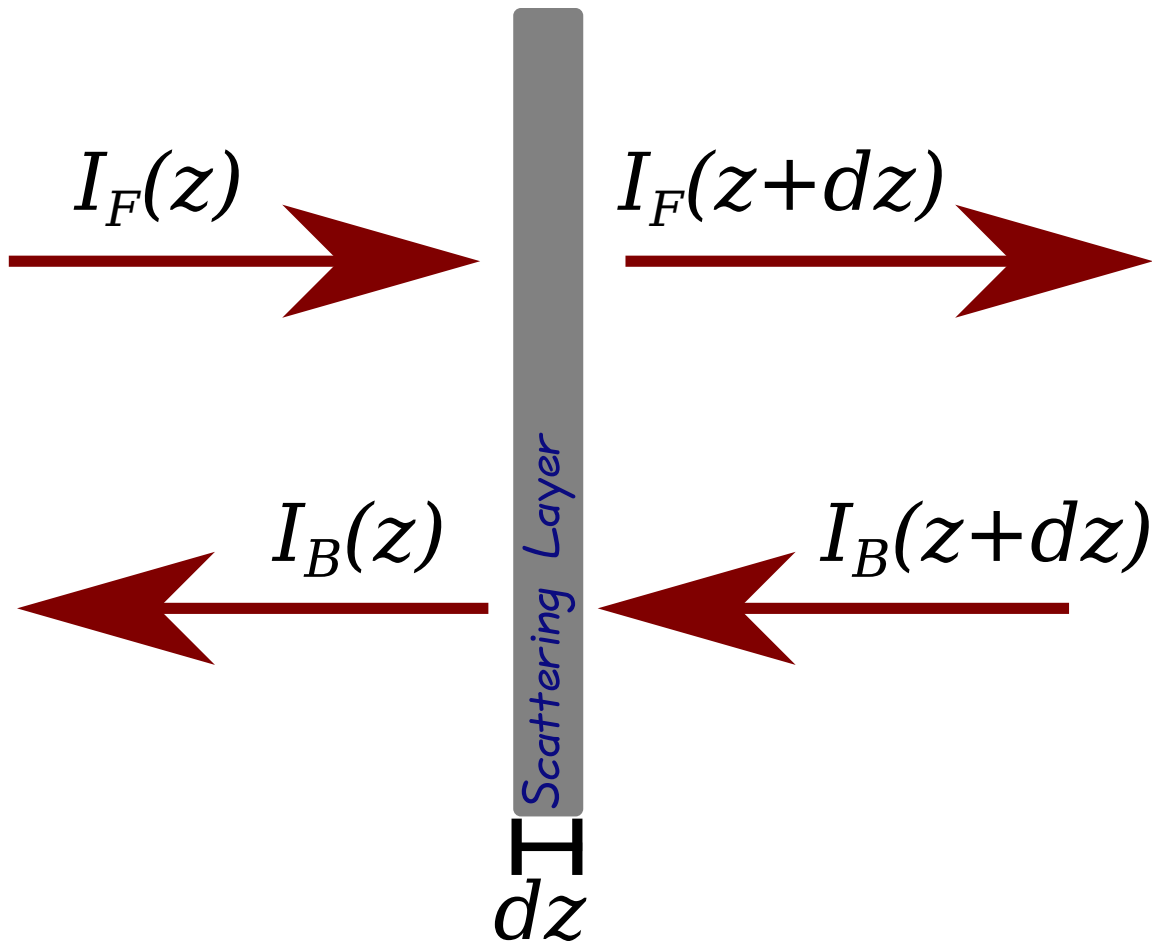
Figure 1.1: When light is scattered in a multiply scattering material, backward scattered light can be scattering again into the forward direction. Calculating the transmittance of such a material must take this into account.

the forward direction, and vise versa. In fact, light scattered from one particle may possibly be scattered many more times from other particles before it exits the medium. It is quickly realized that as soon as multiple scattering events become common, the propagation of light through the medium becomes more complex.

A one-dimensional model can be derived by adding multiple reflections into the derivation of the Beer–Lambert law [27]. This method is similar to the derivation of the reflectance from a stack of many reflectors [22, 28]. Here, we are primarily concerned with

scattering, and will assume absorption to be negligible. We start with a forward prop-

agating wave with intensity $I_F(z)$ incident upon a scattering material with thickness dz

as shown in Fig. 1.1. The intensity of the light on the other side of the scattering layer

is a sum of the light transmitted through the layer with the backward propagating light

backscattered from deeper layers. From Fig. 1.1, we can write a system of equations to

describe the intensity of both the forward and backward propagating light.

$$I_F(z + dz) = I_F(z) - \mu_t I_F(z)dz + \mu_t I_B(z)dz$$
$$I_B(z + dz) = -\mu_t I_F(z)dz + I_B(z) + \mu_t I_B(z + dz)dz \tag{1.11}$$

It is important to recall that in these equations we have assumed absorption to be negligible,

such that $\mu_t = (1 - g)\mu_s$. Thus, we arrive at the following system of equations,

$$\frac{dI_F}{dz} = -\mu_t I_F(z) + \mu_t I_B(z)$$
$$\frac{dI_B}{dz} = -\mu_t I_F(z) + \mu_t I_B(z) \tag{1.12}$$

Because the right hand side of both equations are identical, we solve the system by adding

and subtracting the two equations to get

$$\frac{d(I_F + I_B)}{dz} = -2\mu_t(I_F(z) - I_B(z)) \tag{1.13}$$

$$\frac{d(I_F - I_B)}{dz} = 0 \tag{1.14}$$

Integration of Eq. 1.14 yields

$$I_F(z) - I_B(z) = k_1 \tag{1.15}$$

where k_1 is the integration constant. This constant allows the integration of Eq. 1.13 to

find

$$I_F(z) + I_B(z) = -2\mu_t k_1 z + k_2 \tag{1.16}$$

At this point we select the boundary conditions to be

$$I_F(z = 0) = I_0 \tag{1.17}$$

$$I_B(z = L) = 0 \tag{1.18}$$

This specifies that the initial light is all incident on the material in the forward direction, and there is no light injected in the backward direction (i.e. all backward propagating light is from scattering alone). From the boundary condition on I_B (Eq. 1.18) we find from Eq. 1.15 that $k_1 = I_F(L)$. Then, by adding Eq. 1.15 and Eq. 1.16, we get the expression for $I_F(z)$,

$$I_F(z) = \frac{1}{2}(1 - 2\mu_t z)I_F(L) + k_2 \tag{1.19}$$

From this expression and the boundary condition (Eq. 1.17) we find that

$$k_2 = I_F(0) - \frac{1}{2}I_F(L) = I_0 - \frac{1}{2}I_F(L) \tag{1.20}$$

Thus, Eq. 1.19 becomes

$$I_F(z) = I_0 - \mu_t z I_F(L) \tag{1.21}$$

From here, we see that the total intensity of the light transmitted through the entire medium [27] is

$$I_F(L) = \frac{I_0}{1 + \mu_t L} \tag{1.22}$$

which allows us to rewrite Eq. 1.21 as

$$I_F(z) = \frac{[1 + \mu_t(L - z)]I_0}{1 + \mu_t L} \tag{1.23}$$

Furthermore, using Eq. 1.15 and Eq. 1.22 we can now write the equation for the backscat-

tered light as

$$I_B(z) = \frac{\mu_t(L-z)I_0}{1+\mu_t L} \tag{1.24}$$

This shows that the total intensity reflected by the material is

$$I_B(0) = \frac{\mu_t L I_0}{1+\mu_t L} \tag{1.25}$$

By normalization of Eqs. 1.22 and 1.25 by the incident intensity, we arrive at the transmittance and reflectance of the medium.

$$T = \frac{1}{1+\mu_t L} \tag{1.26}$$

$$R = \frac{\mu_t L}{1+\mu_t L} \tag{1.27}$$

These results indicate that while the decay of light within a one-dimensional multiple scattering medium is linear (Eq. 1.23), the transmittance (Eq. 1.26) and reflectance (Eq. 1.27) are not linear with respect to the optical density, $\mu_t L$. The transmittance and reflectance are plotted as a function of the optical density or thickness of a sample in Fig. 1.2. The transmittance and reflectance ($R = 1 - T$) of light according to the Beer–Lambert law are also shown for comparison. The figure shows that the inclusion of multiple scattering in a one dimensional medium actually increases the amount of light transmitted through the material. This is because light that is backscattered can be scattered into the forward direction again. It will be shown in section 1.5 that it is possible to further enhance this transmission by injecting light through the first few scattering layers.

While this one-dimensional treatment clearly demonstrates some of the differences between single and multiple scattering, the complexity yet again increases when scattering that ocurrs in all three spatial dimensions is considered. In the three-dimensional case,
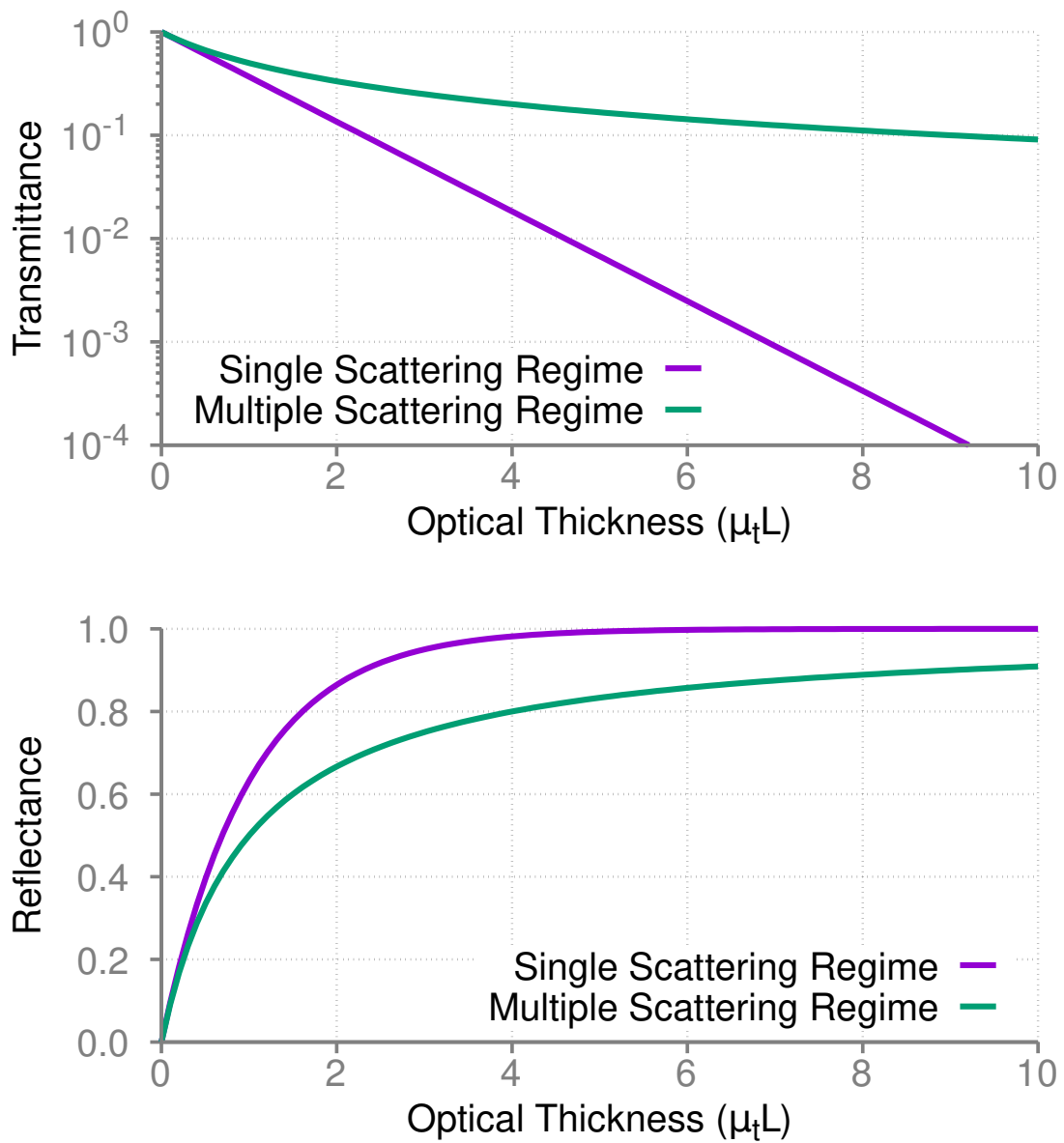
Figure 1.2: Comparison of the transmittance (top) and reflectance (bottom) of scattering materials as calculated in the single or multiple scattering regimes.

the scattering of light can be modeled with the diffusion equation [29, 30] for radiative transfer [31].

$$\frac{1}{c}\frac{\partial\phi(\boldsymbol{r},t)}{\partial t} + \mu_a(\boldsymbol{r})\phi(\boldsymbol{r},t) - D\nabla^2\phi(\boldsymbol{r},t) = S_0(\boldsymbol{r},t) \tag{1.28}$$

In this equation, $\phi(\boldsymbol{r},t)$ is the fluence rate, c is the speed of light, $D = 1/(3\mu_t)$ is the diffusion coefficient, and $S_0(\boldsymbol{r},t)$ is a source term. This equation is derived [29, 30] as an approximation to the radiative transfer equation [31], which is derived from the conservation of energy, while neglecting nonlinear, coherence, and polarization effects. It takes into account energy changes in the scattering volume due to divergence, extinction, scattering, and sources [29]. Because of this, the diffusion equation (Eq. 1.28) also demonstrates the conservation of energy. In particular, we see that the change in optical intensity (or fluence rate) is dependent upon the absorption ($\mu_a(\boldsymbol{r})\phi(\boldsymbol{r},t)$), source terms ($S_0(\boldsymbol{r},t)$), and diffusion ($D\nabla^2\phi(\boldsymbol{r},t)$). The diffusion term comes from the divergence of the net energy flux vector, $\nabla \cdot \boldsymbol{J}(\boldsymbol{r},t)$, which by Fick's law ($\boldsymbol{J}(\boldsymbol{r},t) = -D\nabla\phi(\boldsymbol{r},t)$) [29, 30], can be written as ($-D\nabla^2\phi(\boldsymbol{r},t)$). For full derivations of the radiative transfer equation and the diffusion equation, see [29–31] In chapter 7 this equation is solved for a point source and semi-infinite slab using a Green function approach and the method of images.

1.4 Phase conjugation and wavefront shaping

As was discussed in section 1.1, when a beam of light propagates through a highly scattering material, the fluctuations in the index of refraction cause distortions to the phase or wavefront of the light. These distortions and aberrations make it very difficult to detect or image deep into the material. Classical scattering of light, while complex, is a completely deterministic event. If we were to reverse time and send the distorted waves back into the scattering material [32, 33] the fluctuations in refractive index would actually correct the distortions and the original, flat-wavefront beam would reemerge. In reality, we cannot reverse time in this regard, but it is possible to generate a light wave with the
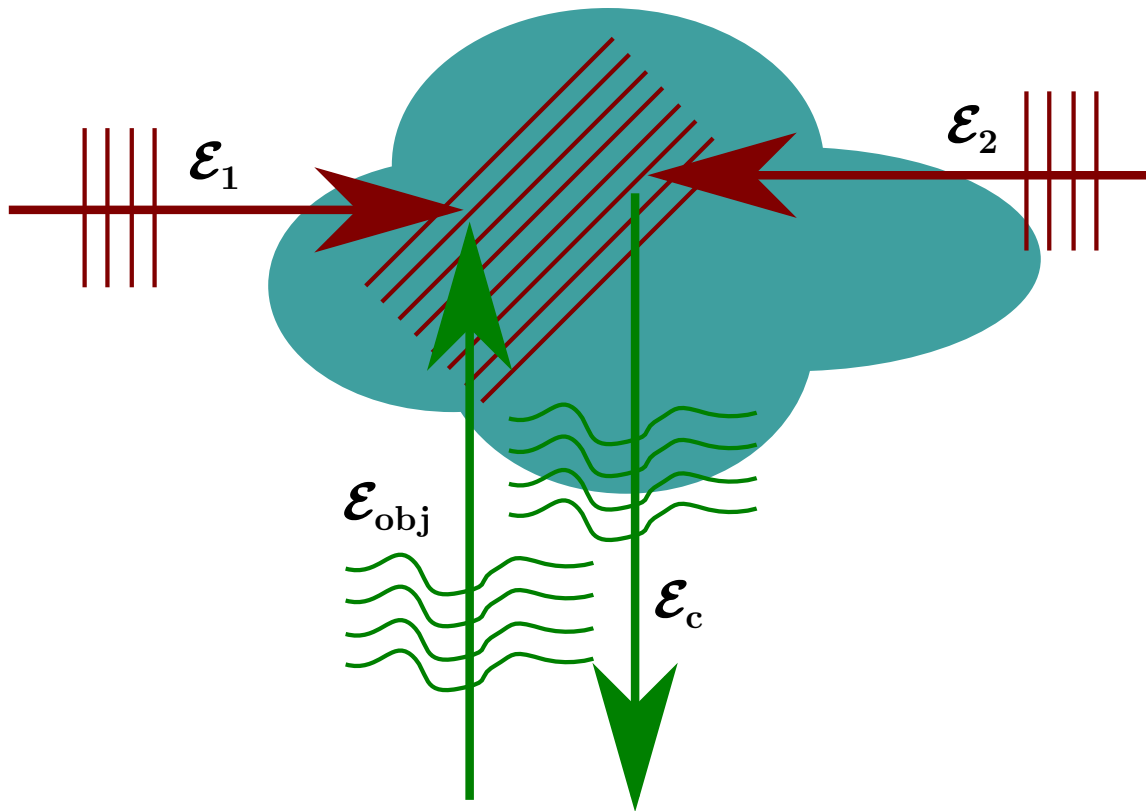
Figure 1.3: Concept of optical phase conjugation generation. Similar to the generation of a hologram, a reference beam ($\mathcal{E}_1$) and a phase modulated beam ($\mathcal{E}_{obj}$) interfere in a medium, forming a grating. The phase information of $\mathcal{E}_{obj}$ is written onto this interference grating, and can be retrieved by scattering a second reference beam ($\mathcal{E}_2$) off of the grating. If this second reference beam is phase conjugate to the first reference beam (propagating in the opposite direction), then the light scattered off of the grating will be phase conjugate to $\mathcal{E}_{obj}$ [34, 35].

time-reversed characteristics of the wave scattered by the material through optical phase conjugation [34–36].

Optical phase conjugated beams are generated using 'dynamic' holography [35, 36]. This refers to the use of lasers to first induce a holographic grating in a medium, and then generate the phase conjugated beam using a backward propagating read out beam [37]. This method is illustrated in Fig. 1.3. A reference laser ($\mathcal{E}_1$) and the object, or distorted, beam ($\mathcal{E}_{obj}$) interfere in a medium, and through nonlinear effects imprints the phase in-

formation of the object beam in the medium in the form of an interference grating. This phase conjugated beam is recovered with a second reference beam ($\mathcal{E}_2$). If the second reference beam is propagating in a direction opposite of the first, i.e. the second reference beam is the phase conjugate of the first reference beam, then the beam scattered ($\mathcal{E}_c$) by the interference grating will be phase conjugate to the object beam [35].

The interference grating for optical phase conjugation is typically generated by a variety of nonlinear processes [34, 37] including four-wave mixing [35], stimulated Brillouin scattering [35], stimulated Raman scattering [38, 39], coherent population trapping [40], and other digital methods [41]. In the case of digital methods, a camera is used to record the interference pattern between the reference and object beams, the conjugate phase is extracted digitally, and a spatial light modulator applies the conjugate phase to the reference beam [41].

Optical phase conjugation methods have been used in a number of experiments to efficiently focus light into or through highly scattering materials [41–46]. However, because this method requires the object beam to first be measured, access to both sides of a scattering sample is required. Because this is not always the case, it is of great interest to utilize phase conjugation techniques without the ability to generate the conjugate beam via the previously described methods. Therefore, iterative methods [47] have been developed as a way to search [48, 49] for the optical wavefront that allows a beam to focus through or deeper into [50–52] a scattering material.

These wavefront shaping techniques have been shown [53, 54] to utilize scattering effects along with optical phase modulation to enhance an optical feedback signals, like fluorescence [51, 52], in a highly scattering material. When a spatially coherent laser beam is scattered by or through a turbid medium, interference occurs, and is typically observed as laser speckle [55, 56]. Because laser speckle is an interference effect, the relative phase of each spatial component in the laser beam contributes to the overall speckle pattern. By

modulation of the phase of each spatial component, it is possible to modify or control the speckle pattern. For example, by applying the right phase modulation to the beam, more of the constructive interference in the speckle pattern can be localized in the same spatial region, essentially focusing the light after it passes through the scattering material [53,57]. Once the light is focused, it is then possible to use other optical techniques, such as the optical memory effect [58,59], to scan the position of the focus and acquire an image [60].

The phase modulation for such techniques can be experimentally realized using liquid crystal spatial light modulators [61]. Liquid crystals are birefringent crystals that can be rotated by applying a voltage. As the crystals are rotated with respect to the incident laser field, the optical path changes, resulting in a phase delay [62]. By arranging a grid of pixels filled with these crystals into a two-dimensional array, it is possible to selectively add a phase delay to specific regions of the laser beam, thus shaping the overall wavefront. In chapters 3, 4, and 5 a two dimensional spatial light modulator will be used to perform wavefront shaping experiments.

Phase modulation techniques are not confined only to modulation of the wavefront as a function of transverse position. A spatial light modulator in a one-dimensional array configuration is also useful in modulating the phase of the spectral components of a laser pulse. This essentially results in a reshaping of the pulse in the time domain. A typical configuration to achieve this uses a spatial light modulator in a 4-f pulse shaper [63,64]. A 4-f pulse shaper generally consists of a diffraction grating to angularly disperse the frequency components of the pulse, a lens to focus each frequency component to a spot in a one-dimensional line. The spatial light modulator is placed in this focal plane of the lens to add a phase delay to selected frequencies. After the frequencies are modulated, another lens and grating recombine and collimate the pulse [65]. One of the great benefits of using spatial light modulators is that they can be computer controlled to apply any phase mask, within the resolution limits of the device, to the pulse. This provides the
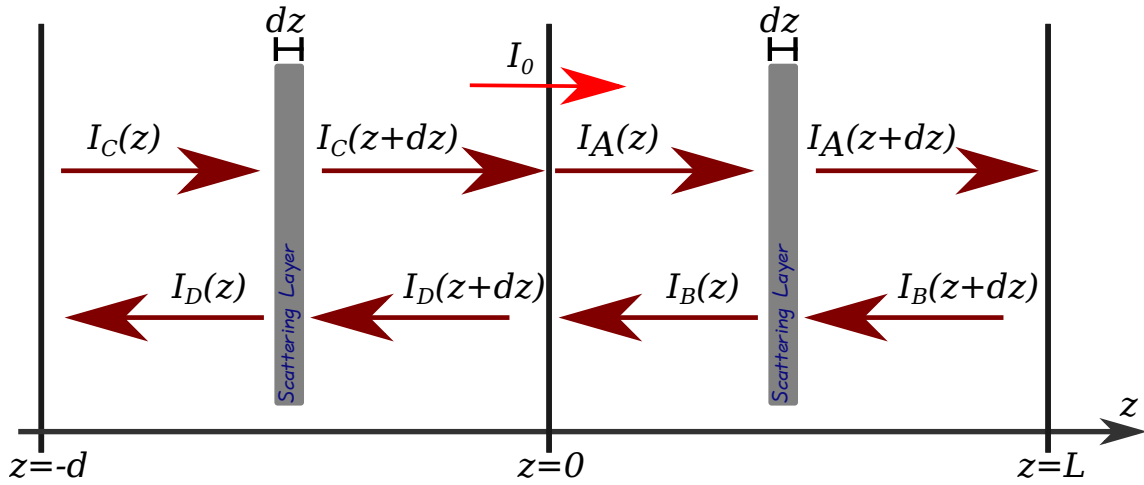
Figure 1.4: To consider the effect of bypassing the top layers of a scattering material upon the transmittance, the previous one dimensional multiple scattering treatment is extended. Here, two regions, which share boundary conditions are considered, with the light injected at into the second region at $z = 0$.

ability to interactively select which frequencies to add a phase delay to. In chapter 6 a one dimensional spatial light modulator will be used to shape femtosecond laser pulses.

1.5 Enhanced transmittance via optical injection below the scattering surface

In section 1.3 a one-dimensional model for light propagation through a multiple scattering medium was derived. The result showed that the transmittance of light increases when the regime of multiple scattering occurs. Here, this model will be extended to the case when laser light is injected underneath or through the top scattering layer with thickness d. This will show that for the same thickness, L, after the injection point, the addition of a top scattering layer will further increase the penetration depth and transmittance of light through the sample.

The layout of the scattering medium in this model is illustrated and defined in Fig. 1.4. Light is injected into the medium at $z = 0$, the thickness of the medium to the right of the injection point is L, and the thickness of the medium to the left of the injection point is d.

On the right side of the injection point ($z = 0$), the intensity of the forward and backward propagating light is denoted by $I_A(z)$ and $I_B(z)$, respectively. The intensity of the forward and backward propagating light to the left of the injection point is denoted by $I_C(z)$ and $I_D(z)$, respectively. In this manner, two separate regions are defined, each described by a system of two differential equations. The differential equations, determined in the same manner as before, are

$$
\left.\begin{aligned}
\frac{dI_A}{dz} &= -\mu_t I_A(z) + \mu_t I_B(z) \\
\frac{dI_B}{dz} &= -\mu_t I_A(z) + \mu_t I_B(z)
\end{aligned}\right\} \text{ for } z \geq 0
$$
$$
\left.\begin{aligned}
\frac{dI_C}{dz} &= -\mu_t I_C(z) + \mu_t I_D(z) \\
\frac{dI_D}{dz} &= -\mu_t I_C(z) + \mu_t I_D(z)
\end{aligned}\right\} \text{ for } z \leq 0
$$
(1.29)

Using the same technique as before (addition and subtraction of equations), these equations can be integrated.

$$
(I_A - I_B) = k_1
$$
$$
(I_A + I_B) = -2\mu_t k_1 z + k_2
$$
$$
(I_C - I_D) = k_3
$$
$$
(I_C + I_D) = -2\mu_t k_3 z + k_4
$$
(1.30)

Here, k_j are the integration constants. The two regions are tied together via the shared boundary conditions, which are as follows.

$$
I_A(z = 0) = I_0 + I_C(z = 0)
$$
$$
I_B(z = L) = 0
$$
$$
I_C(z = -d) = 0
$$
$$
I_D(z = 0) = I_B(z = 0)
$$
(1.31)

Using these boundary conditions, we solve for the integration constants

$$k_1 = I_A(L)$$

$$k_2 = 2I_A(0) - I_A(L) = 2[I_0 + I_C(0)] - I_A(L)$$

$$k_3 = -I_D(-d)$$

$$k_4 = 2I_D(0) - I_D(-d) = 2I_B(0) - I_D(-d)$$

(1.32)

and rewrite our equations as

$$
\left.
\begin{aligned}
I_A(z) &= I_0 + I_C(0) - \mu_t z I_A(L) \\
I_B(z) &= I_0 + I_C(0) - (1 + \mu_t z) I_A(L)
\end{aligned}
\right\} \text{ for } z \geq 0
$$

$$
\left.
\begin{aligned}
I_C(z) &= I_B(0) - (1 - \mu_t z) I_D(-d) \\
I_D(z) &= I_B(0) + \mu_t z I_D(-d)
\end{aligned}
\right\} \text{ for } z \leq 0
$$

(1.33)

The two values of interest here are the transmission ($I_A(L)$) and the reflection ($I_D(-d)$). Solving for these values, we get

$$I_A(L) = \frac{I_0 + I_C(0)}{1 + \mu_t L}$$

$$I_D(-d) = \frac{I_B(0)}{1 + \mu_t d}$$

(1.34)

By substitution of Eq. 1.34 into the equations for I_B and I_C in Eq. 1.33, we solve for $I_B(0)$ and $I_C(0)$

$$I_B(0) = \frac{\mu_t L(1 + \mu_t d) I_0}{1 + \mu_t(d + L)}$$

$$I_C(0) = \frac{(\mu_t L)(\mu_t d) I_0}{1 + \mu_t(d + L)}$$

(1.35)

The transmission of light through the medium can now be written as

$$I_A(L) = \frac{(1 + \mu_t d)I_0}{1 + \mu_t(d + L)} \tag{1.36}$$

and the reflection can also be described as

$$I_D(-d) = \frac{(\mu_t L)I_0}{1 + \mu_t(d + L)} \tag{1.37}$$

Thus, the transmittance ($T = I_A(L)/I_0$) and reflectance ($R = I_D(-d)/I_0$) can be written as

$$T = \frac{(1 + \mu_t d)}{1 + \mu_t(d + L)} \tag{1.38}$$

$$R = \frac{(\mu_t L)}{1 + \mu_t(d + L)} \tag{1.39}$$

It should be noted here that when $d = 0$ these equations reduce to Eqs. 1.26 and 1.27. These results are plotted in Fig. 1.5 as a function of $\mu_t L$ for different values of $\mu_t d$. This shows that as d increases (with fixed L), the transmittance of the light also increases. In agreement, the reflectance, plotted in Fig. 1.6, decreases as the injection depth increases. Figure 1.7 shows the transmittance for scattering materials with much larger optical thicknesses. Orders of magnitude more light can be transmitted through the thick samples, by injecting the light past the top scattering layers ($\leq 1\%$ of the total thickness).

In chapters 7 and 8, these results will be extended into three dimensions using the diffusion equation. Furthermore, experimental results will not only show the substantial improvement in the transmittance, but also significant improvements in the optical interaction time and spatial interaction region caused by this effect. When light propagates from a low scattering medium, like air, to a highly scattering medium, most of the scattering and reflection occurs near the surface, or optical interface, of the material [66–68]. By drilling
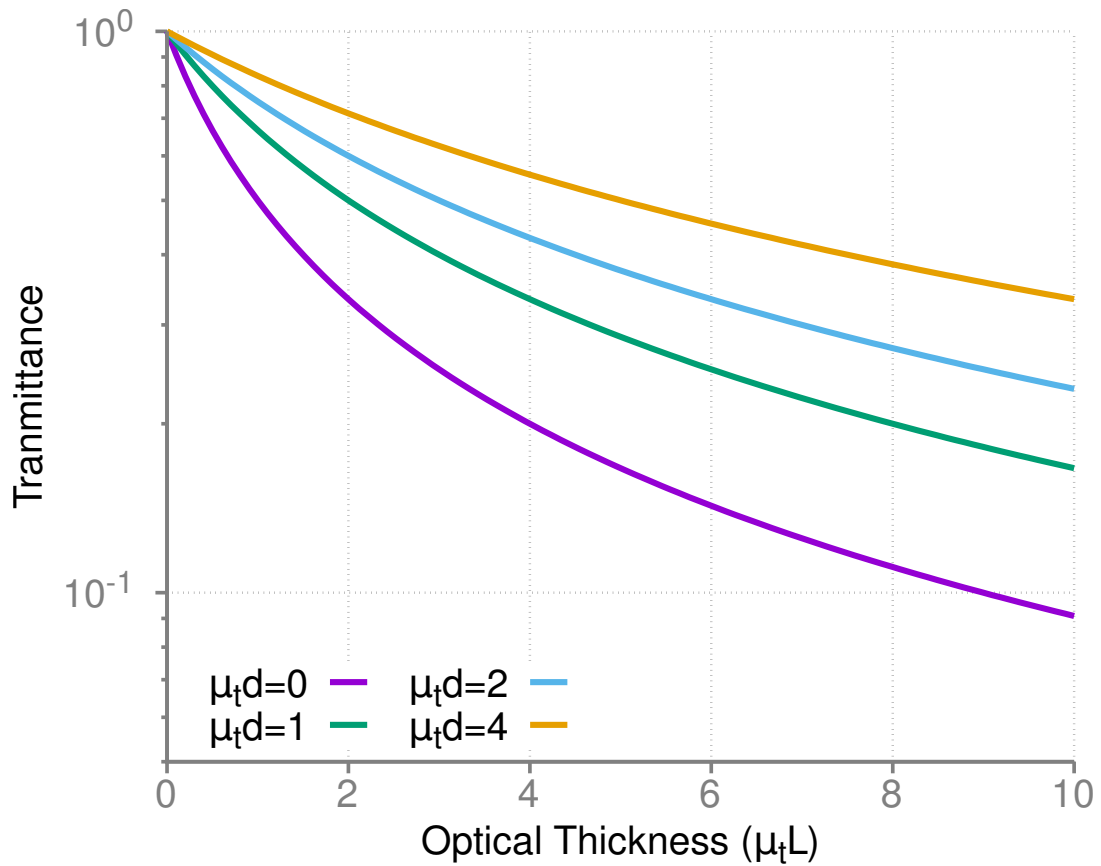
Figure 1.5: Optical transmittance through a highly scattering one-dimensional material as a function of the optical thickness of the material, plotted for different optical injection depths.
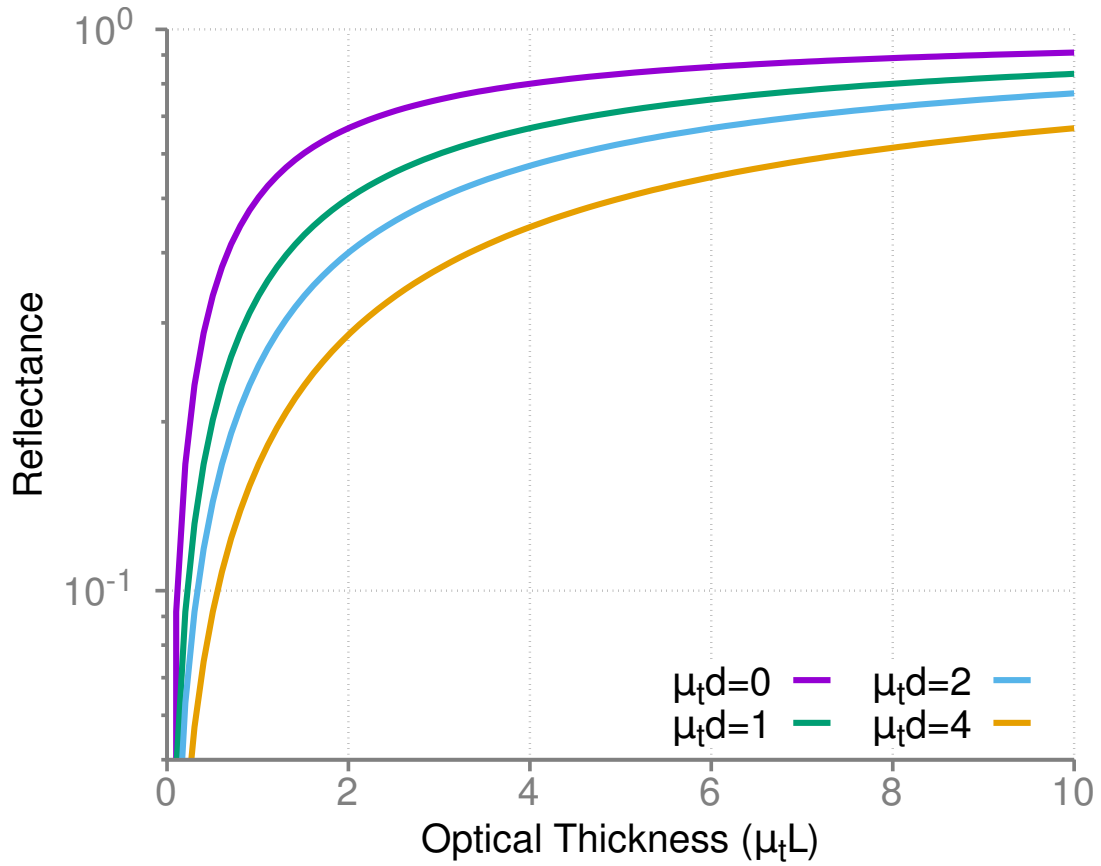
Figure 1.6: Optical reflectance from a highly scattering one dimensional material as a function of the optical thickness of the material, plotted for different optical injection depths.
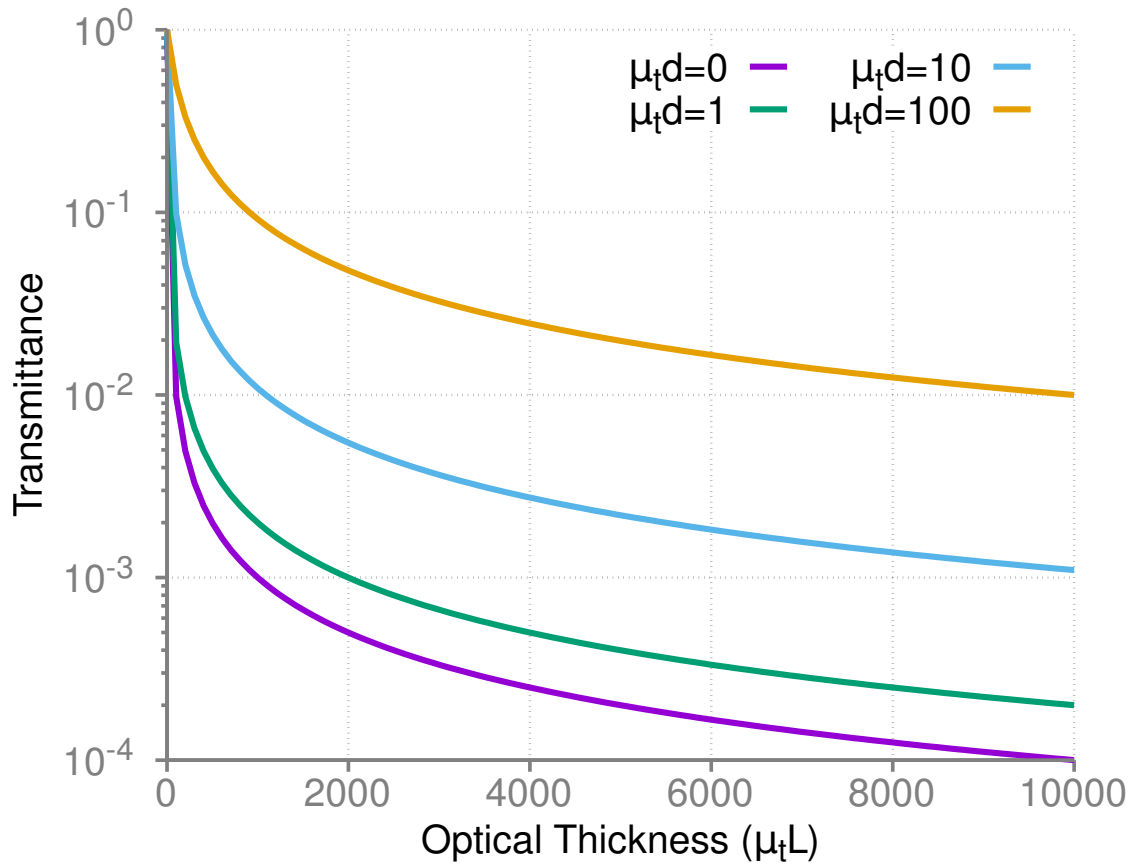
Figure 1.7: For optically thick, one-dimensional scattering materials, the transmittance as a function of the optical thickness can be substantially enhanced by injecting the light past the top scattering layers. Here, the top scattering layer which was bypassed may only be 1% of the total optical thickness, but it yields two orders of magnitude more transmittance.

a microscopic hole in the surface of the highly scattering material, we can essentially inject the light past the top layers and into the medium. While some light escapes back out of the hole, the improvements in optical coupling to the turbid medium are still large. These results, along with others [23, 24], show that by taking advantage of scattering effects, optical signals for spectroscopy can be enhanced, thereby increasing the sensitivity of such techniques.

2. PULSED COOPERATIVE BACKWARD EMISSIONS FROM NON-DEGENERATE ATOMIC TRANSITIONS IN SODIUM*

In this chapter, we study backward cooperative emissions from a dense sodium atomic vapor. Ultrashort pulses produced from a conventional amplified femtosecond laser system with an optical parametric amplifier are used to excite sodium atoms resonantly on the two-photon $3S_{1/2}$–$4S_{1/2}$ transition. Backward superfluorescent emissions (BSFEs), both on the $4S_{1/2}$–$3P_{3/2}$ and $4S_{1/2}$–$3P_{1/2}$ transitions, are observed. The picosecond temporal characteristics of the BSFE are observed using an ultrafast streak camera. The power-laws for the dependencies of average time-delay and intensity of the BSFEs on input power are analyzed in the sense of cooperative emission from non-identical atomic species. As a result, an absolute (rather than relative) time-delay and its fluctuations (free of any possible external noise) are determined experimentally. A possibility of a backward swept-gain superfluorescence and polychromatic artificial guide star in the sodium layer in the above atmosphere (mesosphere) is also proposed.

2.1 Introduction

Species-specific remote sensing/spectroscopy in the sky has been a profound challenge in modern applied physics. The conventional atmospheric light detection and ranging (LIDAR) techniques [69, 70] have been one of the essential tools for detecting traces of air impurity at a long distance. A tremendous amount of research effort has been devoted to upgrade the conventional LIDAR techniques. Among them, the femtosecond-LIDAR, based on commercially available high-intensity femtosecond (fs) lasers, has been demon-

---

strated [71]. A fs filament formation [72] in air enables propagation of fs pulses for distances of tens of kilometers in scale. In any case, LIDAR techniques rely on incoherent light scattering processes which are the fundamental limitation for LIDAR's performance. Therefore, an emerging new technology is inevitable.

Recently, coherent standoff spectroscopic (SOS) techniques have been proposed [73, 74]. In particular, one of the SOS techniques [73] is intended to maintain a backward swept-gain for the successive two-photon induced superradiance (SR) [75, 76]/superfluorescence (SF) [77, 78] emissions. In general, in SF (or SR), a macroscopic dipole moment of the medium builds up from initially incoherently (or coherently) excited atomic states. As an extension to the usual SF for two-level atoms, two-photon absorption laser induced backward SF has recently been observed in cesium [79] and rubidium (Rb) [80, 81]. Coherent temporal control of backward superfluorescence in Rb vapor has been studied as an improvement over conventional standoff sensing [81] and high-gain, directional backward superfluorescence emissions have been observed in air [82, 83]. The backward emissions interpreted as "coherence-brightened laser-like" [83] (via presence of atomic coherence) and "laser-like" [82] (via absence of atomic coherence) are produced from two-photon excited oxygen atoms as a result of two-photon photolysis of oxygen molecules in ambient air. Numerical simulations [84] in terms of cooperative phenomena (SF, SR, etc.) have been performed to elucidate the observed experimental results in [83].

In this work, we study the backward superfluorescent emissions (BSFEs) from two-photon excited sodium (Na) atomic vapor. There are many advantages to work specifically with Na atoms. This two-photon excitation mechanism of Na is similar to that in Refs. [82, 83]. Yet, any relaxations (collisions, dephasings, and spontaneous emissions, etc.) and photolysis or ionizations are discarded for dense Na vapor. This is because superfluorescent emissions occur for short timescales before other relaxation processes have any effect. It is also clean in the sense that it involves the ground ($3S_{1/2}$) and low-

24

est possible two-photon excited ($4S_{1/2}$) states. Since the closely spaced Na D-lines are involved, one should expect double BSFEs which are in the infrared range (around 1140 nm). Conventional spectrometers and ultrafast streak cameras have adequate quantum efficiency in this wavelength range. This is not the case in the Rb atomic system, where the center wavelength of the BSFE is about 5 μm [81]. Moreover, the present research is of great interest from the view point of standoff sensing with superfluorescence. The Last but not least advantage that we mention here is the existence of an atomic layer of Na in the mesosphere. An extensive research effort has recently been dedicated to practical implementations of an artificial Na laser guide star (LGS) for ground based telescopes to improve images distorted due to the atmospheric layer by using adaptive optical techniques [85]. The conventional approach for LGS is based on resonance fluorescence with the sodium D2 line (589 nm) [86–88]. However, there are several fundamental limits [89] including the saturation effect and limited number of return photons to name two. To overcome the saturation effect, polychromatic LGS has been extensively studied [86–89]. In spite of some scalability limitations, the present research may have possible applications in polychromatic LGS technology.

The rest of this paper consists of sections dedicated to the experimental setup, observed results, discussions of the results, and conclusion.

2.2   Experimental setup

In Fig. 2.1(a), the experimental setup used is sketched. The experimental setup consists of a commercial Ti:sapphire amplified laser system (Coherent Inc.) with an optical parametric amplifier (OPA, Coherent Inc. OPerA-VIS/UV), home-made heatpipe oven containing Na metal (Na HPO), two types of fiber spectrometers (Ocean Optics USB2000+, STellarNet EPP2000-NIR-InGaAs), and a Hamamatsu (C5680 with a minimum resolution of 2 ps) streak camera. From the OPA we obtained 100 fs long pulses, centered at 776 nm
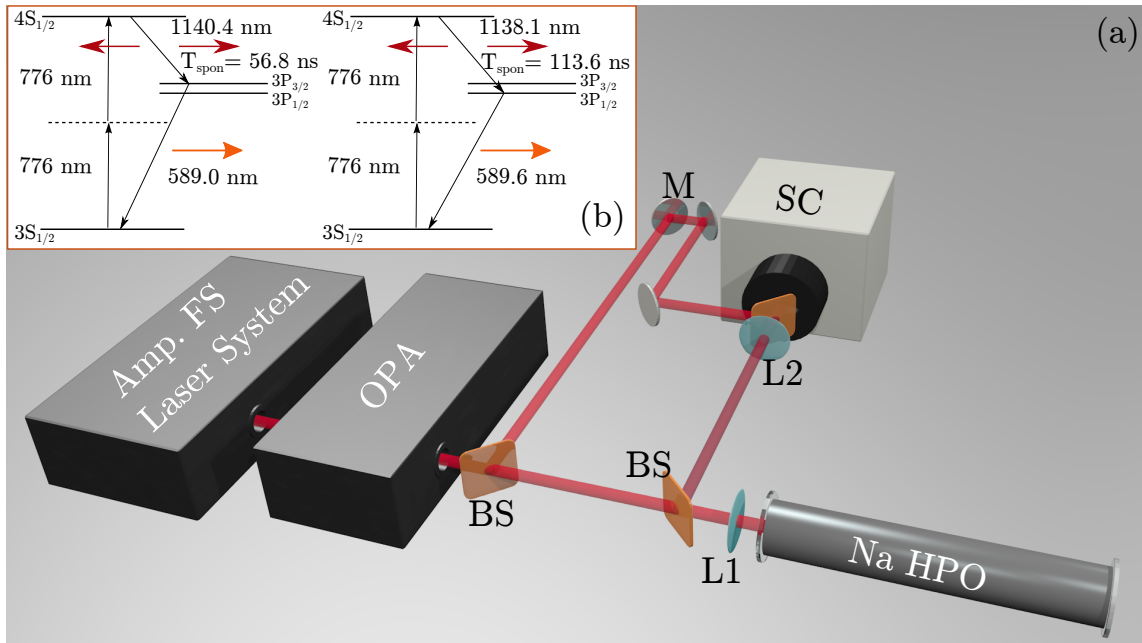
Figure 2.1: (Color online) (a) Experimental setup: Amp. FS laser system - a femtosecond amplified laser system; OPA - optical parametric amplifier; BS - beamsplitter; L1,2 - lenses; SC - streak camera and Na HPO - Na heat pipe oven at 450^0 C. (b) The atomic level scheme.

with a 20 nm full width at half maximum (FWHM) and up to 17 mW average power at a repetition rate of 1 kHz. The beam size was about 3 mm. A reflective attenuator (not shown in Fig. 2.1(a)) was used to control the power of input beam to the heatpipe oven. The reference 776 nm input pulse, as shown in Fig. 2.1(a), was used to remove laser jitter and obtain relative pulse delay with the streak camera. Its temporal width (about 5 ps) also determines the camera resolution obtained in the experiment. Either a 40 or 50 cm focal length lens was used to focus the input beam into the middle of the heatpipe oven. The properties of the BSFE were qualitatively reproducible for both cases. Therefore, in the following, only the results from the 40 cm lens configuration are presented. 15 grams of Na was loaded into the center of the pipe at the time of construction [90, 91]. The heatpipe oven has an inner diameter of 2.5 cm, a total length of 61 cm, and tilted windows to avoid

reflections. The heated region is about 15 cm long with a density of 1.7×10^{16} atoms per cm^3 at 450^{0}C and 15 Torr Argon (buffer gas) pressure. A 1 mm microscope glass slide was used as a beam splitter for detection of the backward emissions.

The Na atomic level scheme and two-photon excitation mechanism are shown in Fig. 2.1(b). The input 776 nm ultrashort pulses excite the Na atoms via two-photon process resonant to the 3S$_{1/2}$–4S$_{1/2}$ transition. The macroscopic atomic dipole moment can eventually build up to initiate the backward and forward SF emissions at 1140 and 1138 nm (on the 4S$_{1/2}$–3P$_{3/2}$ and 4S$_{1/2}$-3P$_{1/2}$ transitions, respectively) as well as the forward SF emissions at 589.0 and 589.6 nm (on the 3P$_{3/2}$–3S$_{1/2}$ and 3P$_{1/2}$–3S$_{1/2}$ transitions, respectively). The forward SF emissions occur simultaneously, also referred to as yoked-SF [79]. The generated BSFEs (at 1140 and 1138 nm) were filtered to eliminate a residual of the 776 nm light by an 830 nm long-pass filter (Semrock, EdgeBasic BLP01-830R-25). To measure the generated forward signals, the microscope glass slides were also used (not shown in Fig. 2.1(a)).

2.3 Observed results

The backward emissions are measured both by spectrometer and streak camera. A simple measurement of the backward emission yields an estimate of the divergence angle to be no larger than 17.5 mrad. The spectra of the backward emitted light were collected by the spectrometer and averaged over 20 samples for different input power.

The normalized spectra are plotted in two different ways in Fig. 2.2. Note here that the resolution of the spectrometer ($\sim$0.7 nm) is not sufficient to clearly separate the 1140 and 1138 nm emission peaks. The edges at the spectral full width at half maximum (FWHM) are plotted by white solid curves. As is seen from Fig. 2.2, the normalized spectra become broader to the blue-side as power increases. This is because of an increased portion of the 1138 nm spectral component in addition to 1140 nm in the actual measured spectra.
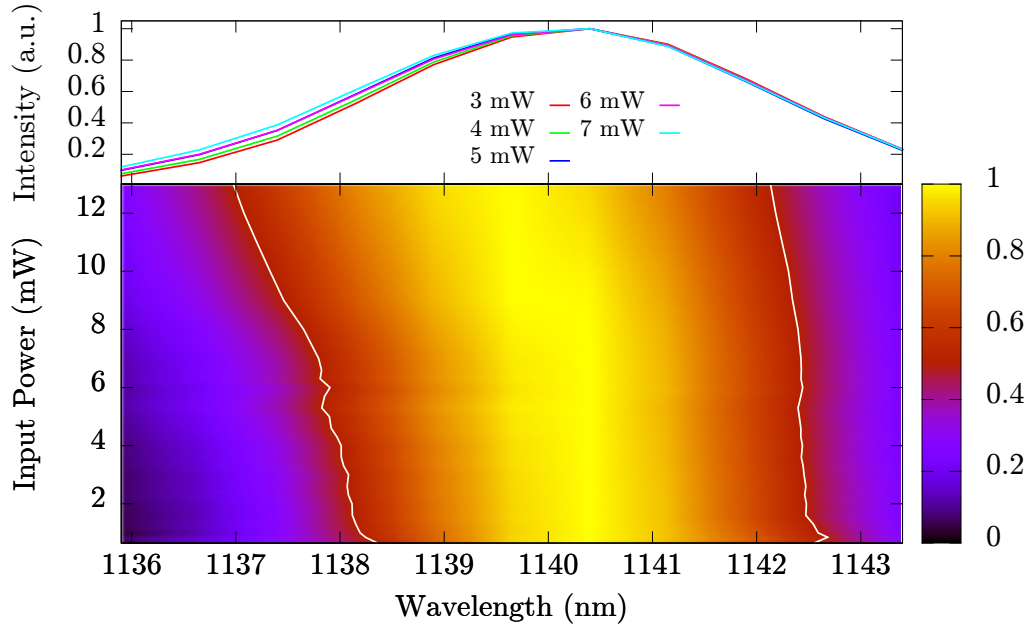
Figure 2.2: The spectra of BSFEs as functions of input power where the 3D figure in the bottom was interpolated from experimental data.

The integrated intensity of the backward spectra is plotted as a function of input power as blue circles in Fig. 2.3. A nonlinear power dependence of the integrated intensity on input power is demonstrated. Backward emitted light was also focused into the streak camera with a 10 cm lens. 200 samples were taken by streak camera per each power setting. Some averaged temporal profiles (filled green curves) of the BSFEs for different input powers are also shown normalized in logscale in Fig. 2.3. For low input power (below 3 mW), only the 1140 nm SF was measured. In this case, the average delay and integrated intensity are fitted with $\sim P^{-1}$ and $\sim P^2$, respectively, where P is the input power. Note that since the threshold power is too small, it is not included here. This type of pure/single SF has already been studied in the literature [79, 81]. However, for input power above 3 mW, picosecond time-resolved double SF pulses were recorded. We identify the second (delayed) pulse as 1138 nm SF pulse, as seen from Fig. 2.2. We obtained the average
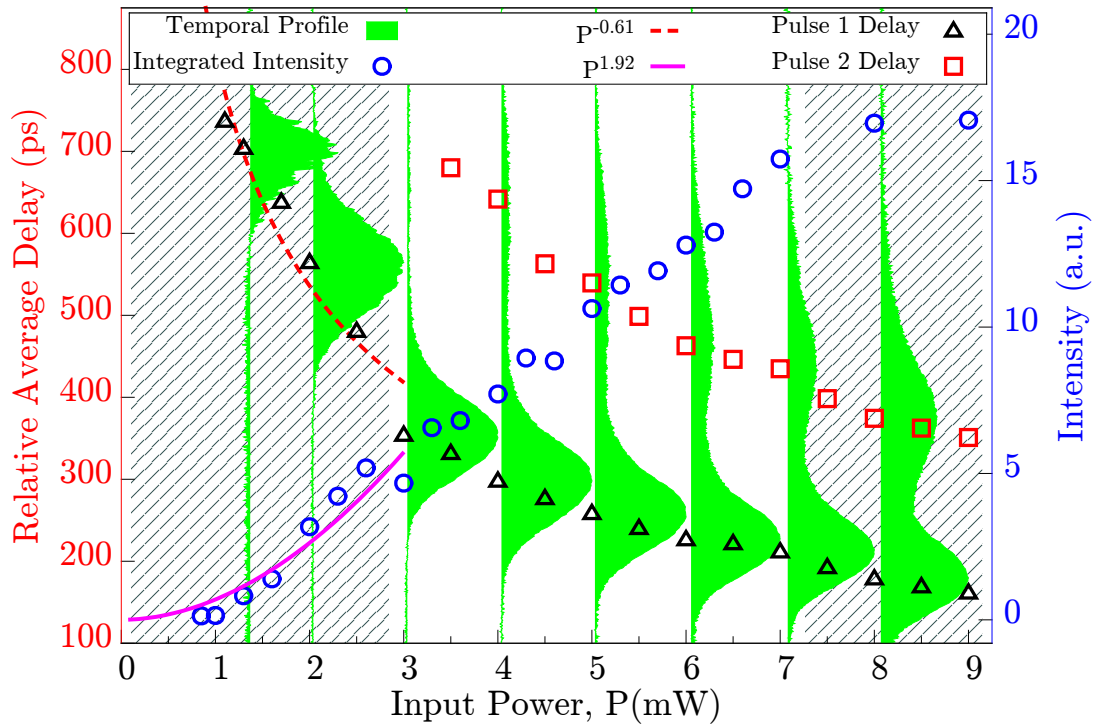
Figure 2.3: Experimentally observed data. The averaged temporal pulse shapes (in logscale and normalized), relative average time-delay and integrated intensity of the backward emitted light as functions of input power are depicted by the filled green curves, red squares and black triangles, and blue circles, respectively.

delay of the SF pulses with respect to the incident pump laser (reference) pulse and its dependence on the input laser intensity. The average time-delay of the 1140 and 1138 nm SF pulses relative to the reference input pulse are plotted as functions of input power, as black triangles and red squares, respectively, in Fig. 2.3. Additionally, the forward SF pulses on upper and lower transitions were also measured for different input powers. The ratio between the forward and backward SF (at about 1140 nm) pulse energies on the upper transitions was about 30. The conversion efficiency of the input 776 nm into the backward emission was 0.0035%.

2.4 Discussion

A cooperative emission in two non-identical atoms has been theoretically studied in [92]. Similarly, cooperative emissions from non-degenerate atomic transitions is sophisticated, and rigorous experimental and theoretical tests are beyond the framework of the present work. Clearly, a simultaneous observation of the double SF pulses in atomic vapor is intriguing in its own right. To understand the observed data we estimate the following. For the sake of simplicity, half of the excited atoms independently emit 1140 nm and the other half emit 1138 nm SF pulses. A SF scaling parameter $\tau_R \sim T_{spon}/N$ and initial (tipping) angle are the only parameters necessary to fully determine the whole SF process [78], where T_{spon} and N are the spontaneous lifetime and number of excited atoms, respectively.

We observe that the spontaneous lifetime, T_{spon}, for the $4S_{1/2}$–$3P_{3/2}$ transition (56.8 ns) is two times faster than that for the $4S_{1/2}$-$3P_{1/2}$ transition (113.6 ns). Consequently, the 1138 nm SF pulse is delayed by two times more than the 1140 nm SF pulse. From this simple statement, one can find an offset between the relative and absolute time-delay for each power. This is a complicated task to determine experimentally. Our analysis is for the unshaded region in Fig. 2.3, i.e., the interval between 3 to 7 mW input power. The offset corrected data for this region are shown in Fig. 2.4 where the offset was about 17 ps and depends very little on input power.

The data were fitted with power laws. As a result, the SF delay is approximately proportional to the inverse of the input power. Note that for two-photon excitation, the number of excited atoms is proportional to the square of the input power. Therefore, this is quantitative evidence that each of the backward 1140 and 1138 nm emissions is independently governed by the laws of oscillatory SF phenomena. Similar (single but not double) oscillatory SF in Rb vapor was reported in our earlier work [93].

30
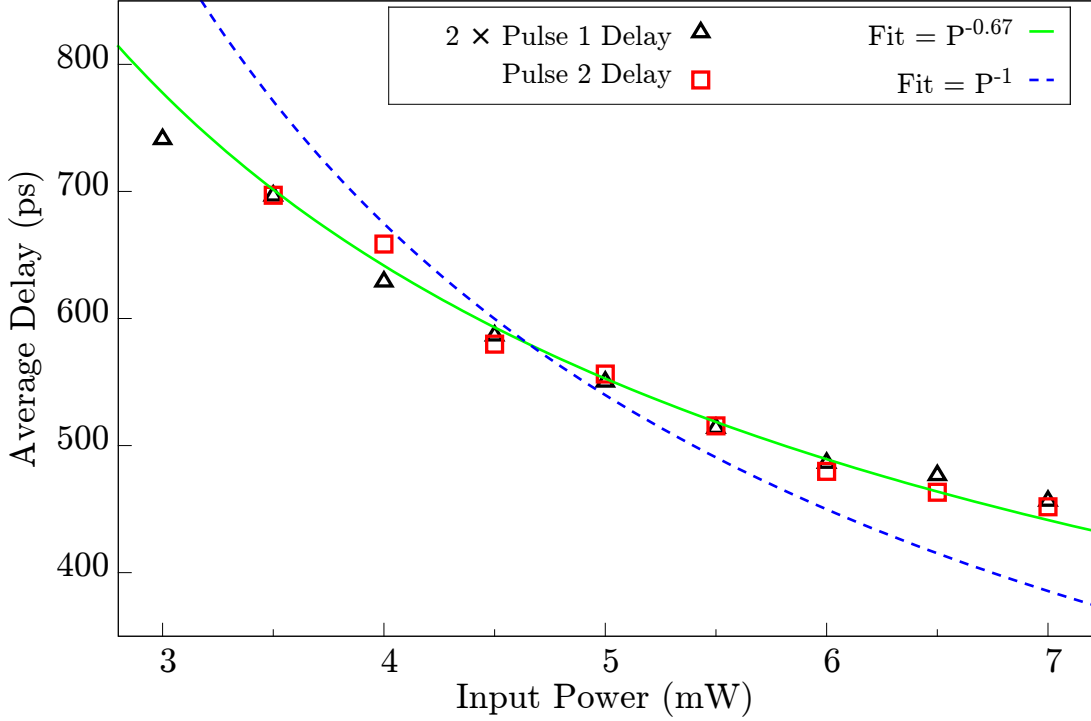
Figure 2.4: Absolute average time-delay of the BSFE with the measurement related offset removed. The time-delay of the 1140 nm BSFE is multiplied by a factor of two to show its relationship with the 1138 nm time-delay. The data points are fitted by a power-law.

Naively, one would expect that starting from the same excited level $4S_{1/2}$ to two states $3P_{1/2}$, and $3P_{3/2}$, the SF would go via the channel with larger coupling to electromagnetic radiation, similar to mode competition in laser physics [94]. In Fig. 2.3, we actually observe two SF pulses. Their relative intensities depend on the level of pump intensity, but the delay times for both SF pulses are different by a factor of 2. This is related to the different electric dipole moments for these transitions because the delay time is inversely proportional to the spontaneous emission rate, γ. For these two transitions, the spontaneous lifetime and cooperative frequencies differ by this same factor of 2. Indeed, the SF pulse (Rabi frequency) is starting as $\Omega_{SF} \propto \sqrt{D\gamma/t}\, I_1(2\sqrt{2D\gamma t})$, and delay time $t_{delay} \simeq 1/(D\gamma)$, where $D = 3\lambda^2 Nz/(8\pi)$, I_1, t, z, and λ are the linear optical density,

first order Bessel function, time, pulse propagation distance, and SF center wavelength, respectively. Because the delays of the SF pulses are different by a factor 2 (the ratio of the spontaneous emission rates), they do not overlap in space and the coherence between the $3P_{1/2}$ and $3P_{3/2}$ states does not play any role.

Based on the simplified theoretical estimations, we find the total number of excited atoms, N, to be 10^{10} and τ_R for the 1140 nm SF pulse to be $\tau_R \approx 20$ ps at an input power of 2 mW. As expected, the two sets of time-delay data for the 1140 and 1138 nm SF pulses coincide by a factor of two as shown in Fig. 2.4. Due to a high gain factor used when recording data with the streak camera, the temporal shape of the 1140 nm pulse might be distorted compared to the 1138 nm pulse. We obtained the width of the 1138 nm SF pulse for different input powers and compared it to the average time-delay. The 1138 nm pulse width is inversely proportional to input power.

We also attained the time-delay fluctuations for each backward SF pulse separately via the formula $\sqrt{\langle(\Delta\tau_i)^2\rangle} = \sqrt{\langle\tau_i^2\rangle - \langle\tau_i\rangle^2}$, where τ_i is the time-delay of a single BSFE relative to the laser reference pulse, as captured by the streak camera. Additionally, histograms for the statistical distribution as in [95] were constructed. The fluctuation of the 1138 nm SF as a function of input power is shown in Fig. 2.5(a).

The time-delay fluctuations decrease as input power increases. The quantum fluctuations in alkali vapor were measured in [95, 96]. The fluctuations of the difference between the two pulses was also obtained and shown in Fig. 2.5. This difference removes the non-reproducible extrinsic fluctuations (e.g. the laser pulse shot to shot noise) [95]. The power dependence of the ratio between the fluctuations and average time-delay is shown in Fig. 2.5(b). It is interesting to point out that this ratio for the 1138 nm SF pulses clearly demonstrates an inverse dependence on input power as is expected. A quantum theory predicts this ratio for SF from N two-level atoms to be proportional to $1/\ln(N)$ [97].

The present study of backward emissions from sodium is important for LGS technol-
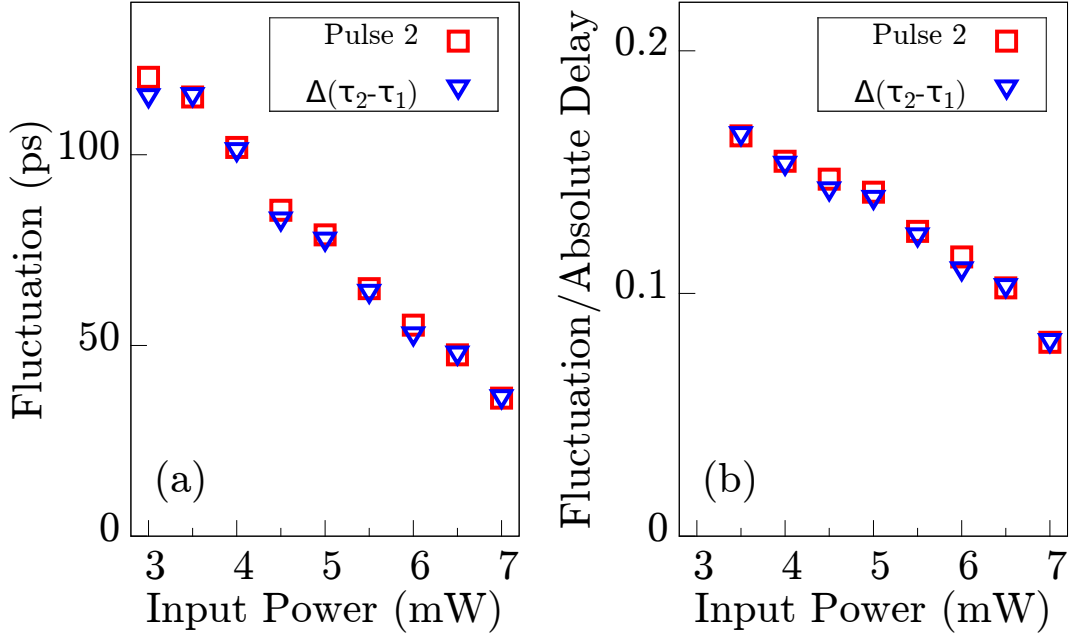
Figure 2.5: Root-mean-square fluctuations ($\sqrt{\langle(\Delta\tau_i)^2\rangle}$) in time delay of the 1138 nm superfluorescent pulses as a function of input power (a). The ratio of the fluctuations and average time delay ($\sqrt{\langle(\Delta\tau_i)^2\rangle}/\langle\tau_i\rangle$) vs. input power is also shown (b).

ogy. Although several worldwide large telescopes already operate with LGS, the number of return photons is fundamentally limited [86]. To overcome these specific limitations, the so-called polychromatic LGS has emerged [87]. The concept of polychromatic LGS is to utilize either a single photon (at 330 nm [88]) or non-degenerate two-photon (at 569 and 589 nm [89] or at 1140 and 589 nm [86]) excitations of Na atoms and detect cascade fluorescence at different wavelengths including 589 nm. In particular, the pulsed bichromatic LGS scheme proposed by Biergert and Diels [86] uses a non-degenerate two-photon excitation, whereas a resonant degenerate two-photon excitation is used in the present work. They estimated that for their bichromatic LGS scheme, about 50 photons (25 times above the detection limit) can be collected in a solid angle of $\sim 10^{-9}$ steradian (sr) from the 4π sr radiated fluorescence from $\sim 10^{12}$ excited atoms in the sodium layer of the

mesosphere [86]. The tendency of directionality of BSFE increases the number of return photons in the same solid angle (10^{-9} sr). A simple estimation has been given in our previous work [81], where it is estimated that a 100 J laser pulse directed into the mesosphere would return a photon flux of 10^8 per second per square centimeter. We estimate there to be hundreds of return photons.

2.5 Conclusion

In conclusion, we observed backward cooperative emissions from non-identical sodium atomic species. Temporally well separated, non-degenerate double SF pulses were measured. The average time-delay and its fluctuations of the measured SF pulses are determined with minimum possible systematic/experimental errors.

The present excitation scheme, which could be applied as a type of polychromatic LGS, has several advantages over conventional (monochromatic) LGS. For instance, the fundamental problems of saturation (less than 50% of the atomic population can be transferred to the excited state via one photon processes) and differential tilt (refraction due to the atmosphere) can be solved using the present two-photon excitation scheme with or without involving cooperative phenomena where nearly 100% population excitation can be achieved, and differential tilt can be corrected with a polychromatic (double SF pulses) return signal. Although there exist only a few sodium atoms in the mesosphere (only about 4 atoms per mm^3), a 10 km thick layer could still validate cooperative effects and provide for a better collimation in the backward direction, thus increasing the number of return photons. A rigorous numerical simulation for both fluorescence (the same as in [86]) and superfluorescence (together with an implementation of the backward swept-gain technique [73]) from the sodium layer utilizing the present two-photon excitation mechanism will be given elsewhere.

3.   OPTIMIZATION OF FOCUSING THROUGH SCATTERING MEDIA USING THE CONTINUOUS SEQUENTIAL ALGORITHM*

The ability to control the propagation of light through scattering media is essential for atmospheric optics, astronomy, biomedical imaging and remote sensing. The optimization of focusing light through a scattering medium is of particular interest for the case of highly scattering materials. Optical wavefront beam-shaping plays a critical role in optimizing such a propagation; however, an enormous field of adjustable parameters makes the overall task complicated. In this chapter, we propose and experimentally evaluate several variations on the standard continuous sequential algorithm that hold a promise of revealing new, faster and more efficient optimization algorithms for selecting an optical wavefront to focus light through a scattering medium. We demonstrate that the order in which pixels are chosen in the continuous sequential algorithm can lead to a 2-fold decrease in the number of iterations required to reach a given enhancement.

3.1   Introduction

As light propagates through a scattering material, interference and scattering effects cause the beam to be scattered in all directions. This reduces the amount of light directly transmitted through the material. This is illustrated in Fig. 3.1, where a laser focus without a scattering material in the beam is compared to the same laser beam with a scattering material in the beam. This scattering of light appears to cause the information of the laser beam to be lost. However, research has discovered that through the use of adaptive optics and wavefront shaping, the scattering effects caused by a material may be suppressed, and the information recovered. This is demonstrated in Fig. 3.1(c).

(a) Without scatterer (b) With scatterer (c) With scatterer and phase optimization
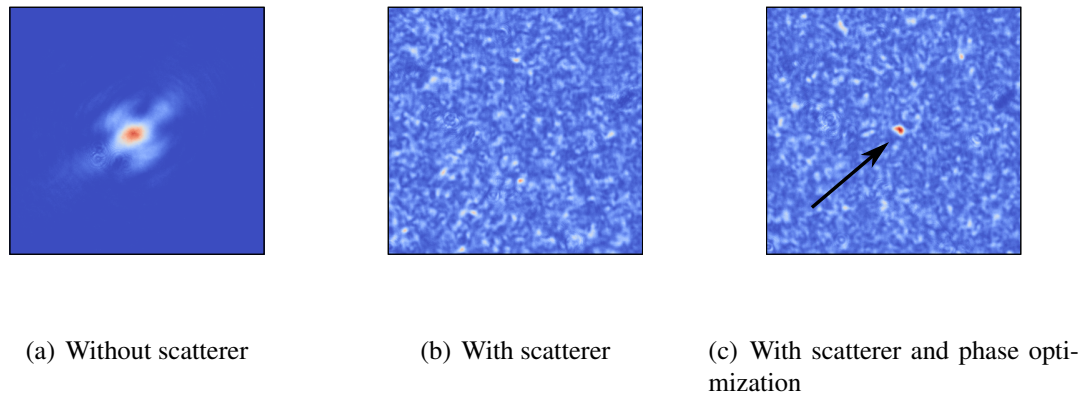
Figure 3.1: Laser spot with (b) and without (a) scatterer in the beam. This illustrates what happens when light propagates through a scattering material. However, wavefront shaping offers a method to counter these effects (c). (a) was attenuated with 4.4 OD and (b) and (c) were attenuated with 1 OD neutral density filters.

These techniques that utilize wavefront shaping to control the way that light scatters in a scattering medium have been the subject of much research recently. Many possible applications for these techniques have been demonstrated. One of the more interesting applications is the use of wavefront correction to image through [44, 98–101] or around [60, 99] scattering material. Other applications include sub-diffraction and subwavelength focusing [57, 102], Compression of ultrashort pulses [103], creating a dynamic waveplate [104], spectral filtering [105], deep tissue chemical imaging [10, 11], and random Raman lasing [106, 107]. It has also been shown that wavefront correction can substantially enhance the total transmission of light through a scattering media [108]. In this case of the enhancement of total transmission, the optimization is not local. On the other hand, the optimization of focusing through scattering media is local and linear, thus larger enhancements are realized more easily.

By modulating the phase of spatial components of a beam of laser light, the amount of light transmitted by a scattering medium can be enhanced [53, 102]. The modulation of

the phase of the beam is typically done by a two dimensional liquid crystal spatial light modulator. A pattern is displayed on the spatial light modulator determined by an optimization algorithm that requires feedback from some sort of detector. Different algorithms have been developed in order to find an algorithm that both converges well and fast. The stepwise sequential and continuous sequential algorithms [48] converge well, but the convergence begins slowly. Another method is to directly measure the transmission matrix of the scattering material and then correct for it with phase modulation [109–112]. Other algorithms, such as the partitioning algorithm [48] and genetic algorithms [113] converge more quickly, but may or may not converge as well as the sequential algorithms, depending on the sample used.

One major obstacle to realizing the goal of real time imaging in tissue is the large number of iterations that each of the above algorithms requires. A typical spatial light modulator has on the order of 4×10^5 8-bit pixels. This means there are 10^8 total independent phase masks possible. At a refresh rate of 10 Hz, it is not possible for a typical spatial light modulator to search every possible phase mask in a reasonable amount of time. A decent algorithm can reduce the number of phase masks required to search down to 10^3 or 10^4. This means a full optimization may still take anywhere from hundreds of seconds to hours. In order to optimize for scattering in living tissue, this time needs to be less than the decorrelation time of the sample which is on the order of one millisecond [114–116] to seconds [43]. Thus, the need for an algorithm that can reach a high level of optimization with a very low number of iterations is vital to the realization of the previously mentioned applications.

In this paper we investigate three geometrical variations of the standard continuous sequential algorithm [48]. This analysis provides some insights into new possible enhancement algorithms. Additionally, by selecting a different geometry of regions of the beam to modulate, the more sensitive regions may be modulated sooner, resulting in a

37
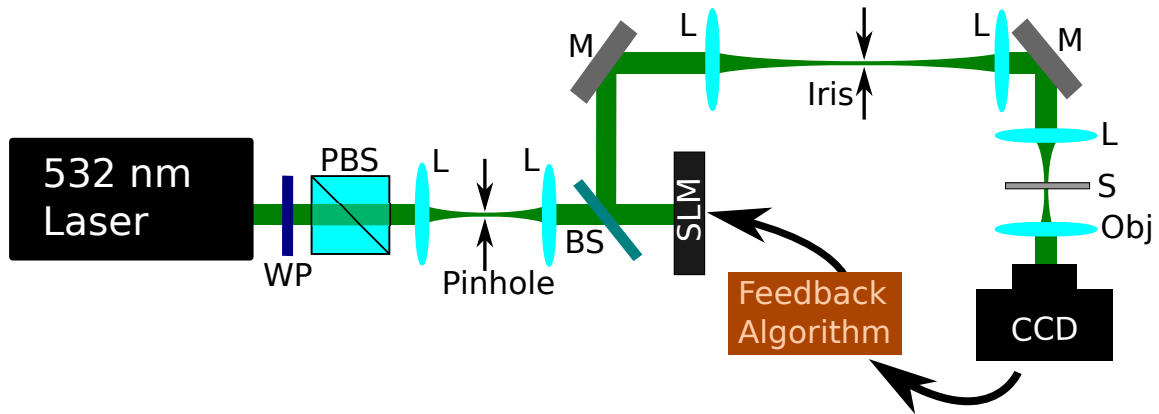
Figure 3.2: Experimental Setup. Laser power and polarization from a 532 nm laser are selected by a half-wave plate (WP) and polarizing beam splitter (PBS). The laser light is then spatially filtered and expanded. Then the light is modulated by a spatial light modulator (SLM). Higher order diffraction modes from the SLM are removed by an iris inside another telescope. The modulated light is focused onto a sample (S) of Teflon. Feedback to the optimization algorithm is supplied by a CCD camera on the backside of the sample. BS, beam splitter; M, mirror; L, lens; Obj, objective.

faster optimization.

3.2 Experimental setup

Our experimental setup is shown in Fig. 3.2. The power and polarization of a 532 nm diode pumped solid state laser are selected by a half-wave plate and polarizing beam cube. The polarization is set to match the phase only modulation orientation of a two dimensional liquid crystal spatial light modulator (Hamamatsu X10468-07). This spatial light modulator has an array of 600×792 8-bit pixels, and refreshes at a frequency of 10 Hz. The transverse mode of the laser is also spatially filtered and the beam expanded before the spatial light modulator to fill more of the 2-D pixel array. After modulation, the light is passed through a telescope with an iris at the focus to remove higher order diffraction modes caused by the spatial light modulator.

After the telescope, the modulated light is directed with a mirror and focused into a

~100 μm thick sample of Teflon. Teflon is chosen as a sample because it has a high scattering cross section and a long persistence time. The power of the laser light focused onto the sample is 0.8 mW. On the other side of the sample, a 20x objective with 0.40 numerical aperture is used to collect the transmitted light and image it onto a CCD detector(Mightex CGE-B013-U). A square region of 100 pixels near the center of the CCD is selected, and the individual intensity counts are summed to provide a single value to use as feedback for the optimization algorithm.

3.3 CSA algorithm variations

The standard continuous sequential algorithm(CSA) [48] works by selecting a square block of pixels on the spatial light modulator. A series of phase shifts are applied to the selected region of pixels, and measurements made for each phase shift. The optimum phase shift is then applied to the spatial light modulator, and a new block of pixels are selected. This process iterates in a linear fashion rastering over the 2 dimensional pixel array as shown in Fig. 3.3(a), and can be repeated for additional enhancement.

We investigate the effect of three variations in the pixel selection method on the standard continuous sequential algorithm. These variations are depicted in Fig. 3.3(b-d). The first two are very similar to the original CSA, however instead of raster scanning through the 2d pixel array, the modulated pixel groups are selected in a spiral pattern starting at the edges (b) or at the middle (c) of the array.

The last geometry (d) selects pixel groups to modulate in a ring geometry. The algorithm cycles through nine rings with different origins, then the radius of the ring is decreased, and the cycle repeats until the ring becomes a spot at each origin. When the rings are large enough to overlap, the phase shift of the new ring is added to the phase shift of the old ring rather than replacing it. The phase shift is wrapped back to zero when the new value exceeds 4π radians. Thus, the structure of the phase mask is not overwritten

(a) Raster geometry

(b) Spiral in geometry

(c) Spiral out geometry

(d) Ring geometry
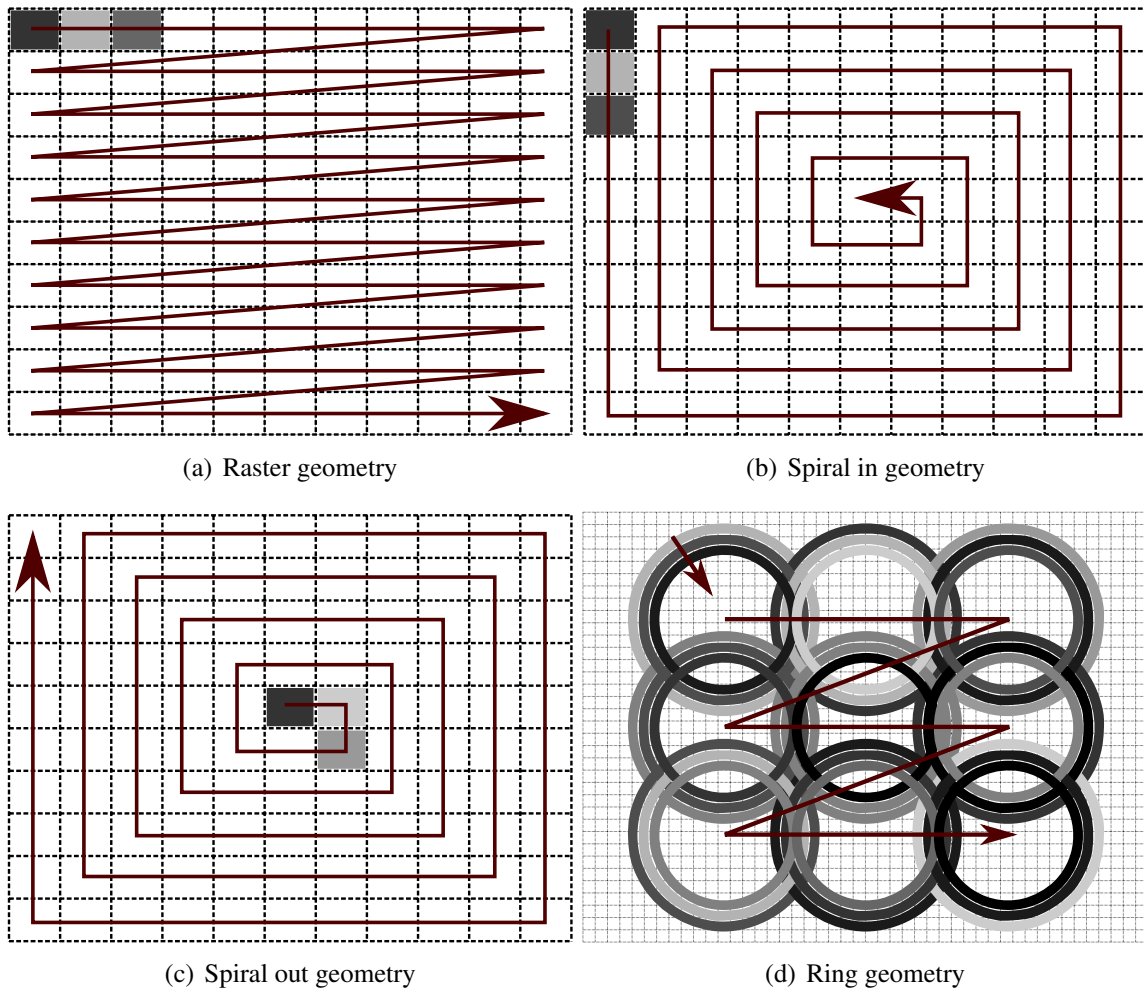
Figure 3.3: Geometry variations of the pixel selection order of the continuous sequential algorithm. The grayscale illustrates the amount of phase shift applied to the spatial light modulator (SLM), and the arrows show in which direction the pixel selection proceeds. The typical geometry is to raster scan (a) through the pixel groups on the SLM. Other methods examined are to start on the edge and spiral inwards (b), or start in the center and spiral outwards (c). Another pixel selection geometry is constructed of rings of decreasing radius centered at nine different origins (d). When the rings overlap, the phase shifts applied by each ring are added.

by new iterations. Additionally, before selecting the rings, the pixel array is grouped into "macropixels" of 36 pixels (6x6) to avoid large power loss due to diffraction.

For the measurements presented here, 12 sizes of rings (or 108 iterations total) are used. For the raster and spiral geometries, 110 pixel blocks are used. Thus, the four algorithms have a comparable number of iterations. For all geometries, eight measurements spanning 2π radians phase shift are made for each iteration.

3.4 Results

The enhancement as a function of iteration number for the four pixel selection geometries are shown in Fig. 3.4. The enhancement is calculated as the intensity of light in the region of interest on the CCD divided by the initial intensity of light in the same region. As can be seen in the figure, the enhancements at the end of the algorithm cycle are comparable. However, the speed at which they reach that level depends on how quickly the algorithm optimizes the center pixels in the 2d pixel array. This is intuitive because the laser beam contains more power in that region.

A simple simulation was done to verify the results of the spiral pixel selection geometries. The intensity of the light detected by the CCD is simulated via the equation [48]

$$|E_m|^2 = \frac{1}{N} \left| \sum_n^N t_{mn} A_n e^{i\phi_n} \right|^2$$

where only one output channel ($m = 1$) is measured, t_{mn} is the transmission matrix of the scattering material, A_n is the 2 dimensional amplitude distribution of the laser (Gaussian), ϕ_n is the phase shift applied by the spatial light modulator, and N is the number of pixel groups (110). t_{mn} is approximated using a complex random Gaussian distribution [48]. While in reality the elements of t_{mn} are correlated [108], this approximation of uncorrelated elements still provides insight into the improvement of optimization algorithms for

41
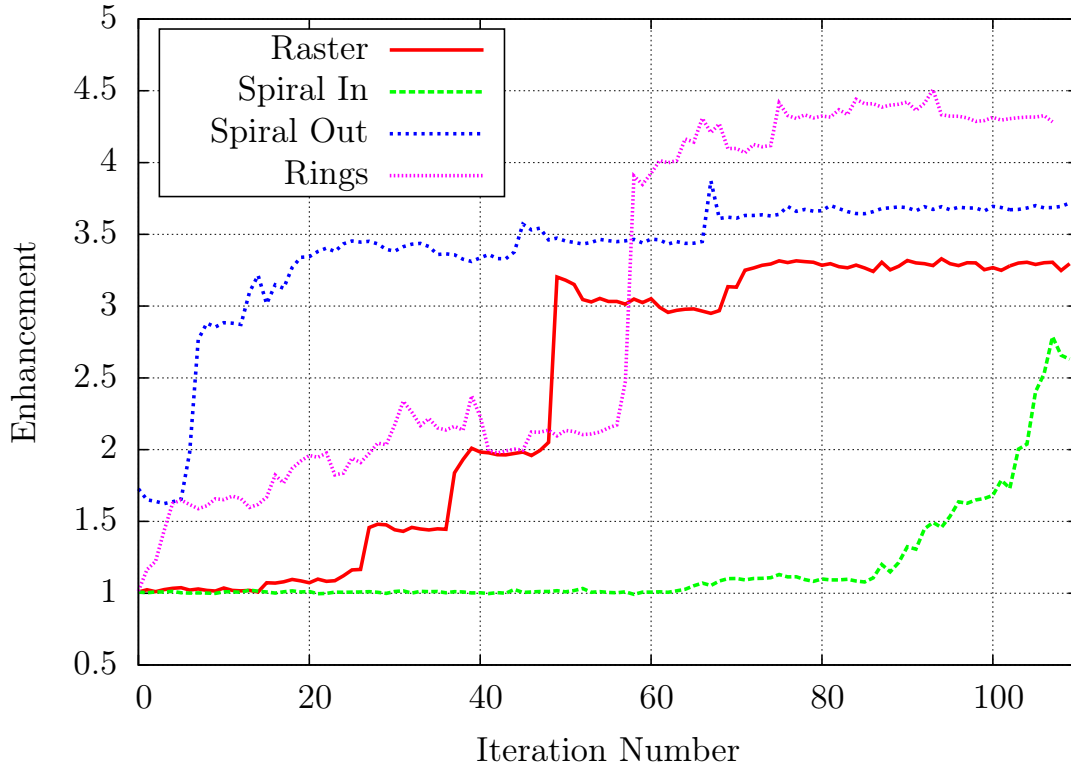
Figure 3.4: Optimization results for four different pixel selection geometries for one complete loop of the continuous sequential algorithm.

the case of focusing.

The simulation results are shown in Fig. 3.5 for zero measurement noise (a) and for noise on the order of $0.1I_0$ (b). In both cases, the spiral out geometry enhances the focus more quickly than the other geometries. This effect comes from the A_n coefficients, which are chosen to mimic the Gaussian profile of the laser beam. Since the center of the beam contains more laser power, modulation of those pixels first returns larger enhancement earlier on in the optimization process. For the zero noise case, the algorithms converge to the same enhancement after a full cycle. However, when noise is introduced, the spiral out geometry does slightly better. This demonstrates the benefit of enhancing the system above the noise earlier on rather than later in the algorithm cycle.

(a) No noise   (b) 10% noise
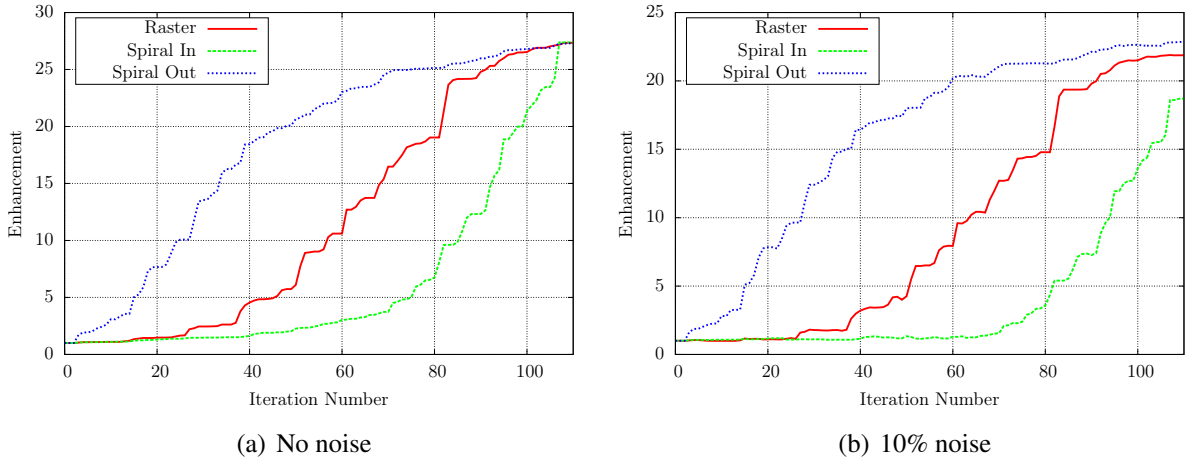
Figure 3.5: Simulation results for the raster and spiral pixel selection geometries for one complete loop of the continuous sequential algorithm. Results for zero noise (a) and noise of 10% of the initial intensity (b) are shown. Note that for the zero noise scenario, the three geometries result in an identical enhancement.

3.5 Conclusion

In conclusion, we have proposed and experimentally evaluated three variations of the continuous sequential algorithm for wavefront optimization. These variations provide insight into possible ways to improve the optimization algorithms of wavefront shaping. Mainly, by first selecting the region where laser light is brightest on the spatial light modulator, the algorithm will have a greater enhancement early on in the optimization process. Additionally, this can be even more beneficial if there is noise in the system since enhancing the signal above the noise early on will improve the sensitivity of the later, less sensitive modulations.

Furthermore, we have presented a pixel selection geometry that takes into consideration the cylindrical nature of the laser beam, but still provides for a symmetry breaking to relate to the random nature of the scattering material. This new geometry performs similar to the standard continuous sequential algorithm, but future modifications to the technique

may prove fruitful. In the very least, it gives new ideas of how faster optimization may be achieved.

The technique of wavefront shaping to control scattered light is a very powerful tool with many diverse applications. More applications will continue to become readily available as further investigation of optimization algorithms improve the speed of enhancement.

4. WAVEFRONT SHAPING ENHANCED RAMAN SCATTERING IN A TURBID MEDIUM*

Spontaneous Raman scattering is a powerful tool for chemical sensing and imaging, but suffers from a weak signal. In this chapter, we present an application of adaptive optics to enhance the Raman scattering signal detected through a turbid, optically thick material. This technique utilizes recent advances in wavefront shaping techniques for focusing light through a turbid media, and applies them to chemical detection to achieve a signal enhancement with little sacrifice to the overall simplicity of the experimental setup. With this technique we demonstrate an enhancement in the Raman signal from TiO_2 particles through a highly scattering material. This technique may pave the way to label-free tracking using the optical memory effect.

4.1 Introduction

The ability to optically detect scattered light with chemical specificity is an integral part of biological imaging, material characterization, and remote sensing [117]. In particular, spontaneous Raman scattering probes molecular energy levels via inelastic scattering off molecular vibrations, which convey chemical information about the sample, and is playing an important role in applications such as biomedical imaging [118, 119], process monitoring, and detection of harmful or explosive substances [106, 120]. Due to low scattering cross section, the signal from Raman scattering is weak, and many approaches have been developed to enhance the amount of Raman signal detected. Among these techniques are coherent anti-Stokes Raman scattering (CARS) [121] and surface enhanced Raman scattering (SERS) [122]. The most recent advancements in Raman spectroscopy have shown

---

substantial signal enhancement as a result of elastic light scattering [23, 123]. These techniques have been very successfully demonstrated, but each method has its own advantages and limitations.

Of particular interest in regards to chemical specific sensing, is the detection of Raman scattering from or through a turbid medium [20]. This is especially important for many practical problems related to biomedical imaging, process monitoring, and security applications, such as explosive and harmful substance detection. A number of emerging technologies such as deep tissue chemical imaging using CARS microspectroscopy, [10, 11] random lasing, [106, 107, 124] and wavefront shaping [53] are being developed to provide a possible solution to different challenging aspects of optical chemical imaging. Furthermore, these techniques, and wavefront shaping in particular, demonstrate ways to not only overcome scattering and interference effects, but to make scattering work in our favor.

Spatially coherent light interacting with a turbid medium produces speckle interference patterns. This is due to the fluctuations in the index of refraction of the material, which means that the optical path of the beam of scattered light is not constant across the wavefront. Since speckle is an interference effect, phase-only modulation via adaptive optics provides the key to manipulation of the speckle pattern. Thus, laser intensity patterns after transmission through a turbid medium can be controlled via phase modulation, or wavefront shaping [53].

Recently, many applications have been demonstrated for the use of feedback controlled wavefront shaping [54]. This technique uses some method of feedback (optical, acoustic, etc.) to drive an optimization algorithm [49, 113, 125] that searches for the optimum phase mask to manipulate the speckle pattern in a desired manner. One of the major applications of these techniques is to image or focus through [53, 57, 60, 98, 100, 102, 111, 126] or around [60] scattering materials. The ability to do so has a clear, direct influence on many biomedical applications [127]. Furthermore, the use of feedback from implanted
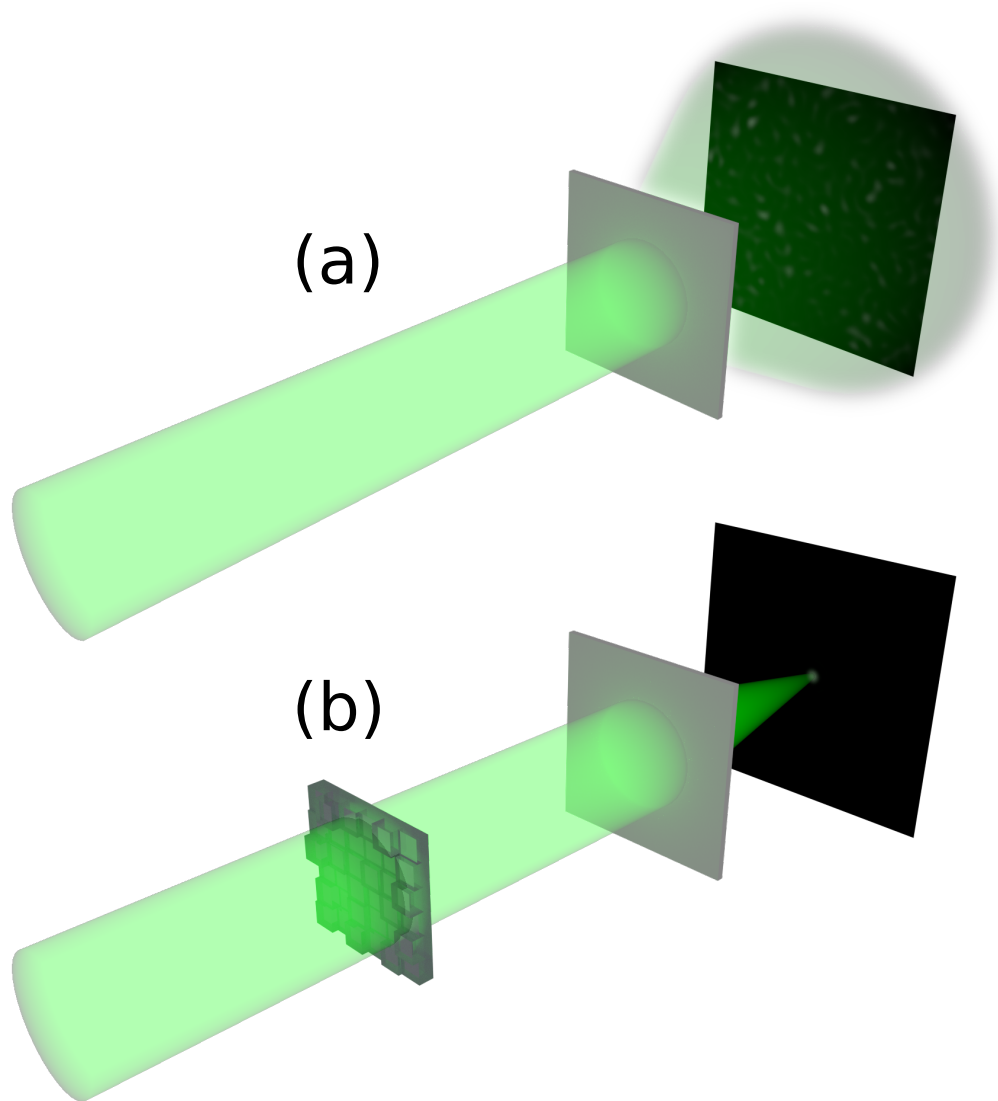
Figure 4.1: Concept of using wavefront shaping to focus laser light on Raman molecules behind a scattering medium. As coherent light scatters through a highly scattering material, it forms a speckle pattern (a). Wavefront shaping techniques can focus the scattered light (b). Enhancement of Raman signal occurs when the Raman molecules are located at the focus.

fluorescent beads in conjunction with the optical memory effect [58,59] has resulted in the ability to image layers of a scattering material at a known depth [50–52, 128].

In this chapter, we experimentally demonstrate the feasibility of Raman signal enhancement in a scattering medium through wavefront shaping. This could be potentially useful for the detection of trace amounts of chemicals inside a scattering medium. As wavefront optimization techniques continue to progress, the use of Raman signal enhancement may also lead to label-free imaging and tracking inside a scattering material.

The concept of wavefront shaping is illustrated in Fig. 4.1. By modulating the phase of the incident beam as shown in Fig. 4.1b, the speckle pattern can be manipulated. With the correct phase mask, a point of constructive interference can be formed in some localized region, effectively focusing the laser beam at this location. This focus is proportional in size to the speckle grain size [57, 129] $S = 1.03(\lambda z/L)$, where λ is the wavelength of the laser, z is the distance from the scattering medium to the focal plane, and L is the diameter of the illuminated spot on the scattering medium. By utilizing Raman scattered light as the feedback for an optimization algorithm, a favorable phase mask can be found that will focus the beam onto the Raman material, enhancing the signal.

4.2   Methods

The experimental setup used to achieve this enhancement is shown in Fig. 4.2a. A half-wave plate and polarizing beam splitter are used to adjust the power and polarization of the beam from a 532 nm diode pumped solid state laser. The polarization is designed to match the phase-only modulation orientation of a two dimensional liquid crystal spatial light modulator (Hamamatsu X10468-7). The laser beam is spatially filtered and expanded to fill the liquid crystal array. The phase modulated beam is imaged via 2 lenses in a 4-f configuration onto the back aperture of a 20x, 0.4 NA microscope objective (Olympus MPlan 20x/0.40). An iris is also placed at the 2f plane of the imaging lenses to remove

48
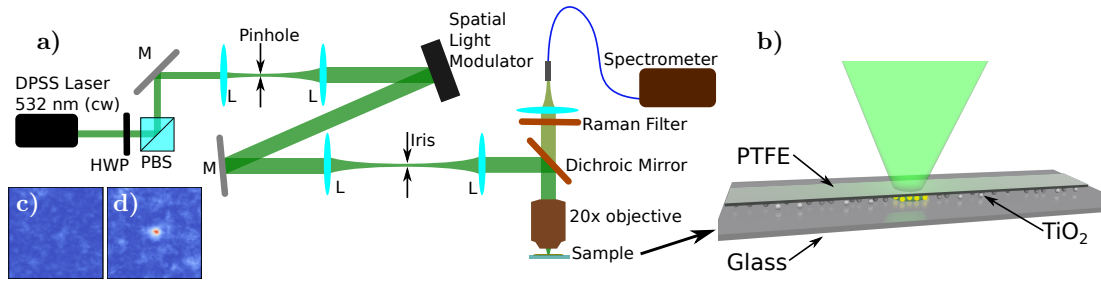
Figure 4.2: Experimental Setup (a). A phase mask is applied to a laser beam from a diode pumped solid state laser (DPSS, 532 nm, cw) by a spatial light modulator. This phase modulated laser beam is imaged onto a sample. The spontaneous Raman scattered light is collected into a spectrometer for detection. M, mirror; L, lens; HWP, half-wave plate; PBS, polarizing beam splitter. A schematic of the prepared sample (b) shows the TiO_2 nanoparticles (550 nm) deposited onto a glass slide, and covered by an approximately 90 μm thick scattering layer (PTFE). Replacing the TiO_2 particles with a ccd demontrates the focusing capabilities of this system (c-d).

the higher order diffraction modes caused by the spatial light modulator. The microscope objective images the phase-modulated beam onto the sample, and collects the spontaneous Raman scattered light in the backward direction.

The use of a 532 nm long-pass dichroic mirror (Semrock LPD01-532RS-25) and another 532 nm long-pass filter (Semrock LP03-532RS-25) allows sufficient rejection of the elastically scattered laser light. The collected Raman scattered light is focused into a fiber bundle which is imaged into a 0.3m Raman spectrometer (Acton Inspectrum). The spectral intensity of selected wavelengths is integrated with respect to the background, and used as feedback for an optimization algorithm to find the best phase mask.

The continuous sequential algorithm [48] in a spiral out geometry [49] is used to find an optimum phase mask for the spatial light modulator. In this algorithm, the wavefront is divided into a grid of pixel groups. Each iteration of the algorithm optimizes a single pixel group starting at the center of the grid and spiraling outward. For each iteration of the algorithm, the phase of the target pixel group is varied from 0 to 2π in 8 steps. This is re-

peated three times, and the results averaged in an effort to reduce noise. Each iteration (24 spectral measurements) takes about 12 seconds. The largest limitation on speed here is the spectrometer integration time. This limitation can be overcome by the use of narrowband tunable filters coupled with a photodiode. Using larger pixel groups increases the signal to noise of the effects of phase modulation on the spectral intensity, but smaller pixel groups allow for better optimization if the modulation signal is above the noise. By starting the algorithm with large pixel groups, and decreasing them for each cycle of the algorithm, both benefits can be realized. Our algorithm uses four stages of pixel-group size starting with 6 groups of 300 by 264 pixels, followed by 16-(150×132) pixels, 100-(60×72) pixels, and lastly by 500-(24×24) pixels. However, most of the enhancement occurred during the first two stages, so for the case of Fig. 4.3, the algorithm was terminated before all 500 pixels in the last stage were optimized. This stresses the importance of a high signal to noise ratio of phase modulation effects over detector noise.

The enhancement capabilities of our setup were characterized by placing a CCD (Mightex CGE-B013-U) 3 cm behind the scattering layer. A focus was generated on a 20x20 pixel region on the CCD by optimizing the wavefront. The intensity of the enhanced focus (Fig. 4.2d) was approximately 20 times greater than that of the average speckle intensity before optimization (Fig. 4.2c). Thus, for a single Raman particle in the field of view, a maximum enhancement of over an order of magnitude could be attainable via focusing. There is a limitation, however, in the detectability of signal from one Raman particle, and a compromise in enhancement is traded for initial detectability.

The samples used (Fig. 4.2b) were prepared by first mixing titanium dioxide (TiO_2) nanoparticles (550 nm) in ethanol. The mixture was deposited onto a glass slide via pipette. After the ethanol evaporated, the dried TiO_2 particles were covered by a piece of polytetrafluoroethylene (PTFE) tape (90 μm thick). PTFE has scattering and transport mean free paths of approximately 6 μm and 60 μm, respectively [130]. This arrangement

50
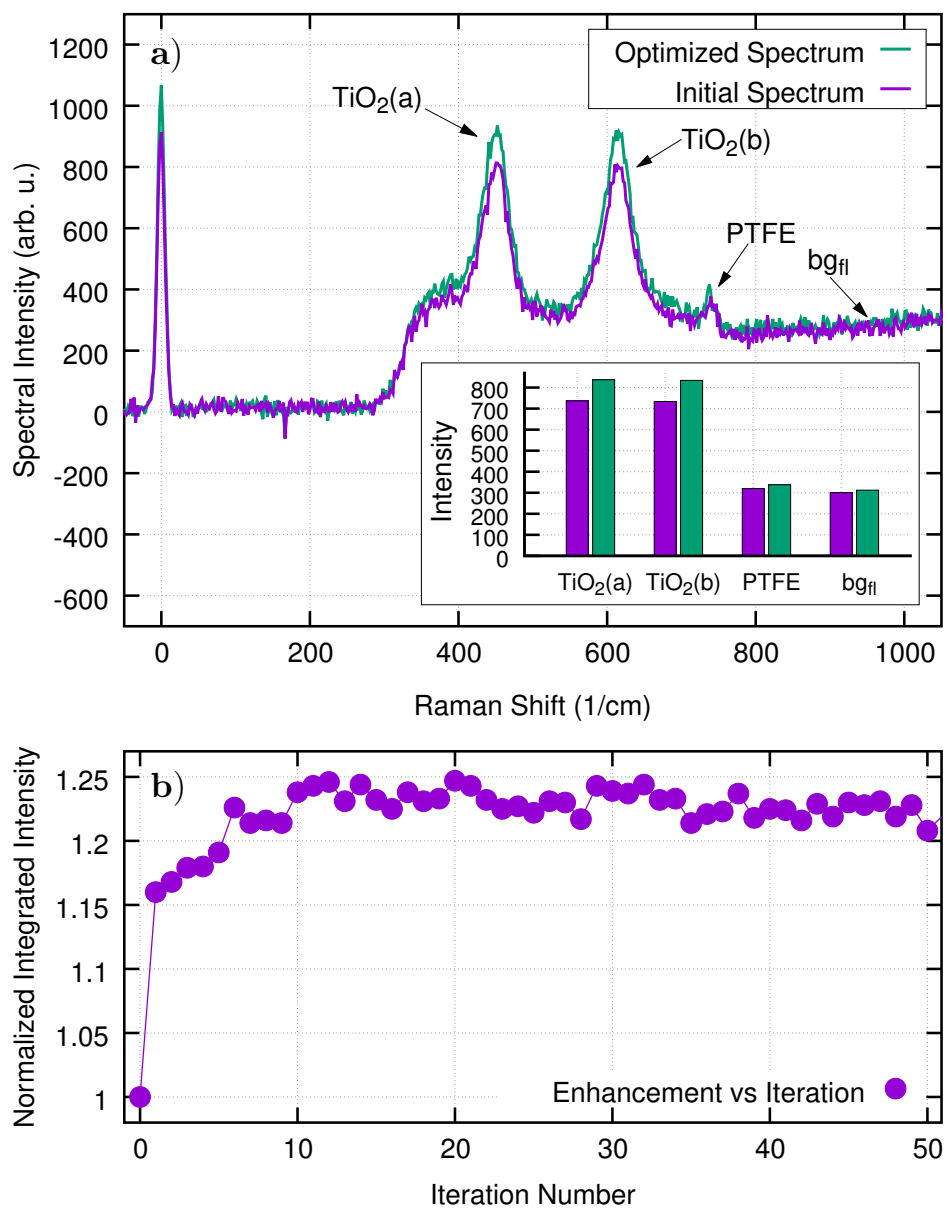
Figure 4.3: Optimized Raman spectrum compared to initial (unoptimized) Raman spectrum (a). The intensity of the Raman peaks integrated over a spectral width of 1 nm are shown in the inset. The integrated intensity of the fluorescent background (integrated over a 10 nm window) is also shown for comparison. The normalized integrated spectral intensity of the two Raman lines of TiO_2 with respect to the fluorescent background is also shown as a function of algorithm iteration (b). The measured value for each iteration is normalized by the initial value to show enhancement.

provided a sample with enough Raman signal to be observed by the spectrometer, but with low enough density of TiO_2 particles for optimization via focusing to be possible. This is necessary because of the nature of the linear feedback of spontaneous Raman scattering. It is also important to note that while our sample is prepared by placing the scattering material on top of the Raman particles, enhancement should work identically if the Raman particles are embedded within the scattering layer [50].

4.3 Results and discussion

By this integration of a spatial light modulator into a typical Raman spectroscopy setup, enhancement of the Raman signal can be achieved. Figure 4.3a shows the enhanced Raman spectrum of TiO_2 nanoparticles behind a scattering layer. The integrated spectral intensity of two of the Raman lines [131] of TiO_2 near 447 cm^{-1} and 612 cm^{-1} are used as feedback for optimization. The inset of Fig. 4.3a shows the spectral intensity of each Raman peak averaged over a 1 nm band before and after optimization. This indicates that the enhancement of these two peaks comes from better focusing onto the TiO_2 particles because the signal from the background fluorescence is relatively unaffected (increase is less than 4%). Furthermore, as shown in Fig. 4.3b, over 20 percent enhancement of the integrated intensity of the two Raman lines with respect to the fluorescent background is achieved within 10 iterations of the optimization algorithm [49].

It is important to consider the size of the Raman active particles when looking for a good enhancement of the signal. If the entire area illuminated by the laser light were to consist of a uniform distribution of Raman active material, there is no enhancement in signal for a focused beam versus an unfocused speckle pattern. In either case, the total power interacting with the molecules is the same. This is due to the linear dependence of spontaneous Raman scattering on pump intensity [132]. Likewise, if the Raman material does not cover the entire area, but is still orders of magnitude larger than the speckle
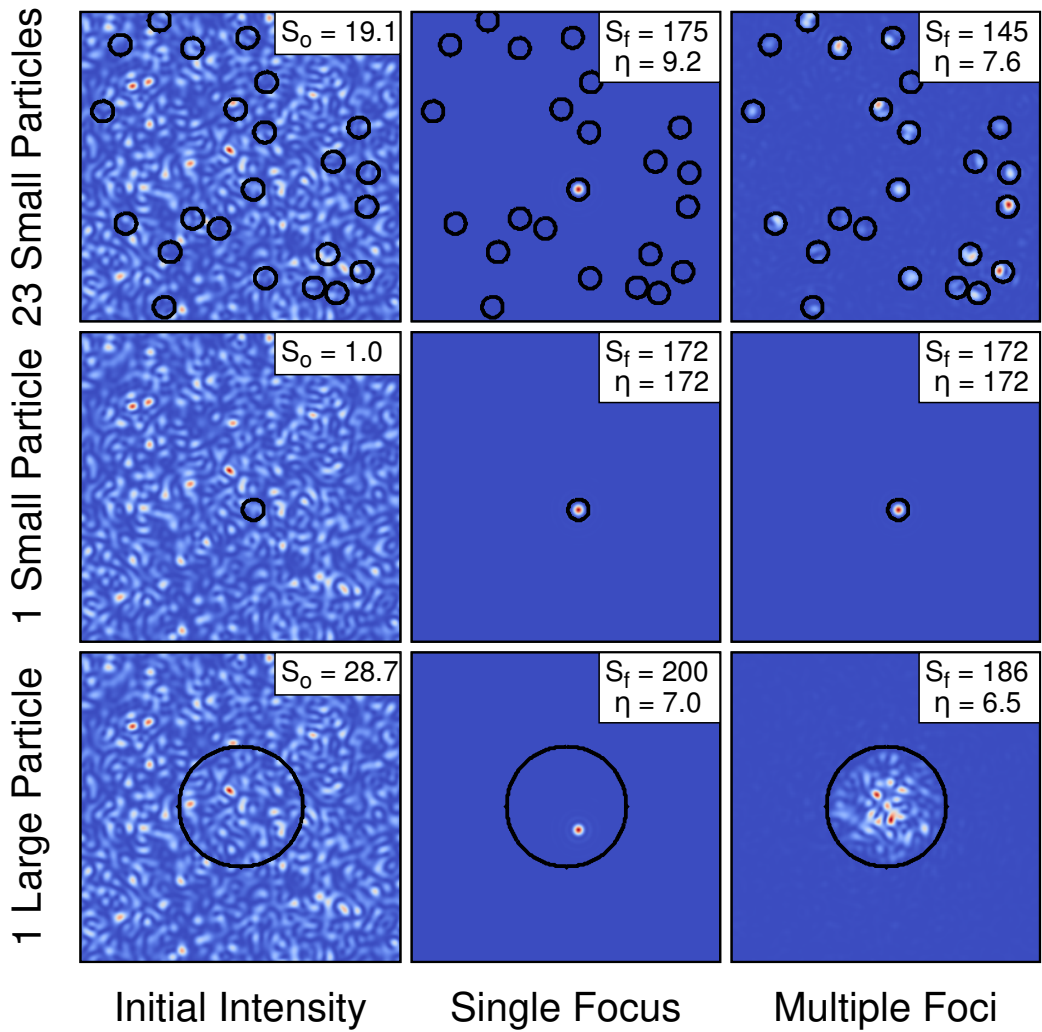
Figure 4.4: Simulation results illustrating the importance of particle size for optimization. The signal is estimated as the sum of the field (colormap) contained in the region of the particles (rings). The signal before (S_o) and after (S_f) focusing to either a single point (middle) or multiple points (right) is normalized to the signal measured from one small particle before focusing (left). The respective enhancement to the measured signal ($\eta = S_f/S_o$) is shown in each image.

size, as illustrated in Fig. 4.4, the enhancement will be averaged out by the many modes not enhanced that still interact with the molecules [54]. In such cases, enhancement from wavefront shaping is still possible by improving the total transmission through the scattering layer [108]. However, since this optimization is non local, it is more difficult to achieve. On the other hand, for the case of focusing, optimization is most easily achieved if the size of the Raman molecules is on the order of the speckle size. Additionally, for the same reasons, the fewer the number of particles in the field of view, the greater the possible enhancement (see Fig. 4.4). Therefore, this technique works best for scenarios where the enhancement of signal from small concentrations of chemicals is desired.

Since the speckle size, and therefore the size of the focus, is directly proportional to the distance from the scattering material to the molecules, the enhancement of the signal is also directly proportional to this distance. This means that the closer the Raman material is to the scattering layer, the smaller the optimum size of the Raman material for enhancement. This effect can be somewhat mitigated by the adjustment of the laser spot size on the scattering layer via focusing optics. However, this is limited on one end by the diffraction limit, and on the other by laser beam power. Taking this into account, it may be possible to measure the distance to the Raman particle (if the particle size is known) or the particle size (if the distance is known) via the enhancement of the Raman signal.

These results may also be directly applied to applications already demonstrated of imaging through a turbid medium [50–52, 128]. In the cited cases, a fluorescent bead provides feedback for the optimization algorithm. By optimizing the feedback, they focus onto the fluorescent bead. An image is then acquired via the optical memory effect [58,59]. For small enough changes to the angle of the incident wavefront (linear phase offset as a function of transverse position), the scattering matrix is approximately the same. At the focus, the linear phase offset becomes a small adjustment to the position of the focus. Thus, the area immediately surrounding the fluorescent bead can be scanned and imaged.

54

Using Raman scattering instead of fluorescence will improve this technique because Raman scattering does not suffer from photobleaching [50]. Furthermore, some scattering samples of interest may already have Raman active chemicals at a known depth. This would remove the need for implanting a probe into the material, thus facilitating a label-free imaging. Additionally, as focusing optimization techniques improve in speed [133], label-free imaging and tracking in real time will become a possibility. The extension of this method into imaging via the optical memory effect requires a single focus. This has been demonstrated for samples with many fluorescent particles, and is achieved via multiple cycles of the optimization process [52]. Nonlinear feedback, such as stimulated Raman scattering, should further improve the ability to produce a single focus [134].

4.4 Conclusion

In conclusion, we have proposed and experimentally demonstrated the enhancement of spontaneous Raman scattering observed through a turbid medium. This technique should work for scattering layers with many mean free paths of optical thickness. More sensitive detectors will extend this depth since some initial signal is necessary for the optimization algorithms used here. Many techniques have been applied to Raman spectroscopy in order to enhance the signal detected. While the approach presented here does not achieve similarly large enhancements, it is simple to implement, quick to run, and, for the correct sample, very valuable. Furthermore, the optimization of the wavefront of the incident laser beam focuses the laser beam tighter onto the Raman active particles, thereby enhancing the detected signal. Thus, if used in conjunction with the optical memory effect, this technique may provide a method for label-free imaging beneath the surface of a scattering layer.

5. ENHANCED SECOND HARMONIC GENERATION EFFICIENCY VIA WAVEFRONT SHAPING

Optical second harmonic generation is a fundamental nonlinear effect with a large impact on laser technology and optical imaging/sensing. For most practical applications of second harmonic generation, high conversion efficiency is required. However, many techniques used to achieve high efficiency are limited to fabrication methods and optical energy requirements. Here, we investigate and demonstrate substantial enhancement in the conversion efficiency of second harmonic generation in a nonlinear crystal via the application of wavefront shaping. In a one-dimensional understanding of second harmonic generation, a phase offset applied to the fundamental wave has no effect on the intensity of the generated light. We show that when the pump field is not a plane wave, enhanced conversion efficiency can be controlled by the application of a phase mask to the fundamental beam. This investigation of the dependence of conversion efficiency upon the transverse phase profile of the incident pump laser yields the promise of new ways to enhance nonlinear generation with limited optical energy and without the need for specific fabrication techniques.

5.1 Introduction

Optical second harmonic generation (SHG) was the first discovered nonlinear optical effect [135], and is now widely used for wavelength conversion, for example, in "green" laser pointers, optical sensing and chemical structure assessment [136–140], and biomedical imaging [14, 141, 142]. For example, second harmonic generation imaging microscopy has been used to image molecular structures [14] such as collagen [143] in tissues. This is useful for the detection and research of cancer [13], fibrosis, and connective tissue disorders [15, 143].

The conversion efficiency of a nonlinear process is a critical parameter for practical applications. Over the years, multiple methods have been used to improve the efficiency of second harmonic generation processes including the selection of the nonlinear material [144, 145], interaction length of the crystal [144, 146, 147], the use of higher intensities [147], photonic crystals [148], or periodic poling [149], to name a few. When it comes to nonlinear biomedical imaging and sensing, the above methods are not always applicable; however, the strength of the signal generated through a nonlinear optical interaction will determine the ultimate sensitivity and imaging speed and depth [150]. It is therefore imperative to explore new ways to increase the nonlinear conversion efficiency. These advances will likely come from our better understanding of the nonlinear optical process in all three dimensions, and, more particularly, from better understanding of the transverse phase profile on the incident fundamental beam.

A one dimensional theory [151, 152] is often sufficient to describe the generation of second harmonic (SH) light. Three-dimensional treatment, however, is necessary when the incident beam is either naturally disturbed by diffraction [153, 154] and scattering [155], or through active preparation of particular beam states ranging from Gaussian [153, 156, 157] to Bessel [158–160] and other sophisticated [161–164] beams states. Other instances that require three-dimensional treatment include the treatment of artificial gauge fields in photon fluids [165], SHG from photonic crystals [166], intensity-dependent phase shifts due to pump fields that are not plane-waves [153, 167], as well as shaping of the second harmonic beam through facet engraving [168], nonlinear holography [169, 170], and plasmonic metasurfaces [164].

Of particular interest is the treatment of nonlinear generation when the wavefront of the pump beam is non-uniform. In the one dimensional case (plane wave), a phase shift in the fundamental beam has no impact upon nonlinear generation. However, when the pump beam is not a plane wave, shaping of the wavefront does have an effect on the nonlinear

57
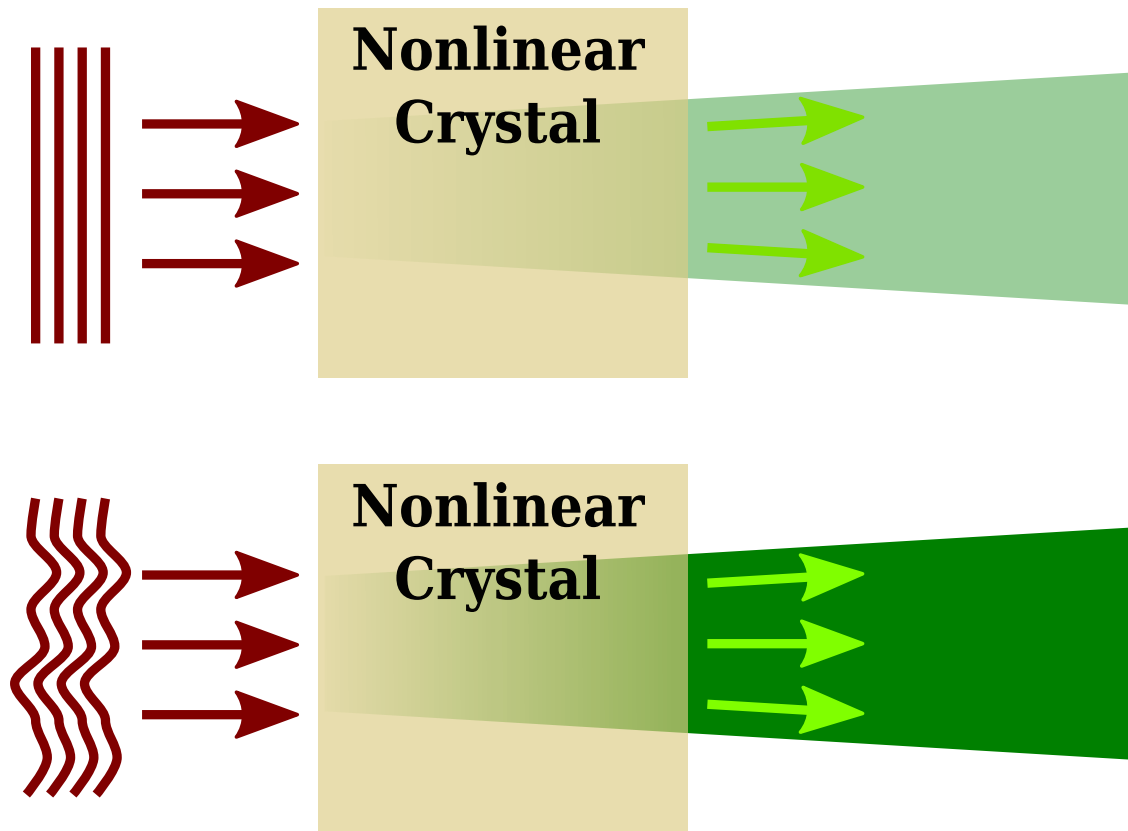
Figure 5.1: Control of the second harmonic generation conversion efficiency is realized by application of a phase mask to the incident fundamental wave.

process. For example, the transverse mode (beam state) of second harmonic light can be controlled by changing the phase profile of the incident fundamental beam [171].

Recent advances in wavefront shaping techniques [48, 49, 172] and technologies [54, 127] have provided efficient and accurate tools to modify the phase profile of a laser beam. These tools include search algorithms for feedback-based optimization [48, 113] of the applied phase mask. In situations with substantial scattering, wavefront shaping has been used to enhance the intensity of second harmonic generation [41, 134]. In this case, wavefront shaping modifies constructive interference due to scattering; effectively creating a tighter, more intense focus of the fundamental beam [57, 155]. The enhanced intensity at

the focus causes an increased second harmonic conversion.

In this report, we present theoretical and experimental results which indicate that in the regime of little or no scattering, wavefront shaping of the fundamental beam not only controls the beam shape, but also substantially impacts the intensity or conversion efficiency of second harmonic generation, as conceptually illustrated in Fig. 5.1. This effect is demonstrated using second harmonic conversion efficiency from a nonlinear crystal (with no scattering present) as a feedback parameter. The utilization of search algorithms with this feedback parameter produces a phase mask for which the generation efficiency is enhanced. We show enhancements in second harmonic conversion efficiency as high as an order of magnitude by implementing an iterative search algorithm. These results may impact laser technologies in the form of lower input powers required for frequency doubling, as well as increasing the sensitivity of second harmonic biomedical imaging and other detection/sensing techniques. These results should also translate to many other nonlinear optical conversion methods.

5.2 Theoretical model

Second harmonic generation is modeled via the three-dimensional wave equation [152, 153, 173]

$$\nabla^2 \tilde{E}_j - \frac{n_j^2}{c^2} \frac{\partial^2 \tilde{E}_j}{\partial t^2} = \frac{1}{\epsilon_o c^2} \frac{\partial^2 \tilde{P}_j}{\partial t^2} \tag{5.1}$$

where $j = 1, 2$ represent the fundamental and second harmonic fields ($\omega_2 = 2\omega_1$), respectively, n_j is the refractive index for the jth field, ϵ_o is the permittivity of free space, and c is the speed of light. The electric field and nonlinear polarization are given by

$$\tilde{E}_j(\boldsymbol{r}, t) = \tilde{A}_j(\boldsymbol{r}) e^{i(k_j z - \omega_j t)} + c.c.$$

$$\tilde{P}_j(\boldsymbol{r}, t) = \tilde{P}_j(\boldsymbol{r}) e^{-i\omega_j t} + c.c. \tag{5.2}$$

59

The tilde indicates complex variables, $\tilde{A}$ is the complex field amplitude, and for second harmonic generation, $\tilde{P}_j$ is written as [152]

$$\tilde{P}_1(\boldsymbol{r}) = 4\epsilon_o d_{\text{eff}} \tilde{A}_2 \tilde{A}_1^* \, e^{i(k_2 - k_1)z}$$
$$\tilde{P}_2(\boldsymbol{r}) = 2\epsilon_o d_{\text{eff}} \tilde{A}_1^2 \, e^{2ik_1 z}$$

(5.3)

Here, d_{eff} is the effective nonlinear coefficient [145] of the medium. Solution of the wave equation (Eq. (5.1)) yields the intensity of the two frequencies of light via the relation

$$I_j = 2n_j \epsilon_0 c \left| \tilde{A}_j(z) \right|^2 .$$

(5.4)

Substitution of Eq. (5.2) into Eq. (5.1), and application of the slowly varying approximation yields a differential equation for the complex amplitude [153],

$$\frac{\partial \tilde{A}_j(\boldsymbol{r})}{\partial z} = \frac{i}{2k_j} \nabla_\perp^2 \tilde{A}_j(\boldsymbol{r}) + \frac{i(\omega_j)^2}{2k_j \epsilon_o c^2} \tilde{P}_j(\boldsymbol{r}) e^{-ik_j z}$$

(5.5)

The dependence of the field amplitude on the transverse phase is more apparent by explicitly writing the amplitude and phase as

$$\tilde{A}_j(\boldsymbol{r}) = A_j(\boldsymbol{r}) e^{i\phi_j(\boldsymbol{r})},$$

and separating the real and imaginary parts of Eq. (5.5). This yields the following system

of equations.

$$\partial_z A_j(\boldsymbol{r}) = \frac{-1}{2k_j}\left\{2\left[(\partial_x A_j)(\partial_x \phi_j) + (\partial_y A_j)(\partial_y \phi_j)\right]\right.$$

$$\left. + A_j \nabla_\perp^2 \phi_j\right\} + (-1)^j F_j \sin\left(\Delta k z + \Delta\phi\right)$$

$$A_j \partial_z \phi_j(\boldsymbol{r}) = \frac{-1}{2k_j}\left\{A_j\left[(\partial_x \phi_j)^2 + (\partial_y \phi_j)^2\right] - \nabla_\perp^2 A_j\right\}$$

$$+ F_j \cos\left(\Delta k z + \Delta\phi\right) \tag{5.6}$$

where $\Delta k = k_2 - 2k_1$, $\Delta\phi = \phi_2 - 2\phi_1$, and

$$F_1 = \frac{2\omega_1^2}{k_1 c^2} d_{\text{eff}} A_2 A_1, \quad F_2 = \frac{\omega_2^2}{k_2 c^2} d_{\text{eff}} A_1^2. \tag{5.7}$$

From the equations in this form, we see that the amplitude has a dependence upon the transverse gradient of the phase. As opposed to the one-dimensional case (plane wave), these terms will survive the absolute value in Eq. (5.4). Thus, a phase mask applied to the fundamental beam will influence the intensity or conversion efficiency of the generated light.

5.3 Methods

5.3.1 Experimental setup

The experimental setup is illustrated in Fig. 5.2. Here, a phase mask was applied to a 1064 nm, 6 picosecond laser pulse (Attodyne APLX-1064-532) by a liquid crystal on silicon spatial light modulator (LCOS-SLM, Hamamatsu X10468-08). Prior to phase shaping, the beam was expanded by a telescope to fill more of the active region of the spatial light modulator. A half-wave plate and polarizing beam cube were used to control the power and set the polarization to the phase-only modulation orientation of the LCOS-SLM. The phase mask applied to the beam was imaged onto the face of a nonlinear crystal
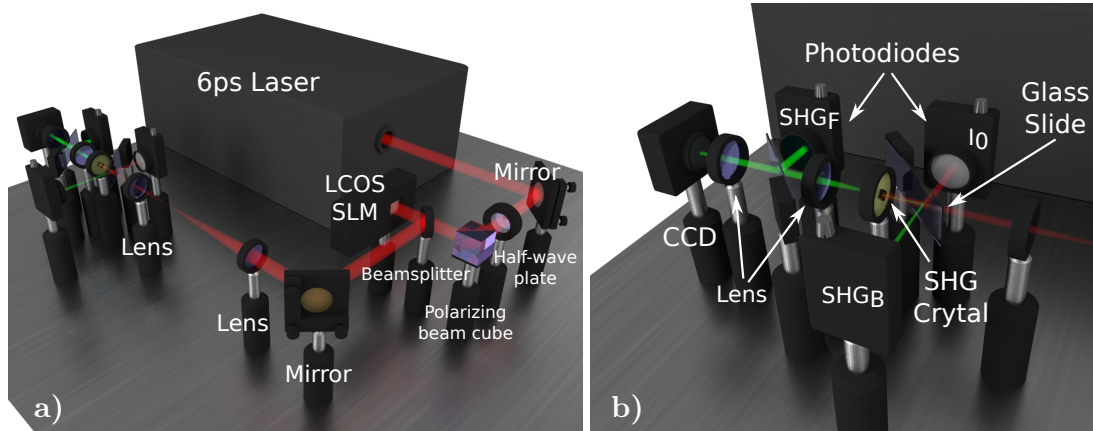
Figure 5.2: Experimental setup. (a) The spatial phase of a 6 picosecond laser pulse was modified via spatial light modulator (SLM). The phase mask was imaged onto the sample with a 4-f imaging setup. For enhanced generation from a nonlinear crystal (b), the forward and backward generated signals (SHG_F, SHG_B) as well as a reference signal (I_0) were collected with photodiodes. These signals were used to create metrics that drove an optimization algorithm to enhance the second harmonic generation by wavefront shaping.

using lenses in a 4-f imaging configuration. The magnification of the lenses (Thorlabs, AC254-400-C-ML, AC254-050-C-ML) was chosen to ensure that the shaped pulse was smaller in diameter (0.7 mm, FWHM) than that of the nonlinear crystal (5 mm).

The second harmonic light was generated by a Potassium Titanyl Phosphate ($KTiOPO_4$, KTP) nonlinear crystal (type II, rotated $45°$ with respect to the beam polarization). The pulse energy incident upon the crystal was approximately 2.3 μJ with a repetition rate of 10 kHz. The crystal was phase matched by hand and the orientation was rotated about the optical axis to optimize the conversion efficiency of the unshaped pulses. The second harmonic light generated (532 nm) was detected in both the forward and backward directions using large area photodiodes (Thorlabs DET100A) with glass color filters (Thorlabs FGB39) to reject the fundamental. The light detected in the backward direction was likely due to reflections from the back surface of the crystal, and was separated from the incident

fundamental for detection by reflection off a glass slide (1 mm thick). This same glass slide was also used to direct a small proportion of the incident beam into an additional large area photodiode (Thorlabs DET100A) to be used as a reference. Both the reference beam and the forward generated beam were further attenuated by neutral density filters with 2 OD (Thorlabs ND20B, ND10B) placed directly before the photodiodes.

The signal from the photodiodes was collected and averaged 128 times by an oscilloscope (Agilent DSO6034A). This signal was used as feedback (I_2/I_1) for an optimization algorithm which searched for a favorable phase mask to enhance the feedback metric; conversion efficiency in this case. A genetic algorithm [113] with a population of 20 individuals cycled over 800 generations was used as the optimization algorithm. The results from this algorithm were compared with those from a continuous sequential algorithm [48] in an outward spiral configuration [49] and found to be similar. Therefore, only results from the genetic algorithm have been presented here. Because the spatial resolution of the spatial light modulator does have influence on the magnitude of the results, two different pixel sizes were used by grouping the pixels of the spatial light modulator into macropixels composed of either (60×72) or (24×24) pixels. For the large or small macropixels, there were a total of (10×11) or (25×33) macropixels in the modulator array, respectively. The genetic algorithm was allowed to select a value between 0 and 2π as the phase delay for each of the macropixels.

After wavefront optimization via the search algorithm, an image of the output from the nonlinear crystal in the forward direction was acquired using imaging lenses (Thorlabs, AC254-035-A-ML, AC254-045-A-ML) and a charge-coupled device (CCD) (Mightex CGE-B013-U). The lenses were placed such that the back surface of the crystal was imaged to the CCD. A glass color filter (Thorlabs FGB39) was used to reject the fundamental light when imaging the generated second harmonic (532 nm). A cold mirror (Thorlabs M254C00) was used to reject the second harmonic light when imaging the fun-

damental. These filters were interchanged without disruption to the alignment. Furthermore, neutral density filters were used to avoid saturation of the CCD in both cases. Care was also taken at each stage to prevent reflections from optics in the forward direction from propagating back into the nonlinear crystal.

5.3.2 Numerical simulations

Comparison of the experimental results with second harmonic theory were performed via numerical simulation of Eq. (5.5). Here, a spectral method in the transverse direction [153], with a grid of 128×128 points, was used in conjunction with a finite difference step in the propagation (z) direction. Enhancements for a total propagation distance of both 5 mm and 10 mm were computed with 128 and 256 total steps in the z direction, respectively. This grid size was sufficient to produce results comparable to established theory for flat wavefronts [153]. Here we used an initial fundamental beam waist of 0.7 mm and intensity of 2×10^6 W/cm^2 (9.8×10^3 W total power). We assumed the effective nonlinear coefficient to be $d_{\text{eff}} = 1.4$ cm/V, and the index of refraction, $n = 1.8$ for both the fundamental (1064 nm) and second harmonic (532 nm) waves [145]. It is also important to note that the simulation assumes that phase matching conditions are satisfied (i.e. wavevector mismatch is zero). The simulation receives a phase mask as input, and calculates the output intensity distribution.

A genetic algorithm [113] comparable to that used in the experiment was used to drive the simulation to find an optimum phase mask for enhanced second harmonic generation. Here, the generated intensity of second harmonic from a population of 20 fundamental beams with randomly generated phase masks were evaluated and ranked. Each pixel in the phase mask was given a value between 0 and 2π. An individual phase mask in the next generation of masks was created by mixing two masks of the current generation with a random binary template, T. Thus, $\phi^{(n+1)} = T\phi_1^{(n)} + (1 - T)\phi_2^{(n)}$. The two parent phase

masks were randomly chosen with a triangular weight giving priority to the masks with highest rank. Furthermore, the mutation rate of $R^{(n)} = [(0.088)e^{(-n/\lambda)} + 0.012]$ percent of the pixels of a mask per nth generation were allowed to mutate to a random number between 0 and 2π. Here, the mutation rate decay, λ, ensures that fewer mutations occur after many generations, and was set to 100 for both the simulations and the experiment.

5.4 Experimental results

The enhancement of second harmonic conversion efficiency was experimentally demonstrated (see Methods for details) by applying a phase mask to a 6 picosecond laser pulse with a wavelength of 1064 nm (Attodyne, APLX-1064-532). As depicted in Fig. 5.2, the phase mask was applied to the fundamental pulse with a spatial light modulator (LCOS-SLM, Hamamatsu X10468-08). The applied phase mask was then imaged to a Potassium Titanyl Phosphate (KTiOPO$_4$, KTP) nonlinear crystal (type II, rotated $45°$ with respect to the beam polarization). The second harmonic light generated in both the forward and backward (reflection from back surface) directions was measured with respect to the incident fundamental using large area photodiodes (Thorlabs, DET100A). The conversion efficiency was used as feedback for a search algorithm, which determined an optimum phase mask for enhancement. In this case, we used both a genetic algorithm [113] and a continuous sequential algorithm [48] in an outward spiral configuration [49]. Both algorithms produced similar results; therefore, only results from the genetic algorithm are shown here. Because enhancement may also depend upon the resolution of the phase mask applied, we also show results for phase masks with low resolution (large macropixels) and higher resolution (small macropixels).

The second harmonic conversion efficiency in both the forward and backward directions as a function of algorithm iteration are shown in Fig. 5.3. For comparison, the conversion efficiencies were normalized by the initial (flat wavefront) value, which was 9.7%
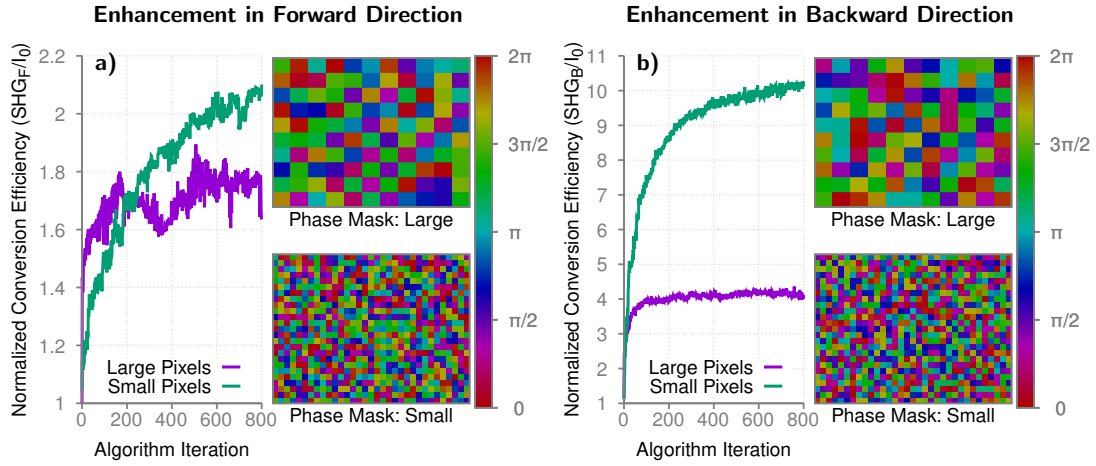
Figure 5.3: Enhanced conversion efficiency of second harmonic generation in in the forward (a) and backward (b) direction from a nonlinear crystal due to wavefront shaping of the fundamental. For both cases, the final phase masks as determined by the search algorithm are shown for large (top) and small (bottom) pixel sizes.

for the forward generated light, and 0.02% for the backward generated light. After 800 iterations, the conversion efficiency was enhanced by a factor of two (19.5%) in the forward direction and as much as an order of magnitude (0.2%) in the backward direction. The final phase masks (both large and small macropixels) as determined by the algorithm are also shown in the figures. Similar results from numerical calculations are shown in Fig. 5.4. As depicted in the figure, numerical simulations were performed for different crystal (propagation) thicknesses. Different enhancements were achieved based upon the crystal lengths, but these enhancements are not necessarily linear with propagation distance. Here, the conversion efficiency was enhanced from 4.4% to 15.2% for a 5 mm propagation length, and from 2.3% to 23% for a 10 mm propagation length. If the reflection efficiency from the back side of the crystal is taken into account, these values correspond to an enhancement in conversion efficiency in the backward direction from 0.01% to 0.1%. The optimum phase masks calculated by the simulation are also shown in

66
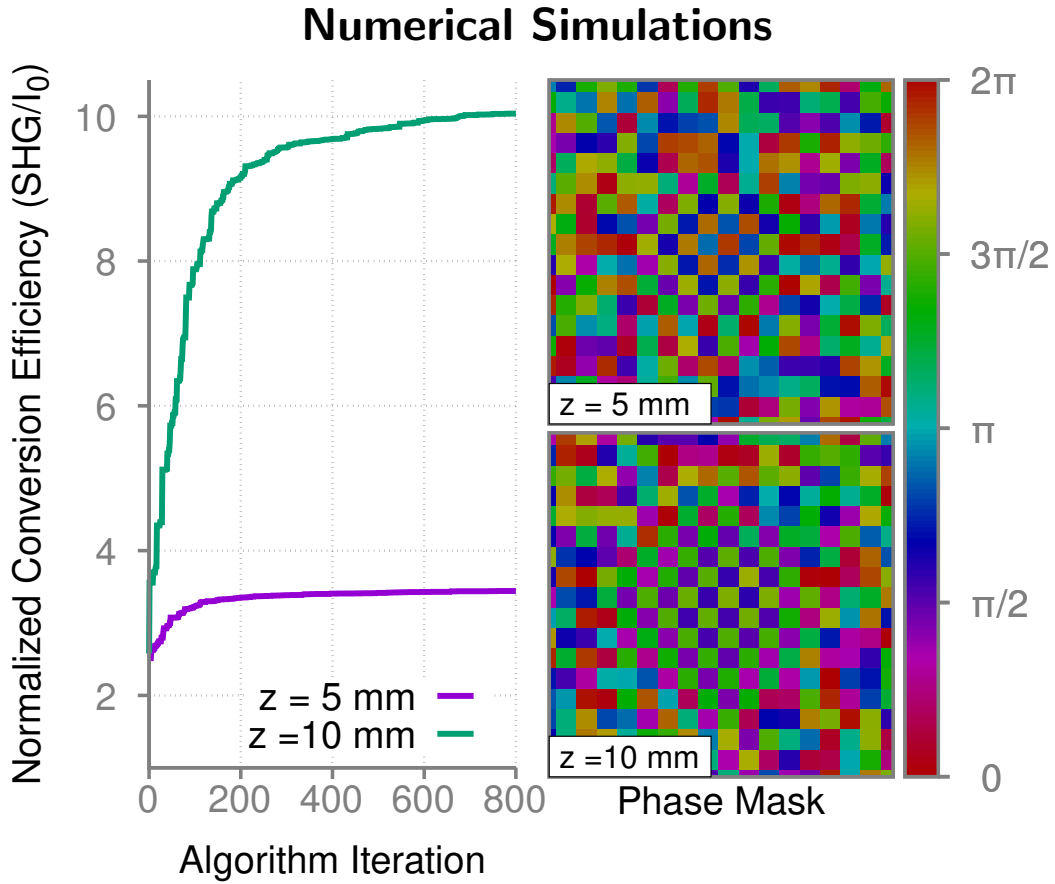
Figure 5.4: Simulated enhancement of second harmonic generation via wavefront shaping for different interaction lengths (left). The optimized phase masks are shown on the right.

Fig. 5.4. Here, the phase pattern more clearly shows a checkerboard-like behavior. This is visible in the experimental results, but not quite as clearly due to experimental factors such as noise and slight aberration effects. This behavior, with large jumps in the phase, gives sharp jumps in the transverse gradient of the phase which in turn effects the conversion efficiency (see Eq. (5.6)).

The transverse intensity profile before and after wavefront shaping of the fundamental and second harmonic pulses are shown in Fig. 5.5. Here, a grid-like pattern in both the fundamental and second harmonic profiles is caused by the wavefront shaping. This causes

Fundamental Profile

Flat wavefront, Large pixels   Shaped wavefront, Large pixels

Flat wavefront, Small pixels   Shaped wavefront, Small pixels

Second Harmonic Profile

Flat wavefront, Large pixels   Shaped wavefront, Large pixels

Flat wavefront, Small pixels   Shaped wavefront, Small pixels
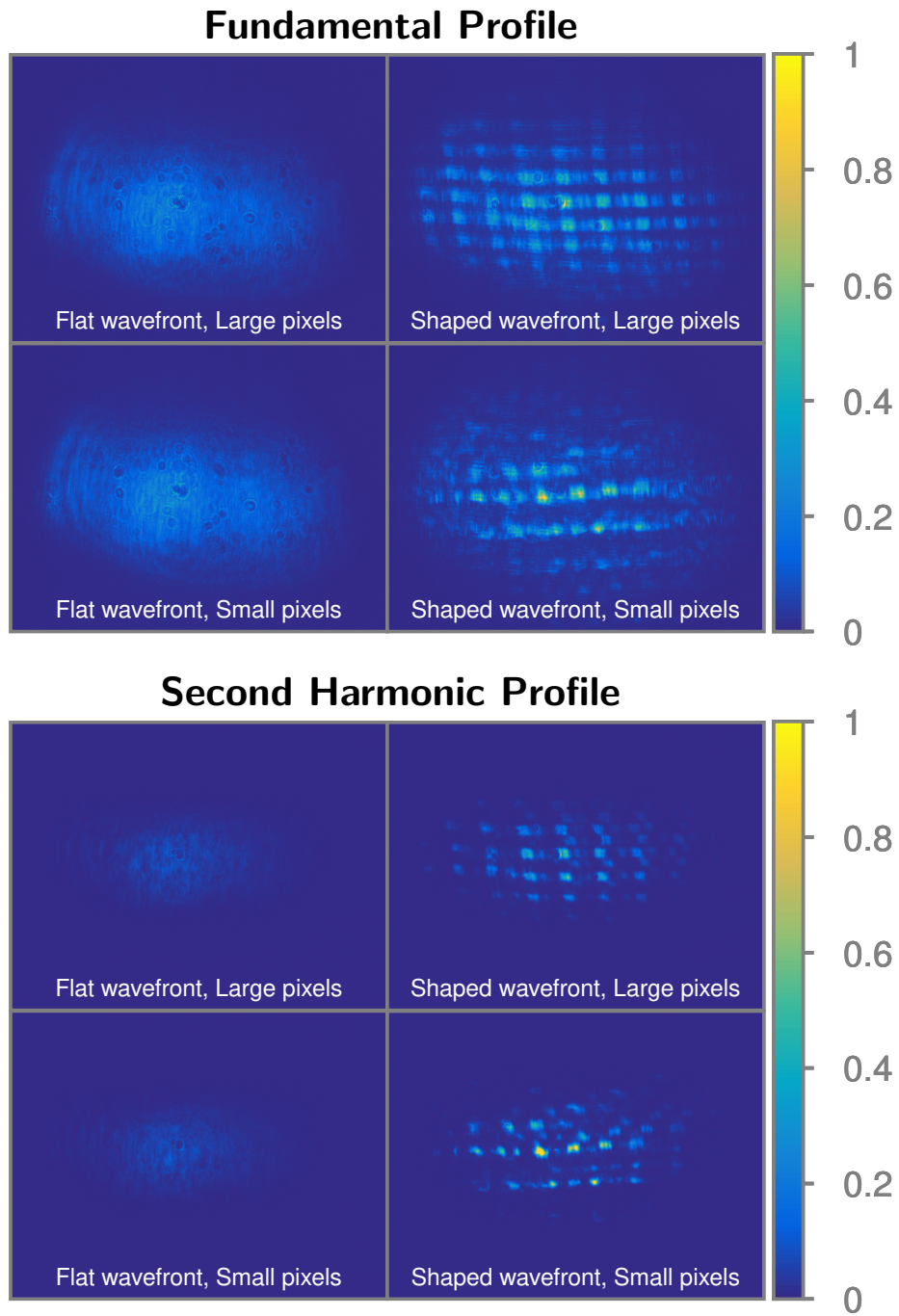
Figure 5.5: Transverse profile of fundamental (top) and second harmonic (bottom) pulse after the nonlinear crystal with (right side) and without (left side) wavefront shaping applied. Both large and small pixel sizes where used for wavefront shaping.
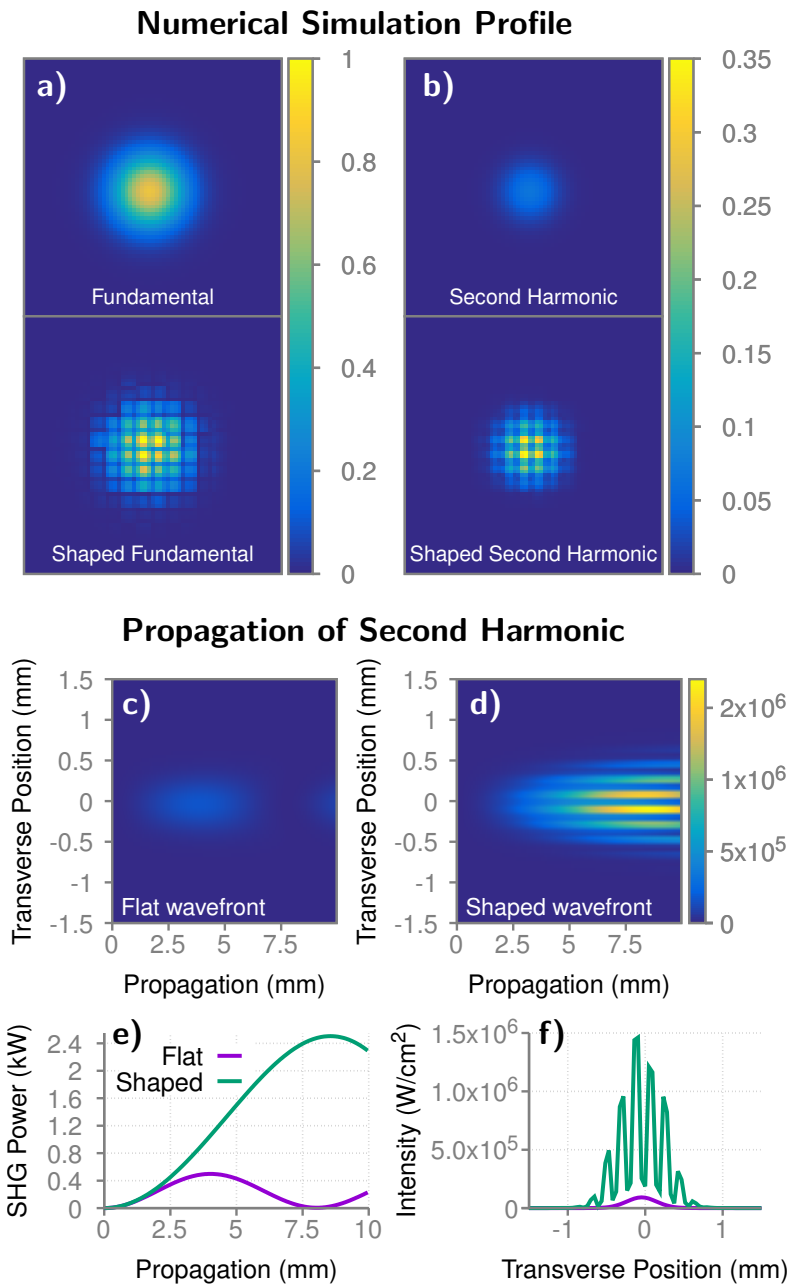
Figure 5.6: Transverse profile of simulated fundamental (a) and second harmonic (b) pulse after the nonlinear crystal with and without wavefront shaping applied. A cross section of the simulated second harmonic intensity inside the interaction region is also shown for flat (c) and shaped (d) incident wavefronts. Integration of the intensity over the transverse direction gives the power as a function of propagation distance (e). A slice of the intensity at the output of the crystal is also shown (f).

localized positions in the profile with intensities much brighter than those without shaping. Numerical simulation results showing similar behavior are shown in Fig. 5.6a-b. Here, a grid-like pattern caused by the shaped wavefront is also observed in the fundamental and generated light at the output of the interaction region.

5.5 Discussion

Further analysis of the theoretical model provides more insight into the effects of wavefront shaping upon second harmonic generation. Taking a cross-section of the second harmonic intensity as is propagates through the crystal (Fig. 5.6c-e) shows that after long propagation distances, the energy in the second harmonic field pumps back into the fundamental field. At this point, it is important to recall that the simulation assumes the wave-vector mismatch is zero ($k_2 = 2k_1$). This behavior was also observed by Sheng et al [153] and is due to diffraction and the complex interplay between second harmonic generation and propagation effects when the pump beam is not a plane-wave [167]. When wavefront shaping is applied, this parametric pumping of energy back into the fundamental field is counteracted, and the harmonic field continues to grow. Integration over the transverse direction shows this effect in the average power as a function of propagation distance (Fig. 5.6e). This indicates that the enhancement attainable via wavefront shaping is dependent upon the length of the crystal. This dependence is not necessarily linear with crystal length, but it depends upon where the turnover in harmonic power occurs with respect to the back surface of the crystal. This length dependence explains the difference in enhancement between the forward and backward direction experimental results. Because the second harmonic light detected in the backward direction was likely due to a reflection from the back surface of the crystal, this light propagated through an effectively thicker nonlinear medium.

A slice through the brightest points of the intensity profile at the output of the crystal is

shown in Fig. 5.6f for both shaped and flat input wavefronts. This gives better perspective to see that not only are the bright intensity spikes enhanced, but the darker regions are at least as bright or brighter than generation from the unshaped fundamental. It also shows how drastic the intensity spikes may be. While this spatial profile may not be ideal for all applications, there are instances, including optical detection, when the spatial profile is less important than the attainment of greater conversion efficiencies.

5.6 Conclusion

In conclusion, we have theoretically and experimentally demonstrated a dependence of second harmonic conversion efficiency upon the spatial phase of the incident fundamental wave. We have shown that the utilization of wavefront shaping techniques can yield a substantial increase to the conversion efficiency of second harmonic generation in nonlinear crystals. These results should apply to other nonlinear effects, and may also be related to artificial gauge fields in photon fluids [165].

Because there is little to no scattering involved in the problem, certain identifiable patterns in the phase mask may be responsible for the majority of the enhancement. This has been observed, with the genetic algorithm converging to a phase mask with checkerboard-like patterns of jumps in phase. Understanding of this phase pattern for specific applications will remove the need for a feedback fed search algorithm. Furthermore, more sophisticated feedback metrics may also provide for the extension of this technique to biological applications including the enhancement of second harmonic images of collagen structures in a mostly transparent sample.

6.   AMPLITUDE PILE-UP IN A PHASE-MODULATED SPECTRUM DUE TO

FEMTOSECOND FILAMENTATION*

In this chapter, I present a method by which the spectral intensity of an ultrafast laser pulse can be accumulated at selected frequencies by a controllable amount. Using a 4-f pulse shaper we modulate the phase of the frequency components of a femtosecond laser. By inducing femtosecond filamentation with the modulated pulse, we can concentrate the spectral amplitude of the pulse at various frequencies. The phase mask applied by the pulse shaper determines the frequencies for which accumulation occurs, as well as the intensity of the spectral concentration. This technique provides a way to obtain pulses with adjustable amplitude using only phase modulation and the nonlinear response of a medium. This provides a means whereby information which is encoded into spectral phase jumps may be decoded into measurable spectral intensity spikes.

6.1   Introduction

The production of femtosecond laser pulses has played a significant role in the advancement of modern science. In addition to their ultrashort pulse duration, femtosecond laser pulses offer a broad spectral bandwidth and a high instantaneous intensity for each pulse [174]. Because of these properties, femtosecond pulses have become a very attractive tool with a wide variety of applications including filamentation [72, 175], communication [176, 177], coherent control [178, 179], metrology [180], micromachining [181], and spectroscopy [182–184]. Of particular interest here is the fact that femtosecond filaments [185] are extremely versatile in application, and have been formed in air [186], wa-

---

ter [187,188], and other condensed media [72,189]. They are used in various types of spectroscopy including remote sensing of the atmosphere [71,190] and filament induced breakdown spectroscopy [191]. They have been used for sub-diffraction imaging [192], and as a trigger and guide to high-voltage discharges [193]. The spectral broadening and pulse compression characteristics of femtosecond filamentation have also been useful in creating pulses with few-cycle pulse duration [194–196]. The filamentation of femtosecond pulses is accompanied by a number of physical effects including conical emission [197], white-light continuum generation, ionization, and nonlinear absorption [198, 199]. In addition to this, femtosecond filaments can propagate for long distances [71,200], making them an attractive mode for laser/filament based communications [177].

In this article, we investigate an approach using phase only pulse shaping with femtosecond filamentation to convert energy from one part of the spectrum of an ultrafast laser pulse to another part of the spectrum. This method may also be used as a possible way to communicate information. In particular, we demonstrate experimental and numerical results wherein the spectral amplitude of a femtosecond laser pulse is accumulated by a controllable amount at selected frequencies. These results have direct impact on the use of femtosecond lasers and filamentation in communication schemes, since in this method, information can be encoded onto a laser pulse with a phase mask, and decoded again as measurable intensity spikes.

A direct result of the broad bandwidth associated with femtosecond pulses is the ability to shape the temporal profile by modulation of the spectral components. This temporal shaping can be done using a 4-f pulse shaper, which consists of a diffraction grating to spatially disperse the pulse into separate frequency components, a lens to perform a spatial Fourier transform, a spatial phase or amplitude mask to modulate the shape, and another lens and grating to recombine and collimate the pulse [65]. Various pulse shaper designs utilize modulation of the spectral amplitude, spectral phase, or both to temporally shape

ultrafast pulses. We use a computer controlled liquid crystal spatial light modulator to apply a phase mask to the pulse as it propagates through the 4-f pulse shaper [63, 64].

One technique that can be implemented with shaped femtosecond pulses is spectral hole filling, which was developed by Warren et al. as a way to detect the onset of two photon absorption [201, 202]. Because nonlinear processes such as two-photon absorption and self-phase modulation alter the frequency content of a pulse, if the input laser pulse contains a spectral hole (i.e. region of missing spectral components), the effect of these nonlinear processes will fill in some of the missing spectral components. Thus, by monitoring the hole in the spectral domain, it is possible to detect the onset of the nonlinear process. This has been shown for both two photon absorption [201] and self-phase modulation [203]. Spectral hole filling has been demonstrated not only to refill a hole but to overfill it via self-phase modulation [204]. This overfilling effect is explained by examining the Fourier decomposition of the pulse into a set of modes in the time domain. A spectral hole is modeled as the destructive interference between frequency modes of the original pulse and quasi-continuous waves of the same frequency. As the pulse undergoes self-phase modulation, the phase of the modes of the original pulse are shifted, while the phase of the quasi-continuous waves are not. Thus, the destructive interference becomes less destructive or even constructive interference depending on the phase shift caused by self-phase modulation. This overfilling was shown to be an intensity dependent effect. Similar studies have investigated spectral hole filling in supercontinuum generation in optical fibers due to phase modulation [205].

In this paper, we present a technique similar to spectral hole overfilling in the regime of femtosecond filamentation. Here, the effect is driven by a phase shift applied by a pulse shaper to a narrow band of frequencies in the pulse, rather than by a spectral hole. While femtosecond filamentation is accompanied by the generation of new frequencies, we focus here on the role and importance of intensity dependent attenuation in the process of

amplitude concentration. This is because of the key role that nonlinear absorption plays in filamentation in water [206]. It is important to note that any other intensity dependent attenuation method (other than filamentation) should yield similar results. The critical point is that ultrafast pulses with high intensity (above threshold) are attenuated by filamentation, whereas pulses with low intensity (below threshold) do not undergo filamentation. This effect is dependent upon the phase shift applied to the frequency components of the pulse. Thus, a pulse shaper provides control over which frequencies to enhance and by how much to enhance them (by changing the phase shift).

6.2 Theoretical description

A laser pulse can be completely described by its Fourier decomposition $A(\omega)$, where

$$A(\omega) = \mathcal{F}\left[E(t)\right] = \frac{1}{\sqrt{2\pi}} \int_{-\infty}^{\infty} E(t)e^{i\omega t} \, dt. \tag{6.1}$$

Here $E(t)$ is the electric field, ω is the angular frequency, and $\mathcal{F}\left[E(t)\right]$ represents the Fourier transform of $E(t)$. In this experiment, a pulse shaper performs a spectral transformation

$$A'(\omega) = \begin{cases} A(\omega)e^{i\phi} & (\omega_0 - \frac{\delta\omega}{2}) \leq \omega \leq (\omega_0 + \frac{\delta\omega}{2}) \\ A(\omega) & \text{otherwise} \end{cases}, \tag{6.2}$$

where $\delta\omega$ is the width of a narrow spectral window about the center frequency ω_0. Note that if the applied phase shift is $\phi = \pi$, the multiplicative factor becomes -1, denoting a phase flip. After this transformation, the pulse can be written in terms of a superposition

$$A'(\omega) = A(\omega) - (1 - e^{i\phi})A(\omega) \Pi(\frac{\omega - \omega_0}{\delta\omega}), \tag{6.3}$$

where Π is the unit box function. Note that in the case that the applied phase shift is replaced by a spectral hole (i.e. replace $e^{i\phi}$ with 0), this equation is equivalent to the

75

explanation for spectral hole overfilling discussed previously [204]. The modified pulse is again treated as a superposition of two waves; however, here the amplitude of the second wave is dependent upon the phase shift applied.

The Fourier transform obeys the principle of superposition.

$$\mathcal{F}^{-1}\left[A(\omega)\right] + \mathcal{F}^{-1}\left[-2A(\omega)\,\Pi\left(\frac{\omega - \omega_0}{\delta\omega}\right)\right] = \mathcal{F}^{-1}\left[A(\omega) - 2A(\omega)\,\Pi\left(\frac{\omega - \omega_0}{\delta\omega}\right)\right]$$

Heuristically the first term represents the broad-bandwidth pulse before transformation by the spectrometer. The second term is a narrow-bandwidth pulse superposed on the original broad-bandwidth pulse. The amplitude of this narrow-bandwidth pulse in the spectral domain varies little over the region within the narrow unit box, and may be approximated as a constant. Thus this term under inverse Fourier transform becomes effectively

$$\mathcal{F}^{-1}\left(-(1 - e^{i\phi})A(\omega_0)\,\Pi(\frac{\omega - \omega_0}{\delta\omega})\right) = -(1 - e^{i\phi})A(\omega_0)\mathcal{F}^{-1}\left(\Pi(\frac{\omega - \omega_0}{\delta\omega})\right). \quad (6.4)$$

The inverse Fourier transform of the unit box is $\mathcal{F}^{-1}(\Pi(\frac{\omega - \omega_0}{\delta\omega}))) = \frac{2\sin\frac{\delta\omega\,t}{2}e^{i\omega_0 t}}{t}$. As such, the narrow-bandwidth slice of the modulated pulse in the frequency domain is effectively approximated in the time domain with an envelope whose temporal width is inversely proportional to the modulated bandwidth $\delta\omega$. Because the modulated bandwidth is spectrally narrower than the original pulse, the time-domain representation of the modulated bandwidth is a much longer pulse. Thus, the superposition principle allows the modulated pulse in the time domain to be described as the original time-domain pulse overlapped with a low-amplitude much longer pedestal pulse. These results are depicted in Fig. 6.1.

At this point, the Fourier description of the modulated pulse in the time domain as the superposition of a short pulse and a long pulse has been conducted entirely in the linear regime. In the nonlinear regime, the intensity of the pulse is a relevant factor in its propaga-
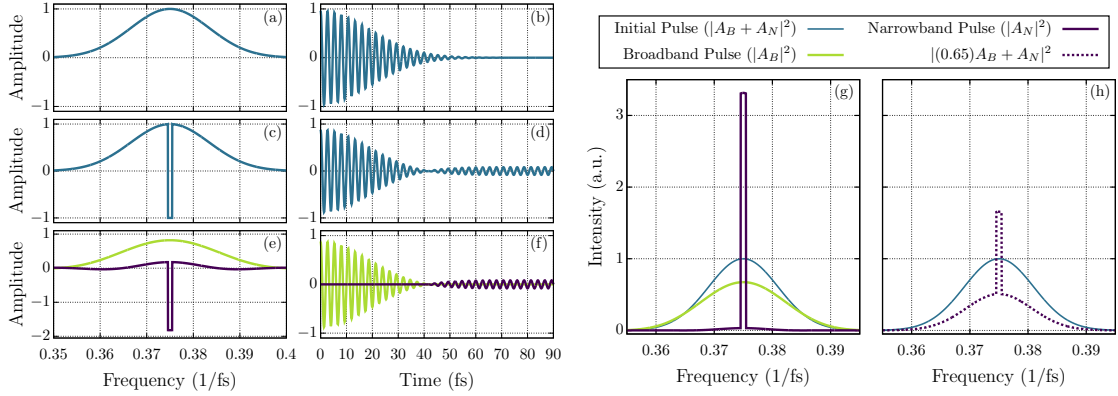
Figure 6.1: Overview of theory in frequency domain (first column) and time domain (second column). A narrow region of frequencies in a laser pulse (a,b) undergoes a π phase shift (c,d). The amplitude of the shaped pulse is described as the sum of two pulses (e,f). We assume a symmetric pulse in the time domain, however, for better clarity, we only show half of the pulse in the figure. The spectra of these pulses are shown in (g) and (h). The original pulse is given for reference (blue). The spectrum of the separate components ((g), violet, green) of the shaped pulse are obtained if the other component is removed completely. The scenario of slight attenuation of the broadband pulse is also shown ((h), violet, dashed).

tion; in particular, the attenuation of a sufficiently intense pulse can be intensity-dependent through such loss mechanisms as multiphoton absorption and plasma generation. For the two pulses considered here, the long pulse is much lower in instantaneous intensity due to the facts that it is generated by a modulation of only a small fraction of the original bandwidth, and this much smaller quantity of energy is distributed over a much longer span of time than the original broad-bandwidth short pulse.

If the short pulse is intense enough to undergo nonlinear loss mechanisms while the long, less intense pulse only undergoes linear loss, the $-(1 - e^{i\phi})A(\omega)\Pi(\frac{\omega-\omega_0}{\delta\omega})$ term in the modulated pulse experiences less attenuation than the $A(\omega)$ part of the pulse. In the (not realizable in practice) limit of total attenuation of the short pulse and no attenuation of the long pulse, the observed intensity spectrum of the pulse will be proportional to $|(1 - e^{i\phi})A(\omega)|^2$ over the modulated bandwidth, which for the case of a phase flip ($\phi = \pi$)

is $|2A(\omega)|^2$, a factor of 4 greater than the pulse before the nonlinear propagation. In this manner, a time-domain attenuation process can cause intensity of the pulse to be concentrated at selected frequencies in the spectrum. This is illustrated in Fig. 6.1g-h, where a sharp spectral spike is generated by attenuating the short pulse components either completely (Fig. 6.1g) or to 65% of its original intensity (Fig. 6.1h). Notice that the intensity of the spectral spike is greater than the intensity of the same frequency components of the initial pulse.

6.3 Methods

6.3.1 Experimental setup

The experimental setup is depicted in Fig. 6.2. The phase of a 50 fs laser pulse from a Coherent Legend Elite system with a center wavelength near 800 nm is modulated by a 128 pixel Meadowlark liquid crystal spatial light modulator (D3128). This spatial light modulator is placed at the Fourier plane of a 4-f pulse shaper constructed using a 600 groove/mm holographic grating (Edmund Optics, NT47-555) and a cylindrical lens with a 20 cm focal length (Thorlabs, LJ1653L1). This pulse shaper was constructed in a folded geometry [63] with a slight vertical separation between the output and input pulse. The pulse after the pulse shaper (8 μJ/pulse) is then focused into a 15 cm long tank of tap water using a 40 cm focal length lens (Thorlabs, LA1422). A filament is induced, and the light emitted in the forward direction is collected by an integrating cavity (home-built, 2.5 cm diameter entrance aperture) and measured by an Ocean Optics USB 2000+ spectrometer (1.3 nm resolution). The intensity of the spectra were calibrated using a Coherent PM10 power meter. Changing the phase mask applied by the spatial light modulator alters the resulting spectrum of the filament's forward emission. Note that it is important to consider chromatic dispersion in water, since the group-velocity dispersion (GVD) coefficient is large for these wavelengths. However, in the regime of our pulse parameters ($t_p = 50$ fs,

78
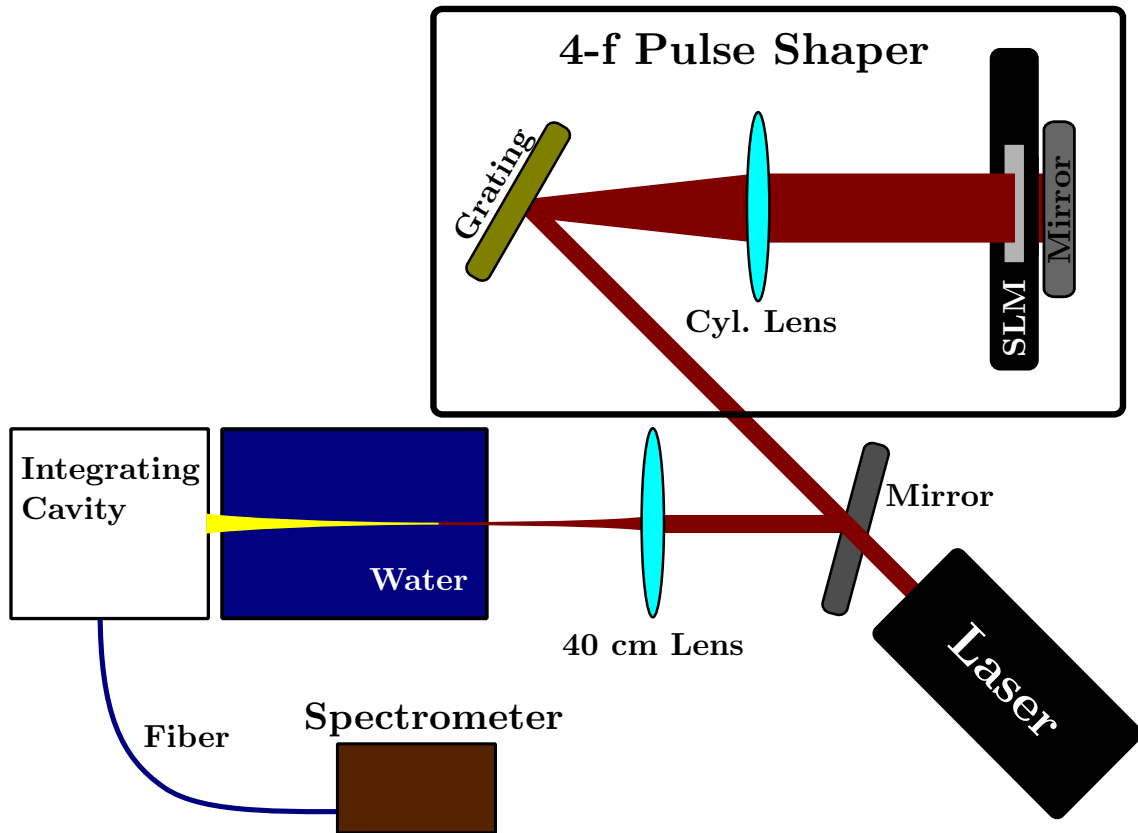
Figure 6.2: Experimental setup. A pulse shaper is used to apply a π phase shift to a narrow window of frequencies. This shaped pulse then undergoes filamentation in water. The resulting pulse has a modified spectral amplitude.

$w_0 \sim 100\,\mu$m, $P_{\text{peak}} \sim 30\,P_{\text{cr}}$), chromatic dispersion cannot stop self-focusing and plasma generation [206, 207]. Furthermore, in this regime, nonlinear absorption plays a key role in filamentation [206].

In order to compare the initial spectrum of the laser pulse to the spectrum of the forward emission, measurements of both spectra are taken after the tank of water, thus accounting for linear absorption from the water. Filamentation is induced by the focusing from the 40 cm lens placed before the tank of water. Thus, by collecting the spectrum with and without this lens we are able to compare the emission spectrum of the shaped and unshaped

filament to the laser pulse without filamentation.

However, because the laser is focused into the water in one case and not in the other, coupling into the spectrometer requires an integrating cavity to collect the light emitted into the forward direction ($\leq 5°$ from optical axis). Thus, the spectral measurements are comparable regardless of the focusing geometry. The intensity measurement of the spectrometer is also further calibrated by normalization using a power measurement for each case.

Power loss due to reflection from the uncoated focusing lens also introduces inconsistency when comparing the intensity of the spectrum with the lens to the spectrum without it. We measured and accounted for this power loss in the normalization process of the data. Thus, we have obtained a calibrated measurement of spectral intensity for shaped and unshaped laser pulses with and without filamentation.

6.3.2 Numerical simulations

Our experimental results are compared to theory via numerical simulations where we use the generalized nonlinear Schrödinger equation for the field envelope $A \equiv A\left(t, r, z\right)$, modified to include ionization effects [72, 175, 208, 209]:

$$
\frac{\partial A}{\partial z} = iT^{-1}\frac{\nabla_r^2 A}{2k_0} + \mathcal{R}_i\left[A\right] + iD(\omega)A + iT\frac{\omega_0}{c}\left(n_2|A|^2 A\right) \tag{6.5}
$$

Here r is the radial coordinate, $\nabla_r^2 = \frac{1}{r}\frac{\partial}{\partial r}\left(r\frac{\partial}{\partial r}\right)$ is the transverse Laplacian, z is the propagation coordinate, $k(\omega) = \frac{\omega}{c}n(\omega)$, ω is the radiation frequency, $n(\omega)$ is the frequency dependent linear refractive index [210], $T = 1 + \frac{i}{\omega_0}\frac{\partial}{\partial t}$ is the self-steepening operator, t is the retarded time, ω_0 is the central frequency of the pulse, $n_2 = 2 \times 10^{-4}$ cm^2/TW [211] is the nonlinear refractive index, and $D(\omega) = k(\omega) - \frac{\omega}{V}$ is the dispersion operator, $V = \left(\frac{\partial k(\omega)}{\partial \omega}\right)_{\omega_0}^{-1}$ being the group velocity.

Ionization effects are included through the $\mathcal{R}_i[A]$ term:

$$\mathcal{R}_i = -\mathcal{F}^{-1}\left[\frac{\sigma(\omega)(1+i\omega\tau_c)}{2}\mathcal{F}[N_e A]\right] - U_i\frac{N_{at}W(|A|^2)}{|A|^2} \tag{6.6}$$

where $\mathcal{F}$ is the Fourier transform from t to ω, $\mathcal{F}^{-1}$ is the inverse Fourier transform, $\sigma(\omega) = \frac{\mu_0 e^2 \omega \tau_c}{mk(\omega)(1+\omega^2\tau_c^2)}$ is the inverse bremsstrahlung cross-section, e is the electron charge, m is the electron mass, μ_0 is the vacuum permeability, τ_c is the electron momentum transfer time, $N_{at} = 3.3 \times 10^{22}$ cm^{-3} is the number density of water molecules, $W(|A|^2)$ is the single-molecule photoionization rate (calculated through Perelomov-Popov-Terent'ev formulas, [212, 213]), $U_i = 6.5$ eV is the effective ionization potential of water. The electron density $N_e \equiv N_e(t, r, z)$ is found from the equation

$$\frac{\partial N_e}{\partial t} = N_{at}W(|A|^2) + \frac{\sigma(\omega_0)}{U_i}N_e|A|^2, \tag{6.7}$$

which accounts for photoionization and impact ionization. Simulations are started 5 cm before linear focus ($z = -5$ cm). The shape of the input pulse without a phase flip is calculated from experimental spectra, assuming the pulse is Fourier-limited at the cell entrance. While the experiment may deviate slightly from this assumption, the results should remain similar because of the robust nature of filamentation above threshold. The key point here is that the main pulse is well above threshold while the phase-shifted part of the pulse is well below threshold. These simulations have been performed in parallel codes using supercomputer complex of Lomonosov Moscow State University.

6.4 Results and discussion

By applying a π phase shift (i.e. a phase flip) to a narrow spectral region (two pixels at the center of a spatial light modulator in a pulse shaper) of a 50 fs laser pulse (Coherent, Legend Elite), we observe a sharp peak arise in the emission spectrum of a femtosecond
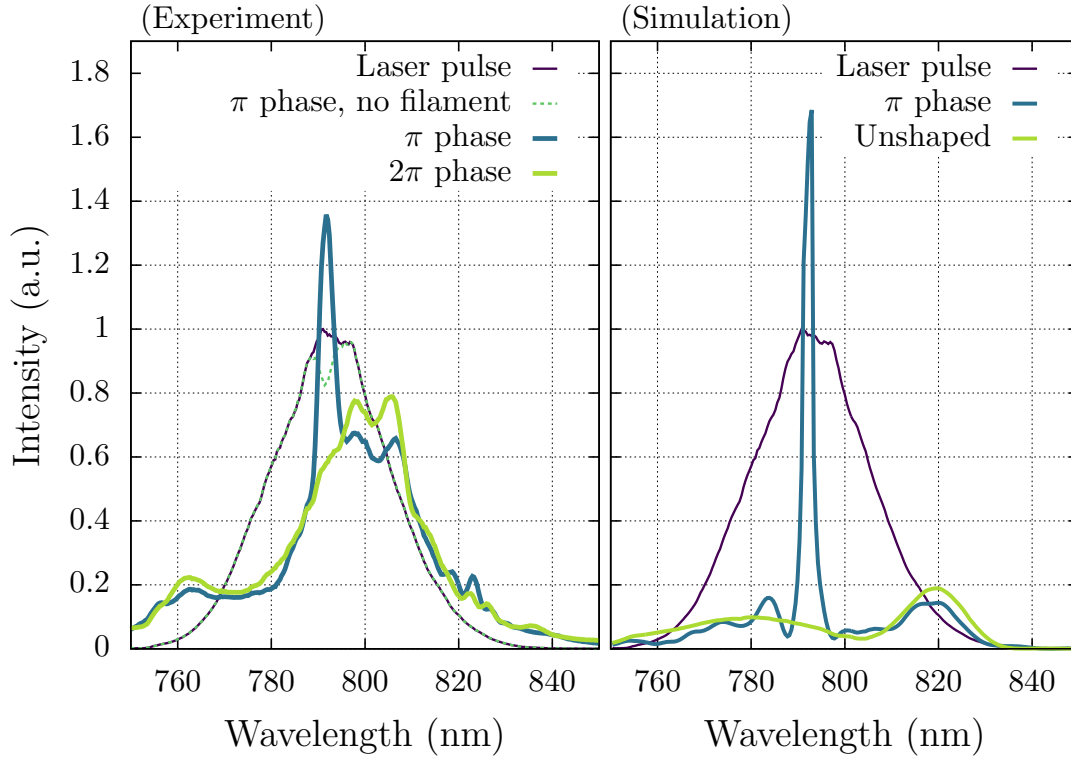
Figure 6.3: Resulting experimental and simulated spectra after filamentation when applying a π or 2π phase shift to a selected window of frequency components. Notice that applying a 2π phase shift removes the effect. All spectra were normalized by the peak of the laser pulse spectrum (no filamentation), which is shown for reference. The spectrum of the shaped laser pulse without filamentation is also shown for reference.

filament in the forward direction. The filament was approximately 7 cm long. This peak has a strong dependence upon the phase shift applied by the pulse shaper. As the phase applied is scanned from 0 to π, the peak rises to a maximum, and then disappears again as the phase is scanned further to a 2π phase shift. The measured spectra for π and 2π phase shifts are shown in Fig. 6.3. The spectra of the laser pulse and unshaped filament are given for reference. The spectrum of the shaped laser pulse without filamentation (acquired by removing the focusing lens) is also shown to demonstrate the importance of the self-guiding stage in this process. It is observed that the spike in the spectrum of
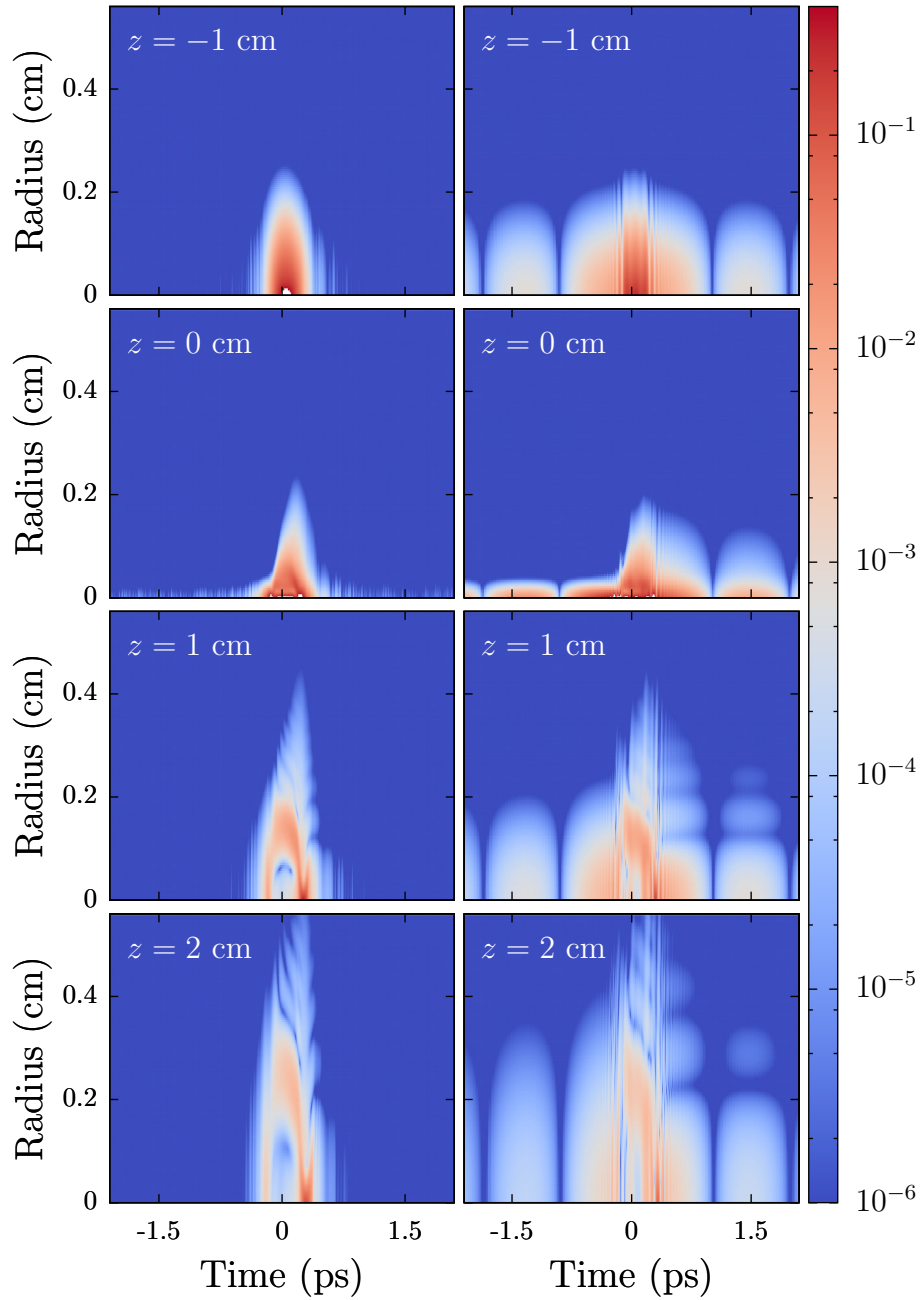
Figure 6.4: Snapshots of the intensity of the unshaped (left) and shaped (right) pulses as they propagate. The central component of both pulses undergoes filamentation, while the low-intensity leading and trailing edges do not. The trailing edge is also influenced by the plasma trail of the filament causing it to not focus as tightly as the leading edge. Linear focus is at $z = 0$ cm.

the shaped filament has a larger spectral intensity than the same frequencies of the laser pulse without filamentation. The appearance of this intensity spike is also shown in the numerical simulation results of Fig. 6.3. The numerical results are integrated over the entire beam to account for the light collected by the integrating cavity. Some discrepancy in the behavior of the spectral wings between the experiment and numerical results is observed. This is possibly due to a combination of a number of effects such as the Raman effect [72, 186, 214], ionization-induced effects [215], or slight asymmetry in the experimental beam causing a portion of it to not undergo filamentation. Some discrepancy may also be due to diffraction effects from the spatial light modulator where the π phase step is applied within two pixels width ($200~\mu$m). Evidence of this is shown in the spectrum of the shaped laser pulse without filamentation (Fig. 6.3, left). However, the qualitative agreement remains that when a π phase flip is applied to certain spectral ranges, the amplitude in those ranges after filamentation is enhanced.

From the numerical results, insight to the dynamics of this effect are attained. In Fig. 6.4, numerical simulation results for shaped and unshaped pulses as a function of propagation position, radius from the center of the beam, and time are shown. Here we see that the propagation of the shorter, high intensity component of the pulse in the phase flipped case (right column) is essentially the same as the pulse in the unshaped case (left column). The difference arises from the longer, low intensity component of the pulse that does not undergo filamentation. Because the beam was focused, we see the leading edge of the pulse (negative time) undergo linear focusing and defocusing as it approaches and passes $z = 0$. The trailing edge (positive time) also focuses, but not nearly as much. Furthermore, ripples are observed in the trailing edge. This asymmetry between the behavior of the leading and trailing edges of the pulse is due to the plasma trail that is left in the wake of the filament.

Integration of the spectrum of the various components of the pulse yields the energy
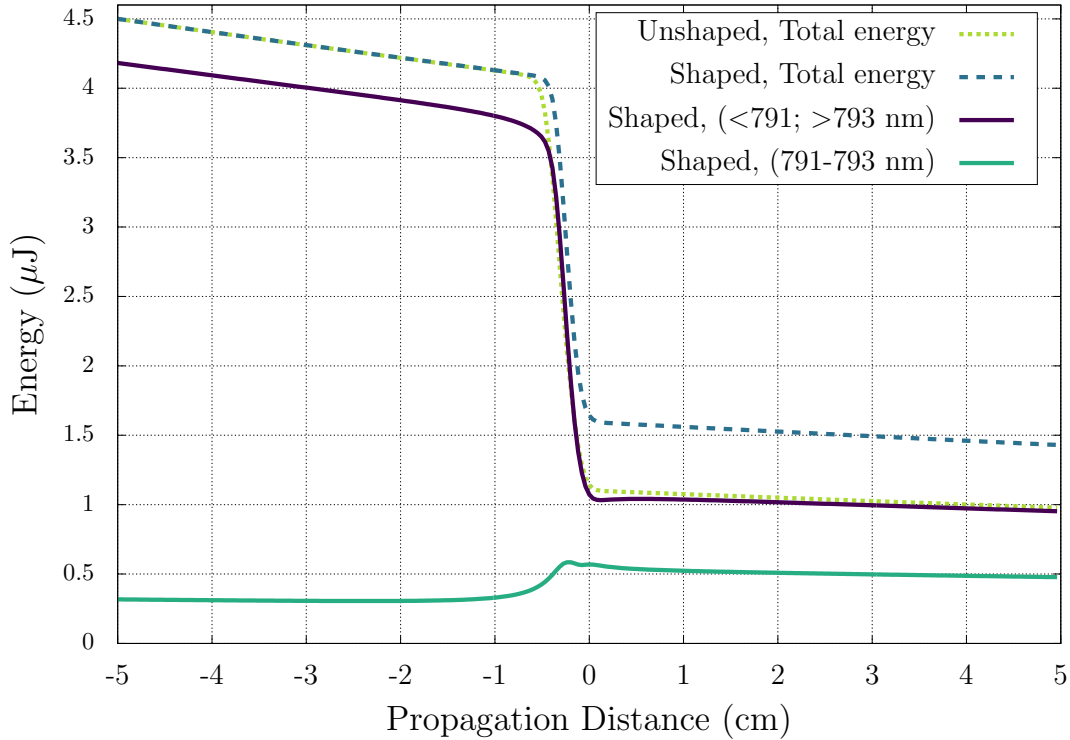
Figure 6.5: Energy of the simulated pulse propagation as a function of distance (linear focus is at 0 cm) for the case of a π phase flip at 791-793 nm (blue, dashed) compared to the case of no phase flip (light green, dashed). The total energy contained in the pulse drops as it propagates through filamentation. However, in the case of a π phase flip, this energy drop is considerably less. Plotting the energy contained in the spectral band of the phase flip (green, solid) versus the energy not in the phase flipped region (violet, solid), it is shown that energy is actually transferred to the frequencies that were phase flipped.

contained in each component as a function of propagation distance. These are shown in Fig. 6.5, where the total energy in the shaped and unshaped pulse as a function of propagation are shown in green and violet, respectively. We see that the energy of the unshaped pulse decreases more than that of the shaped pulse as it undergoes filamentation. Also shown is the energy contained in the low-intensity and high-intensity components of the pulse for the phase flipped case. We see that the energy contained in the spectral region of the low-intensity component is actually increased as it undergoes filamentation, while
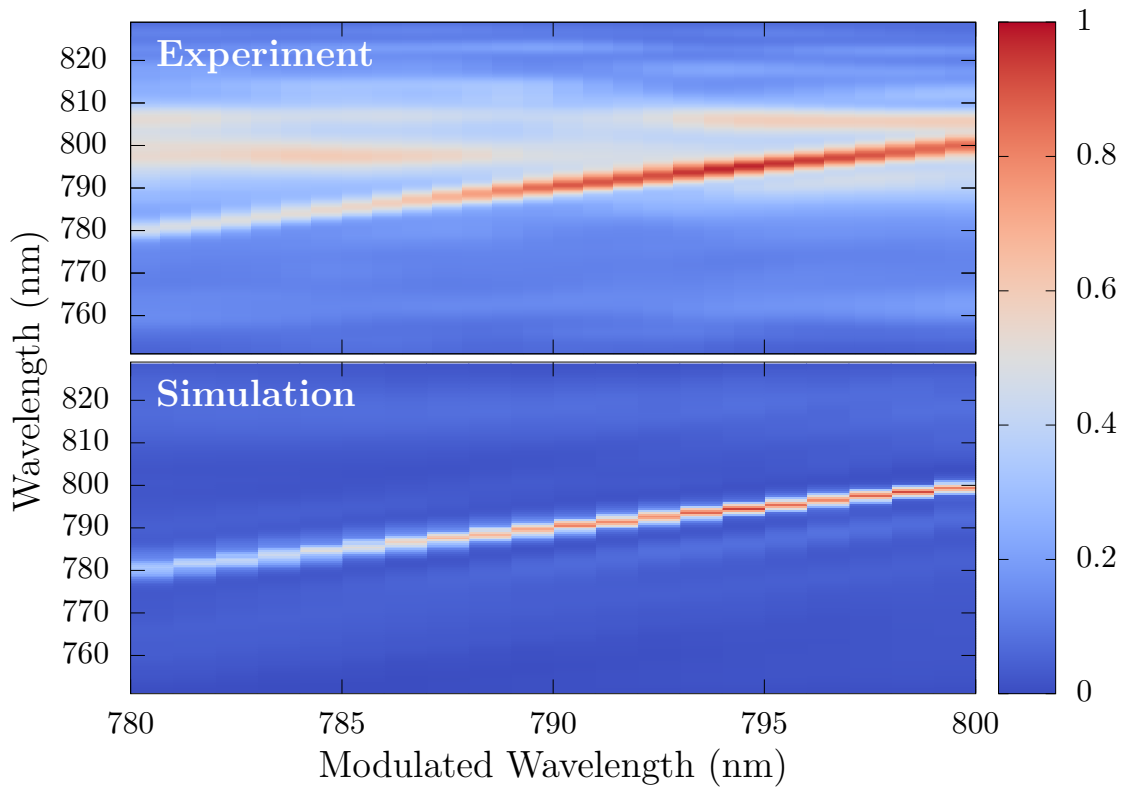
Figure 6.6: (Top) Spectra of the shaped filament as the modulated pixel is scanned across the spatial light modulator. The narrow peak created by phase modulation (see Fig. 6.3) follows as the pixel causing the phase shift is changed. (Bottom) Simulated spectra that show the same effect.

the high intensity component is attenuated as usual.

Furthermore, in simulation and experiment, the frequency of the peak generated by the amplitude concentration moves according to the frequency of light being modulated. This is achieved experimentally by simply scanning the modulating pixels across the spatial light modulator, and results are shown in Fig. 6.6. These results provide insights to applications of this technique. By selecting a pixel in a computer controlled spatial light modulator, we are able to tune the frequency of the narrow-bandwidth component of the pulse. Thus, a narrow-bandwidth laser pulse can be created tunable to any frequency within the limits of the original bandwidth of the femtosecond laser pulse.
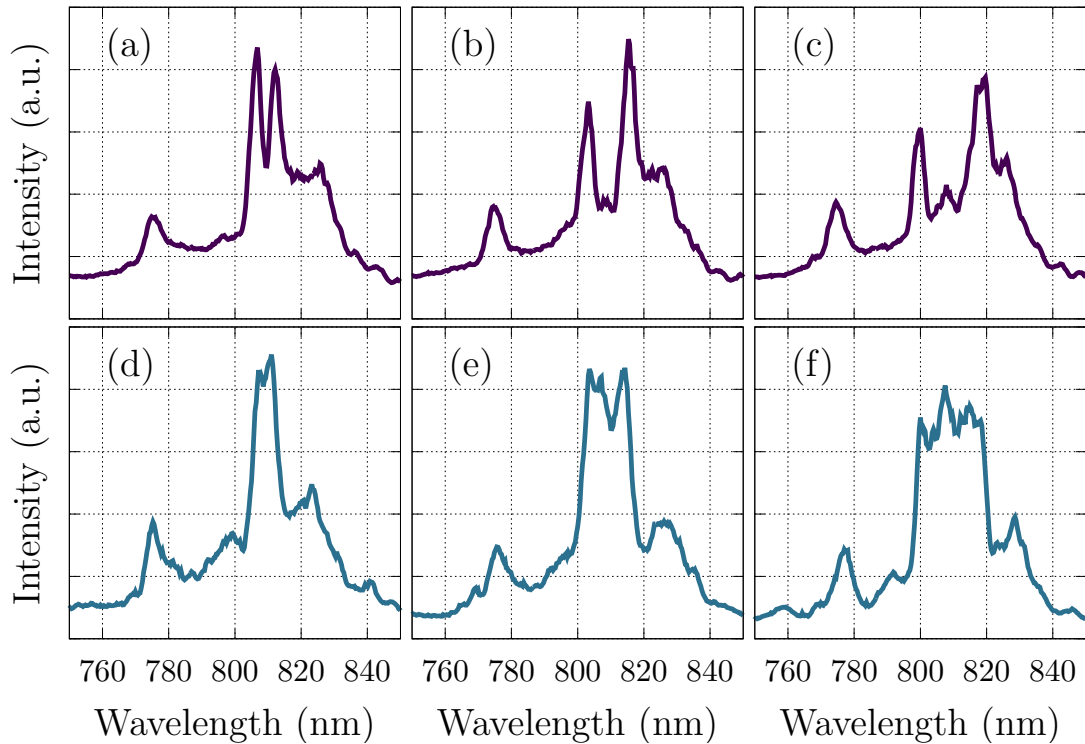
Figure 6.7: Spectra of Shaped Filament for different phase mask configurations. Here, two narrow intensity spikes (top row) are formed or one wide intensity spike (bottom row) is formed by correctly choosing which pixels of the spatial light modulator to modulate. The phase mask configurations used to obtain these spectral patterns are specified in the text. There is a possibility to create many different shapes in the output spectrum.

It is also possible to have multiple peaks as shown in the top row of Fig. 6.7. Here, a π phase shift is applied experimentally to two pixels with a gap between them in the spatial light modulator. In Fig. 6.7a, the two modulating pixels have a gap of six pixels with zero phase shift between them. In Fig. 6.7b, the gap is increased to 14 pixels, and 22 pixels in Fig. 6.7c. The peaks separate according to the modulating pixel separation. This demonstrates the ability to encode information onto the laser pulse in the form of simple phase flips, and the information is decoded using a simple spectrometer. Other spectral shapes can also be formed such as those shown in the bottom row of Fig. 6.7.

Here, subfigures d,e, and f have the same configuration as a,b, and c except that instead of a gap of non-modulating pixels between the two modulating pixels, a set of 6, 14, and 22 pixels respectively are all set to apply a π phase shift. Thus, to within the resolution limits of our spatial light modulator, we can control which frequencies to amplify.

6.5 Conclusion

We have experimentally and theoretically demonstrated an example of amplitude concentration in a femtosecond filament. A π phase shift is applied to a laser pulse by a 4-f pulse shaper resulting in a pulse composed of a superposition of a long (narrow-bandwidth) pulse component with low intensity and a short (broad-bandwidth) pulse component with high intensity. Through intensity-dependent attenuation from femtosecond filamentation, energy is transferred into the spectral regions where the phase shift was applied. This amplitude accumulation process in femtosecond filaments is due to the nonlinear effects associated with filamentation; namely, nonlinear absorption due to ionization. It should be possible to generate similar results with any attenuating effect that has a similar threshold-like behavior, thereby attenuating the broad-bandwidth portion of the shaped pulse while leaving the narrow-bandwidth portion unaffected. Furthermore, the efficiency of this process may be improved by modifying the pulse characteristics (pulse duration, filament length, etc.) to increase the degree of nonlinear loss experienced by the high intensity component of the pulse.

Computer controlled spatial light modulators provide control over this result. Not only can the wavelength of the intensity spike be adjusted by choosing which pixel to modulate, but the height of the intensity spike can also be set by choosing the phase of the modulation applied. In this manner, it is possible to encode information into spectral phase jumps by the spatial light modulator. The information can then be decoded into measurable intensity spikes.

7. ENHANCED COUPLING OF LIGHT INTO A TURBID MEDIUM THROUGH MICROSCOPIC INTERFACE ENGINEERING

There are many optical detection and sensing methods used today that provide powerful ways to diagnose, characterize, and study materials. For example, the measurement of spontaneous Raman scattering allows for remote detection and identification of chemicals. Many other optical techniques provide unique solutions to learn about biological, chemical, and even structural systems. However, when these systems exist in a highly scattering or turbid medium, the optical scattering effects reduce the effectiveness of these methods. In this chapter, we demonstrate a method to engineer the geometry of the optical interface of a turbid medium, thereby drastically enhancing the coupling efficiency of light into the material. This means that light incident on the material will penetrate deeper into (and through) the medium. It also means that light thus injected into the material will have an enhanced interaction time with particles contained within the material. These results show that by utilizing the multiple scattering of light in a turbid medium, enhanced light-matter interaction can be achieved. This has direct impact on spectroscopic methods such as Raman scattering and fluorescence detection in highly scattering regimes. Furthermore, the enhanced penetration depth achieved by this method, will directly impact optical techniques that have previously been limited by the inability to deposit sufficient amounts of optical energy below or through highly scattering layers.

7.1 Introduction

Optical detection and spectroscopy has drastically changed the way we look at and measure the world today. Observation of the interaction of light with matter provides us with a host of tools to promote research, security, safety, and health. These optical tools include the detection of harmful or explosive materials [216–218], the remote detection

of chemicals from a distance [106], the optical diagnosis of colloidal suspensions for genomics and drug delivery [219], and even the use of lasers for defense [220]. Remote sensing techniques [221, 222] allow us to image/detect structures through the atmosphere or ocean [223–225]. Optical methods are also an integral part of biomedical research, diagnosis [226], and treatment [227, 228] of many of today's most prevalent illnesses [229]. However, the sensitivity and usefulness of any optical method is severely limited by the occurrence of optical scattering. This limitation is further amplified when the density of scatterers is high enough for multiple scattering to occur. In this letter, we show that modification of the geometry of the optical interface significantly improves the coupling efficiency of light into a highly scattering medium, thereby reducing the detrimental effects of scattering. This enhanced coupling is evident through the observation of increased spatial diffusion, two orders of magnitude greater transmission, and over an order of magnitude greater interaction time of light within the material. This translates to over an order of magnitude greater sensitivity for linear optical detection methods such as spontaneous Raman scattering or fluorescence. Thus, by utilizing the multiply scattering nature of a material, we can substantially increase the effectiveness and sensitivity of optical methods in and through turbid media. These results may also impact technologies such as random lasing [107], optical systems on a chip [230, 231], and photon management in films and solar cells [232, 233].

When light is incident upon a disordered, highly scattering material, the injection depth and optical path length of the light within the medium is limited by its scattering properties [31, 234]. Thus, light-matter interactions are confined to regions near the optical entrance, as shown in Fig. 7.1 (left). One way to circumvent the scattering at the surface of a material is to physically insert an optical needle-probe [235, 236] into the material and deposit/collect light directly at the location of interest; however, physical access to the scattering material is not always possible.

90
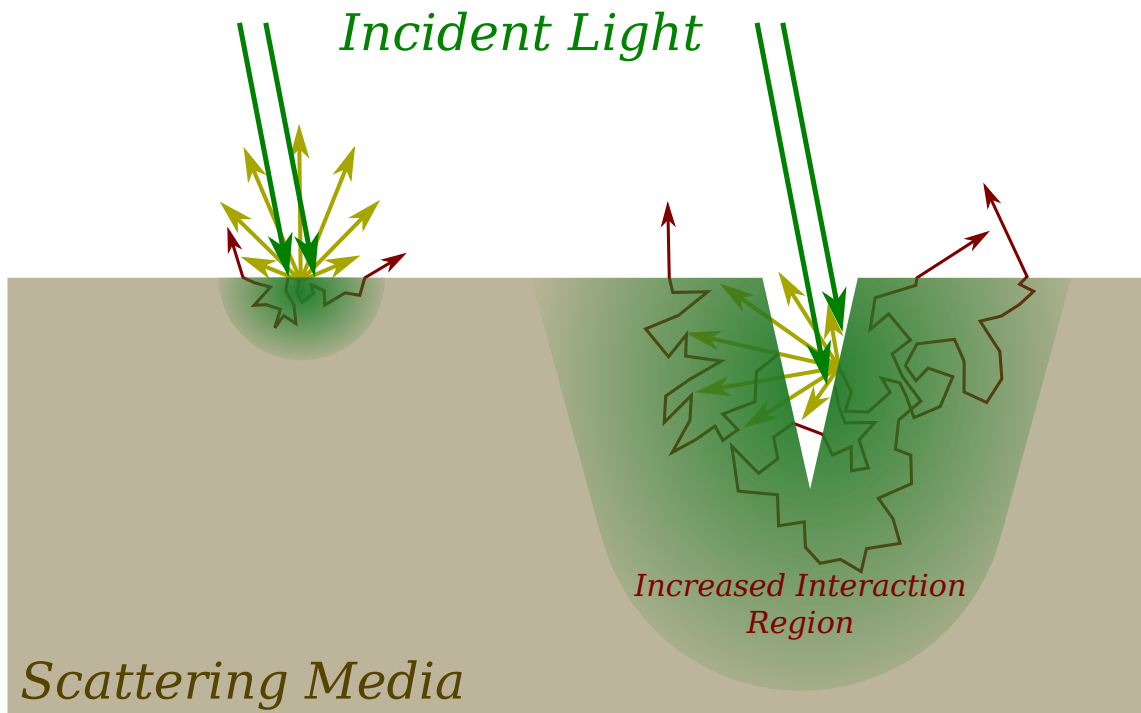
Figure 7.1: When light is scattered by a highly turbid material, the majority of the light is scattered in all directions near the surface (left). If the surface geometry of the material is such that the light scattered near the surface is directed toward another surface, the likelihood of the light scattering into the material increases. A geometry such as that depicted above (right) would provide light rays with many scattering events before it escapes. This greatly improves the chance that it will be injected deeper into the material, thereby enhancing the interaction region of light with the material.

Other ways to overcome inefficient coupling of light into scattering materials have included the use of wavefront shaping [53, 102] to promote coupling into the fundamental diffusion mode [237] or the open/closed eigenchannels [111, 125, 238] of the material, thereby controlling energy density [231]. An optimum wavefront of the incident light is determined via iterative search algorithms [48, 49] or measurement of the transmission/reflection matrix [239–241] to promote coupling into these modes. In practice, the sample must remain static for the entire measurement procedure, which may require seconds to minutes of time to complete. Some of the limitations of wavefront shaping, namely, the

incomplete channel control of the input light, measurement noise in the optimization algorithm, and measurement time, have been avoided by placing the scattering material inside a waveguide with an engineered geometry [242]. While the control of light coupling into the scattering material was achieved without wavefront shaping, each sample required a custom-built waveguide to greatly enhance energy delivery deep inside the random medium. Other methods include the use of an ultrasonic guide star and optical phase conjugation [44] for enhanced focusing of light in a turbid medium. Plasmonic or photonic structures with nano-scale fabrication have also been used to demonstrate enhanced optical coupling [232] or transmission [243].

In this chapter, we demonstrate an approach to achieve substantially enhanced coupling efficiency of light into a turbid medium via engineering of the optical interface at scales much larger than that required for plasmonic devices. Here, the interface modification is achieved via laser ablation. In the multiple scattering regime, the diffusion of light within a turbid medium is described by the optical diffusion equation for radiative transport [67, 244] (see Methods). The penetration depth, and therefore the interaction region, of light within the material is limited by the transport mean free path, $l_t = 1/\mu_t$. Here, the extinction coefficient of the material, $\mu_t = \mu'_s + \mu_a$, is proportional to both the absorption (μ_a) and reduced scattering (μ'_s) coefficients. The reduced scattering coefficient, $\mu'_s = (1 - g)\mu_s$, takes into account anisotropric scattering via the anisotropy parameter $g = \langle \cos(\theta) \rangle$, where θ is the scattering angle. Therefore, when light is incident upon a material with a large extinction coefficient, the shallow penetration depth confines light-matter interactions to regions near the injection point (see Fig. 7.1). If, however, we inject the light past the top layer of the material (see right side of Fig. 7.1), the scattering properties of the top layer will scatter more light back into the sample, effectively trapping, or coupling, the light inside the medium. As a result, the light will interact with the medium for longer periods of time and diffuse further in all directions (including the
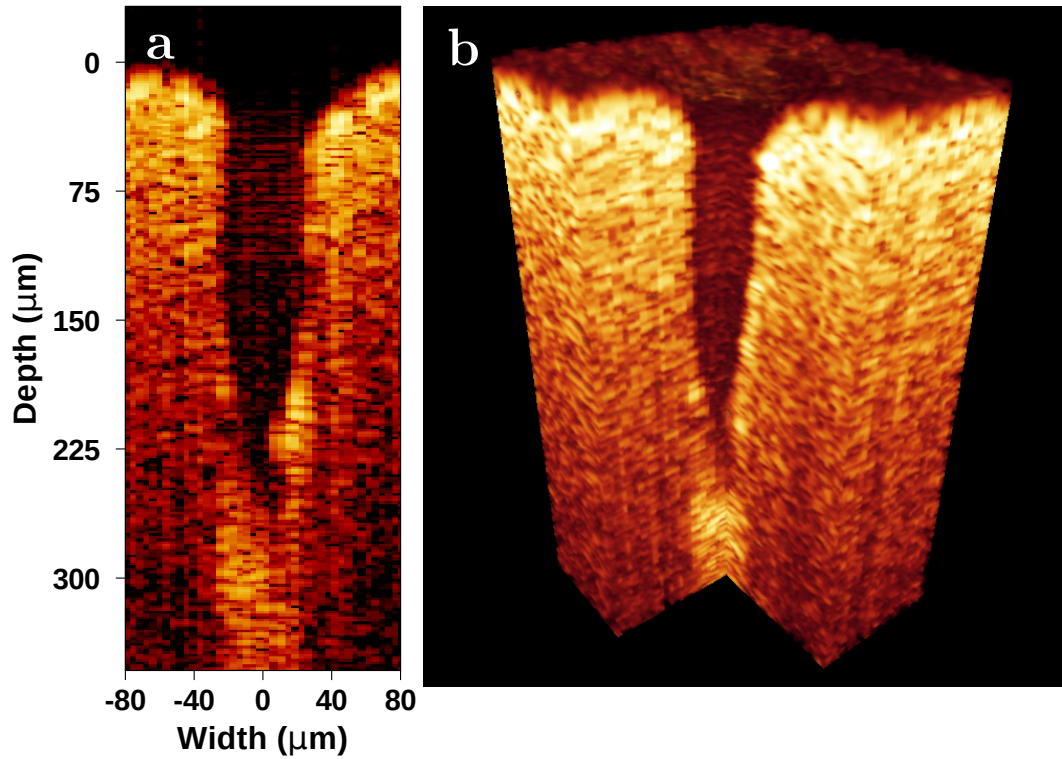
Figure 7.2: Cross section (a) and three dimensional rendering (b) of a scattering sample with microscopic hole in the surface as measured by optical coherence tomography. The laser ablated hole is measured to be about 100 μm in diameter and 300 μm deep.

forward direction) before escaping.

We show that this enhanced coupling can be realized by microscopic engineering of the geometry of the optical interface of a scattering medium. In particular, by focusing light into a narrow, conically shaped hole (0.3 mm deep) in the surface of a highly scattering material, we achieve an enhanced coupling of light into the material. This enhanced coupling is experimentally observed through the measurement of an increased diffusion radius of the backscattered light, an increased dwell time of light in the material (over an order of magnitude), and an increased transmission of light through the material (over two
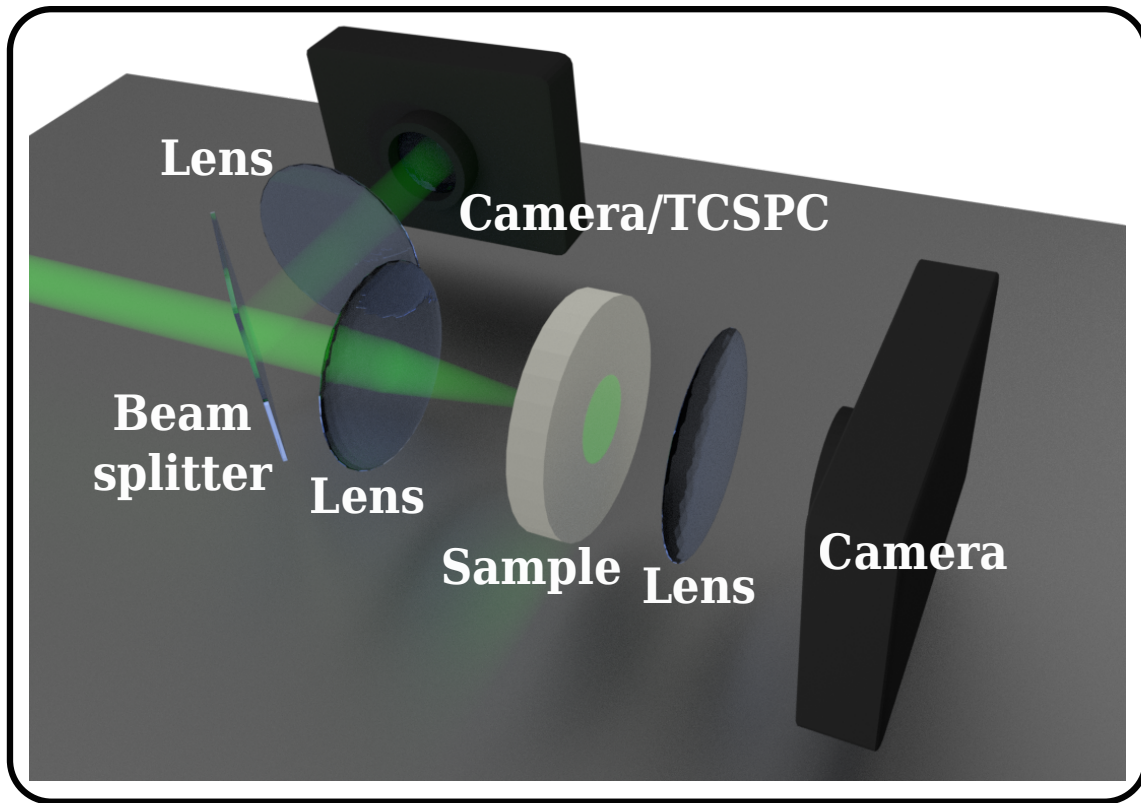
Figure 7.3: Schematic illustrating the orientation of the experimental apparatus used to characterize the enhanced coupling of light into a scattering medium. See Fig. 7.10 for a more detailed layout.

orders of magnitude). We also show that as the depth of the narrow hole increases, this coupling can be further enhanced.

7.2   Results and discussion

A scattering sample with an engineered optical interface is constructed using laser ablation from a picosecond laser (Attodyne APL-X, 532 nm, 35 μJ) to drill a microscopic hole in the surface of a packed barium sulfate (Sigma-Aldrich, 243353) sample. Barium sulfate has a transport mean free path of $l_t = 1.2$ μm ($\mu_t = 833.2$ mm^{-1}) as measured by coherent backscattering [124]. Figure 7.2 shows a hole in this material ablated with 250 laser pulses as measured by optical coherence tomography. The hole is approximately
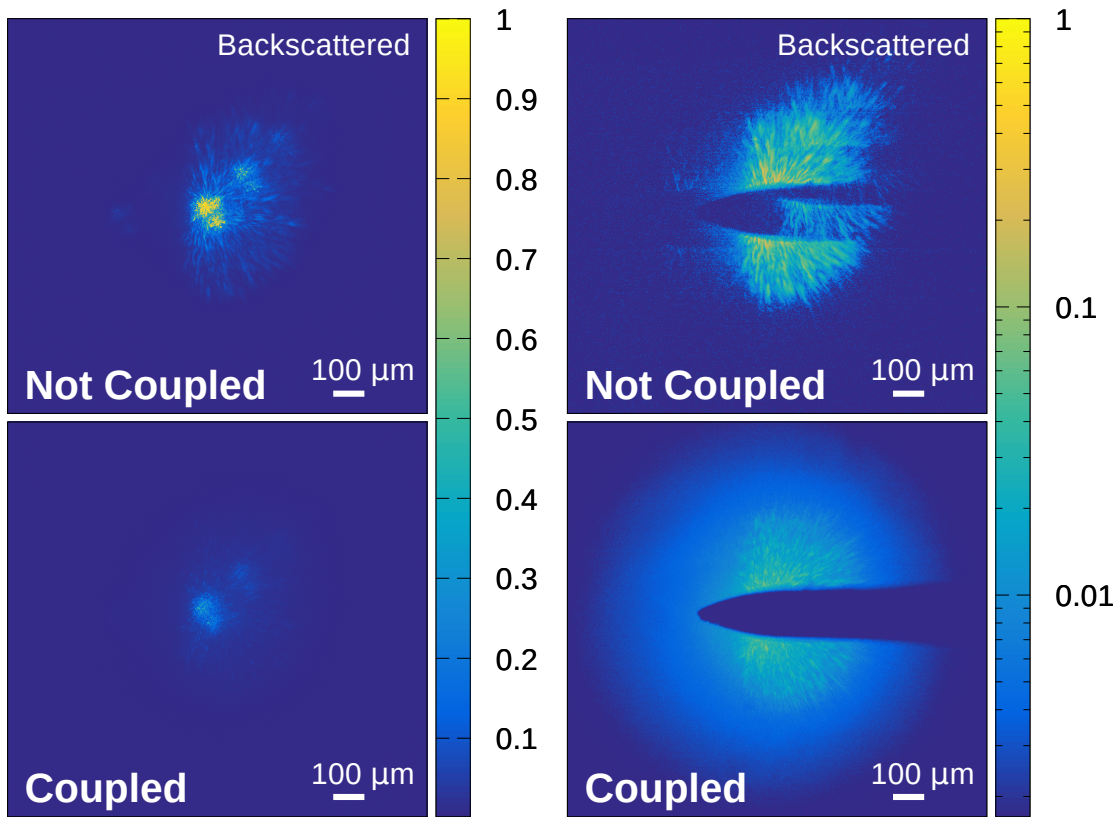
Figure 7.4: Backscattered light is measured by imaging the surface of the sample onto a CCD. Here, the backscattered light is shown for the case when the incident light is either uncoupled (top) or coupled (bottom) into a microscopic hole in the sample. When the incident light is coupled, the reflected light at the focus decreases in intensity (left). On the right, a needle placed in an intermediate image plane is used to block the bright focus, allowing observation of the enhanced spatial diffusion.

300 μm deep, and has a diameter of about 100 μm at the surface. Because the hole is very narrow and deep, most of the light focused into it will have an increased likelihood of scattering, or coupling, into the sample.

The first indication of increased optical coupling is the observation of an enhanced diffusion radius in the backscattered light. Images acquired in the backward direction (See Fig. 7.3) of light scattered from samples with and without a hole are shown in Fig. 7.4(left).

As measured by these images, the intensity of the backscattered light near the focus of the laser decreases by a factor of 3.5 times after the hole is drilled. By blocking the focus with a needle as in Fig. 7.4(right), we also see that more light is detected far away from the focus (radially) when the hole is present. In particular, the intensity of light 0.6 mm away from the focus is enhanced by over an order of magnitude when the light is focused into the hole. These two observations indicate that substantially more of the incident laser light is successfully injected into and diffuses further inside the material with an engineered interface present.

The enhanced diffusion from improved optical coupling is also observed in the forward direction as enhanced transmission. To measure this, the intensity of light transmitted through a 1 cm thick (10^4 transport mean free paths) sample was measured with a large area photodiode (Thorlabs, DET100A) for scenarios with the laser coupled and uncoupled into the hole in the sample. The transmittance of the light through the sample was measured to be 4×10^{-6} for the uncoupled case, and 9.6×10^{-4} for the coupled case. This is an increased transmission of over 200 times even though the hole is only 3% of the total thickness of the sample. The back surface of the powder was imaged onto a CCD (Mightex, CGE-B013-U), and the images for both cases are shown in Fig. 7.5. Plotted in log scale, these images clearly show the drastic enhancement in optical penetration depth. Optical diffusion theory [244] (see Methods) indicates that this enhanced transmission is not merely due to reduction of the axial thickness of the scattering medium, with a prediction that the transmittance of a 1 cm thick sample will increase by only 19% after reducing the thickness by 350 μm. The same theory predicts that injecting the light 350 μm beneath the surface of the 1 cm thick sample will enhance the transmittance by over 160 times.

The interaction time of light within the medium is also directly related to the coupling efficiency. This interaction time was observed through time correlated single photon counting measurements (SPC-150, Becker-Hickl, 50 ps resolution) [245]. of the backscat-
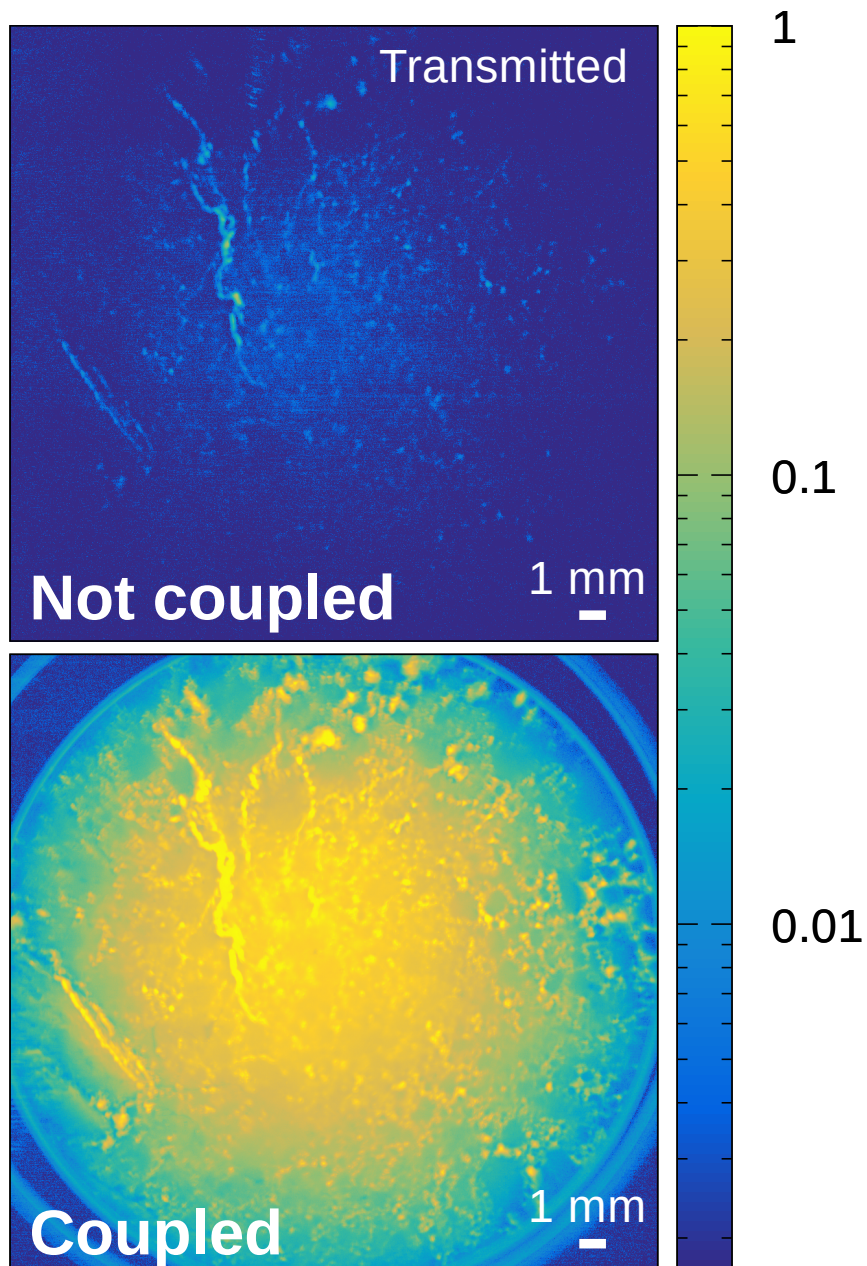
Figure 7.5: Transmitted light is measured by imaging the back surface of the sample onto a CCD. Here, the transmitted light is shown for the case when the incident light is either uncoupled (top) or coupled (bottom) into a microscopic hole in the sample. When the incident light is coupled, over two orders of magnitude more light is transmitted through the 1 cm thick sample.
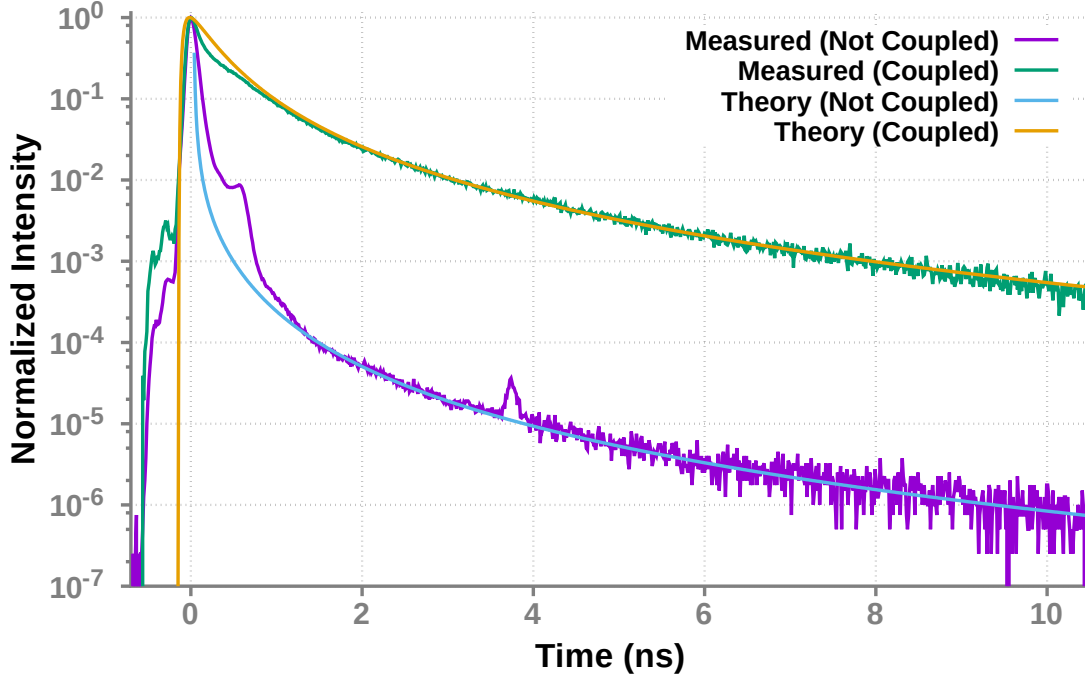
Figure 7.6: The normalized temporal profile of backscattered light is measured with time correlated single photon counting. From this measurement, a significant enhancement in the interaction time of the light in the medium is observed for the coupled (green) case compared to the uncoupled (violet) case. Nearly three orders of magnitude more light is still trapped in the powder after 10 ns when it is coupled via a hole in the surface. Diffusion theory (cyan and gold) from Eq. 7.1 fits with good agreement.

tered intensity as a function of time, as shown in Fig. 7.6 (normalized by peak photon count). From the normalized time domain picture we see that when the light is focused into the microscopic hole, the decay time of the light is drastically increased. After 10 ns from the arrival of the incident pulse, nearly three orders of magnitude more light is still present in the sample with a hole in it compared to that without.

From optical diffusion theory (see Methods), the temporal decay curve of light backscattered from a scattering sample with incident light injected at a depth, h, is described as

$$P(t) = \frac{c}{\sqrt{4\pi Dct}} e^{-\mu_a ct} \left[1 - e^{-\frac{R^2}{4Dct}}\right] \times \left[e^{-\frac{(l_t+h)^2}{4Dct}} - e^{-\frac{(2L_s+l_t+h)^2}{4Dct}}\right]. \qquad (7.1)$$

98
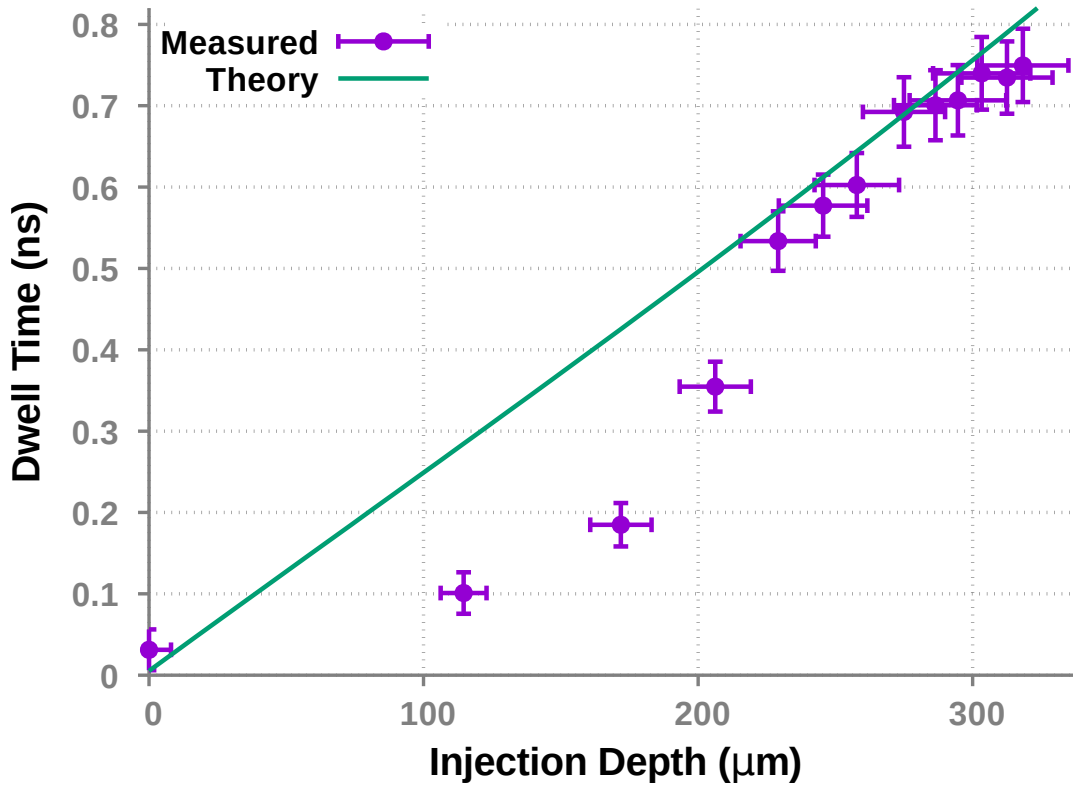
Figure 7.7: The average dwell time is calculated from the measured temporal profile (Fig. 7.6), and as shown, it scales with the hole depth. Here, diffusion theory assumes a 0.7 mm optical collection radius from the sample, and $\mu_a = 10^{-4}$ mm^{-1}. We see that as the holes become deeper, less light is lost via the hole, and the measured value approaches theory.

where c is the speed of light, $D = l_t/3$ is the diffusion coefficient, l_t is the transport mean free path, μ_a is the absorption coefficient, R is the detector radius, L_s is is the distance used in the extrapolated zero-boundary approximation [67], and t is the time after the arrival of the pulse. Consideration of the detector radius is required because light emitted from the sample further from the injection point likely has a longer dwell time, and not all backscattered light was collected. The effective injection depth, h, is related to the depth of the hole, and includes a geometrical factor related to the shape of the hole. Leakage of light back through the narrow and deep holes is assumed to be small. This curve is

compared to data for cases with ($h = 325\ \mu$m) and without ($h = 0$) an engineered interface in Fig. 7.6. Here, fitting parameters are used to adjust for normalization and location of $t = 0$. As predicted, the interaction time scales with hole depth. This is further verified by calculating and measuring the average dwell time of the light in the material.

The average time that the scattered light dwells inside the material is calculated using $\langle t \rangle = \int tP(t)dt / \int P(t)dt$ where $P(t)$ is the optical power emitted from the sample as a function of time. This was measured using time correlated single photon counting for samples with different hole depths, and is shown in Fig. 7.7. The values predicted by diffusion theory are also shown. For shallow holes, the observed dwell times dip below the theory curve. This is due to the theoretical assumption that no light leaks back out of the hole being a poor approximation for shallow holes. As the hole depth increases; however, this assumption becomes more valid, and the measured dwell time approaches theory. It is important to point out that by coupling light into the scattering medium via the laser ablated holes, the dwell time increases from less than 50 ps to 750 ps, more than an order of magnitude enhancement.

7.3 Conclusion

In summary, we have experimentally demonstrated a drastic increase in the coupling of light into a turbid material, as evident by the increased interaction time and spatial diffusion of laser light within the material. In particular, we have shown over an order of magnitude increase in optical dwell time, and over two orders of magnitude more light penetrating a 1 cm thick sample. This was achieved by ablating a microscopic hole into the optical interface of a material and focusing light into the hole. When compared to diffusion theory, this suggests that as the depth of the narrow hole deepens, the coupling will increase and the amount of light leakage back out of the hole will become negligible.

Many significant consequences result from this technique. First, the increased dwell

time and diffusion distance will enhance the interaction of light with chemicals contained within the scattering medium. Optical signal generated from this interaction (i.e. Raman scattering, fluorescence, etc.), will be likewise enhanced, making it possible to achieve more sensitive optical measurements in the presence of scattering. Second, the extended penetration depth will not only allow us to probe deeper into a scattering medium for detection purposes, it will also allow us to deliver more optical energy through scattering media (such as tissue, bone, containers, etc.) for medical [227, 228] or defense purposes.

7.4 Supplemental: materials and methods

7.4.1 Sample preparation

A sample of highly scattering material is constructed by packing barium sulfate ($BaSO_4$) powder (Sigma-Aldrich, 243353) into a 1 inch diameter lens tube (Thorlabs, SM1L10) with lengths of either 2.5 cm or 1 cm. Barium sulfate has a transport mean free path of 1.2 μm ($\mu_t = 833.2$ mm^{-1}) as measured by coherent backscattering [124]; therefore, these sample thicknesses correspond to 10^4 transport mean free paths. The scattering coefficient and anisotropy parameter of $BaSO_4$, calculated from Mie theory, are $\mu_s = 2083$ mm^{-1} and $g = 0.6$, respectively. A hole is ablated in the surface of the sample by focusing 6 ps long laser pulses (Attodyne APL-X, 532 nm) onto the surface of the powder with a 50 mm lens (Thorlabs, AC254-050-A-ML). The pulse energy for ablation was measured to be 35μJ per pulse. Because the depth of ablation will saturate [246], the hole reaches a stable depth after a large number of pulses. This depth as a function of the number of ablation pulses was measured via optical coherence tomography, and is shown in Fig. 7.8.

7.4.2 Optical coherence tomography

In order to measure the depth of the hole, we used an optical coherence tomography (OCT) system. This system can provide non-destructive morphological images of optical scattering media at depths of 1-2 mm with high resolution imaging. The axial resolution
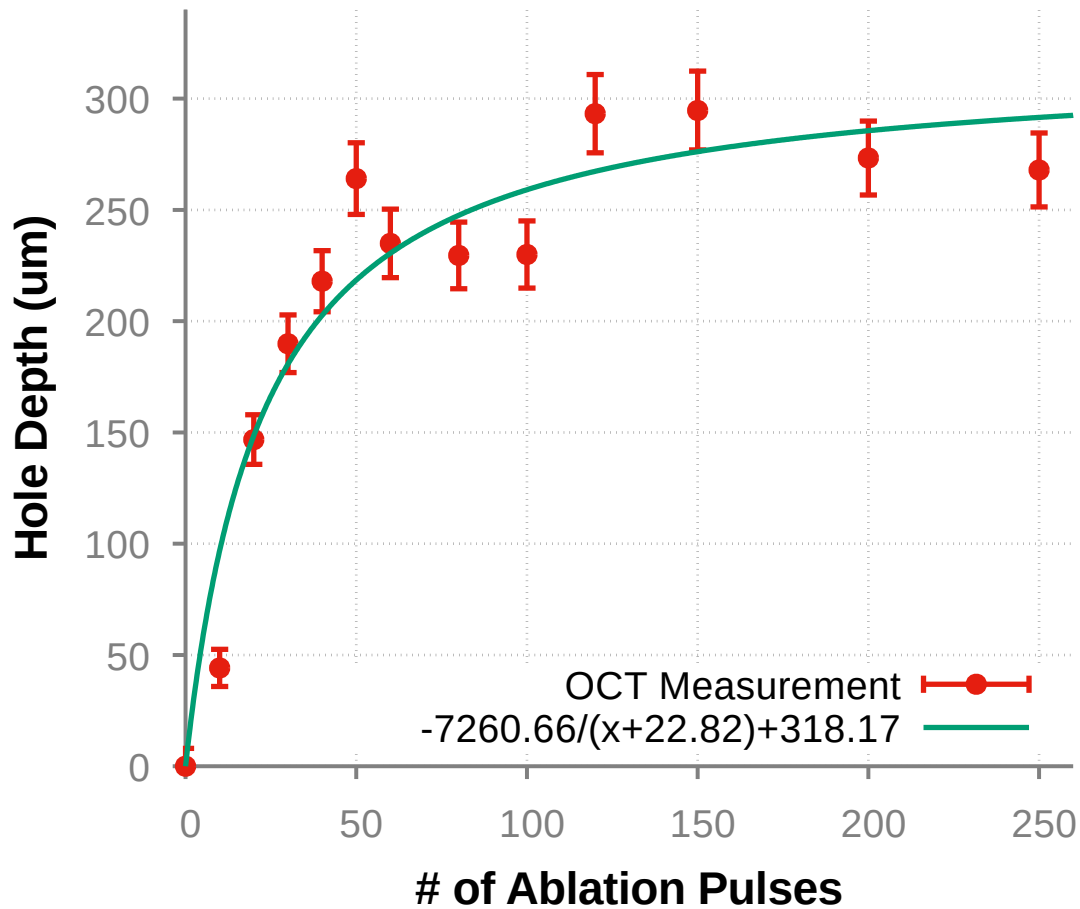
Figure 7.8: Hole depths as a function of number of laser pulses fired as measured by optical coherence tomography. This measurement is used to calibrate the dwell time measurements shown in Fig. 7.7.

of OCT is a function of the light source coherence length. The super-luminescent diode (SLD) source used here had a center wavelength of 830 nm with a full-width at half maximum of 40 nm, yielding an axial resolution of 7.6 μm. The lateral resolution is a function of the focal spot on the sample, which in this case was 6 μm. These high resolutions allow us to acquire a topographical image of the hole. Figure 7.2a shows an OCT cross-sectional image of a hole in this material ablated with 250 laser pulses. The hole is approximately 300 um deep. We scanned the entire hole, and Fig. 7.2b shows the OCT volume image.
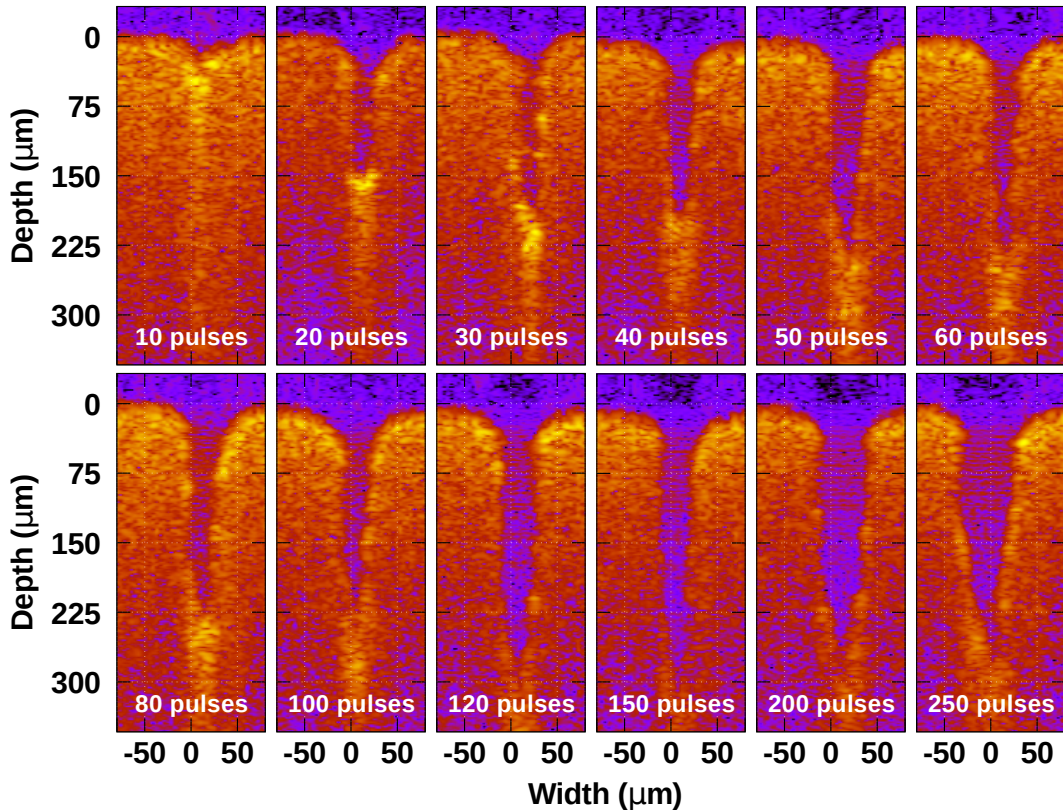
Figure 7.9: Cross sections from optical coherence tomography measurements of the holes as a function of the number of laser pulses used to ablate them.

The 3D volume clearly shows the conical shape of the hole.

To measure the depth of the hole as a function of the number of laser pulses, an array of 12 holes was ablated into a 1 cm thick sample of packed $BaSO_4$ using a different numbers of pulses for each hole. Each hole was separated from its neighbors by approximately 2 mm. This sample was then imaged using the OCT system. The cross section of each hole is shown in Fig. 7.9, and the measured hole depths as a function of the number of ablation pulses are shown in Fig. 7.8. A curve was fit to these data points in order to calibrate the hole depth versus the number of ablation pulses for the system, as is also shown in Fig. 7.8. The values from this calibration curve were used in Fig. 7.7, which shows the dwell time
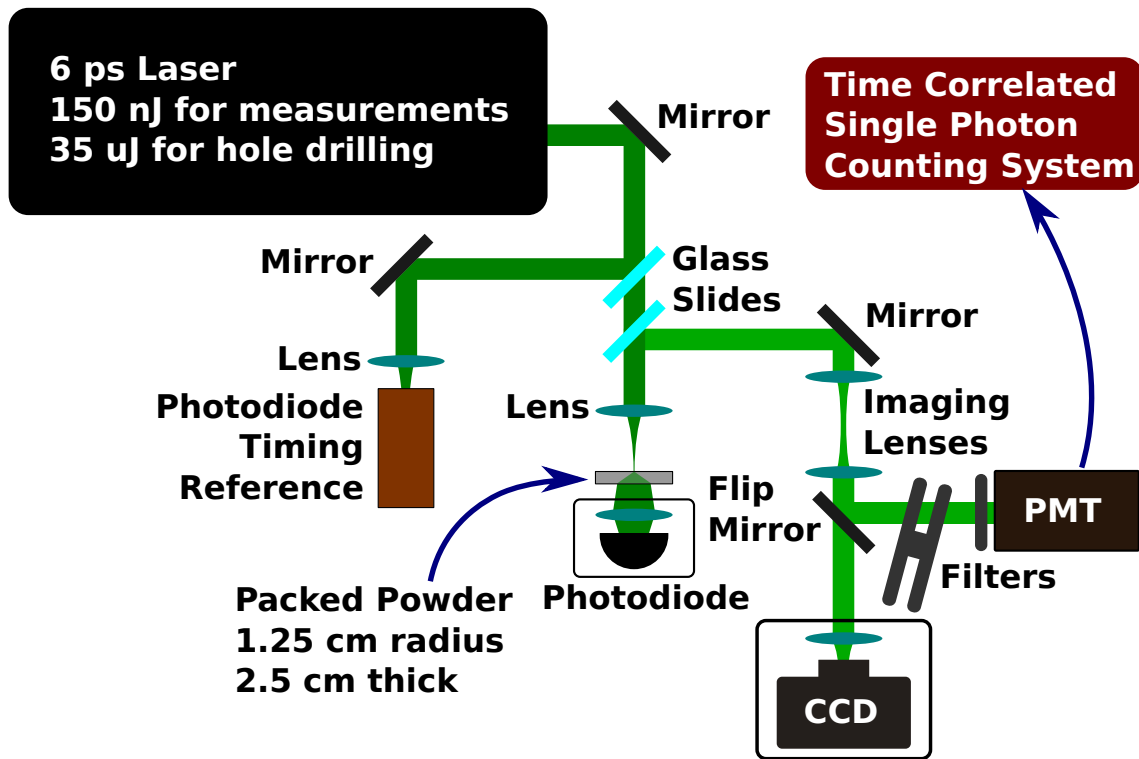
Figure 7.10: Experimental Setup. 6 ps laser pulses are used to ablate a microscopic hole in a packed slab of highly scattering powder. A photomultiplier tube is used as input to a time correlated single photon counting system to measure the decay of the light scattering off of the powder. A CCD also images the spatial scattering in the sample, and a large area photodiode measures the amount of light transmitted through the sample.

measurements as a function of hole depth.

7.4.3 Experimental setup

The experimental setup for ablation, imaging of the powder, and time correlated single photon counting is shown in Fig. 7.10. A picosecond laser (Attodyne APL-X, 532 nm) was used both to ablate the hole as well as for all measurements except optical coherence tomography. The beam is first expanded by a factor of 5 using two lenses in a telescope configuration. It is then focused onto the sample with a 50 mm achromatic lens (Thorlabs, AC254-050-A-ML). This same lens also collects the scattered light in the backward

direction. While the hole was ablated in the sample with laser pulse energy at 35 μJ per pulse, the measurements were made with the laser pulse energy tuned down to 150 nJ per pulse. Thus, measurements were acquired in a regime where ablation would not continue to occur.

The images of the backscattered light were acquired by relaying the image of the sample surface with lenses (Thorlabs, BPX070 ($f = 100$ mm), AC254-035-A-ML ($f = 35$ mm), & AC254-045-A-ML ($f = 45$ mm)) to a charge-coupled device (CCD, Mightex, CGE-B013-U) as shown in Fig. 7.10. A glass slide and mirror (Thorlabs, PF10-03-P01) were used to collect and direct the backscattered light with minimal disruption to the incident laser light. In this case the flip mirror (Thorlabs, FM90) (see Fig. 7.10) was opened to let the light enter the CCD. Images of the backscattered light from the sample were acquired for samples with and without a hole ablated in the surface. Furthermore, a hypodermic needle (Monoject, 250) was inserted into the intermediate image plane to block the focus of the laser, allowing us to more clearly see the increased diffusion radius of light emitted from the sample. These images were acquired for a 2.5 cm thick sample.

Measurements of the light transmitted through a 1 cm thick sample were acquired by a large area photodiode (Thorlabs, DET100A) placed at the back side of the sample, with a 25.4 mm focal length lens (Thorlabs, LA1951-ML) to collect the transmitted light onto the photodiode detector. The intensity of the transmitted light was then measured with the incident light both focused into the hole or onto the surface about 1 mm away from the hole. This coupling and uncoupling of the laser into the hole was achieved by translating the sample, lens, and photodiode in a direction perpendicular to the beam. Thus a ratio of the transmitted light through the sample when the incident light is coupled into vs uncoupled from the hole was measured to be over 200 times. Furthermore, this effect was imaged by removing the photodiode and lens, and placing a CCD with two imaging lenses of focal length 300 mm (Thorlabs, AC254-300-A-ML) and 45 mm (Thorlabs, AC254-

045-A-ML) behind the sample. These images are shown in Fig. 7.5.

7.4.4 Time correlated single photon counting

Temporal measurements of the backscattered light were measured via time correlated single photon counting. In this case, roughly 1.16% of the backscattered light was collected again with the focusing lens ($f = 50$ mm), glass slide, and mirror (Thorlabs, PF10-03-P01). The imaging lenses shown in Fig. 7.10 were removed, and the flip mirror (Thorlabs, FM90) closed so that the scattered light was directed into a multichannel plate photomultiplier tube (Hamamatsu R3809U-50). With the laser running at a 1 MHz repetition rate, the detection rate of the photomultiplier tube was kept between 10 and 15 kHz using various combinations of neutral density filters (Newport, 5215 and Thorlabs, NDK01/NEK01). This limiting of the detection rate to one photon for every 66–100 laser pulses was to avoid biased or uneven temporal distribution of the counted photons. The timing of the signal from the photomultiplier tube was measured with respect to a reference pulse by a time correlated single photon counting module (SPC-150, Becker-Hickl, 50 ps resolution). The reference pulse was taken from the laser beam before the scattering material with a glass slide, and collected onto a photodiode module (Becker Hickl, PHD-400). After collecting a sufficient number of signals, the time of arrival for each signal is binned to create a statistical representation of the scattered light as a function of time.

Because of the sensitivity of the time correlated single photon counting method to small changes in the setup parameters, such as the photomultiplier voltage and the threshold values for both the signal and reference pulse, these parameters were first determined by calibration to the fluorescent lifetime of Rhodamine 6G in water (2 μM concentration). Once calibrated, we used the same parameters for all other measurements. We also used the neutral density filters to ensure that the photon rate of the signal stayed nearly the same. With our calibrated system, we measured the lifetime of Rhodamine 6G in water to be 4.1
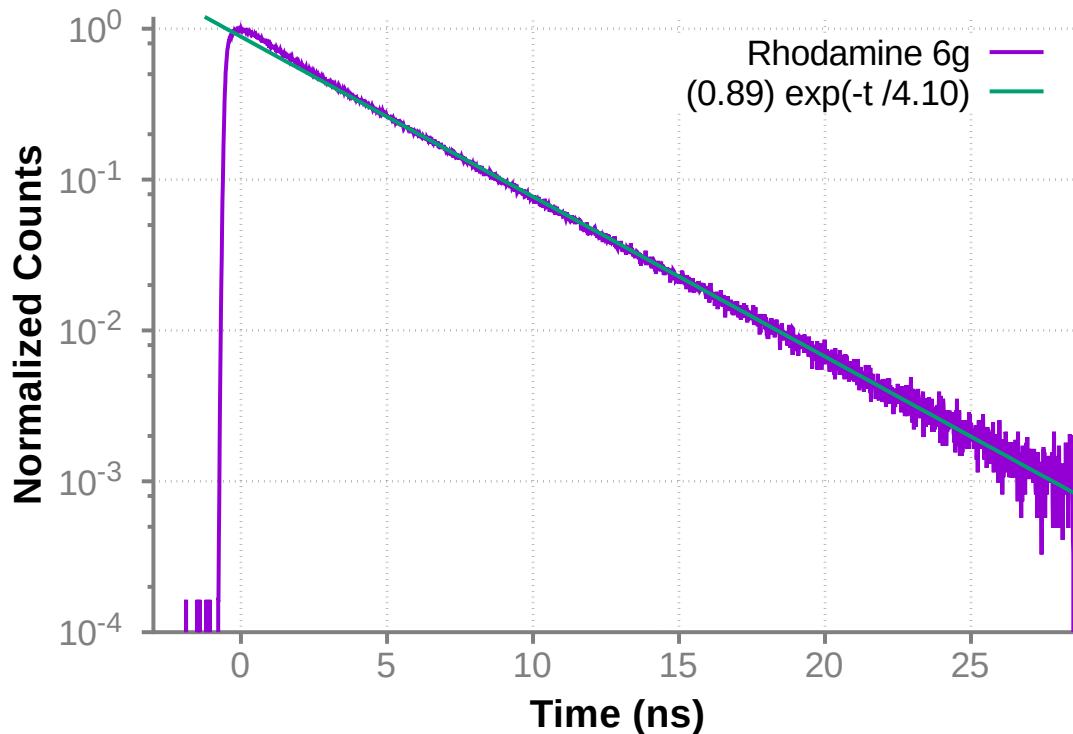
Figure 7.11: Fluorescent decay of Rhodamine 6g dye as measured by the time correlated single photon counting setup. The threshold and gain parameters were calibrated using Rhodamine 6g dye mixed in distilled water. At a concentration of approximately 2.2 μM, the fluorescent decay has a decay constant of about 4.08 ns [247].

ns (Fig. 7.11), which is comparable to the previously reported value of 4.08 ns [247].

The time of arrival of the scattered light from a sample with and without a hole is shown in Fig. 7.6. The signal for the sample with a hole was acquired with a collection time of 6 minutes. The signal from the sample without a hole required 60 minutes of collection time to realize good signal to noise at longer times. Careful shielding of the photomultiplier tube was critical to remove the light from any stray reflections in the room; however, a couple very weak reflections ($< 10^{-4}$) are still visible in the signal from the sample without a hole at 4 ns and 12 ns after the pulse arrives.

For the measurement of the average dwell time, 2 minute acquisitions were used to

measure the temporal signal as a function of hole depth. The shorter collection time allowed for faster acquisition of the data with very little effect upon the dwell time measurement. This is because of the orders of magnitude falloff soon after the pulse arrives and the nature of the time weighted integral ($\int tP(t)dt$). Different hole depths were ablated by controlling the number of ablation pulses used, and the depths were calibrated using optical coherence tomography as previously discussed.

7.4.5 Theoretical model

7.4.5.1 Interaction time

The dynamics of the backscattered light are modeled with the optical diffusion equation for radiative transport [30]

$$\frac{1}{c}\frac{\partial\Phi(\boldsymbol{r},t)}{\partial t} + \mu_a\Phi(\boldsymbol{r},t) - D\nabla^2\Phi(\boldsymbol{r},t) = S(\boldsymbol{r},t) \tag{7.2}$$

Here c is the speed of light, $\Phi(\boldsymbol{r},t)$ is the optical fluence rate, μ_a is the absorption coefficient, $D = l_t/3$ is the diffusion coefficient, and $S(\boldsymbol{r},t)$ is a source term. Also, $l_t = 1/\mu_t$ is the transport mean free path, where μ_t is the extinction coefficient with anisotropy parameter $g = \langle\cos(\theta)\rangle$ and is defined as $\mu_t = (1-g)\mu_s + \mu_a$, for scattering coefficient μ_s. This equation is solved using the Green function for a point light source [67] and the method of images. Here, we assume a point light source is located at $\boldsymbol{r'} = \langle 0,0,l_t+h\rangle$ where h denotes the injection depth of the light. Using a point source assumes that all of the injected light enters the material at the same depth. A more rigorous approach would model the injected light as an extended source, based upon the geometry of the hole. However, there is an equivalent depth, $h = \eta h_0$, at which a point source can be placed to approximate the more rigorous extended source. Here, h_0 is the depth of the hole, and the geometrical factor is $0 \leq \eta \leq 1$. Thus, for simplicity, we assume that the only effect of the hole is to

inject the light into the scattering slab at this equivalent depth of $(l_t + h)$. This approach still neglects any light that escapes back through the hole, assuming it is small for deep and narrow holes.

The optical power of the light that exits the medium to the surface $(\Phi(z = 0, t))$ is found by integrating the Green function solution over the detector area (circle with radius R), yielding Eq. 7.1 in the main text. Here, L_s is the distance used in the extrapolated zero-boundary approximation [67], at which the fluence rate, $\Phi(\boldsymbol{r}, t)$, is equal to zero. This equation is compared to the data in Fig. 7.6 using a scaling parameter and slight temporal offset as fitting parameters to adjust for normalization and location of $t = 0$. Here, we assumed a collection radius of 0.7 mm, $\mu_a = 10^{-4}$ mm^{-1}, and an equivalent hole depth, $h = 325$ μm for the coupled case. For the uncoupled case, the hole depth is set to zero.

It is also intuitive to see that for long times ($t \gg R^2/(4Dc)$ and $t \gg h^2/(4Dc)$), Eq. 7.1 simplifies to

$$P(t) \approx \frac{cR^2 L_s(L_s + l_t + h)}{8\sqrt{\pi}} \frac{1}{[Dct]^{5/2}} e^{-\mu_a ct}.$$ (7.3)

Thus, the interaction time of light with the material should scale with hole depth. This is measured by computing the average dwell time of the light in the medium.

From the integration of Eq. 7.1, the dwell time of light in the scattering medium, $\langle t \rangle = \int tP(t)dt / \int P(t)dt$, is found to have the form

$$\langle t \rangle = \frac{1}{2\mu_a c}\left[1 + \frac{k_0 e^{-k_0} - k_1 e^{-k_1} - k_2 e^{-k_2} + k_3 e^{-k_3}}{e^{-k_0} - e^{-k_1} - e^{-k_2} + e^{-k_3}}\right]$$ (7.4)
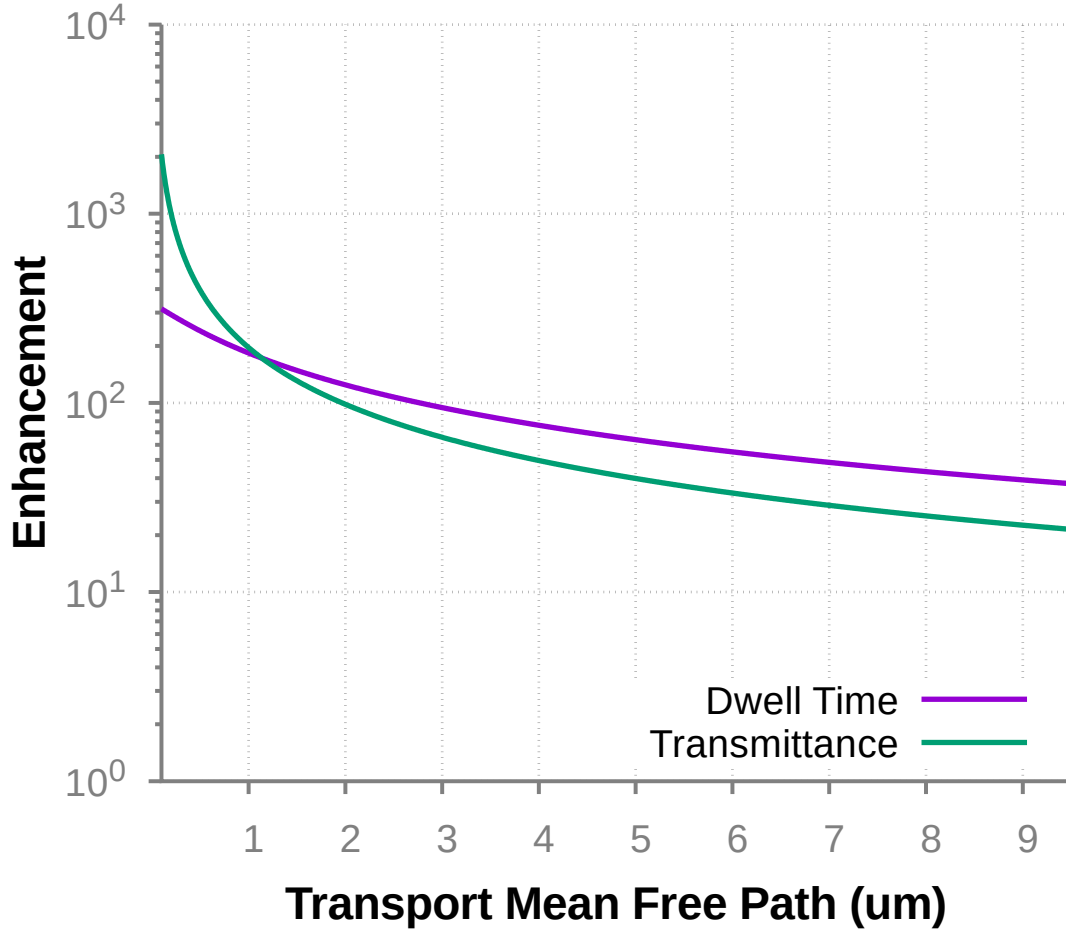
Figure 7.12: Theoretical enhancement of transmittance and dwell time due to micro-scopic interface engineering as a function of the transport mean free path. Calculated from Eq. 7.4) and Eq. 7.9).

where the coefficients, k_j, are equal to

$$
\begin{aligned}
k_0 &= \sqrt{\frac{\mu_a}{D}}(l_t + h) \\
k_1 &= \sqrt{\frac{\mu_a}{D}}(2L_s + l_t + h) \\
k_2 &= \sqrt{\frac{\mu_a}{D}}\sqrt{(l_t + h)^2 + R^2} \\
k_3 &= \sqrt{\frac{\mu_a}{D}}\sqrt{(2L_S + l_t + h)^2 + R^2}
\end{aligned}
\tag{7.5}
$$

While Eq. 7.4 is plotted in Fig. 7.7, it is intuitive to see that for $h \ll R$ (as well as $h \gg l_t$ and $h \gg L_s$), the dwell time has a linear dependence upon h. In this regime, Eq. 7.4 simplifies to

$$\langle t \rangle \approx \frac{h + l_t + L_s}{2c\sqrt{D\mu_a}} \left(1 - e^{-R\sqrt{\frac{\mu_a}{D}}} \right) \tag{7.6}$$

We note here the dependence of the dwell time upon the scattering properties. In particular, as the diffusion coefficient, D, decreases (i.e. increased scattering coefficient), the dwell time increases. Thus, for a given hole depth, the dwell time is longer for media with stronger scattering. The enhancement due to an effective hole depth of $h = 350$ μm is shown in Fig. 7.12 as a function of transport mean free path.

7.4.5.2 *Enhanced transmittance*

The optical transmittance through a scattering sample is modeled for a slab of finite thickness with an infinite series of dipole sources. Here, keeping terms from the first four dipoles, as calculated in [244], with extension to include the extrapolated zero-boundary approximation [67], the transmittance is written as

$$T(\rho, d, t) = \frac{1}{2}(4\pi Dc)^{-3/2}t^{-5/2}e^{-\mu_a ct}e^{-\frac{\rho^2}{4Dct}} \times \sum_{n=0}^{N=7}(-1)^n \alpha_n e^{-\frac{\alpha_n^2}{4Dct}} \tag{7.7}$$

where d is the thickness of the medium, ρ is the radius from the optical axis, and the α_n coefficients are

$$\alpha_0 = d - h - l_t$$

$$\alpha_1 = d + h + l_t + 2L_S$$

$$\alpha_2 = d - h - l_t + 2L_s$$

$$\alpha_3 = d + h + l_t + 4L_s$$

$$\alpha_4 = 3d - h - l_t + 4L_s \tag{7.8}$$

$$\alpha_5 = 3d + h + l_t + 6L_s$$

$$\alpha_6 = 3d - h - l_t + 6L_s$$

$$\alpha_7 = 3d + h + l_t + 8L_s$$

Integration over the transverse direction and time ($\int_0^\infty \int_0^{2\pi} \int_0^R T(\rho, d, t)\rho \, \mathrm{d}\rho \, \mathrm{d}\phi \, \mathrm{d}t$) yields the total transmittance as a function of sample thickness (d), optical injection depth (h), and detector radius (R).

$$T(d, h, R) = \frac{1}{2} \sum_{n=0}^{N=7} (-1)^n \left[e^{-\sqrt{\frac{\mu_a}{D}}\alpha_n} - \frac{\alpha_n}{\sqrt{R^2 + \alpha_n^2}} e^{-\sqrt{\frac{\mu_a}{D}(R^2 + \alpha_n^2)}} \right] \tag{7.9}$$

From this equation, we find that by placing the source 0.35 mm below the surface of a $d = 10$ mm thick sample with $\mu_a = 10^{-4}$ mm^{-1} and $\mu_t = 833.2$ mm^{-1}, the transmittance is enhanced by a factor of over 160 times. In comparison, reducing the thickness to $d = 9.65$ mm with $h = 0$ will only increase the transmitted light by 19%.

The relationship between transmittance and the diffusion coefficient is less obvious in this case than in the case of dwell time. However, plotting Eq. (7.9) (see Fig. 7.12) as a function of l_t, for $h = 350$ μm and $d = 10$ mm, we see that the enhancement of transmittance due to the microscopic interface is also greater for samples with a stronger scattering coefficient.

8. ENHANCED OPTICAL COUPLING AND RAMAN SCATTERING VIA MICROSCOPIC INTERFACE ENGINEERING

Spontaneous Raman scattering is an extremely powerful tool for the remote detection and identification of various chemical materials. However, when those materials are contained within strongly scattering or turbid media, as is the case in many biological and security related systems, the sensitivity and range of Raman signal generation and detection is severely limited. In this chapter, we demonstrate that through microscopic engineering of the optical interface, the optical coupling of light into a turbid material can be substantially enhanced. This improved coupling facilitates the enhancement of the Raman scattering signal generated by molecules within the medium. In particular, we detect at least two-orders of magnitude more spontaneous Raman scattering from a sample when the pump laser light is focused into a microscopic hole in the surface of the sample. Because this approach enhances both the interaction time and interaction region of the laser light within the material, its use will greatly improve the range and sensitivity of many spectroscopic techniques, including Raman scattering and fluorescence emission detection, inside highly scattering environments.

8.1 Introduction

The use of Raman scattering has proven to be a powerful way to detect substances with high chemical specificity. It has been used effectively in a variety of circumstances, ranging from the remote sensing of subsurface water temperatures [248] to material/biomedical imaging [118, 249] and the detection of explosive or harmful substances [182, 218, 250].

Unfortunately, the signal from spontaneous Raman scattering is weak, requiring the use of expensive and sensitive detectors, as well as long integration times. For this reason, many complementary techniques and methods, built on the fundamental principle of

Raman scattering, have been developed to enhance signal and decrease acquisition time. Some of these techniques include stimulated Raman scattering [107, 152], coherent anti-Stokes Raman scattering [121, 182], and surface enhanced Raman scattering [122]. Other methods use integrating cavities [21, 22] to increase the interaction time and region of the laser with the sample, thereby enhancing signal and sensitivity.

However, in many instances, the substance/chemical of interest is either contained in or behind a highly scattering material. This imposes a limitation on the effectiveness of both spontaneous Raman scattering as well as the previously mentioned enhancement techniques. For example, the optical detection of a harmful substance, such as anthrax, is more challenging when it is contained inside a scattering envelope [10, 11]. The presence of a scattering material reduces the intensity of light that can actually penetrate to the chemical and generate spectroscopic signals. This limitation is very common in biomedical applications where imaging/detection of structures beneath the surface of skin, bone, or other tissue would allow for the detection of cancer [251–253] or other diseases [254].

Recently, techniques like optical phase conjugation [34, 35] and wavefront shaping have offered ways to focus light through a scattering material [53, 54, 255] to enhance Raman scattering [172] or other [50] signals. Ultimately, these techniques are limited by the penetration depth of the light through the material. While the transmission of light through the material can be somewhat enhanced via wavefront shaping [108,231] methods, access to both or multiple sides of the material are required. In other words, for a system where only epi detection is allowed, a feedback method like fluorescence [50,51] or Raman scattering [172] must be used, yet these methods require adequate penetration of the pump light to begin with. Therefore, in order to acquire Raman scattering signal from deep inside a turbid medium, there is a need to first enhance the penetration depth and interaction time of the light with the medium. Once this is achieved, techniques like wavefront shaping can work in tandem to further enhance the signal generated by the desired chemicals [256,257].
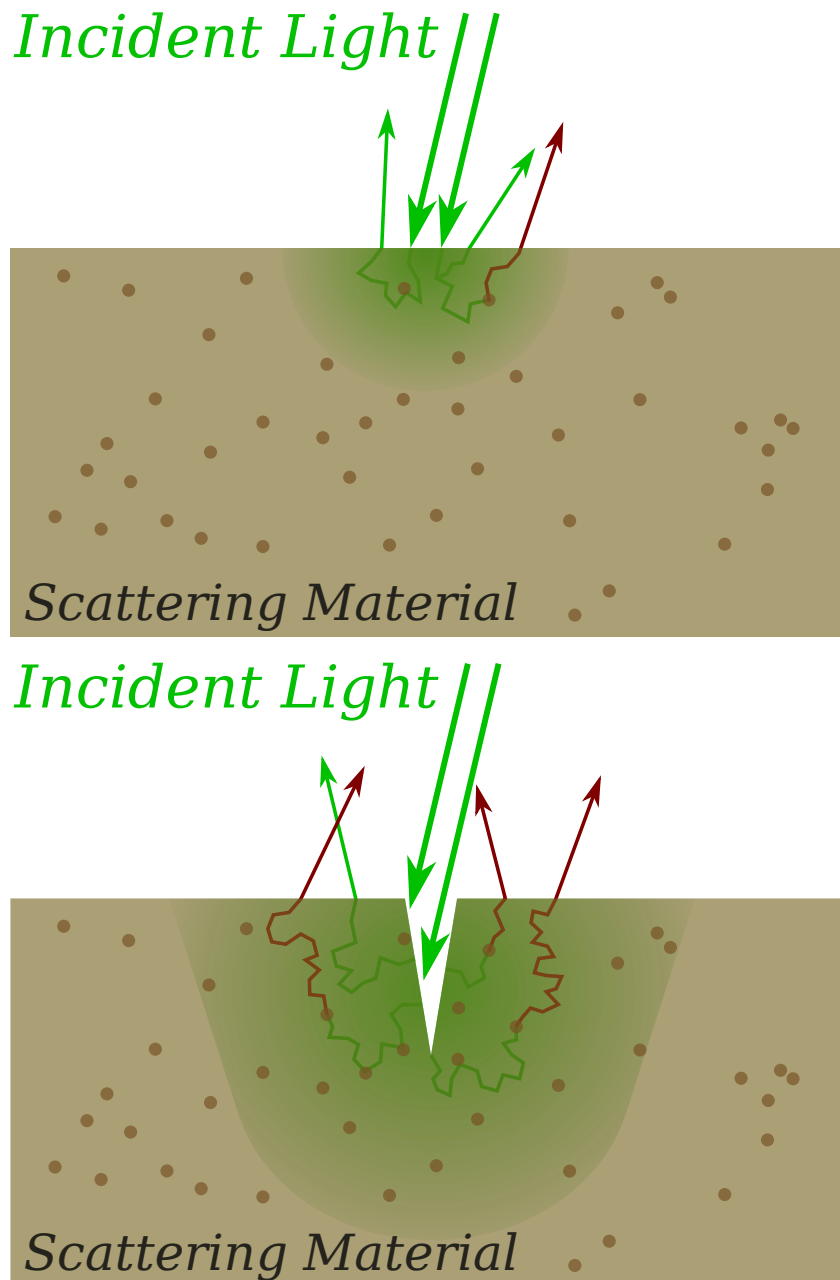
Figure 8.1: When light is incident upon a scattering material which contains Raman active particle, the limited penetration depth restricts the interaction of light with the particles (top), and thereby the amount of Raman signal generated. Enhanced coupling of light into a turbid medium is achieved by focusing the light into a microscopic interface engineered in the surface (bottom). This coupling increases the interaction time and region of light with the material, which directly impacts the amount of generated Raman signal.

The elastic scattering of light can be used to increase the optical path length, and interaction time, of light with molecules within a material [23, 24]. For instance, using highly scattering materials as the walls of an integrating cavity [22] has lead to more sensitive detection of fluorescent markers in fluids [21]. Furthermore, adding small amounts of scattering materials to a transparent fluid has also shown some degree of signal enhancement [24]. While these techniques were demonstrated for transparent or nearly transparent samples, the working principle is that elastic scattering of light can increase optical path length and interaction time with a substance, thereby enhancing spectroscopic signals. For highly scattering materials, the scattering medium itself can be used to obtain this increased path length. In practice, the main obstacle to the realization of this effect is the short penetration depth of light incident on the surface of turbid media. Because most of the light is scattered near the surface of the material, it is not injected deep enough to realize an increased path length due to multiple scattering events.

In chapter 7, we have shown that enhanced coupling of light into turbid media can be achieved by microscopic engineering of the geometry of the optical interface. In this chapter, we extend the previous results to show that when light is more efficiently coupled into a turbid medium, it facilitates a drastic improvement in the sensitivity of spectroscopic detection techniques. The concept behind this enhancement is illustrated in Fig. 8.1. As optical coupling into the medium enhances, the interaction time of light with molecules within the sample also increases. Thus, more of the incident optical energy has opportunity to be converted into spectroscopic signal. In particular, here we will show that the enhanced interaction time and penetration distances of the pump light within a turbid medium can yield at least two orders of magnitude enhancement in the spontaneous Raman scattering signal generated by the medium.

These results, namely the enhanced spectroscopic signal and penetration depth, directly influence remote detection methods, including spatially offset Raman spectroscopy [7,
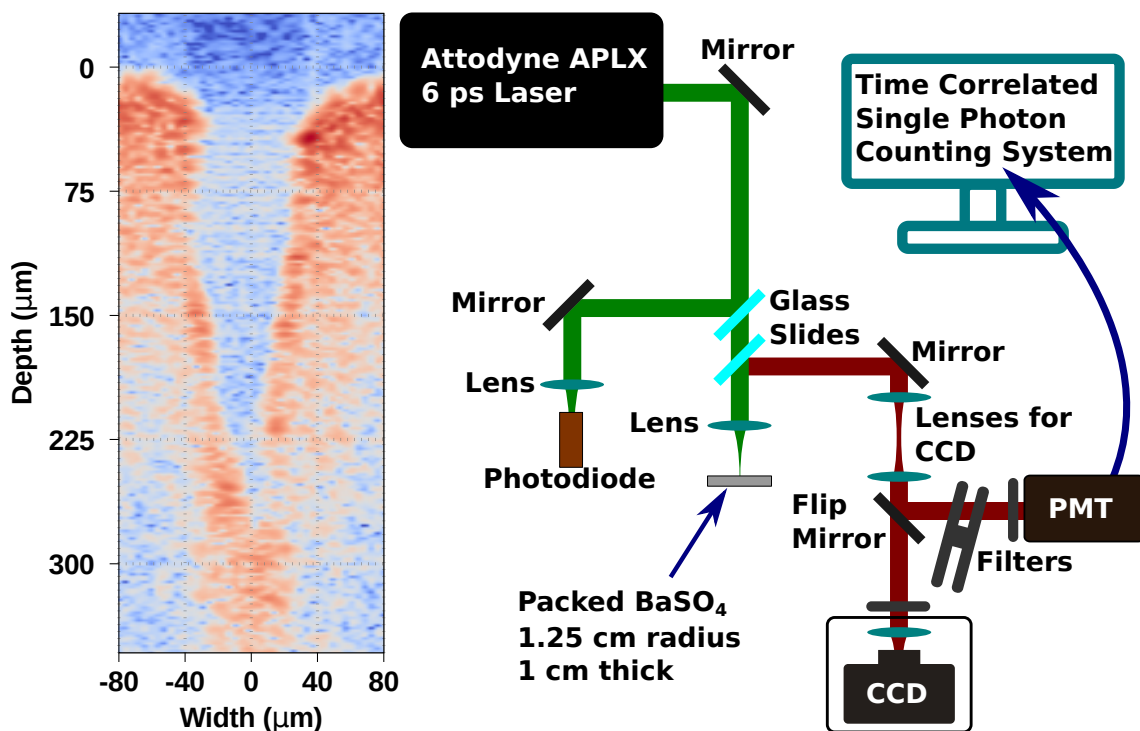
Figure 8.2: Cross section (left) of hole ablated in packed BaSO$_4$ powder as measured by optical coherence tomography. On the right, the experimental setup used to acquire images and the temporal profile of the Raman scattered light is shown. The lenses for the CCD were removed for the temporal measurements (time correlated single photon counting). Raman Spectra were also collected by replacing the CCD with a fiber coupled spectrometer.

258]. This technique also makes it possible to sensitively detect small concentrations of chemicals in a material using relatively inexpensive detectors. Furthermore, the combination of this approach with wavefront shaping techniques may yield even greater enhancements and finer control of the signal generated [256, 257].

8.2 Experimental methods

Barium sulfate (BaSO$_4$) powder (Sigma Aldrich, 243353) was packed into a 1 inch lens tube (Thorlabs, SM1L03, 1 cm thick) to form a highly scattering sample. Barium sulfate was chosen for its high scattering coefficient ($\mu_s = 2083 \ mm^{-1}$), simple Raman

spectrum [106], and its ability to be physically packed into a container. In this case, $BaSO_4$ served as both the scattering medium and the source of Raman scattering, but this method is also applicable to the case where the source of Raman scattering is not the same material as the strongly scattering particles. Once packed, a microscopic hole approximately 300 μm deep and 100 μm in diameter was engineered into the surface of the sample using laser ablation from 6 ps long laser pulses (Attodyne, APL-X, 532 nm) with 35 μJ of energy per pulse. These pulses were focused onto the sample with a 50 mm lens, and multiple pulses were fired until the ablation reached a saturation point. The cross-section of a characteristic hole was measured using optical coherence tomography (chapter 7) and is shown in Fig. 8.2. Laser light is coupled into the packed powder by focusing the laser light into the hole with the same 50 mm lens used to create the hole. Laser light can be uncoupled from the hole by translating the sample in the transverse direction such that the light is incident upon the flat face of the sample and does not enter the hole. While the holes were ablated with laser energies at 35 μJ per pulse, all measurements (unless noted) were obtained with the laser energy at 150 nJ per pulse.

8.3 Experimental results

The spatial profile of the Raman scattered light emitted from the sample in the backward direction was imaged onto a CCD (Mightex CGE-B013-U) with a long pass filter (Semrock LP03-532RS-25) to reject the 532 nm laser light. The measured profiles with and without a hole present are shown on the left in Fig. 8.3. With equivalent scales, we see the enhanced Raman scattering produced near the focus of the laser. We also see enhanced Raman light emitted further away from the laser focus. This is more clearly visible when the laser focus is blocked by placing a needle in an intermediate image plane and plotting the image in log scale, as is shown on the right in Fig. 8.3. The normalized Raman spectra of the $BaSO_4$ sample measured for cases with the laser light coupled/uncoupled into
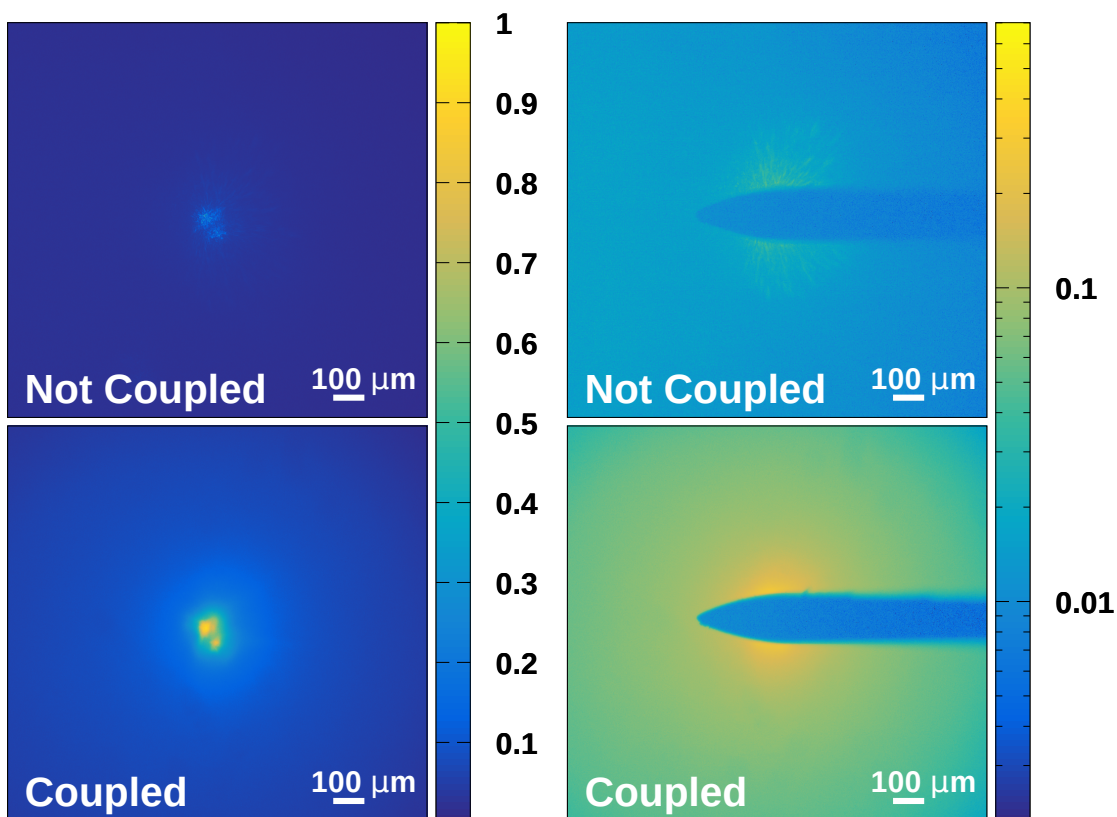
Figure 8.3: Images of spontaneous Raman scattering from packed $BaSO_4$ powder samples. More Raman signal is observed when the pump laser light is coupled (bottom) into the sample through a microscopic hole in the surface. For comparison, the case without a microscopic interface (Not coupled) is also shown (top). A needle was used (right) to block out the focus of the laser, showing more clearly the increased spatial diffusion of the Raman scattered light.

the microscopic hole, are shown in Fig. 8.4. These spectra were measured with a fiber-coupled, uncooled spectrometer (ASEQ, LR1), and show at least two orders of magnitude enhancement of the Raman scattered light from the $BaSO_4$ powder when the pump laser is more efficiently coupled into the sample.

Time correlated single photon counting (TCSPC) [245] was employed to measure the time dynamics of the emission of Raman scattered light. As shown in Fig. 8.2, the Raman

119
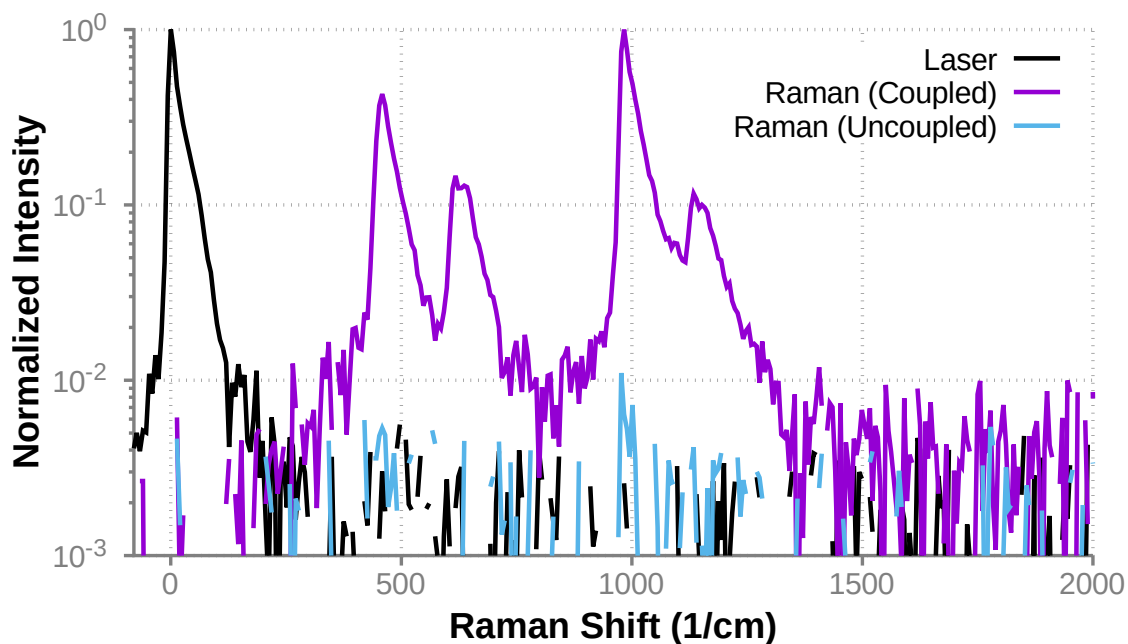
Figure 8.4: Normalized spectral intensity of Raman scattering from a $BaSO_4$ sample with the pump laser coupled (violet) vs uncoupled (blue) into the sample through a microscopic hole. The laser spectrum is given for reference (black). Note that the spectrum for the uncoupled case was normalized by the peak Raman intensity of the coupled case.

light emitted in the backward direction was collected by the focusing lens, and directed through neutral density filters and a long-pass (Semrock LP03-532RS-25) filter into a photomultiplier tube (Hamamatsu R3809U-50). The long-pass filter was used to reject the elastically scattered light, and pass the Raman scattered signal. The neutral density filters were used to control the intensity of the Raman signal on the photomultiplier tube. The electronic signal from the photomultiplier tube was amplified (Hamamatsu C5594-12) and used as the signal for a TCSPC card (SPC-150, Becker-Hickl). A pulse from the laser was also used as a temporal reference. By counting the arrival time of many photons, a statistical representation of the Raman scattered light with resolution of less than 50 ps [245] was accumulated. One benefit of using this method is the extremely large dynamic range achievable by simply counting more photons. More than adequate signal
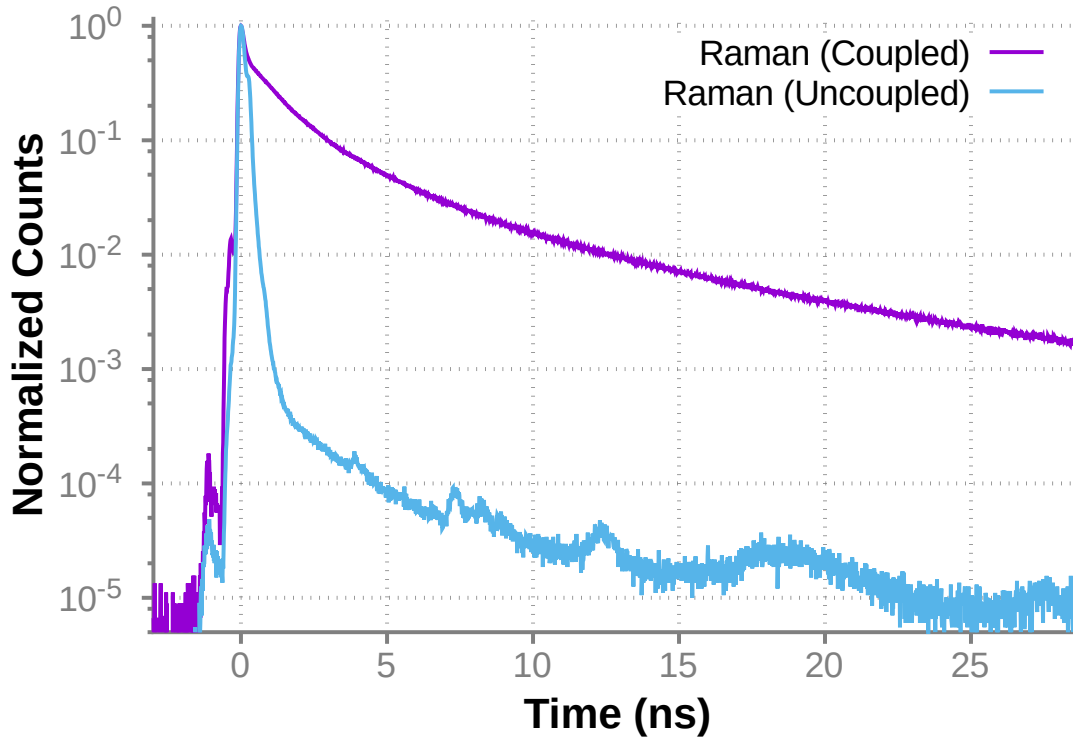
Figure 8.5: Intensity of Raman scattering signal detected as a function of time for samples with (violet) and without (blue) a microscopic hole. As the average interaction time of the pump light inside the sample increases, the number of inelastically scattered (i.e. Raman) photons is greatly enhanced.

to noise was achieved for Raman generated light by integrating photons at a rate of 10 kHz for approximately 60 minutes, with the laser running with a repetition rate of 1 MHz and 150 nJ per pulse.

From the temporal picture acquired of the Raman scattered light, shown in Fig. 8.5, we see a vast increase in the interaction time of the laser with the sample when the laser is focused into the hole in the surface of the sample. More specifically, more than 25 ns after the laser pulse has arrived, there is still a significant amount of Raman light being emitted from the sample. This is an enhancement of over two orders of magnitude more light emitted at this point in time when compared to the case of a sample without a hole.
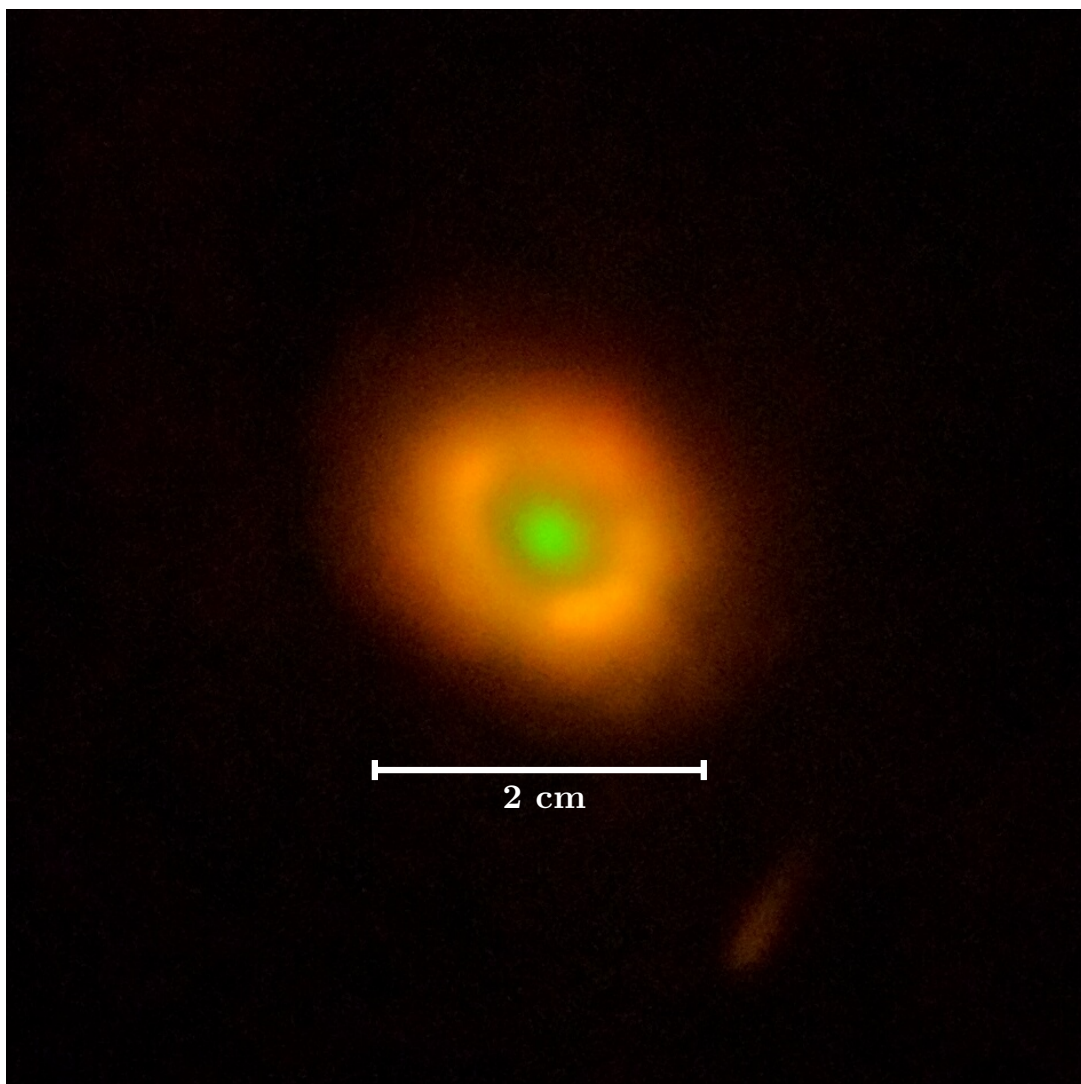
Figure 8.6: Image of Raman scattering from a BaSO$_4$ sample acquired using a cell phone camera and laser safety glasses (Thorlabs, LG12) to filter out the scattered pump light. This image illustrates the substantial enhancement achieved by this method, as the spontaneous Raman scattering signal is clearly visible by the unaided eye.

A better understanding of the substantial amount of Raman scattered light generated by the coupled sample is gained from Fig. 8.6. This image was acquired using a cellular phone camera (Huawei, Nexus 6P) with laser safety glasses (Thorlabs, LG12) used to filter out the elastically scattered pump light. Here, the pump laser was set to approximately 35 μJ per pulse. From this image, we see that the spontaneous Raman scattering from the coupled sample was brightly visible to the unaided, human eye. We also see that a large portion of the sample surface is emitting Raman scattered light (the sample diameter is 2.5 cm). Even with the laser energy turned down to 150 nJ per pulse, the spontaneous Raman scattering was clearly visible by eye, and could be used as an indicator of the quality of the laser coupling alignment.

In addition to the large spectroscopic enhancements provided by microscopic interface engineering, samples can be conveniently transplanted to light sources other than the laser used to create the interface. To demonstrate this, a hole was drilled into a packed powder sample using the picosecond laser as previously explained. This sample was removed from the ablation setup, and placed into the beam of a continuous wave diode pumped solid state laser (532 nm) with 2.5 mW of optical power. The laser beam was focused into the hole using a 50 mm lens. Alignment/coupling of the laser into the microscopic structure was achieved here by monitoring the enhancement of the diffusion radius and transmission (see chapter 7) of the elastically scattered light in the sample as the sample was translated with respect to the beam. The surface of the sample was imaged in the backward direction using an uncooled CCD (Mightex CGE-B013-U), and the images were acquired with 15 ms integration times. These images are shown in Fig. 8.7, and again, nearly two orders of magnitude (91$\times$) more Raman light was detected near the focus of the laser. Note that Fig. 8.7 is plotted in log scale in order to show the additional features visible from distances well over 300 μm away from the microscopic structure and laser focus. It is also important to note that here, the uncoupled image was obtained by translating the sample
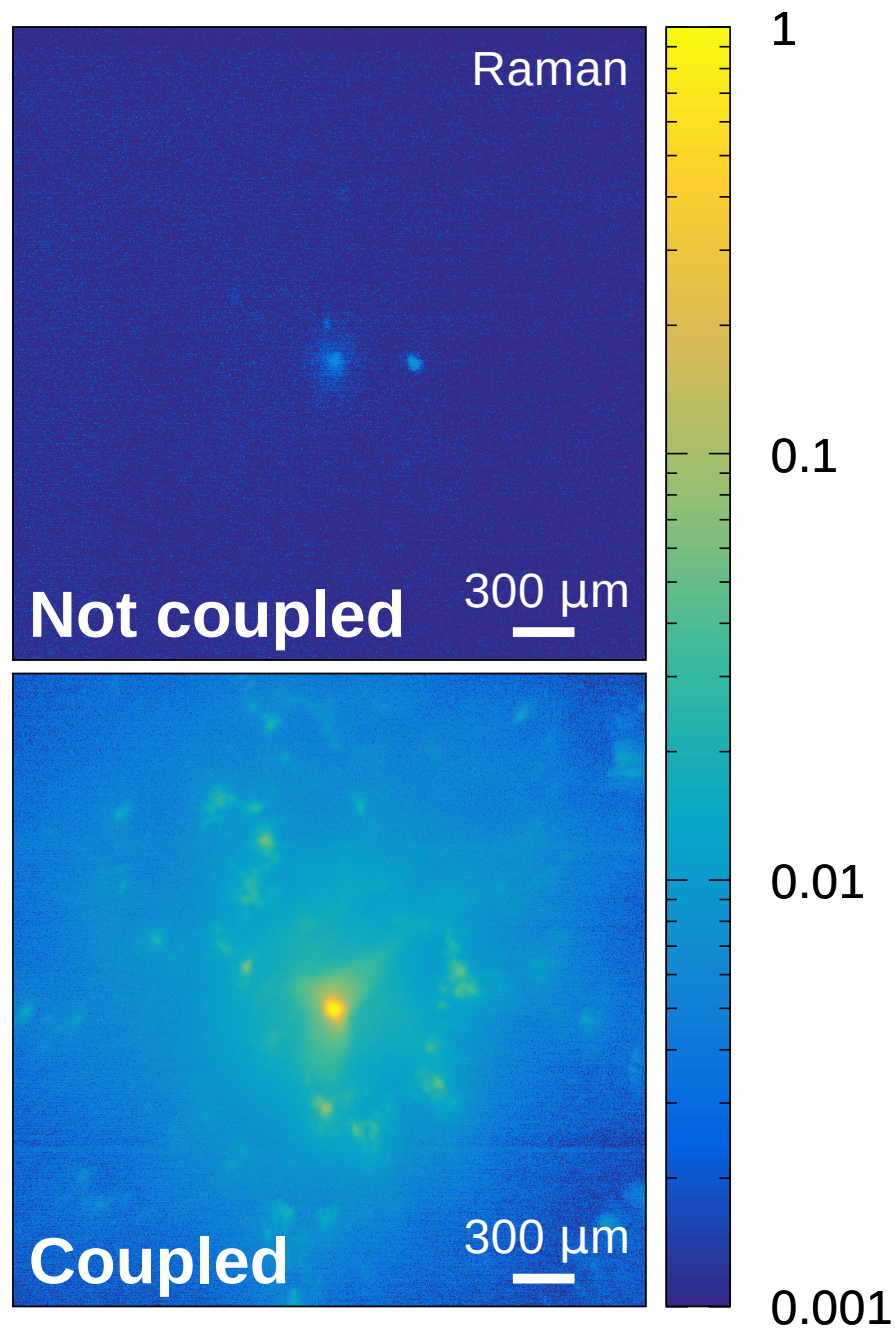
Figure 8.7: Image of Raman scattering from a $BaSO_4$ sample comparing cases when the pump laser was coupled (bottom) vs uncoupled (top) into the microscopic hole in the surface of the sample. These images were acquired in 15 ms using an uncooled CCD, and about 2.5 mW of optical pump power (cw). Nearly two orders of magnitude more Raman scattered light was detected near the focal region when the light was coupled into the hole.

in the transverse direction, so that the laser was focused onto the flat sample surface, and no longer coupled. Even though the light is not coupled into the hole, Fig. 8.7 (top) shows a localized spot of Raman scattered light emitted from the hole (about 400 μm to the right of the laser focus). This suggests that this type of structure may be used to both couple light into and out of the turbid sample.

8.4 Conclusion

In conclusion, we have demonstrated enhanced optical coupling and Raman scattering of light in a turbid medium by focusing the pump laser light into an engineered microscopic optical interface. In particular, we have observed two orders of magnitude enhancements in the measured Raman scattering signal from a barium sulfate ($BaSO_4$) sample. This enhancement comes from the increased coupling, penetration depth, and interaction time of the laser with the sample, and is a direct result of utilizing the large elastic scattering coefficient to more effectively contain light inside the turbid medium.

While this method is not entirely non-invasive, the size of the hole ablated in the surface of the material is very small compared to the size of the sample itself, and is at least two to five times smaller than typical hypodermic needles (Ted Pella, Inc.). Furthermore, because it is a geometry related effect, narrower and deeper holes should further improve this coupling of light into the medium, yielding even larger interaction times and Raman signal. Because this technique increases both the interaction time and the spatial interaction region of the pump laser within a material, it is an excellent way to increase the signal from low concentrations of particles distributed throughout the medium. In some instances, it may even facilitate Raman-based detection of chemicals using the unaided, human eye.

125

9. SUMMARY AND CONCLUSIONS

In summary, we have experimentally and theoretically studied the use of wavefront shaping and microscopic optical interface engineering in order to achieve enhanced optical signals for sensing and detection purposes. In particular, a backward propagating pulse was generated from superfluorescent emission in dense Sodium vapor. Signals generated in the backward direction hold much promise for remote spectroscopic techniques. After this, we studied wavefront shaping optimization algorithms for a better understanding of ways to improve their convergence rates. Wavefront shaping techniques were also investigated to show the enhancement of spontaneous Raman scattering signal from chemicals placed behind a highly scattering medium. These wavefront shaping methods hold much promise for the control of the propagation of spatially coherent light through turbid media. However, these techniques are useful in many other situations. As an example, we have also demonstrated the use of these wavefront shaping methods to enhance the conversion efficiency of second harmonic generation in nonlinear crystals. In addition to wavefront shaping, we have applied phase only pulse shaping to femtosecond laser pulses before they undergo femtosecond filamentation. The applied pulse shape along with filamentation was shown to concentrate the amplitude of the pulse into frequency windows defined by the applied pulse shape.

Lastly, we have shown that by engineering the optical interface of a highly scattering material on the microscopic scale, it is possible to substantially enhance the coupling of light into the scattering material. This has a number of consequences. First, the enhanced coupling allows the light to dwell inside the material for over an order of magnitude longer period of time. Secondly, the interaction region of the injected light within the material is drastically enhanced. This means that the amount of light transmitted through the material

is also increased. We observed at least two orders of magnitude more light transmitting through a scattering sample via this method. And finally, we have shown that these enhancements from improved coupling can be applied to the spectroscopic measurement of chemicals within the scattering medium. In particular, we measured two orders of magnitude more light generated by spontaneous Raman scattering from a coupled sample compared to a control (uncoupled) sample. Thus we have shown that by control of the scattering of light within a turbid medium, we can enhance the sensitivity and range of optical sensing techniques.

REFERENCES

[1] A. L. Schawlow and C. H. Townes, "Infrared and optical masers," *Phys. Rev.*, vol. 112, no. 6, pp. 1940–1949, 1958.

[2] T. H. Maiman, "Stimulated optical radiation in ruby," *Nature*, vol. 187, no. 4736, pp. 493–494, 1960.

[3] J. Hecht, "Beam: The race to make the laser," *Opt. Photonics News*, vol. 16, no. August 2005, p. 24, 2005.

[4] J. Hecht, *Beam: The race to make the laser*. Oxford: Oxford University Press, 2005.

[5] C. F. Bohren and D. R. Huffman, *Absorption and scattering of light by small particles*. New York: Wiley, 1998.

[6] J. C. Ricklin and F. M. Davidson, "Atmospheric turbulence effects on a partially coherent Gaussian beam: implications for free-space laser communication.," *J. Opt. Soc. Am. A. Opt. Image Sci. Vis.*, vol. 19, no. 9, pp. 1794–1802, 2002.

[7] Z. Di, B. H. Hokr, H. Cai, K. Wang, V. V. Yakovlev, A. V. Sokolov, and M. O. Scully, "Spatially offset Raman microspectroscopy of highly scattering tissue: theory and experiment," *J. Mod. Opt.*, vol. 0340, no. January 2016, pp. 1–5, 2014.

[8] S. Srinivasan, M. Schulmerich, J. H. Cole, K. A. Dooley, J. M. Kreider, B. W. Pogue, M. D. Morris, and S. A. Goldstein, "Image-guided Raman spectroscopic recovery of canine cortical bone contrast in situ.," *Opt. Express*, vol. 16, no. 16, pp. 12190–12200, 2008.

[9] A. Pifferi, A. Torricelli, P. Taroni, A. Bassi, E. Chikoidze, E. Giambattistelli, and R. Cubeddu, "Optical biopsy of bone tissue: a step toward the diagnosis of bone pathologies.," *J. Biomed. Opt.*, vol. 9, no. 3, pp. 474–80, 2004.

[10] R. Arora, G. I. Petrov, V. V. Yakovlev, and M. O. Scully, "Detecting anthrax in the mail by coherent Raman microspectroscopy," *Proc. Natl. Acad. Sci.*, vol. 109, no. 4, pp. 1151–1153, 2012.

[11] R. Arora, G. I. Petrov, V. V. Yakovlev, and M. O. Scully, "Chemical analysis of molecular species through turbid medium," *Anal. Chem.*, vol. 86, no. 3, pp. 1445–1451, 2014.

[12] N. Stone, R. Baker, C. Hart Prieto, and P. Matousek, "Novel Raman signal recovery from deeply buried tissue components," *Proc. SPIE*, vol. 6853, pp. 68530N–1 – 68530N–15, 2008.

[13] K. Tilbury and P. J. Campagnola, "Applications of second-harmonic generation imaging microscopy in ovarian and breast cancer," *Perspect. Medicin. Chem.*, vol. 7, pp. 21–32, 2015.

[14] P. J. Campagnola and L. M. Loew, "Second-harmonic imaging microscopy for visualizing biomolecular arrays in cells, tissues and organisms," *Nat. Biotechnol.*, vol. 21, no. 11, pp. 1356–1360, 2003.

[15] J. R. Mao and J. Bristow, "The Ehlers-Danlos syndrome: on beyond collagens," *J. Clin. Invest.*, vol. 107, no. 9, pp. 1063–9, 2001.

[16] S. M. Weis, J. L. Emery, K. D. Becker, D. J. McBride, J. H. Omens, and A. D. McCulloch, "Myocardial mechanics and collagen structure in the osteogenesis imperfecta murine (oim)," *Circ. Res.*, vol. 87, no. 8, pp. 663–669, 2000.

[17] R. A. R. Rao, M. R. Mehta, and K. C. Toussaint, "Fourier transform-second-harmonic generation imaging of biological tissues," *Opt. Express*, vol. 17, no. 17, pp. 14534–14542, 2009.

[18] C. Eliasson and P. Matousek, "Noninvasive authentication of pharmaceutical products through packaging using spatially offset Raman spectroscopy," *Anal. Chem.*, vol. 79, no. 4, pp. 1696–1701, 2007.

[19] P. Matousek, "Inverse spatially offset Raman spectroscopy for deep noninvasive probing of turbid media," *Appl. Spectrosc.*, vol. 60, no. 11, pp. 1341–1347, 2006.

[20] D. Oelkrug, E. Ostertag, and R. W. Kessler, "Quantitative Raman spectroscopy in turbid matter: Reflection or transmission mode?," *Anal. Bioanal. Chem.*, vol. 405, pp. 3367–3379, 2013.

[21] J. N. Bixler, M. T. Cone, B. H. Hokr, J. D. Mason, E. Figueroa, E. S. Fry, V. V. Yakovlev, and M. O. Scully, "Ultrasensitive detection of waste products in water using fluorescence emission cavity-enhanced spectroscopy.," *Proc. Natl. Acad. Sci.*, vol. 111, no. 20, pp. 7208–11, 2014.

[22] M. T. Cone, J. A. Musser, E. Figueroa, J. D. Mason, and E. S. Fry, "Diffuse reflecting material for integrating cavity spectroscopy, including ring-down spectroscopy," *Appl. Opt.*, vol. 54, no. 2, p. 334, 2015.

[23] B. H. Hokr and V. V. Yakovlev, "Raman signal enhancement via elastic light scattering.," *Opt. Express*, vol. 21, no. 10, pp. 11757–62, 2013.

[24] J. N. Bixler, C. A. Winkler, B. H. Hokr, J. D. Mason, and V. V. Yakovlev, "Utilizing scattering to further enhance integrating cavity-enhanced spectroscopy," *J. Mod. Opt.*, vol. 0340, no. August 2015, pp. 1–4, 2015.

[25] H. C. Van de Hulst, *Light scattering by small particles*. New York: Wiley, 1957.

[26] E. Hecht, *Optics*. Reading, Mass.: Addison-Wesley, 4th ed., 2002.

[27] M. P. Silverman, *Waves and grains: reflections on light and learning*. Princeton, N.J.: Princeton University Press, 1998.

[28] G. G. Stokes, "On the intensity of the light reflected from or transmitted through a pile of plates," *Proc. R. Soc. London*, vol. 11, pp. 545–556, 1862.

[29] L. V. Wang and H.-i. Wu, *Biomedical optics: principles and imaging*. Hoboken, N.J.: Wiley-Interscience, 2007.

[30] A. J. Welch and M. J. C. Van Gemert, *Optical-thermal response of laser-irradiated tissue*. New York: Springer, 2nd ed., 2011.

[31] S. Chandrasekhar, *Radiative transfer*. New York: Dover Publications, Inc., 1960.

[32] M. Fink, "Time-reversed acoustics," *Sci. Am. Inc.*, pp. 91–97, nov 1999.

[33] G. Lerosey, J. De Rosny, A. Tourin, A. Derode, G. Montaldo, and M. Fink, "Time reversal of electromagnetic waves," *Phys. Rev. Lett.*, vol. 92, no. 19, pp. 193904–1, 2004.

[34] R. A. Fisher, *Optical phase conjugation*. New York: Academic Press, 1983.

[35] M. Damzen, "Optical phase conjugation," *Opt. Acta Int. J. Opt.*, vol. 32, no. 6, pp. 639–639, 1985.

[36] A. Yariv, "Phase conjugate optics and realtime holography," *IEEE J. Quantum Electron.*, vol. 14, no. 9, pp. 650–660, 1978.

[37] G. He, "Optical phase conjugation: principles, techniques, and applications," *Prog. Quantum Electron.*, vol. 26, no. 3, pp. 131–191, 2002.

[38] B. Y. Zel'dovich and V. V. Shkunov, "Wavefront reproduction in stimulated Raman scattering," *Sov. J. Quantum Electron1*, vol. 7, no. 5, pp. 610–615, 1977.

[39] B. Y. Zel'dovich, N. A. Mel'nikov, N. F. Pilipetskii, and V. V. Ragul'skii, "Observation of wave-front inversion in stimulated Raman scattering of light," *JETP Lett.*, vol. 25, no. 1, p. 36, 1977.

[40] P. R. Hemmer, D. P. Katz, J. Donoghue, M. S. Shahriar, P. Kumar, and M. Cronin-Golomb, "Efficient low-intensity optical phase conjugation based on coherent population trapping in sodium," *Opt. Lett.*, vol. 20, no. 9, pp. 982–984, 1995.

[41] C.-L. Hsieh, Y. Pu, R. Grange, and D. Psaltis, "Digital phase conjugation of second harmonic radiation emitted by nanoparticles in turbid media," *Opt. Express*, vol. 18, no. 12, pp. 12283–12290, 2010.

[42] Z. Yaqoob, D. Psaltis, M. S. Feld, and C. Yang, "Optical phase conjugation for turbidity suppression in biological samples," *Nat. Photonics*, vol. 2, no. 2, pp. 110–115, 2008.

[43] M. Cui, E. J. McDowell, and C. Yang, "An in vivo study of turbidity suppression by optical phase conjugation (TSOPC) on rabbit ear," *Opt. Express*, vol. 18, no. 1, pp. 25–30, 2010.

[44] X. Xu, H. Liu, and L. V. Wang, "Time-reversed ultrasonically encoded optical focusing into scattering media," *Nat. Photonics*, vol. 5, no. 3, pp. 154–157, 2011.

[45] T. R. Hillman, T. Yamauchi, W. Choi, R. R. Dasari, M. S. Feld, Y. Park, and Z. Yaqoob, "Digital optical phase conjugation for delivering two-dimensional images through turbid media," *Sci. Rep.*, vol. 3, p. 1909, 2013.

[46] D. A. W. Ang, E. D. H. A. Z. Hou, J. O. B. Rake, H. A. R. Uan, M. O. J. Ang, and C. H. Y. Ang, "Focusing through dynamic tissue with millisecond digital optical phase conjugation," *Optica*, vol. 2, no. 8, pp. 728–735, 2015.

[47] C. Prada, "The iterative time reversal process: Analysis of the convergence," *J. Acoust. Soc. Am.*, vol. 97, no. 1, p. 62, 1995.

[48] I. M. Vellekoop and A. P. Mosk, "Phase control algorithms for focusing light through turbid media," *Opt. Commun.*, vol. 281, no. 11, pp. 3071–3080, 2008.

[49] J. Thompson, B. Hokr, and V. Yakovlev, "Optimization of focusing through scattering media using the continuous sequential algorithm," *J. Mod. Opt.*, vol. 63, pp. 80–84, jan 2016.

[50] I. M. Vellekoop, E. G. van Putten, A. Lagendijk, and A. P. Mosk, "Demixing light paths inside disordered metamaterials," *Opt. Express*, vol. 16, no. 1, pp. 67–80, 2008.

[51] G. Ghielmetti and C. M. Aegerter, "Scattered light fluorescence microscopy in three dimensions," *Opt. Express*, vol. 20, no. 4, pp. 110–115, 2012.

[52] G. Ghielmetti and C. M. Aegerter, "Direct imaging of fluorescent structures behind turbid layers.," *Opt. Express*, vol. 22, no. 2, pp. 1981–9, 2014.

[53] I. M. Vellekoop and A. P. Mosk, "Focusing coherent light through opaque strongly scattering media," *Opt. Lett.*, vol. 32, no. 16, pp. 2309–2311, 2007.

[54] I. M. Vellekoop, "Feedback-based wavefront shaping," *Opt. Express*, vol. 23, no. 9, pp. 12189–12206, 2015.

[55] J. W. Goodman, "Some fundamental properties of speckle," *J. Opt. Soc. Am.*, vol. 66, no. 11, p. 1145, 1976.

[56] J. W. Goodman, *Speckle phenomena in optics: Theory and applications*. Englewood, Colo.: Roberts and Company Publishers, 2007.

[57] I. M. Vellekoop, A. Lagendijk, and A. P. Mosk, "Exploiting disorder for perfect focusing," *Nat. Photonics*, vol. 4, no. 5, pp. 320–322, 2010.

[58] S. Feng, C. Kane, P. A. Lee, and A. D. Stone, "Correlations and fluctuations of coherent wave transmission through disordered media," *Phys. Rev. Lett.*, vol. 61, no. 7, pp. 834–837, 1988.

[59] I. Freund, M. Rosenbluh, and S. Feng, "Memory effects in propagation of optical waves through disordered media," *Phys. Rev. Lett.*, vol. 61, no. 20, pp. 2328–2331, 1988.

[60] O. Katz, E. Small, and Y. Silberberg, "Looking around corners and through thin turbid layers in real time with scattered incoherent light," *Nat. Photonics*, vol. 6, pp. 549–553, jul 2012.

[61] N. Konforti, E. Marom, and S. T. Wu, "Phase-only modulation with twisted nematic liquid-crystal spatial light modulators.," *Opt. Lett.*, vol. 13, no. 3, pp. 251–253, 1988.

[62] B. E. A. Saleh and K. Lu, "Theory and design of the liquid crystal TV as an optical spatial phase modulator," *Opt. Eng.*, vol. 29, no. 3, pp. 240–246, 1990.

[63] A. Monmayrant, S. Weber, and B. Chatel, "A newcomer's guide to ultrashort pulse shaping and characterization," *J. Phys. B At. Mol. Opt. Phys.*, vol. 43, p. 103001, may 2010.

[64] A. M. Weiner, "Ultrafast optical pulse shaping: A tutorial review," *Opt. Commun.*, vol. 284, pp. 3669–3692, jul 2011.

[65] A. M. Weiner, "Femtosecond pulse shaping using spatial light modulators," *Rev. Sci. Instrum.*, vol. 71, p. 1929, may 2000.

[66] S. T. Flock, M. S. Patterson, B. C. Wilson, and D. R. Wyman, "Monte Carlo modeling of light propagation in highly scattering tissue - I: Model predictions and com-

parison with diffusion theory," *IEEE Trans. Biomed. Eng.*, vol. 36, no. 12, pp. 1162–1168, 1989.

[67] R. C. Haskell, L. O. Svaasand, T.-T. Tsay, T.-C. Feng, M. S. McAdams, and B. J. Tromberg, "Boundary conditions for the diffusion equation in radiative transfer," *J. Opt. Soc. Am. A*, vol. 11, no. 10, pp. 2727–2741, 1994.

[68] S. Stolik, J. A. Delgado, A. Perez, and L. Anasagasti, "Measurement of the penetration depths of red and near infrared light in human "ex vivo" tissues," *J. Photochem. Photobiol. B Biol.*, vol. 57, no. 2-3, pp. 90–93, 2000.

[69] W. Steinbrecht, K. Rothe, and H. Walther, "Lidar setup for daytime and nighttime probing of stratospheric ozone and measurements in polar and equatorial regions," *Appl. Opt.*, vol. 28, no. 17, pp. 3616–24, 1989.

[70] S. E. Bisson, J. E. Goldsmith, and M. G. Mitchell, "Narrow-band, narrow-field-of-view Raman lidar with combined day and night capability for tropospheric water-vapor profile measurements," *Appl. Opt.*, vol. 38, no. 9, pp. 1841–1849, 1999.

[71] J. Kasparian, M. Rodriguez, G. Méjean, J. Yu, E. Salmon, H. Wille, R. Bourayou, S. Frey, Y. B. Andre, A. Mysyrowicz, R. Sauerbrey, J. P. Wolf, and L. Wöste, "White-light filaments for atmospheric analysis," *Science*, vol. 301, pp. 61–4, jul 2003.

[72] A. Couairon and A. Mysyrowicz, "Femtosecond filamentation in transparent media," *Phys. Rep.*, vol. 441, pp. 47–189, mar 2007.

[73] V. Kocharovsky, S. Cameron, K. Lehmann, R. Lucht, R. Miles, Y. Rostovtsev, W. Warren, G. R. Welch, and M. O. Scully, "Gain-swept superradiance applied to the stand-off detection of trace impurities in the atmosphere," *Proc. Natl. Acad. Sci. U. S. A.*, vol. 102, no. 22, pp. 7806–11, 2005.

[74] P. R. Hemmer, R. B. Miles, P. Polynkin, T. Siebert, A. V. Sokolov, P. Sprangle, and M. O. Scully, "Standoff spectroscopy via remote generation of a backward-propagating laser beam," *Proc. Natl. Acad. Sci. U. S. A.*, vol. 108, pp. 3130–4, feb 2011.

[75] R. Dicke, "Coherence in spontaneous radiation processes," *Phys. Rev.*, vol. 93, no. 1, pp. 99–110, 1954.

[76] N. E. Rehler and J. H. Eberly, "Superradiance," *Phys. Rev. A*, vol. 3, no. 5, pp. 1735–1751, 1971.

[77] R. Bonifacio and L. A. Lugiato, "Cooperative radiation processes in two-level systems: Superfluorescence. II," *Phys. Rev. A*, vol. 12, no. 2, pp. 587–598, 1975.

[78] J. MacGillivray and M. Feld, "Theory of superradiance in an extended, optically thick medium," *Phys. Rev. A*, vol. 14, no. 3, pp. 1169–1189, 1976.

[79] J. Brownell, X. Lu, and S. Hartmann, "Yoked superfluorescence," *Phys. Rev. Lett.*, vol. 75, no. 18, pp. 3265–3268, 1995.

[80] A. Lvovsky, *Omnidirectional superfluorescence transients*. Ph.D. thesis, Columbia University, New York City, NY, 1998.

[81] G. O. Ariunbold, V. A. Sautenkov, Y. V. Rostovtsev, and M. O. Scully, "Ultrafast laser control of backward superfluorescence towards standoff sensing," *Appl. Phys. Lett.*, vol. 104, p. 021114, jan 2014.

[82] A. Dogariu, J. B. Michael, M. O. Scully, and R. B. Miles, "High-gain backward lasing in air.," *Science*, vol. 331, no. 6016, pp. 442–445, 2011.

[83] A. J. Traverso, R. Sanchez-Gonzalez, L. Yuan, K. Wang, D. V. Voronine, A. M. Zheltikov, Y. Rostovtsev, V. A. Sautenkov, A. V. Sokolov, S. W. North, and M. O.

Scully, "Coherence brightened laser source for atmospheric remote sensing," *Proc. Natl. Acad. Sci.*, vol. 109, no. 38, pp. 15185–15190, 2012.

[84] L. Yuan, B. H. Hokr, A. J. Traverso, D. V. Voronine, Y. Rostovtsev, A. V. Sokolov, and M. O. Scully, "Theoretical analysis of the coherence-brightened laser in air," *Phys. Rev. A*, vol. 87, p. 023826, feb 2013.

[85] N. Ageorges and C. Dainty, *Laser guide star adaptive optics for astronomy*. Dordrecht: Springer Science & Business Media, 2013.

[86] J. Biegert and J.-C. Diels, "Feasibility study to create a polychromatic guidestar in atomic sodium," *Phys. Rev. A*, vol. 67, p. 043403, apr 2003.

[87] R. Foy, M. Chatagnat, D. Dubet, P. Éric, J. Eysseric, F.-C. Foy, T. Fusco, J. Girard, A. Laloge, A. Le van Suu, B. Messaoudi, S. Perruchot, P. Richaud, Y. Richaud, X. Rondeau, M. Tallon, É. Thiébaut, and M. Boër, "The polychromatic laser guide star for the tilt measurement. Progress report of the demonstrator at Observatoire de Haute Provence," *Proc. SPIE*, vol. 6691, p. 66910R, 2007.

[88] J.-P. Pique, I. C. Moldovan, and V. Fesquet, "Concept for polychromatic laser guide stars: one-photon excitation of the 4P3/2 level of a sodium atom.," *J. Opt. Soc. Am. A, Opt. image Sci. Vis.*, vol. 23, pp. 2817–28, nov 2006.

[89] H. Guillet de Chatellus, J.-P. Pique, and I. C. Moldovan, "Return flux budget of polychromatic laser guide stars.," *J. Opt. Soc. Am. A*, vol. 25, pp. 400–15, feb 2008.

[90] D. Hite, "Construction of a heat pipe oven on a small budget," *Am. J. Phys.*, vol. 65, no. 10, p. 1017, 1997.

[91] T. T. Grove, W. a. Hockensmith, N. Cheviron, W. Grieser, R. Dill, and M. F. Masters, "Construction of an inexpensive copper heat-pipe oven," *Eur. J. Phys.*, vol. 30, pp. 1229–1237, nov 2009.

[92] Z. Ficek, R. Tanas, and S. Kielich, "Cooperative effects in the spontaneous emission from two non-identical atoms," *Opt. Acta (Lond).*, vol. 33, no. 9, pp. 1149–1160, 1986.

[93] G. O. Ariunbold, M. M. Kash, V. a. Sautenkov, H. Li, Y. V. Rostovtsev, G. R. Welch, and M. O. Scully, "Observation of picosecond superfluorescent pulses in rubidium atomic vapor pumped by 100-fs laser pulses," *Phys. Rev. A*, vol. 82, p. 043421, oct 2010.

[94] M. Sargent III, M. O. Scully, and W. E. Lamb Jr, *Laser physics*. Reading, Mass.: Addison-Wesley, 1974.

[95] G. O. Ariunbold, V. a. Sautenkov, and M. O. Scully, "Quantum fluctuations of superfluorescence delay observed with ultrashort optical excitations," *Phys. Lett. A*, vol. 376, pp. 335–338, jan 2012.

[96] Q. H. F. Vrehen and J. J. Der Weduwe, "Quantum fluctuations in superfluorescence delay times," *Phys. Rev. A*, vol. 24, no. 5, pp. 2857–2860, 1981.

[97] V. Degiorgio, "Statistical properties of superradiant pulses," *Opt. Commun.*, vol. 2, no. 8, pp. 362–364, 1971.

[98] J. Bertolotti, E. G. van Putten, C. Blum, A. Lagendijk, W. L. Vos, and A. P. Mosk, "Non-invasive imaging through opaque scattering layers," *Nature*, vol. 491, no. 7423, pp. 232–4, 2012.

[99] O. Katz, P. Heidmann, M. Fink, and S. Gigan, "Non-invasive single-shot imaging through scattering layers and around corners via speckle correlations," *Nat. Photonics*, vol. 8, pp. 784–790, aug 2014.

[100] P. Lai, L. Wang, J. W. Tay, and L. V. Wang, "Photoacoustically guided wavefront shaping for enhanced optical focusing in scattering media," *Nat. Photonics*, vol. 9,

no. 2, pp. 126–132, 2015.

[101] B. Judkewitz, Y. Wang, and R. Horstmeyer, "Speckle-scale focusing in the diffusive regime with time reversal of variance-encoded light (TROVE)," *Nat. Photonics*, vol. 7, no. 4, pp. 300–305, 2013.

[102] A. P. Mosk, A. Lagendijk, G. Lerosey, and M. Fink, "Controlling waves in space and time for imaging and focusing in complex media," *Nat. Photonics*, vol. 6, no. 5, pp. 283–292, 2012.

[103] O. Katz, E. Small, Y. Bromberg, and Y. Silberberg, "Focusing and compression of ultrashort pulses through scattering media," *Nat. Photonics*, vol. 5, pp. 372–377, may 2011.

[104] J.-H. Park, C. Park, H. Yu, Y.-H. Cho, and Y. Park, "Dynamic active wave plate using random nanoparticles," *Opt. Express*, vol. 20, no. 15, pp. 17010–17016, 2012.

[105] J.-H. Park, C. Park, H. Yu, Y.-H. Cho, and Y. Park, "Active spectral filtering through turbid media," *Opt. Lett.*, vol. 37, no. 15, pp. 3261–3263, 2012.

[106] B. H. Hokr, J. N. Bixler, G. D. Noojin, R. J. Thomas, B. A. Rockwell, V. V. Yakovlev, and M. O. Scully, "Single-shot stand-off chemical identification of powders using random Raman lasing," *Proc. Natl. Acad. Sci.*, vol. 111, no. 34, pp. 12320–12324, 2014.

[107] B. H. Hokr, J. N. Bixler, M. T. Cone, J. D. Mason, H. T. Beier, G. D. Noojin, G. I. Petrov, L. A. Golovan, R. J. Thomas, B. A. Rockwell, and V. V. Yakovlev, "Bright emission from a random Raman laser.," *Nat. Commun.*, vol. 5, p. 4356, 2014.

[108] S. M. Popoff, A. Goetschy, S. F. Liew, A. D. Stone, and H. Cao, "Coherent control of total transmission of light through disordered media," *Phys. Rev. Lett.*, vol. 112, no. 13, p. 133903, 2014.

[109] T. Chaigne, O. Katz, A. C. Boccara, M. Fink, E. Bossy, and S. Gigan, "Controlling light in scattering media non-invasively using the photoacoustic transmission matrix," *Nat. Photonics*, vol. 8, pp. 58–64, nov 2014.

[110] S. M. Popoff, G. Lerosey, M. Fink, A. C. Boccara, and S. Gigan, "Controlling light through optical disordered media: Transmission matrix approach," *New J. Phys.*, vol. 13, no. 12, p. 123021, 2011.

[111] S. Popoff, G. Lerosey, M. Fink, A. C. Boccara, and S. Gigan, "Image transmission through an opaque material," *Nat. Commun.*, vol. 1, p. 81, 2010.

[112] J. Yoon, K. Lee, J. Park, and Y. Park, "Measuring optical transmission matrices by wavefront shaping," *arXiv Prepr. arXiv 1502.04761*, 2015.

[113] D. B. Conkey, A. N. Brown, A. M. Caravaca-Aguirre, and R. Piestun, "Genetic algorithm optimization for focusing through turbid media in noisy environments," *Opt. Express*, vol. 20, no. 5, pp. 4840–4849, 2012.

[114] Y. M. Wang, B. Judkewitz, C. A. DiMarzio, and C. Yang, "Deep-tissue focal fluorescence imaging with digitally time-reversed ultrasound-encoded light," *Nat. Commun.*, vol. 3, p. 928, 2012.

[115] M. Draijer, E. Hondebrink, T. Van Leeuwen, and W. Steenbergen, "Review of laser speckle contrast techniques for visualizing tissue perfusion," *Lasers Med. Sci.*, vol. 24, no. 4, pp. 639–651, 2009.

[116] Z. Hajjarian, J. Xi, F. a. Jaffer, G. J. Tearney, and S. K. Nadkarni, "Intravascular laser speckle imaging catheter for the mechanical evaluation of the arterial wall," *J. Biomed. Opt.*, vol. 16, no. 2, p. 026005, 2011.

[117] D. C. Harris, *Quantitative chemical analysis*. New York: W. H. Freeman and Company, 2010.

[118] C. H. Camp Jr and M. T. Cicerone, "Chemically sensitive bioimaging with coherent Raman scattering," *Nat. Photonics*, vol. 9, no. 5, pp. 295–305, 2015.

[119] A. J. Traverso, J. V. Thompson, Z. A. Steelman, Z. Meng, M. O. Scully, and V. V. Yakovlev, "Dual Raman-Brillouin microscope for chemical and mechanical characterization and imaging," *Anal. Chem.*, vol. 87, no. 15, pp. 7519–7523, 2015.

[120] E. B. Hanlon, R. Manoharan, T. W. Koo, K. E. Shafer, J. T. Motz, M. Fitzmaurice, J. R. Kramer, I. Itzkan, R. R. Dasari, and M. S. Feld, "Prospects for in vivo Raman spectroscopy," *Phys. Med. Biol.*, vol. 45, no. 2, pp. R1–R59, 2000.

[121] G. I. Petrov, R. Arora, V. V. Yakovlev, X. Wang, A. V. Sokolov, and M. O. Scully, "Comparison of coherent and spontaneous Raman microspectroscopies for noninvasive detection of single bacterial endospores," *Proc. Natl. Acad. Sci.*, vol. 104, no. 19, pp. 7776–7779, 2007.

[122] A. Campion and P. Kambhampati, "Surface-enhanced Raman scattering," *Chem. Soc. Rev.*, vol. 27, pp. 241–250, 1998.

[123] J. N. Bixler and V. V. Yakovlev, "A new SERS: scattering enhanced Raman scattering," *Proc. SPIE*, vol. 8939, p. 893909, 2014.

[124] H. Cao, Y. Zhao, S. Ho, E. Seelig, Q. Wang, and R. Chang, "Random laser action in semiconductor powder," *Phys. Rev. Lett.*, vol. 82, no. 11, pp. 2278–2281, 1999.

[125] I. M. Vellekoop and A. P. Mosk, "Universal optimal transmission of light through disordered materials," *Phys. Rev. Lett.*, vol. 101, no. 12, pp. 1–4, 2008.

[126] M. Cui, "Parallel wavefront optimization method for focusing light through random scattering media," *Opt. Lett.*, vol. 36, no. 6, pp. 870–872, 2011.

[127] H. Yu, J. Park, K. Lee, J. Yoon, K. Kim, S. Lee, and Y. Park, "Recent advances in wavefront shaping techniques for biomedical applications," *Curr. Appl. Phys.*, vol. 15, no. 5, pp. 632–641, 2015.

[128] I. M. Vellekoop and C. M. Aegerter, "Scattered light fluorescence microscopy: imaging through turbid layers," *Opt. Lett.*, vol. 35, no. 8, pp. 1245–1247, 2010.

[129] S. J. Kirkpatrick, D. D. Duncan, and E. M. Wells-Gray, "Detrimental effects of speckle-pixel size matching in laser speckle contrast imaging," *Opt. Lett.*, vol. 33, no. 24, pp. 2886–2888, 2008.

[130] Q. Li, B. J. Lee, Z. M. Zhang, and D. W. Allen, "Light scattering of semitransparent sintered polytetrafluoroethylene films," *J. Biomed. Opt.*, vol. 13, no. 5, p. 054064, 2010.

[131] S. P. S. Porto, P. a. Fleury, and T. C. Damen, "Raman Spectra of TiO_2, MgF_2, ZnF_2, FeF_2, and MnF_2," *Phys. Rev.*, vol. 154, no. 2, pp. 522–526, 1967.

[132] J. M. Ralston and R. K. Chang, "Spontaneous-raman-scattering efficiency and stimulated scattering in silicon," *Phys. Rev. B*, vol. 2, no. 6, pp. 1858–1862, 1970.

[133] C. Ma, F. Zhou, Y. Liu, and L. V. Wang, "Single-exposure optical focusing inside scattering media using binarized time-reversed adapted perturbation," *Optica*, vol. 2, no. 10, pp. 869–876, 2015.

[134] O. Katz, E. Small, Y. Guan, and Y. Silberberg, "Noninvasive nonlinear focusing and imaging through strongly scattering turbid layers," *Optica*, vol. 1, no. 3, pp. 170–174, 2014.

[135] P. A. Franken, A. E. Hill, C. W. Peters, and G. Weinreich, "Generation of optical harmonics," *Phys. Rev. Lett.*, vol. 7, no. 4, pp. 118–119, 1961.

[136] Y. R. Shen, "Surface properties probed by second-harmonic and sum-frequency generation," *Nature*, vol. 337, no. 6207, pp. 519–525, 1989.

[137] R. Corn, "Optical second harmonic generation as a probe of surface chemistry," *Chem. Rev.*, vol. 25, no. 6, pp. 411–3, 1994.

[138] K. B. Eisenthal, "Liquid interfaces probed by second-harmonic and sum-frequency spectroscopy," *Chem. Rev.*, vol. 96, no. 4, pp. 1343–1360, 1996.

[139] S. I. Stupp, "Supramolecular materials: self-organized nanostructures," *Science*, vol. 276, no. 5311, pp. 384–389, 1997.

[140] R. M. Williams, W. R. Zipfel, and W. W. Webb, "Interpreting second-harmonic generation images of collagen I fibrils," *Biophys. J.*, vol. 88, no. 2, pp. 1377–86, 2005.

[141] A. Zoumi, A. Yeh, and B. J. Tromberg, "Imaging cells and extracellular matrix in vivo by using second-harmonic generation and two-photon excited fluorescence," *Proc. Natl. Acad. Sci. U. S. A.*, vol. 99, no. 17, pp. 11014–9, 2002.

[142] E. Brown, T. McKee, E. DiTomaso, A. Pluen, B. Seed, Y. Boucher, and R. Jain, "Dynamic imaging of collagen and its modulation in tumors in vivo using second-harmonic generation," *Nat. Med.*, vol. 9, no. 6, pp. 796–800, 2003.

[143] X. Chen, O. Nadiarynkh, S. Plotnikov, and P. J. Campagnola, "Second harmonic generation microscopy for quantitative analysis of collagen fibrillar structure," *Nat. Protoc.*, vol. 7, no. 4, pp. 654–669, 2012.

[144] T. A. Driscoll, P. E. Perkins, H. J. Hoffman, and R. E. Stone, "Efficient second-harmonic generation in KTP crystals," *J. Opt. Soc. Am. B*, vol. 3, no. 5, p. 683, 1986.

[145] V. Dmitriev, G. Gurzadyan, and D. Nikogosyan, *Handbook of nonlinear optical crystals*. Berlin: Springer-Verlag, 1991.

[146] Y. Shen, *The principles of nonlinear optics*. New York: Wiley, 1984.

[147] J. Reintjes and R. C. Eckardt, "Efficient harmonic generation from 532 to 266 nm in ADP and KD*P," *Appl. Phys. Lett.*, vol. 30, no. 2, pp. 91–93, 1977.

[148] B.-Q. Chen, M.-L. Ren, R.-J. Liu, C. Zhang, Y. Sheng, B.-Q. Ma, and Z.-Y. Li, "Simultaneous broadband generation of second and third harmonics from chirped nonlinear photonic crystals," *Light Sci. Appl.*, vol. 3, no. 7, p. e189, 2014.

[149] D. H. Jundt, G. A. Magel, M. M. Fejer, and R. L. Byer, "Periodically poled LiNbO3 for high-efficiency second-harmonic generation," *Appl. Phys. Lett.*, vol. 59, no. 21, pp. 2657–2659, 1991.

[150] L. Sacconi, D. a. Dombeck, and W. W. Webb, "Overcoming photodamage in second-harmonic generation microscopy: real-time optical recording of neuronal action potentials," *Proc. Natl. Acad. Sci.*, vol. 103, no. 9, pp. 3124–3129, 2006.

[151] J. A. Armstrong, B. N., D. J., and P. S. Pershan, "Interactions between Light Waves in a Nonlinear Dielectric," *Phys. Rev.*, vol. 127, no. 6, pp. 1918–1939, 1962.

[152] R. W. Boyd, *Nonlinear Optics*. Burlington, MA: Academic Press, 3rd ed., 2008.

[153] S. C. Sheng and A. E. Siegman, "Nonlinear-optical calculations using fast-transform methods: Second-harmonic generation with depletion and diffraction," *Phys. Rev. A*, vol. 21, no. 2, pp. 599–606, 1980.

[154] M. A. Dreger and J. K. McIver, "Second-harmonic generation in a nonlinear, anisotropic medium with diffraction and depletion," *J. Opt. Soc. Am. B*, vol. 7, no. 5, p. 776, 1990.

[155] H. Frostig, E. Small, S. Derevyanko, and Y. Silberberg, "Focusing coherent light through a nonlinear scattering medium," *arXiv:1607.08105*, 2016.

[156] G. D. Boyd and D. A. Kleinman, "Parametric interaction of focused Gaussian light beams," *J. Appl. Phys.*, vol. 39, no. 8, pp. 3597–3639, 1968.

[157] A. A. Asatryan, C. J. R. Sheppard, and C. M. de Sterke, "Vector treatment of second-harmonic generation produced by tightly focused vignetted Gaussian beams," *J. Opt. Soc. Am. B*, vol. 21, no. 12, p. 2206, 2004.

[158] J. Arlt, K. Dholakia, L. Allen, and M. Padgett, "Efficiency of second-harmonic generation with Bessel beams," *Phys. Rev. A*, vol. 60, no. 3, pp. 2438–2441, 1999.

[159] K. Shinozaki, C.-Q. Xu, H. Sasaki, and T. Kamijoh, "A comparison of optical second-harmonic generation efficiency using Bessel and Gaussian beams in bulk crystals," *Opt. Commun.*, vol. 133, no. 1-6, pp. 300–304, 1997.

[160] T. A. Planchon, L. Gao, D. E. Milkie, M. W. Davidson, J. A. Galbraith, C. G. Galbraith, and E. Betzig, "Rapid three-dimensional isotropic imaging of living cells using Bessel beam plane illumination," *Nat. Methods*, vol. 8, no. 5, pp. 417–423, 2011.

[161] H. Wang, L. Shi, B. Lukyanchuk, C. Sheppard, and C. T. Chong, "Creation of a needle of longitudinally polarized light in vacuum using binary optics," *Nat. Photonics*, vol. 2, no. 8, pp. 501–505, 2008.

[162] N. B. Abraham and W. J. Firth, "Overview of transverse effects in nonlinear-optical systems," *J. Opt. Soc. Am. B*, vol. 7, no. 6, p. 951, 1990.

[163] V. Magni, "Optimum beam for second harmonic generation," *Opt. Commun.*, vol. 176, no. 1, pp. 245–251, 2000.

[164] S. Keren-Zur, O. Avayu, L. Michaeli, and T. Ellenbogen, "Nonlinear beam shaping with plasmonic metasurfaces," *ACS Photonics*, vol. 3, pp. 117–123, 2016.

[165] N. Westerberg, C. Maitland, D. Faccio, K. Wilson, P. Öhberg, and E. M. Wright, "Synthetic magnetism for photon fluids," *Phys. Rev. A*, vol. 94, p. 023805, 2016.

[166] R. Iliew, C. Etrich, T. Pertsch, F. Lederer, and Y. S. Kivshar, "Huge enhancement of backward second-harmonic generation with slow light in photonic crystals," *Phys. Rev. A*, vol. 81, pp. 1–10, 2010.

[167] A. V. Smith and M. S. Bowers, "Phase distortions in sum- and difference-frequency mixing in crystals," *J. Opt. Soc. Am. B*, vol. 12, no. 1, p. 49, 1995.

[168] S. Lightman, R. Gvishi, G. Hurvitz, and A. Arie, "Shaping of light beams by 3D direct laser writing on facets of nonlinear crystals," *Opt. Lett.*, vol. 40, no. 19, p. 4460, 2015.

[169] X. H. Hong, B. Yang, C. Zhang, Y. Q. Qin, and Y. Y. Zhu, "Nonlinear volume holography for wave-front engineering," *Phys. Rev. Lett.*, vol. 113, no. 16, pp. 1–5, 2014.

[170] S. Trajtenberg-Mills, I. Juwiler, and A. Arie, "On-axis shaping of second-harmonic beams," *Laser Photonics Rev.*, vol. 44, no. 6, pp. 40–44, 2015.

[171] A. Libster-hershko, S. Trajtenberg-mills, and A. Arie, "Dynamic control of light beams in second harmonic generation," *Opt. Lett.*, vol. 40, no. 9, pp. 1944–1947, 2015.

[172] J. V. Thompson, G. A. Throckmorton, B. H. Hokr, and V. V. Yakovlev, "Wave-front shaping enhanced Raman scattering in a turbid medium," *Opt. Lett.*, vol. 41, pp. 1769–1772, apr 2016.

[173] D. A. Kleinman, "Theory of second harmonic generation of light," *Phys. Rev.*, vol. 128, pp. 1761–1775, nov 1962.

[174] A. M. Weiner, *Ultrafast optics*. Hoboken, N.J.: Wiley, 2009.

[175] L. Bergé, S. Skupin, R. Nuter, J. Kasparian, and J.-P. Wolf, "Ultrashort filaments of light in weakly ionized, optically transparent media," *Reports Prog. Phys.*, vol. 70, pp. 1633–1713, oct 2007.

[176] O. Wada, "Femtosecond all-optical devices for ultrafast communication and signal processing," *New J. Phys.*, vol. 6, pp. 1–35, 2004.

[177] F. Courvoisier, V. Boutou, J. Kasparian, E. Salmon, G. Méjean, J. Yu, and J. P. Wolf, "Ultraintense light filaments transmitted through clouds," *Appl. Phys. Lett.*, vol. 83, no. 2, pp. 213–215, 2003.

[178] B. Kohler, V. V. Yakovlev, J. Che, J. L. Krause, M. Messina, K. R. Wilson, N. Schwentner, R. M. Whitnell, and Y. Yan, "Quantum control of wave packet evolution with tailored femtosecond pulses," *Phys. Rev. Lett.*, vol. 74, no. 17, pp. 3360–3363, 1995.

[179] C. J. Bardeen, V. V. Yakovlev, K. R. Wilson, S. D. Carpenter, P. M. Weber, and W. S. Warren, "Feedback quantum control of molecular electronic population transfer," *Chem. Phys. Lett.*, vol. 280, pp. 151–158, 1997.

[180] T. Udem, R. Holzwarth, and T. W. Hänsch, "Optical frequency metrology," *Nature*, vol. 416, no. 6877, pp. 233–237, 2002.

[181] R. R. Gattass and E. Mazur, "Femtosecond laser micromachining in transparent materials," *Nat. Photonics*, vol. 2, no. 4, pp. 219–225, 2008.

[182] M. O. Scully, G. W. Kattawar, R. P. Lucht, T. Opatrny, H. Pilloff, A. Rebane, A. V. Sokolov, and M. S. Zubairy, "FAST CARS: engineering a laser spectroscopic tech-

nique for rapid identification of bacterial spores," *Proc. Natl. Acad. Sci.*, vol. 99, no. 17, pp. 10994–1001, 2002.

[183] D. Pestov, R. K. Murawski, G. O. Ariunbold, X. Wang, M. Zhi, A. V. Sokolov, V. A. Sautenkov, Y. V. Rostovtsev, A. Dogariu, Y. Huang, and M. O. Scully, "Optimizing the laser-pulse configuration for coherent Raman spectroscopy," *Science*, vol. 316, no. 5822, pp. 265–268, 2007.

[184] S. A. Diddams, L. Hollberg, and V. Mbele, "Molecular fingerprinting with the resolved modes of a femtosecond laser frequency comb," *Nature*, vol. 445, no. 7128, pp. 627–630, 2007.

[185] A. Braun, G. Korn, X. Liu, D. Du, J. Squier, and G. Mourou, "Self-channeling of high-peak-power femtosecond laser pulses in air," *Opt. Lett.*, vol. 20, p. 73, jan 1995.

[186] S. L. Chin, T. J. Wang, C. Marceau, J. Wu, J. S. Liu, O. Kosareva, N. Panov, Y. P. Chen, J. F. Daigle, S. Yuan, A. Azarm, W. W. Liu, T. Seideman, H. P. Zeng, M. Richardson, R. Li, and Z. Z. Xu, "Advances in intense femtosecond laser filamentation in air," *Laser Phys.*, vol. 22, pp. 1–53, sep 2011.

[187] A. Brodeur, F. Ilkov, and S. Chin, "Beam filamentation and the white light continuum divergence," *Opt. Commun.*, vol. 129, pp. 193–198, aug 1996.

[188] A. Dubietis, G. Tamošauskas, I. Diomin, and A. Varanavičius, "Self-guided propagation of femtosecond light pulses in water," *Opt. Lett.*, vol. 28, p. 1269, jul 2003.

[189] S. Tzortzakis, L. Sudrie, M. Franco, B. Prade, A. Mysyrowicz, A. Couairon, and L. Bergé, "Self-guided propagation of ultrashort IR laser pulses in fused silica," *Phys. Rev. Lett.*, vol. 87, p. 213902, nov 2001.

[190] I. Dicaire, V. Jukna, C. Praz, C. Milián, L. Summerer, and A. Couairon, "Space-borne laser filamentation for atmospheric remote sensing," *Laser & Photonics Rev.*, vol. 10, no. 3, pp. 481–493, 2016.

[191] K. Stelmaszczyk, P. Rohwetter, G. Méjean, J. Yu, E. Salmon, J. Kasparian, R. Ackermann, J.-P. Wolf, and L. Wöste, "Long-distance remote laser-induced breakdown spectroscopy using filamentation in air," *Appl. Phys. Lett.*, vol. 85, no. 18, p. 3977, 2004.

[192] K. Wang, B. D. Strycker, D. V. Voronine, P. K. Jha, M. O. Scully, R. E. Meyers, P. Hemmer, and A. V. Sokolov, "Remote sub-diffraction imaging with femtosecond laser filaments," *Opt. Lett.*, vol. 37, pp. 1343–5, apr 2012.

[193] M. Rodriguez, R. Sauerbrey, H. Wille, L. Wöste, T. Fujii, Y.-B. André, A. Mysyrowicz, L. Klingbeil, K. Rethmeier, W. Kalkner, J. Kasparian, E. Salmon, J. Yu, and J.-P. Wolf, "Triggering and guiding megavolt discharges by use of laser-induced ionized filaments," *Opt. Lett.*, vol. 27, pp. 772–4, may 2002.

[194] C. P. Hauri, W. Kornelis, F. W. Helbing, A. Heinrich, A. Couairon, A. Mysyrowicz, J. Biegert, and U. Keller, "Generation of intense, carrier-envelope phase-locked few-cycle laser pulses through filamentation," *Appl. Phys. B*, vol. 79, no. 6, pp. 673–677, 2004.

[195] A. Couairon, M. Franco, A. Mysyrowicz, J. Biegert, and U. Keller, "Pulse self-compression to the single-cycle limit by filamentation in a gas with a pressure gradient," *Opt. Lett.*, vol. 30, no. 19, p. 2657, 2005.

[196] S. Skupin, G. Stibenz, L. Bergé, F. Lederer, T. Sokollik, M. Schnürer, N. Zhavoronkov, and G. Steinmeyer, "Self-compression by femtosecond pulse filamentation: Experiments versus numerical simulations," *Phys. Rev. E*, vol. 74, no. 5, pp. 1–9, 2006.

[197] E. T. J. Nibbering, P. F. Curley, G. Grillon, B. S. Prade, M. A. Franco, F. Salin, and A. Mysyrowicz, "Conical emission from self-guided femtosecond pulses in air," *Opt. Lett.*, vol. 21, p. 62, jan 1996.

[198] A. Dubietis, A. Couairon, E. Kučinskas, G. Tamošauskas, E. Gaižauskas, D. Faccio, and P. Di Trapani, "Measurement and calculation of nonlinear absorption associated with femtosecond filaments in water," *Appl. Phys. B*, vol. 84, pp. 439–446, may 2006.

[199] A. L. Gaeta, "Collapsing light really shines," *Science*, vol. 301, pp. 54–5, jul 2003.

[200] B. La Fontaine, F. Vidal, Z. Jiang, C. Y. Chien, D. Comtois, A. Desparois, T. W. Johnston, J.-C. Kieffer, H. Pépin, and H. P. Mercure, "Filamentation of ultrashort pulse laser beams resulting from their propagation over long distances in air," *Phys. Plasmas*, vol. 6, no. 5, p. 1615, 1999.

[201] W. S. Warren, W. Wagner, and T. Ye, "The prospects for high resolution optical brain imaging: the magnetic resonance perspective," *Magn. Reson. Imaging*, vol. 21, pp. 1225–1233, dec 2003.

[202] M. C. Fischer, T. Ye, G. Yurtsever, A. Miller, M. Ciocca, W. Wagner, and W. S. Warren, "Two-photon absorption and self-phase modulation measurements with shaped femtosecond laser pulses," *Opt. Lett.*, vol. 30, p. 1551, jun 2005.

[203] A. V. Sokolov, L. M. Naveira, M. P. Poudel, J. Strohaber, C. S. Trendafilova, W. C. Buck, J. Wang, B. D. Strycker, C. Wang, H. Schuessler, A. Kolomenskii, and G. W. Kattawar, "Propagation of ultrashort laser pulses in water: linear absorption and onset of nonlinear spectral transformation," *Appl. Opt.*, vol. 49, pp. 513–9, jan 2010.

[204] A. Präkelt, M. Wollenhaupt, C. Sarpe-Tudoran, A. Assion, and T. Baumert, "Filling a spectral hole via self-phase modulation," *Appl. Phys. Lett.*, vol. 87, no. 12,

p. 121113, 2005.

[205] D. R. Austin, J. A. Bolger, C. M. De Sterke, B. J. Eggleton, and T. G. Brown, "Narrowband supercontinuum control using phase shaping," *Opt. Express*, vol. 14, no. 26, pp. 13142–13150, 2006.

[206] S. Skupin, R. Nuter, and L. Bergé, "Optical femtosecond filaments in condensed media," *Phys. Rev. A - At. Mol. Opt. Phys.*, vol. 74, no. 4, pp. 1–6, 2006.

[207] M. Kolesik, E. M. Wright, and J. V. Moloney, "Dynamic nonlinear X waves for femtosecond pulse propagation in water," *Phys. Rev. Lett.*, vol. 92, no. 25 I, pp. 253901–1, 2004.

[208] T. Brabec and F. Krausz, "Nonlinear optical pulse propagation in the single-cycle regime," *Phys. Rev. Lett.*, vol. 78, pp. 3282–3285, apr 1997.

[209] P. A. Zhokhov and A. M. Zheltikov, "Attosecond shock waves," *Phys. Rev. Lett.*, vol. 110, no. 18, pp. 1–5, 2013.

[210] G. M. Hale and M. R. Querry, "Optical constants of water in the 200-nm to 200-μm wavelength region," *Appl. Opt.*, vol. 12, no. 3, p. 555, 1973.

[211] W. Liu, O. Kosareva, I. S. Golubtsov, A. Iwasaki, A. Becker, V. P. Kandidov, and S. L. Chin, "Femtosecond laser pulse filamentation versus optical breakdown in H_2O," *Appl. Phys. B*, vol. 76, pp. 215–229, mar 2003.

[212] A. M. Perelomov, V. S. Popov, and M. V. Terent'ev, "Ionization of atoms in an alternating electric field," *Sov. Phys. JETP*, vol. 23, no. 5, p. 924, 1966.

[213] V. S. Popov, "Tunnel and multiphoton ionization of atoms and ions in a strong laser field (Keldysh theory)," *Physics-Uspekhi*, vol. 47, pp. 855–885, sep 2004.

[214] Y. Chen, F. Théberge, C. Marceau, H. Xu, N. Aközbek, O. Kosareva, and S. L. Chin, "Observation of filamentation-induced continuous self-frequency down shift in air," *Appl. Phys. B*, vol. 91, no. 2, pp. 219–222, 2008.

[215] B. M. Penetrante, J. N. Bardsley, W. M. Wood, C. W. Sliders, and M. C. Downer, "Ionization-induced frequency shifts in intense femtosecond laser pulses," *J. Opt. Soc. Am. B*, vol. 9, no. 11, pp. 2032–2040, 1992.

[216] A. W. Czarnik, "A sense for landmines," *Nature*, vol. 394, no. July, pp. 417–418, 1998.

[217] Y. Geng, M. A. Ali, A. J. Clulow, S. Fan, P. L. Burn, I. R. Gentle, P. Meredith, and P. E. Shaw, "Unambiguous detection of nitrated explosive vapours by fluorescence quenching of dendrimer films," *Nat. Commun.*, vol. 6, p. 8240, 2015.

[218] S. Ben-Jaber, W. J. Peveler, R. Quesada-Cabrera, E. Cortés, C. Sotelo-Vazquez, N. Abdul-Karim, S. A. Maier, and I. P. Parkin, "Photo-induced enhanced Raman spectroscopy for universal ultra-trace detection of explosives, pollutants and biomolecules," *Nat. Commun.*, vol. 7, no. May, p. 12189, 2016.

[219] B. J. Battersby, G. A. Lawrie, A. P. R. Johnston, and M. Trau, "Optical barcoding of colloidal suspensions: applications in genomics, proteomics and drug discovery," *Chem. Commun.*, no. 14, pp. 1435–41, 2002.

[220] A. Extance, "Laser weapons get real," *Nature*, vol. 521, no. 7553, pp. 408–410, 2015.

[221] M. G. B. O. Regan, "Estimation of new production in the ocean by compound remote sensing," *Nature*, vol. 353, no. September 1991, pp. 129–133, 1991.

[222] J. Yang, P. Gong, R. Fu, M. Zhang, J. Chen, S. Liang, B. Xu, J. Shi, and R. Dickinson, "The role of satellite remote sensing in climate change studies," *Nat. Clim.*

Chang., vol. 4, no. 1, pp. 74–74, 2014.

[223] J. W. Hardy, "Adaptive Optics," *Sci. Am.*, vol. 270, no. 6, pp. 60–65, 1994.

[224] C. Cunningham, "Future optical technologies for telescopes," *Nat. Photonics*, vol. 3, no. 5, pp. 239–241, 2009.

[225] A. B. Davis, "Multiple-scattering lidar from both sides of the clouds: Addressing internal structure," *J. Geophys. Res. Atmos.*, vol. 113, no. 14, pp. 1–16, 2008.

[226] V. Backman, M. B. Wallace, L. T. Perelman, J. T. Arendt, R. Gurjar, M. G. Müller, Q. Zhang, G. Zonios, E. Kline, J. a. McGilligan, S. Shapshay, T. Valdez, K. Badizadegan, J. M. Crawford, M. Fitzmaurice, S. Kabani, H. S. Levin, M. Seiler, R. R. Dasari, I. Itzkan, J. Van Dam, and M. S. Feld, "Detection of preinvasive cancer cells.," *Nature*, vol. 406, no. 6791, pp. 35–36, 2000.

[227] T. Sugiura, D. Matsuki, J. Okajima, A. Komiya, S. Mori, S. Maruyama, and T. Kodama, "Photothermal therapy of tumors in lymph nodes using gold nanorods and near-infrared laser light with controlled surface cooling," *Nano Res.*, vol. 8, no. 12, pp. 3842–3852, 2015.

[228] J. Yoon, M. Lee, K. Lee, N. Kim, J. M. Kim, J. Park, H. Yu, C. Choi, W. D. Heo, and Y. Park, "Optogenetic control of cell signaling pathway through scattering skull using wavefront shaping," *Sci. Rep.*, vol. 5, no. August, p. 13289, 2015.

[229] K. Kong, C. Kendall, N. Stone, and I. Notingher, "Raman spectroscopy for medical diagnostics - From in-vitro biofluid assays to in-vivo cancer detection," *Adv. Drug Deliv. Rev.*, vol. 89, pp. 121–134, 2015.

[230] D. J. Harrison, K. Fluri, K. Seiler, Z. Fan, C. S. Effenhauser, and A. Manz, "Micromachining a miniaturized capillary electrophoresis-based chemical analysis system on a chip," *Science*, vol. 261, no. SEPTEMBER, pp. 895–897, 1993.

[231] R. Sarma, A. Yamilov, S. Petrenko, Y. Bromberg, and H. Cao, "Control of energy density inside disordered medium by coupling to open or closed channels," *Phys. Rev. Lett.*, vol. 117, p. 086803, 2016.

[232] K. Vynck, M. Burresi, F. Riboli, and D. S. Wiersma, "Photon management in two-dimensional disordered media," *Nat. Mater.*, vol. 11, no. 12, pp. 1017–1022, 2012.

[233] D. S. Wiersma, "Disordered photonics," *Nat. Photonics*, vol. 7, pp. 188–196, feb 2013.

[234] S. A. Carp, S. A. Prahl, and V. Venugopalan, "Radiative transport in the delta-P1 approximation: accuracy of fluence rate and optical penetration depth predictions in turbid semi-infinite media," *J. Biomed. Opt.*, vol. 9, no. 3, pp. 632–647, 2004.

[235] J. C. C. Day and N. Stone, "A subcutaneous Raman needle probe," *Appl. Spectrosc.*, vol. 67, no. 3, pp. 349–354, 2013.

[236] B. Redding, G. Allen, E. R. Dufresne, and H. Cao, "Low-loss high-speed speckle reduction using a colloidal dispersion," *Appl. Opt.*, vol. 52, no. 6, pp. 1168–72, 2013.

[237] O. S. Ojambati, H. Yilmaz, A. Lagendijk, A. P. Mosk, and W. L. Vos, "Selective coupling of optical energy into the fundamental diffusion mode of a scattering medium," *New J. Phys.*, vol. 18, no. 4, p. 0432032, 2016.

[238] M. Davy, Z. Shi, J. Park, C. Tian, and A. Z. Genack, "Universal structure of transmission eigenchannels inside opaque media," *Nat. Commun.*, vol. 6, p. 6893, 2015.

[239] S. M. Popoff, G. Lerosey, R. Carminati, M. Fink, a. C. Boccara, and S. Gigan, "Measuring the transmission matrix in optics: An approach to the study and control of light propagation in disordered media," *Phys. Rev. Lett.*, vol. 104, no. March, pp. 1–4, 2010.

[240] Y. Choi, T. R. Hillman, W. Choi, N. Lue, R. R. Dasari, P. T. C. So, W. Choi, and Z. Yaqoob, "Measurement of the time-resolved reflection matrix for enhancing light energy delivery into a scattering medium," *Phys. Rev. Lett.*, vol. 111, no. 24, pp. 1–5, 2013.

[241] M. Mounaix, D. Andreoli, H. Defienne, G. Volpe, O. Katz, S. Grésillon, and S. Gigan, "Spatiotemporal Coherent Control of Light through a Multiple Scattering Medium with the Multispectral Transmission Matrix," *Phys. Rev. Lett.*, vol. 116, no. 25, pp. 1–5, 2016.

[242] R. Sarma, A. Yamilov, S. F. Liew, M. Guy, and H. Cao, "Control of mesoscopic transport by modifying transmission channels in opaque media," *Phys. Rev. B - Condens. Matter Mater. Phys.*, vol. 92, no. 21, pp. 1–10, 2015.

[243] T. Ebbesen, H. J. Lezec, H. F. Ghaemi, T. Thio, P. A.Wolff, T. Thio, and P. A.Wolff, "Extraordinary optical transmission through sub-wavelength hole arrays," *Nature*, vol. 86, no. 6, pp. 1114–7, 1998.

[244] M. S. Patterson, B. Chance, and B. C. Wilson, "Time resolved reflectance and transmittance for the non-invasive measurement of tissue optical properties," *Appl. Opt.*, vol. 28, no. 12, pp. 2331–2336, 1989.

[245] W. Becker, *The bh TCSPC Handbook*. Berlin: Becker & Hickl, 6 ed., 2014.

[246] M.-C. Chuang and A. C. Tam, "On the saturation effect in the picosecond near ultraviolet laser ablation of polymide," *J. Appl. Phys.*, vol. 65, no. 7, pp. 2591–2595, 1989.

[247] D. Magde, G. E. Rojas, and P. G. Seybold, "Solvent dependence of the fluorescence lifetimes of xanthene dyes," *Photochem. Photobiol.*, vol. 70, no. 5, pp. 737–744, 1999.

[248] D. A. Leonard, B. Caputo, and F. E. Hoge, "Remote sensing of subsurface water temperature by Raman scattering," *Appl. Opt.*, vol. 18, no. 11, pp. 1732–45, 1979.

[249] C. Krafft, I. W. Schie, T. Meyer, M. Schmitt, and J. Popp, "Developments in spontaneous and coherent Raman scattering microscopic imaging for biomedical applications," *Chem. Soc. Rev.*, vol. 45, no. 7, pp. 1819–1849, 2016.

[250] S. Wallin, A. Pettersson, H. Östmark, and A. Hobro, "Laser-based standoff detection of explosives: A critical review," *Anal. Bioanal. Chem.*, vol. 395, no. 2, pp. 259–274, 2009.

[251] A. Mahadevan-Jansen, M. F. Mitchell, N. Ramanujam, A. Malpica, S. Thomsen, U. Utzinger, and R. Richards-Kortum, "Near-infrared Raman spectroscopy for in vitro detection of cervical precancers," *Photochem. Photobiol.*, vol. 68, no. 1, pp. 123–132, 1998.

[252] S. Duraipandian, W. Zheng, J. Ng, J. J. H. Low, A. Ilancheran, and Z. Huang, "Near-infrared-excited confocal Raman spectroscopy advances in vivo diagnosis of cervical precancer," *J. Biomed. Opt.*, vol. 18, no. 6, p. 067007, 2013.

[253] A. S. Haka, K. E. Shafer-Peltier, M. Fitzmaurice, J. Crowe, R. R. Dasari, and M. S. Feld, "Diagnosing breast cancer by using Raman spectroscopy," *Proc. Natl. Acad. Sci. U. S. A.*, vol. 102, no. 35, pp. 12371–6, 2005.

[254] S. McAughtrie, K. Faulds, and D. Graham, "Surface enhanced Raman spectroscopy (SERS): Potential applications for disease detection and treatment," *J. Photochem. Photobiol. C Photochem. Rev.*, vol. 21, pp. 40–53, 2014.

[255] C.-L. Hsieh, Y. Pu, R. Grange, G. Laporte, and D. Psaltis, "Imaging through turbid layers by scanning the phase conjugated second harmonic radiation from a nanoparticle," *Opt. Express*, vol. 18, no. 20, pp. 20723–20731, 2010.

[256] O. S. Ojambati, J. T. Hosmer-quint, K.-j. Gorter, A. P. Mosk, and W. L. Vos, "Controlling the intensity of light in large areas at the interfaces of a scattering medium," *Phys. Rev. A*, vol. 043834, pp. 1–9, 2016.

[257] O. S. Ojambati, H. Yilmaz, A. Lagendijk, A. P. Mosk, and W. L. Vos, "Selective coupling of optical energy into the fundamental diffusion mode of a scattering medium," *New J. Phys.*, vol. 18, no. 4, p. 0432032, 2016.

[258] P. Matousek, I. P. Clark, E. R. C. Draper, M. D. Morris, A. E. Goodship, N. Everall, M. Towrie, W. F. Finney, and A. W. Parker, "Subsurface probing in diffusely scattering media using spatially offset Raman spectroscopy," *Appl. Spectrosc.*, vol. 59, no. 4, pp. 393–400, 2005.

[259] T. E. Oliphant, "Python for scientific computing," *Comput. Sci. Eng.*, vol. 9, pp. 10–20, 2007.

[260] K. J. Millman and M. Aivazis, "Python for scientists and engineers," *Comput. Sci. Eng.*, vol. 13, pp. 9–12, 2011.

[261] S. Van Der Walt, S. C. Colbert, and G. Varoquaux, "The NumPy array: A structure for efficient numerical computation," *Comput. Sci. Eng.*, vol. 13, no. 2, pp. 22–30, 2011.

[262] F. Pérez and B. Granger, "IPython: A system for interactive scientific computing," *Comput. Sci. Eng.*, vol. 9, no. 3, pp. 21–29, 2007.

[263] P. Peterson, "F2PY: a tool for connecting Fortran and Python programs," *Int. J. Comput. Sci. Eng.*, vol. 4, no. 4, pp. 296–305, 2009.

APPENDIX A

HEATPIPE OVEN CONSTRUCTION AND OPERATION

The superfluorescence experiments performed in chapter 2 were done with sodium vapor. Because alkali metals are highly reactive, a special environment is needed to isolate them from other materials. Furthermore, optical access is also require if lasers are to be used in the experiment. A heatpipe oven provides us with an isolated environment to study the interaction of light with alkali vapors. This system provides control of the density of the vapor via temperature of the environment and pressure of a non-reactive buffer gas. In this appendix, I document the construction and operational procedures of two heat pipe ovens containing sodium and rubidium alkali metals respectively. The first (sodium) oven was critical to the execution of the experiments contained in chapter 2. These heatpipe ovens were designed to achieve high vapor densities via high temperatures (up to 700 degrees Celsius). However, for most of our experiments we kept it at a much lower temperature (450 degrees Celsius).

A.1 Heat pipe oven construction

The constructed heatpipe ovens were based on typical designs [90, 91], but adapted for our specific needs. They have the following three major components: a vacuum system to control the atmospheric content, a heating system to vaporize the loaded metal, and a cooling system to condense the metalic vapor before it reaches the windows to the cell. The body of the oven itself is made of a stainless steel pipe or tube with a stainless steel mesh to act as a wick inside the tube. Stainless steel is used because it does not react with the vaporized alkali metals. The main point of a heatpipe oven is to vaporize atomic metals to high densities, but to keep them contained in the heated region of the oven. This

is desired because the hot alkali gases will react with the optical windows making the oven unusable for optical experiments. This is acheived by heating the metal in the center of the pipe, and cooling the pipe near the ends. Thus, the vaporized metal will condense before it reaches the windows. The stainless steel mesh inside the tube will help wick the condensed metal back to the center, heated region.

A.1.1 Vacuum system

The vacuum system is designed to first remove atmospheric gas from the pipe, and second to control the pressure of the buffer gas (Argon). This vacuum portion of the system is comprised of the stainless steal pipe, stainless steal Tee's, the windows, copper tubing, a system of valves and pressure gauges, and a rotary pump. The connections for the pipe are all either compression fittings or tapered thread fittings with PTFE tape to help them seal. The windows were glued onto an angled wedge of transparent acrylic which had a whole cut in it. The acrylic was glued onto one end of a stainless steel Tee. The angled window helps remove effects from backscattered beams. A high temperature silicon was used as glue. Figure A.1 shows the windows and stainless steel Tee after they were glued together.

A system of four valves was used to control the removal and injection of argon buffer gas. This valve system is shown in Fig. A.2. For the first heatpipe oven that we constructed, we used compression fittings to connect copper tubing from the window connections to the valve system, which consists of copper tubing, compression tee's and valves. Furthermore, a manual pressure gauge, which does not need electricity, and a more sensitive millitorr gauge (Cole-Parmer, EW-68808-20) were connected using compression to NPT thread adapters. By opening valves A, B, and C with the rotary pump running, we were able to vacuum out the system, removing atmospheric gases. Closing valve B will seal off the oven, and opening valve D with C open and the pump running will allow us to
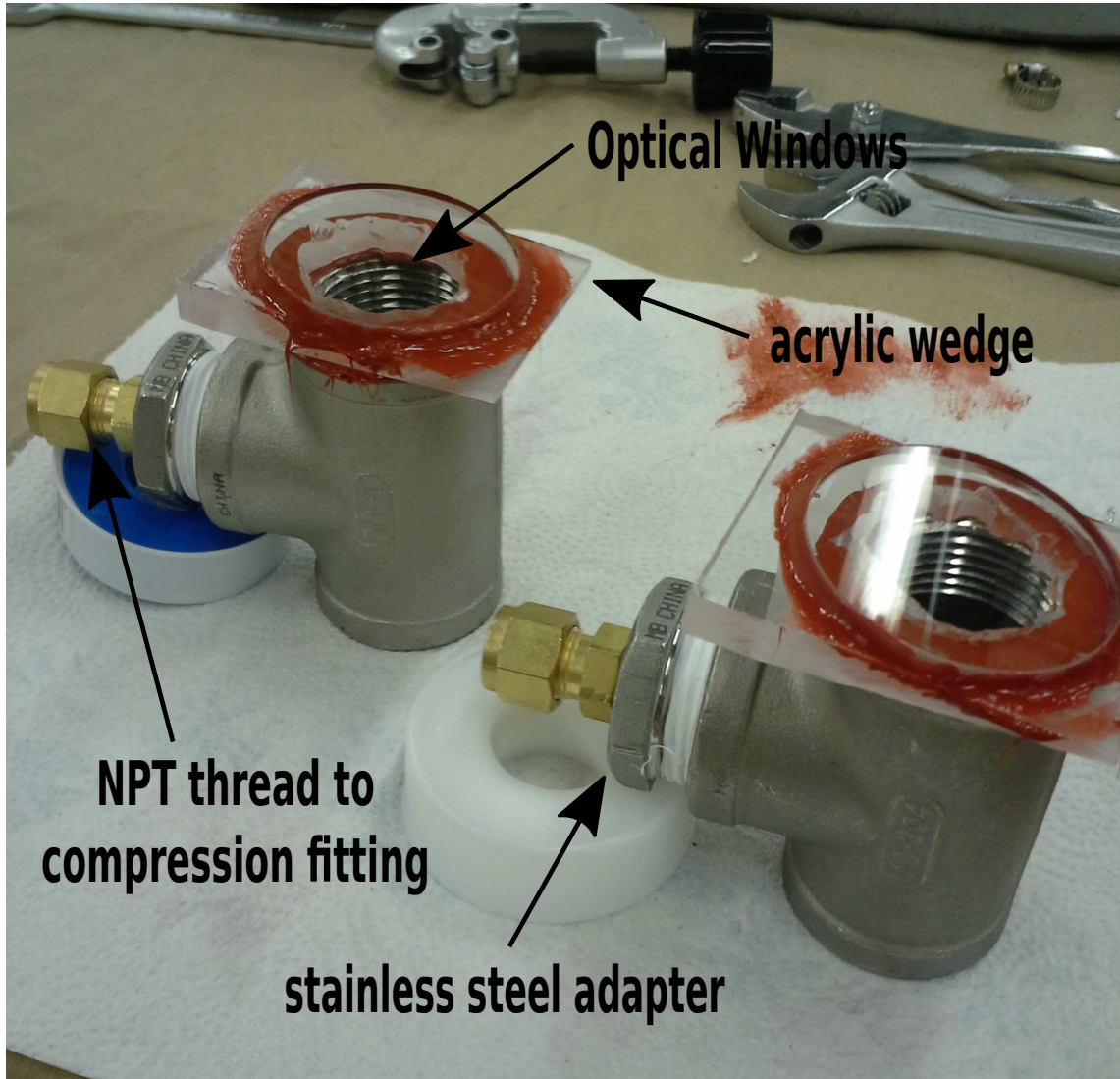
Figure A.1: Optical window connection for heatpipe. The optical windows were glued to a wedge made of acrylic with high temperature grade silicon. The wedges were in turn glued to one edge of a 1 inch diameter stainless steel T. The center connection of the Tee was connected to the valve system with a NPT thread to compression fitting adapter. The third entrance to the Tee was connected to the chamber of the heatpipe.
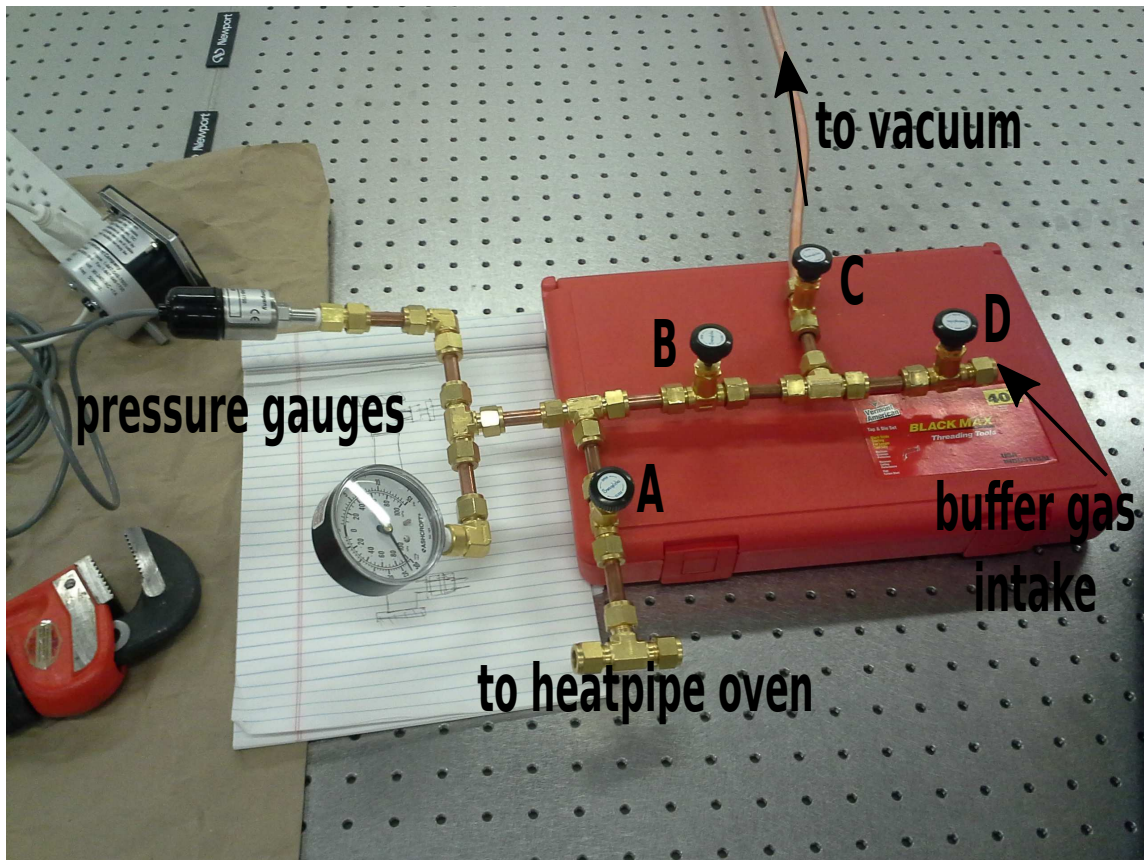
Figure A.2: Valve system for the heatpipe oven. Four valves gives complete control over removal (open A,B,D) or addition (open A,B,C) of buffer gas. It also allows you to seal off the inner chamber completely (close A), or check the pressure (open A, close B) without losing air to the intake or vacuum lines.

clean out the input line from a gas cylinder with the buffer gas. This needs to be done each time the line is disconnected and reconnected. As a good practice, we vacuumed this line every time we turned on the oven. Closing valve C and turning off the pump will cease the removal of gas. With valve D still open, we can open valve B again to repopulate the oven with buffer gas to the desired pressure as measured by the pressure gauges. Once the pressure is set correctly valves B and D can be closed. The purpose of valve A is for storage when the oven is not in use since it will isolate just the heatpipe oven from any other components of the vacuum system.
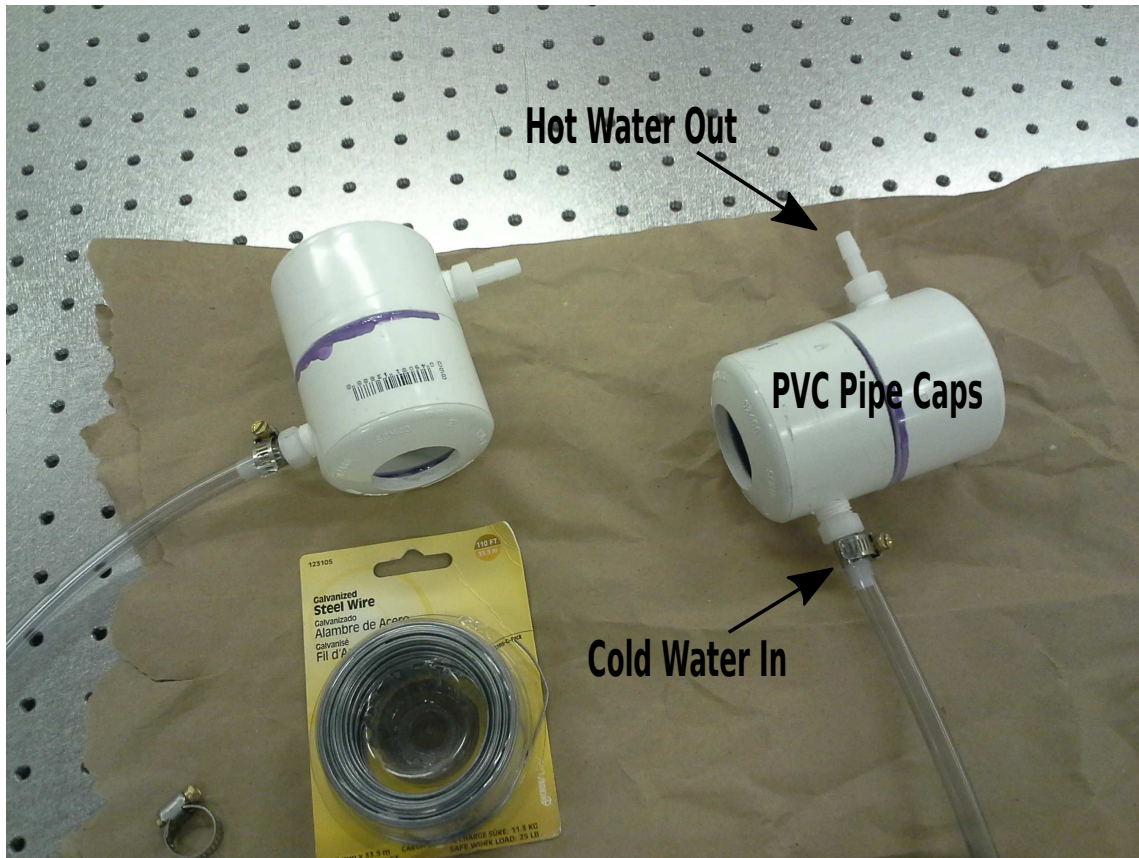
Figure A.3: Water cooling jacket to wrap around the ends of the heatpipe oven. They were constructed of PVC pipe caps with holes drilled into the ends. Cool water was flowed into the jacket from the bottom, and the heat was carried away by the water leaving the top of the jacket.

A.1.2 Cooling system

The cooling system consists of PVC jackets wrapped around both ends of the heatpipe oven, water lines into and out of the jackets, and a water reservoir with a garden pump driving the system. The PVC jackets were constructed by drilling a large hole into PVC end caps, and glueing them to a small piece of PVC pipe. Since the main body of our first oven was just a pipe, we constructed these caps first with the hole, then slipped the caps onto the pipe. Then we fastened the cap into place using high-temperature silicon. For

the second heatpipe, the main body of the oven was a tube with KF flanges. Therefore we could not slip the jacket over the pipe, and the jackets had to be cut in half, and glued back together once in place. Figure A.3 shows the cooling jackets before placing them onto the oven, and the attached cooling jackets are shown later (Fig. A.5).

Cool water was pumped into the cooling jackets from a water reservoir using a common garden water pump placed in a plastic bucket as shown in Fig A.4. The water was pumped from the reservoir into a single line which was then split and connected to both cooling jackets. This way, one pump could supply both jackets with sufficient cool water. The water leaving the jackets was then returned to the reservoir with two small plastic hoses.

A.1.3 Heating system

The center of the heatpipe oven is heated by an ultra-high temperature electric heat tape (Omega, STH051-040) which is rated for temperatures up to 760 degrees Celsius. A variable transformer is used to drive the heat tape, controling the temperature by changing the set voltage. High temperature insulated thermocouples (Omega, XC-20-K-24) were placed underneath the heat tape to provide temperature measurement feedback. The heatpipe with the tape attached is shown in Fig. A.5. High temperature rock wool insulation (Roxul, RXCB301525) was cut to size and placed around the heat tape in order to confine the heat to that particular section of pipe, and to keep the heat from leaking. Heavy duty aluminum foil and galvanized steel wire was wrapped around the insulation to keep it in place. The completed heatpipe oven is shown in Fig. A.6.

A.1.4 Loading the oven with alkali metal

Because of the high reactivity of alkali metals with moisture, care was taken in loading the heatpipe ovens. The first oven was loaded with 15 grams of sodium metal through an opening of the pipe at one of the Tee connections. The oven was opened and a plastic bag
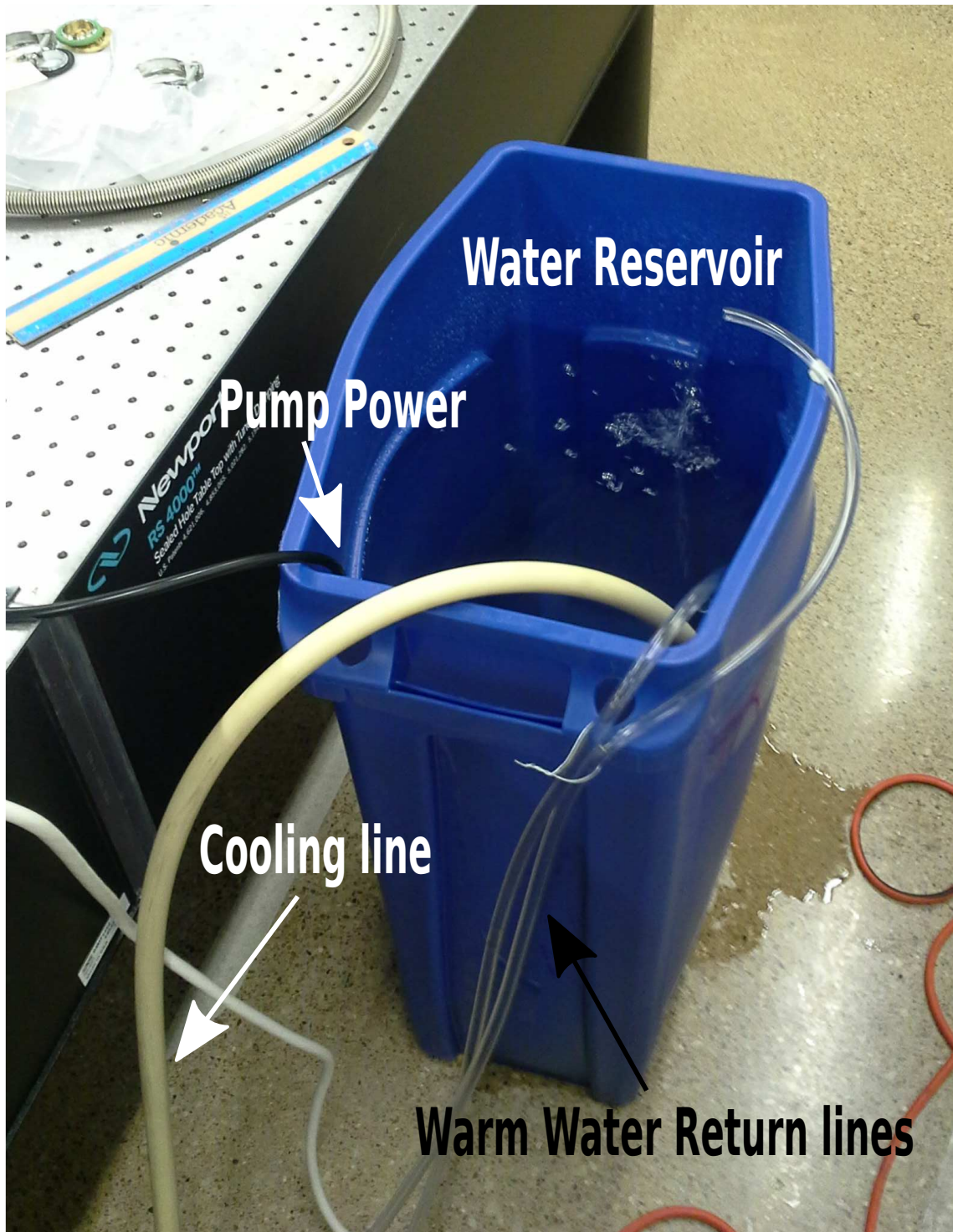
Figure A.4: Cooling water reservoir. Cool water was pumped from the bottom of the bucket to the heatpipe cooling jackets by a garden pump. The warm water was returned to the top of the reservoir via two plastic hoses.
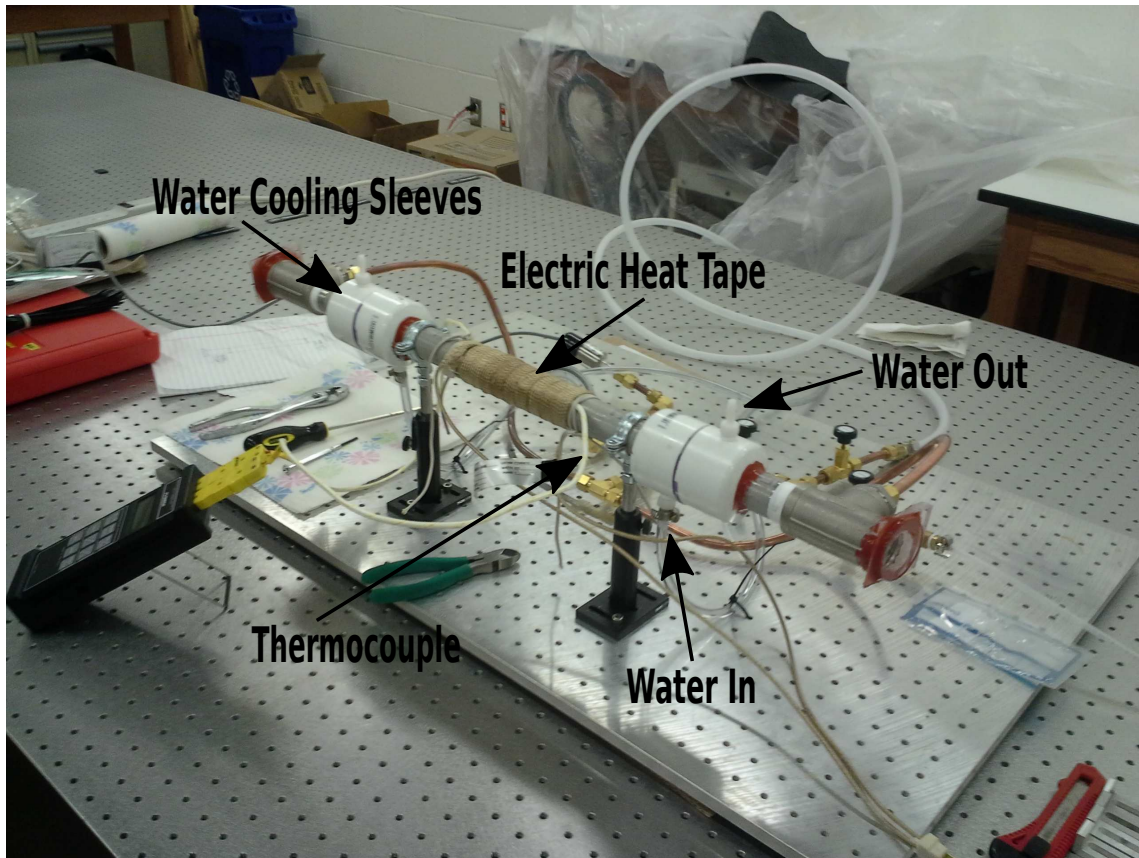
Figure A.5: High temperature electric heat tape attached to the center of the heatpipe oven. Thermocouples are placed below the heat tape to measure the temperature of the heated pipe.

was wrapped around the opening. The entire system and plastic bag were pressurized with Argon to clear any humidity and other atmoshperic gases from the system. Glass ampules containing the sodium metal were heated and then passed into the bag where they were opened and loaded into the oven. Once loaded, the opening was closed and sealed. The system was then vacuumed down and repressurized with Argon. The completed heatpipe oven system is shown in Fig. A.6
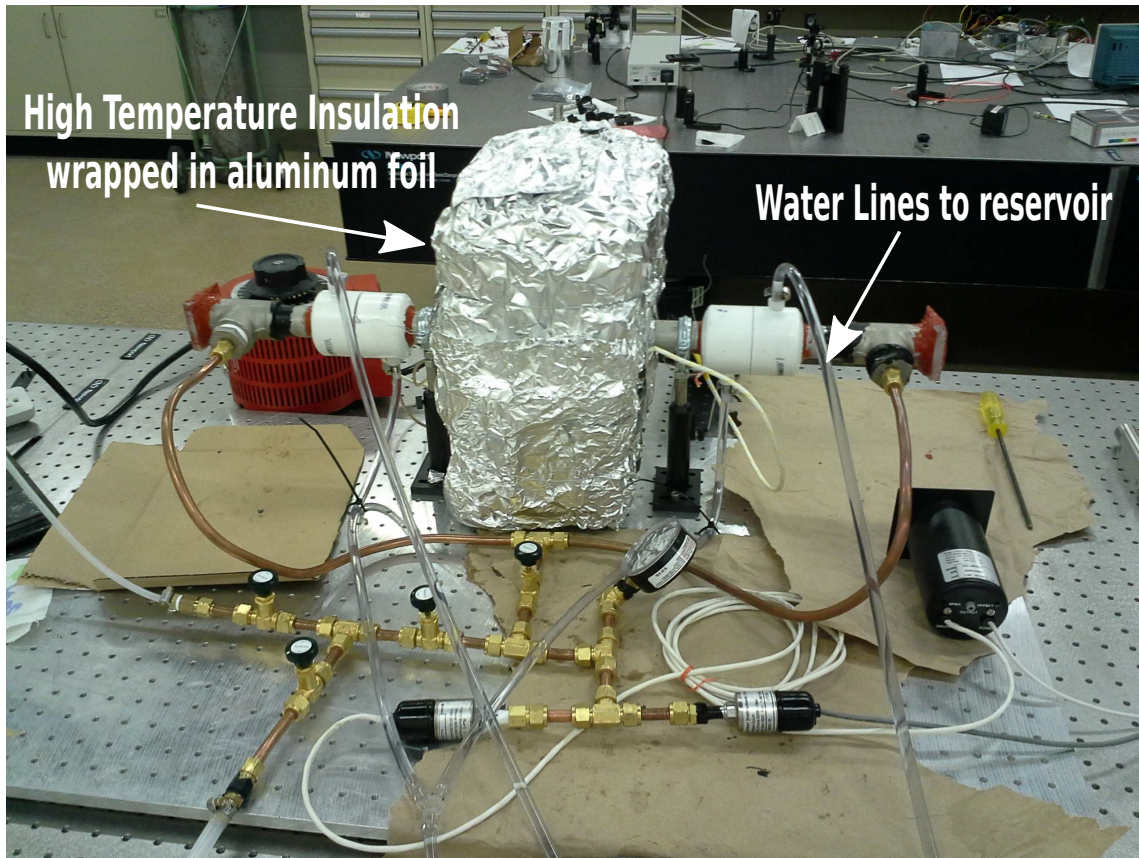
Figure A.6: Completed heatpipe oven. This particular oven was loaded with sodium metal.

A.1.5 Upgrades for second generation

With the construction of the first heatpipe, we found a number of items that could be improved upon, so upgrades were made in the construction of a second heatpipe oven. These upgrades are visible in Fig. A.7 which shows the second completed heatpipe oven. The upgrades are largely related to the vacuum system and the oven diameter. Originally, we thought a 1 inch pipe would provide plenty of room for a laser beam to be transmitted down the pipe. While this is true, the addition of the wick and alkali metal reduced this diameter significantly. So for our second oven, we opted to use a 2 inch diameter pipe to increase the room for the laser beam. This increase in beam diamter required us to
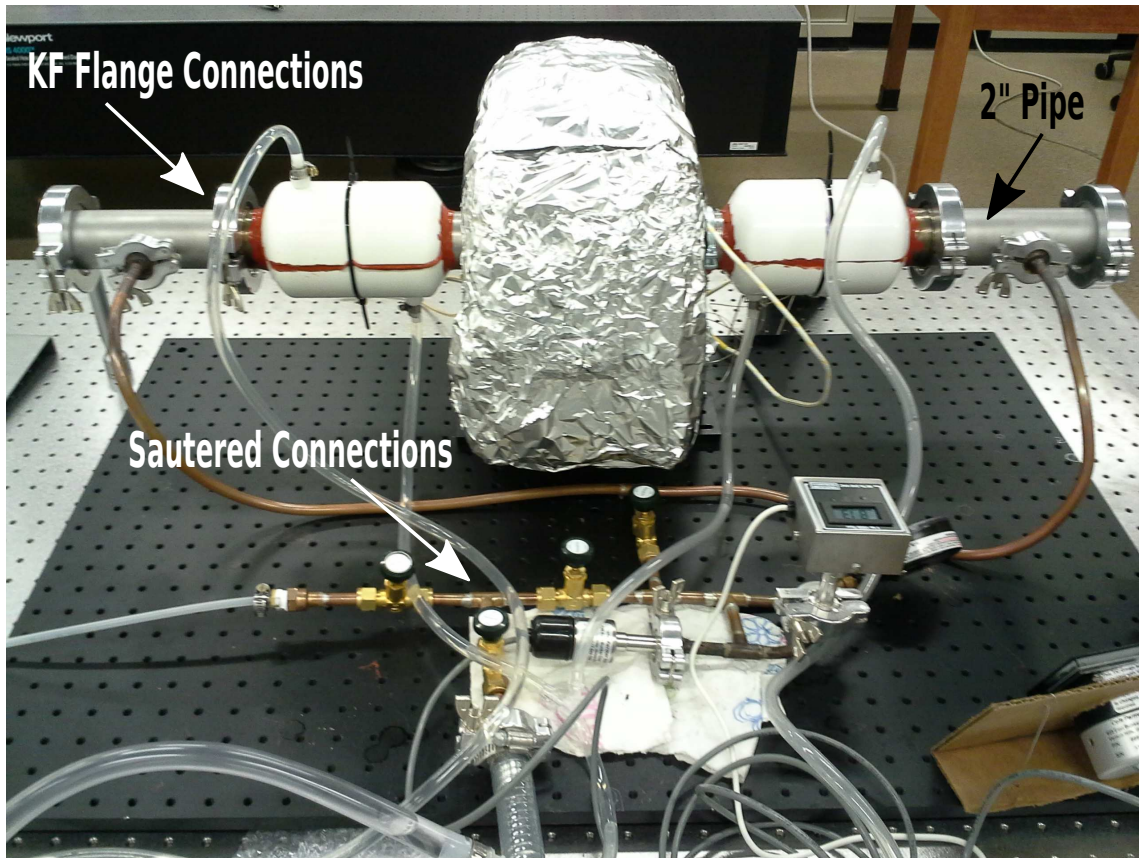
Figure A.7: Second completed heatpipe oven. This oven was loaded with Rubidium metal, and uses different connections to prevent leakage.

also increase the size of the water cooling jackets since the previous jackets would not fit around this size of pipe.

One of the main issues we faced in construction of the first heatpipe oven was gas leakage. Sealing the NPT threaded connections was tricky and prooved difficult. Therefore, for this second version, we replaced almost all of the threaded connections with KF flange connections. These connections are fast to connect, and they use an o-ring to achieve a better seal. Because they are all outside of the cooling regions, we did not need to worry about the alkali metal reacting with the o-ring material. Using KF flange connections required flanges to be welded onto the main stainless steel tube. In addition to the KF

flanges, many of the compression fittings were also replaced with sautered connections. These connections seemed less prone to leakage with movement of the entire system.

This second heatpipe oven was loaded with Rubidium metal instead of Sodium. The loading method followed was similar to that used for sodium. The main difference in this case was that a boat was made out of the stainless steel mesh, the melted Rubidium was poured into the boat, and the boat was pushed into the pipe. This made it easier to load the metal into the center of the pipe than the previous method. Since the boat was made of the same material as the wick, it did not interfere with the performance of the oven.

A.2 Heat pipe oven operation

In this section, I will outline the typical procedure for operation of both heatpipe ovens.

A.2.1 Turn on procedure

The turn on procedure for the heatpipe ovens is described in the following steps. The valve numbers refer to Fig. A.2.

1. Turn on the water pump to start the cooling system.

2. Vacuum down the heatpipe oven by turning on the vacuum and opening valves A, B, and C.

3. Close valve B and open valve D and the argon gas cylinder to briefly vacuum out the input line.

4. Close valve C and turn off the vacuum pump.

5. Open valve B slowly until the desired pressure of buffer gas is reached. (We set this to 15 Torr for Sodium, and about 80 Torr for Rubidium)

6. Close valves B and D as well as the gas cylinder.

7. Turn on the variable transformer and set it to a voltage to get the desired temperature (This can be determined experimentally).

8. Wait for the temperature to reach the desired set point and stabalize

A.2.2   Shutdown procedure

The shutdown procedure consists of the following steps. The valve numbers refer to Fig. A.2.

1. Turn off the variable transformer.

2. Wait for the temperature to descend below 100 degrees Celsius (Typically an hour or so depending on what temperature the system was run). At this point the water cooling system can safely be turned off.

3. Briefly vacuum out the gas input line by turning on the vacuum pump and opening valves C and D and the buffer gas cylinder.

4. Close valve C, open valve B, and repressurize the system back to slightly above atmospheric pressure (about 780 torr) for storage.

5. Close all valves and the gas cylinder. The Water pump can be turned off, and any other electronic parts (i.e. Thermocouple meter, pressure gauges, etc.) can be turned off.

APPENDIX B

SOFTWARE/CODE DOCUMENTATION

In this Appendix, I document the LabVIEW software and Python/FORTRAN code used to run experiments, analyze data, and perform simulations and calculations for the referenced chapters. First, the LabVIEW control for wavefront shaping will be documented in section B.1. Because LabVIEW is a graphical programming language, screen shots of the programs are provided. After this, Python code, which numerically simulates the wavefront shaping process is documented in section B.2. This simulation makes use of a genetic algorithm, also programmed in Python, which is contained in section B.3. Section B.4 contains FORTRAN code written to simulate second harmonic generation as well as a Python program written to optimize the output of the second harmonic simulation based on the phase mask of the input beam. Lastly, section B.5 contains Python code used to calculate the equations from our solution to the diffusion equation contained in chapter 7. The Python code which is presented in this appendix to perform scientific computations [259, 260] makes use of the NumPy and SciPy packages [261], and was developed using IPython [262], which provides an interactive computing environment.

B.1 Wavefront shaping control with LabVIEW

The labview software written to perform wavefront shaping experiments was designed to be adaptable and modular. Thus, if the optimization of a measurement from a new detector is desired, it should be a straightforward process to modify the existing program to accept signal from this new detector. Because of this modularity, the optimization algorithm has some complexity to it; however, the modification or addition of new algorithms should not be difficult.

Figures B.1, B.2, and B.3 show the front panel of the main VI. Figures B.4 and B.5 show the block diagram for the main VI. There are nine subVI's contained in the top level block diagram. The code for each of these will be organized into subsections following the order (left to right) shown in the top level diagram.
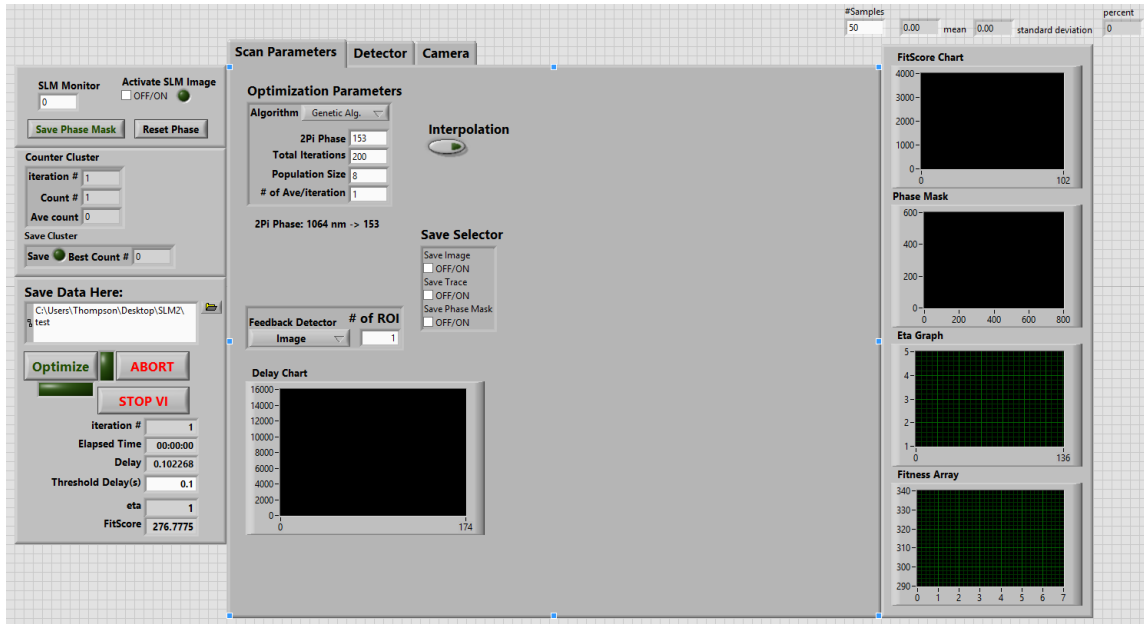
Figure B.1: Wavfront shaping VI front panel, scan parameter tab. The left column allows connection to the spatial light modulator (Hamamatsu, LCOS-SLM), as well as setting the output directory for data. Buttons on the left also allow the user to start or abort the optimization process. The scan parameters tab allows the user to select the optimization algorithm, number of iterations, number of steps/population size per iteration, and whether or not to average mutliple measurements per iteration. The 2π phase value (based on SLM type, and laser wavelength) can also be set here. A drop-down menu allows the selection of feedback detector, and the save selector specifies which files are saved after each iteration. The delay chart is for diagnostic purposes of the program. The interpolation button is an experimental feature which interpolates between points/steps in the iteration and attempts to remove noise and improve step resolution. The right column provides four diagnostic charts. The FitScore Chart shows the fitness of each measurement as a function of time, the Phase Mask plot shows the current phase mask applied to the SLM, the Eta Graph shows the enhancement as a function of iteration, and the Fitness Array shows the fitness value for each step in the iteration. The Detector and Camera tabs are shown in Fig. B.2 and Fig. B.2, respectively.
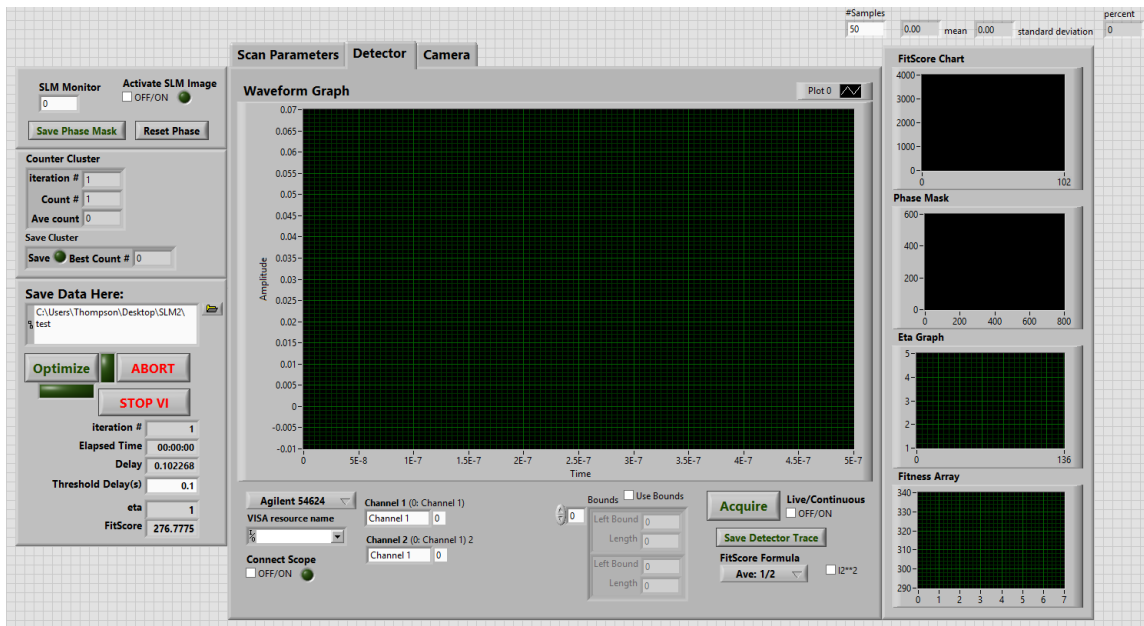
Figure B.2: Wavefront shaping VI front panel, detector tab. This tab controls connection to oscilloscopes, as well as the collection of signal, and the ability to save traces individually. Three different oscilloscopes are programmed into the dropdown menu, but more can be added. Current functionality allows for two channels to be collected. The Bounds box allows the user to select regions of interest in the collected trace. The FitScore Formula allows the user to select/control how the collected signal is computed into a fitness score. If the I2**2 checkbox is selected the value from the second trace will be squared.
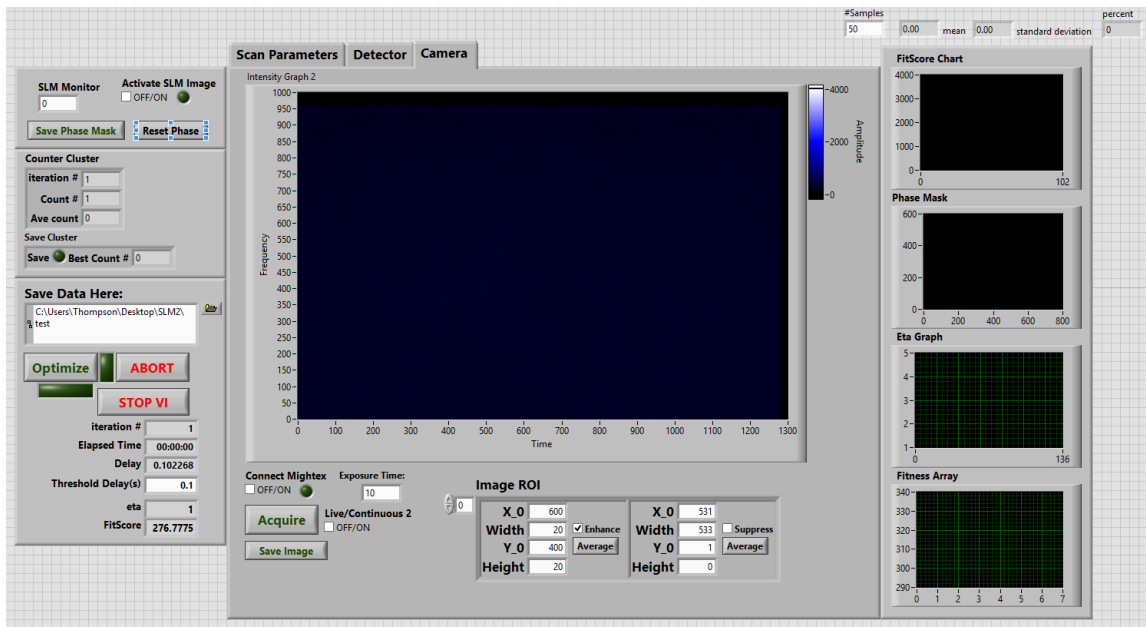
Figure B.3: Wavefront shaping VI front panel, camera tab. This tab controls the connection to a Mightex camera. The Image ROI box allows the user to select one or more regions of interest, and tell the algorithm to either enhance or suppress intensity in that region.
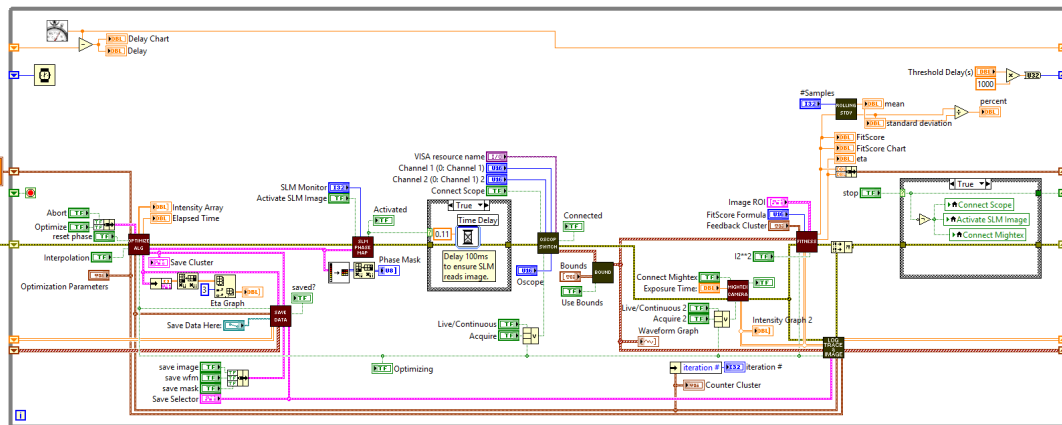
Figure B.4: Wavefront shaping VI block diagram. This figure shows all case structures set to "True". Figure B.5 shows this same diagram witht the case structures set to "False".

174
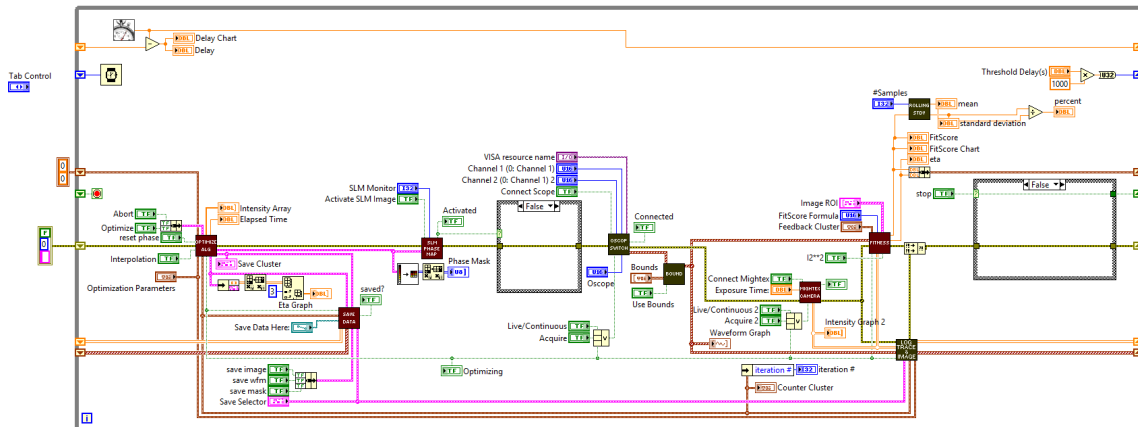
Figure B.5: Wavefront shaping VI block diagram. The only difference between this figure and Fig. B.4 is the case structures have been set to False.

B.1.1 Optimization algorithm sub-VI

The Optimization Algorithm sub-VI uses the previous measurement and the selected algorithm to determine the actions of the program for the next step. This includes the selection of the next phase mask and whether or not to save any information to file. The block diagram (shown in Figs. B.6, B.7, B.8, B.9, B.10, & B.11) has one large case structure. This case structure has four options computed from the boolean values of the optimize and abort controls, as well as the optimizing indicator. If optimize is false, and it was false on the previous loop (indicator is false), case 0 (Fig. B.6 & Fig. B.7) is exectuted. If the optimize button is pressed (true), but was false on the previous loop, case 1 (Fig. B.8) is executed. This case initializes the optimization process. If the optimizing value of the previous loop was true, regardless of the current optimization button status, case 2 (Fig. B.9 & Fig. B.10) will execute. This case runs the optimization process. If the abort button is pressed, case 4 (Fig. B.11) will execute. This case triggers the save sub-VI to save data, and turns off the optimizing indicator. Figures 12-55 show the sub-VI's that drive the various optimization algorithms.

175
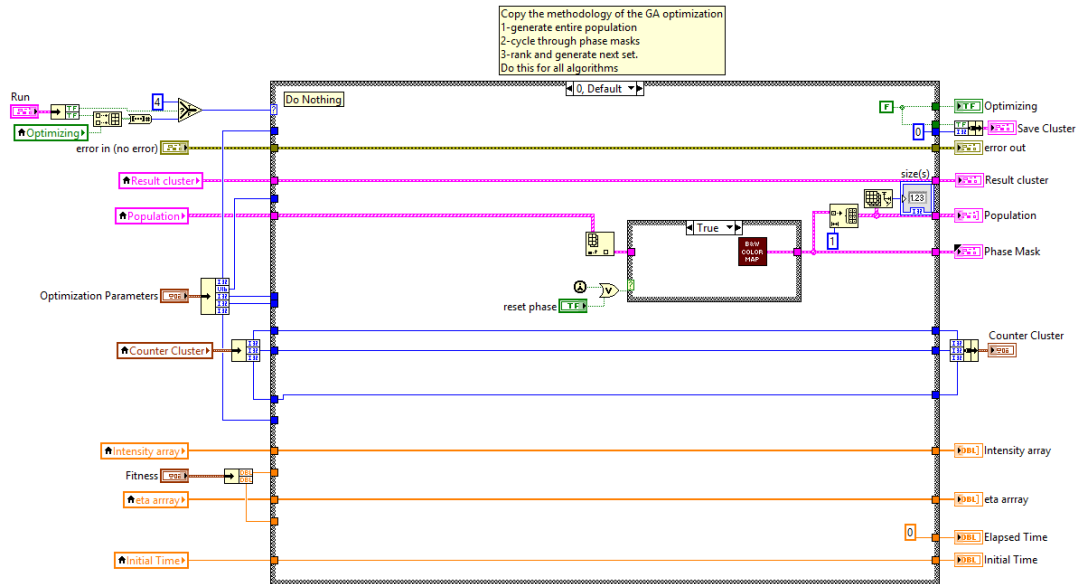
Figure B.6: Optimization Algorithm sub-VI block diagram for case 0, Default. If the reset phase button is selected/true, the phase mask is replaced by a blank mask. If the reset phase button is false (Fig. B.7), nothing happens. The B&W color map sub-VI is shown in Fig. B.12.
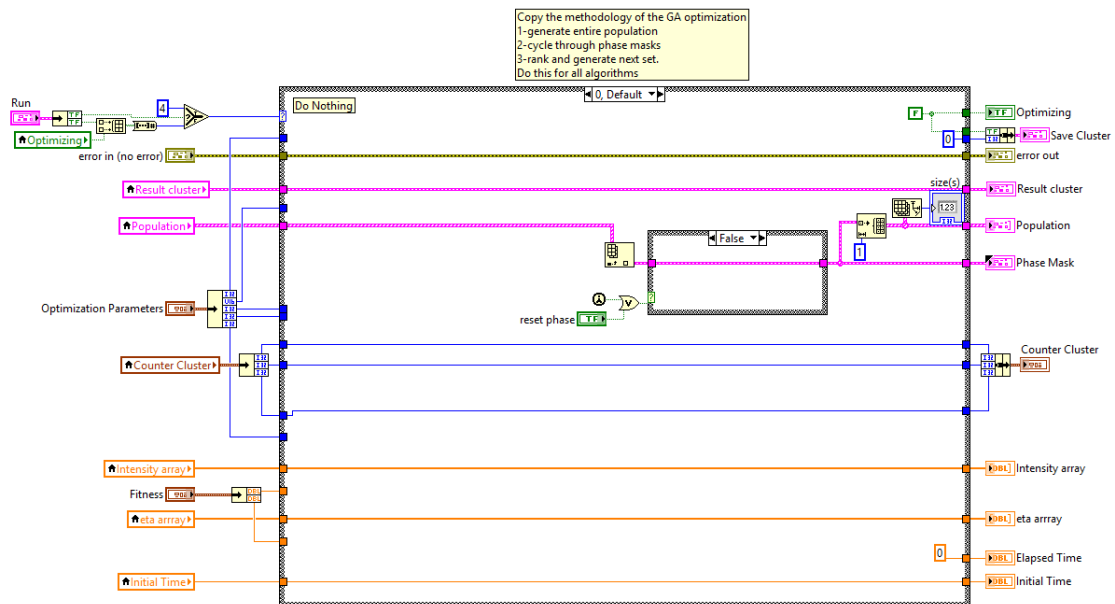
Figure B.7: Optimization Algorithm sub-VI block diagram for case 0, Default. If the reset phase button is not selected/false, the phase mask is not changed.
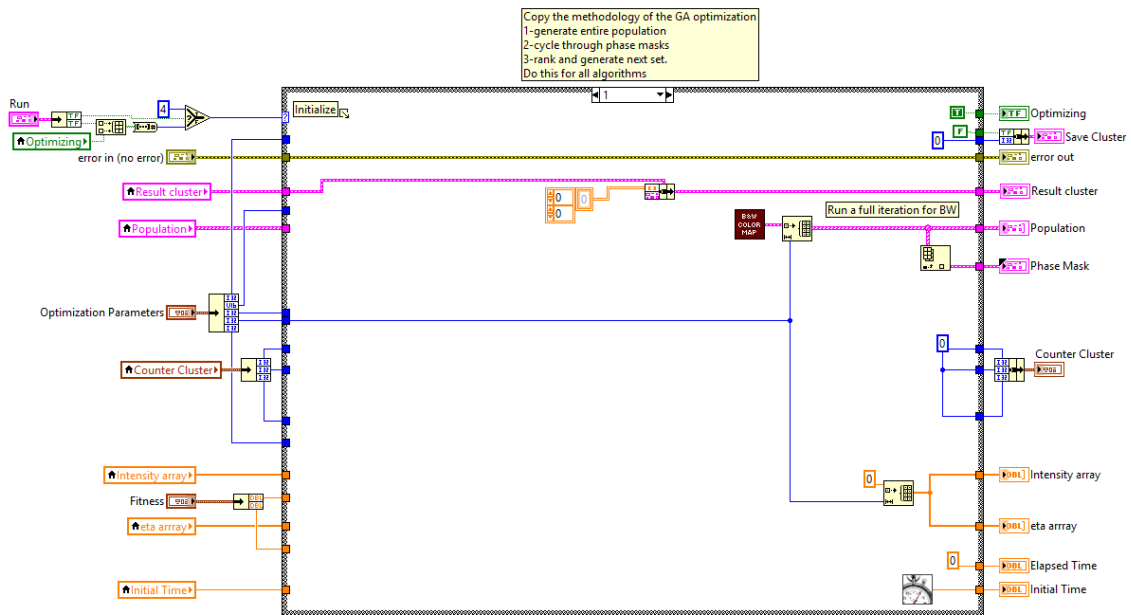
Figure B.8: Optimization Algorithm sub-VI block diagram for case 1, initialization of the optimization process. The population of phase masks is prepared. The counters and fitness arrays are also cleared and set to zero. The B&W color map sub-VI is shown in Fig. B.8.
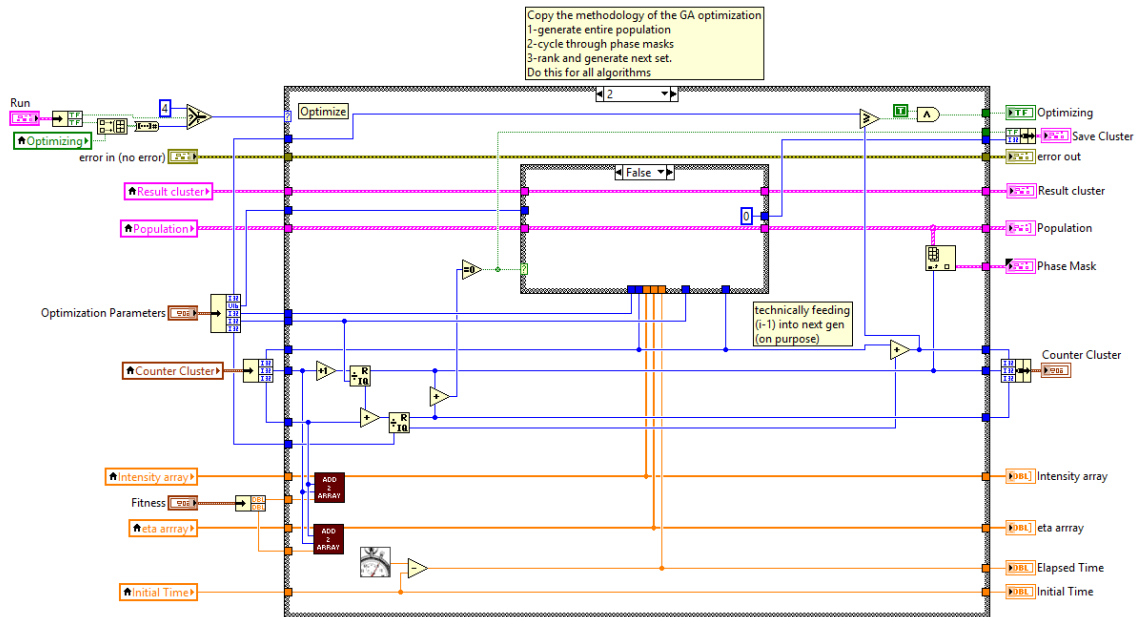
Figure B.9: Optimization Algorithm sub-VI block diagram for case 2, running the optimization process. All phase masks are generated at the begining of each iteration. In the middle of the iteration (center case set to False), the set of phase masks are unchanged. The sub-VI "Add 2 Array" is shown in Fig. B.13.
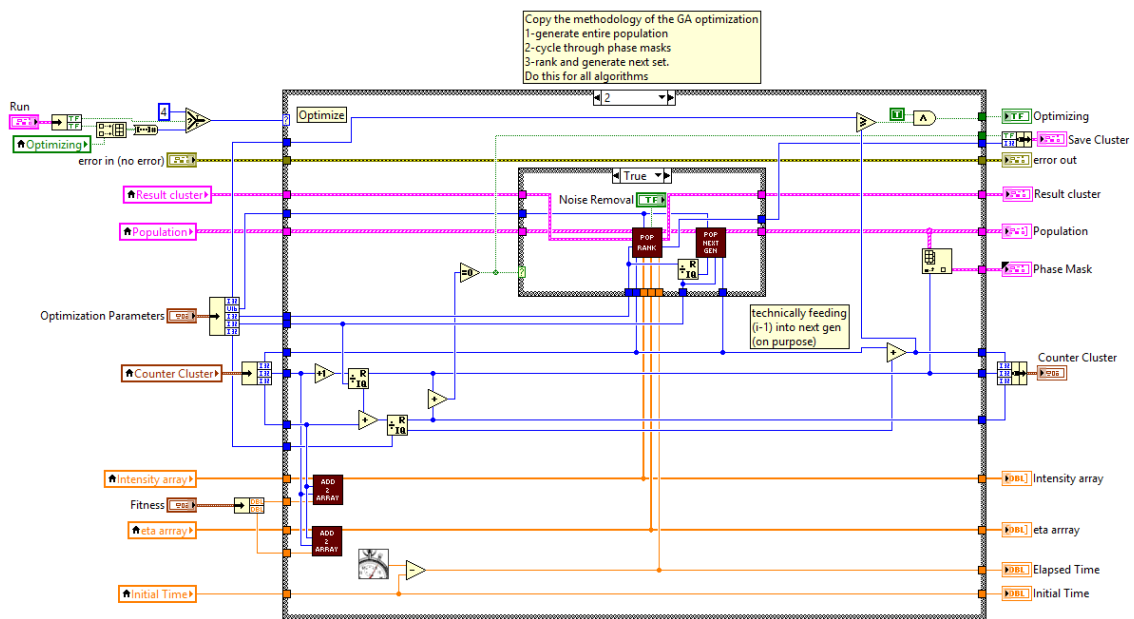
Figure B.10: Optimization Algorithm sub-VI block diagram for case 2, which runs the optimization process. All phase masks are generated at the begining of each iteration. This is done by first ranking the scores of the previous set of phase masks ("Pop Rank", Figs. B.14, B.15, B.16) and then generating the next population ("Pop Next Gen", Figs. B.18, B.19). The sub-VI "Add 2 Array" is shown in Fig. B.13.
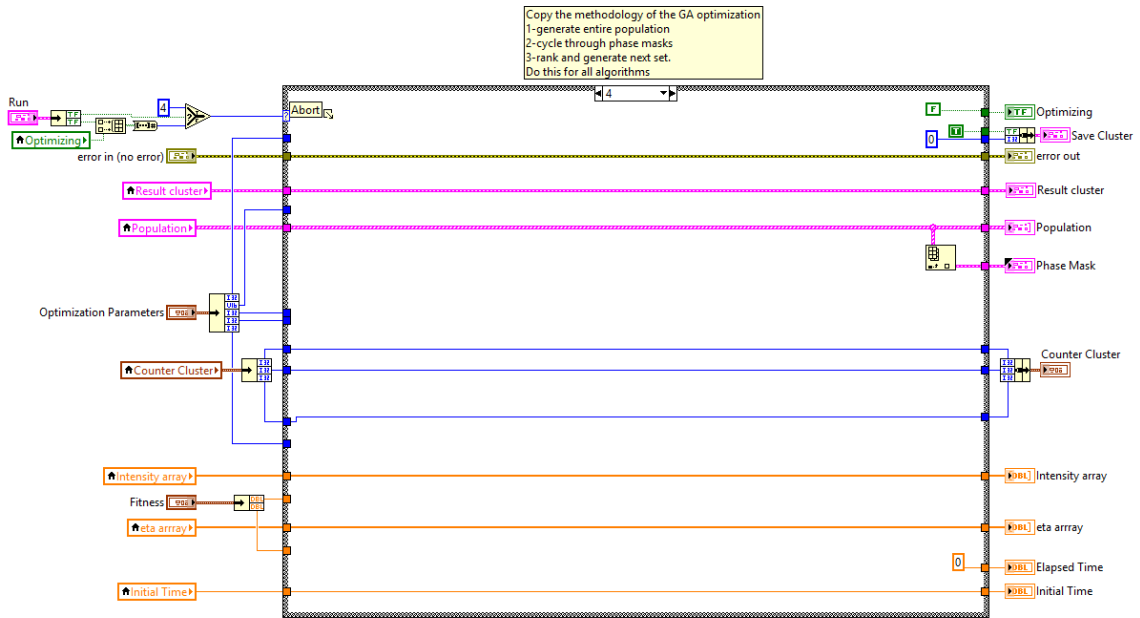
Figure B.11: Optimization Algorithm sub-VI block diagram for case 4, terminating the optimization process. The save indicator is set to true, and the optimizing indicator is set to false.
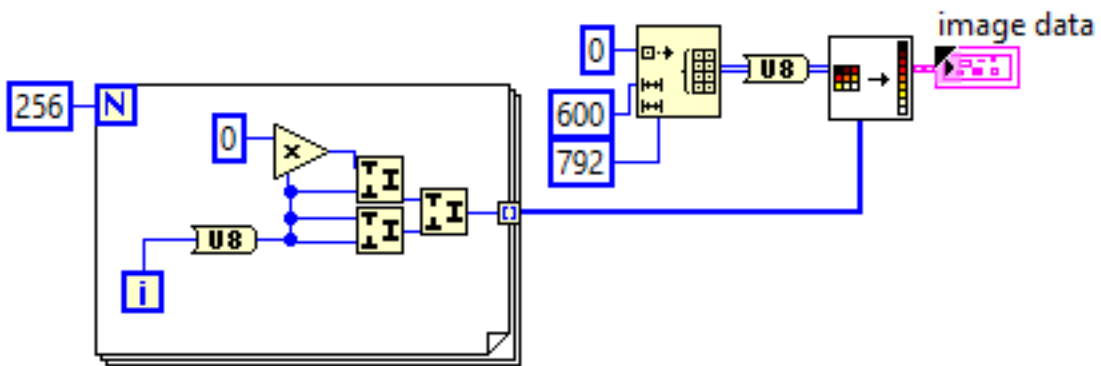
Figure B.12: B&W color map sub-VI block diagram. This sub-VI generates a flat, black image. i.e. each element of the array is set to zero.
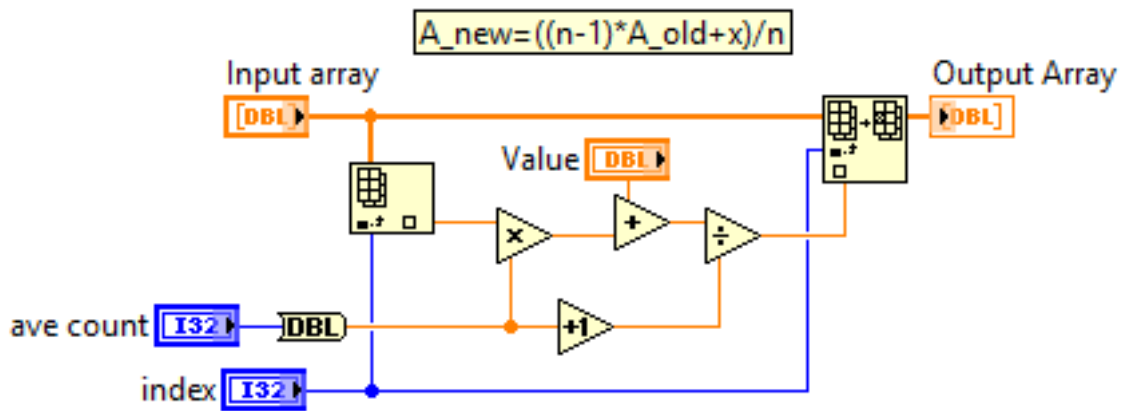
Figure B.13: Add 2 Array sub-VI block diagram. This sub-VI averages a new value with the specified element of an existing array. It takes into account the total number of values to be averaged into this element, i.e. it can be considered as a live, updated average.
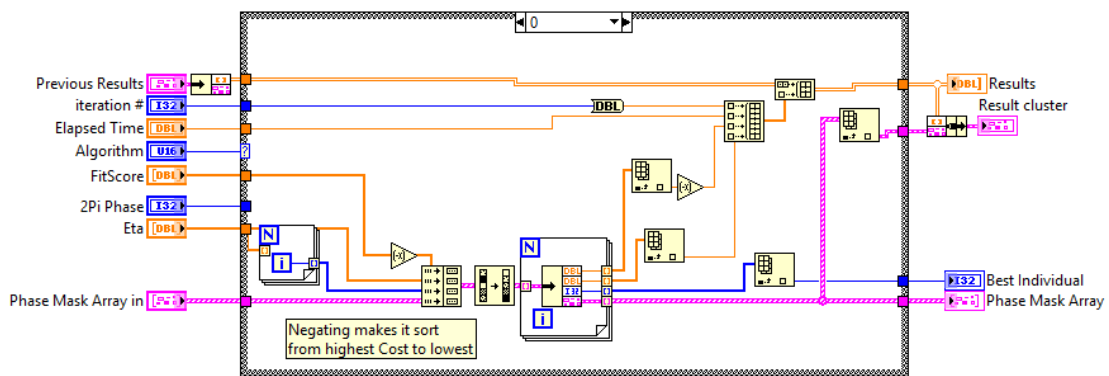
Figure B.14: Pop Rank sub-VI block diagram. Case 0 of this sub-VI is for the genetic algorithm. Here, it reorders the array of phase masks according to the fitness score of each mask.
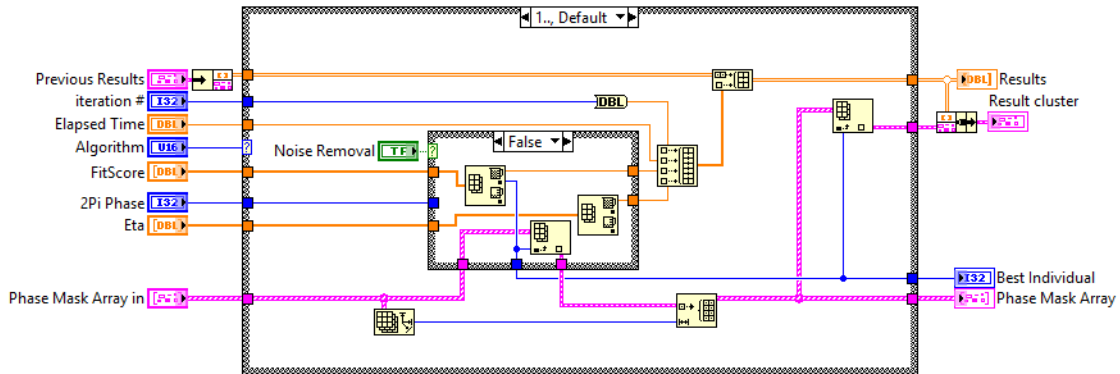
Figure B.15: Pop Rank sub-VI block diagram. Case 1 of this sub-VI is for the all algorithms other than the genetic algorithm. Here, it replaces the array of phase masks with a new array populated by copies of the best phase mask from the replaced array.
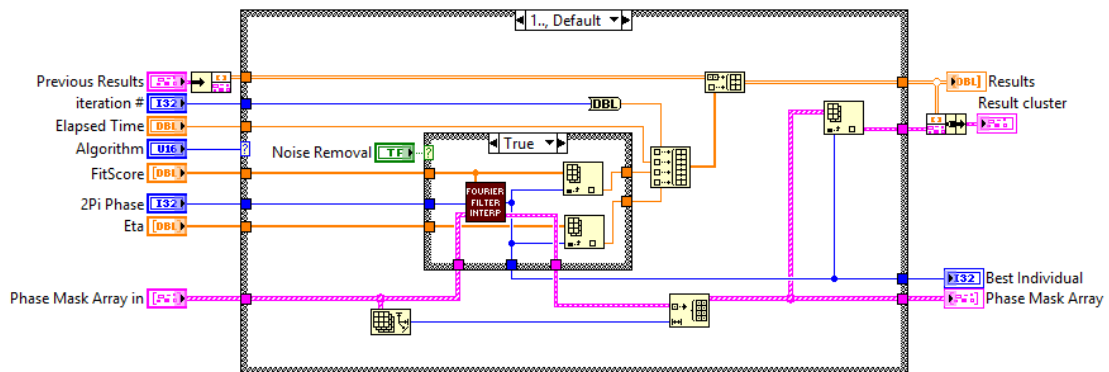
Figure B.16: Pop Rank sub-VI block diagram. Case 1 of this sub-VI is for the all algorithms other than the genetic algorithm. When the noise removal switch is true, it applies a fourier filter to interpolate the phase masks, picking the best phase mask according to the interpolation. The next generation of phase masks is initialized with a new array populated by copies of this interpolated phase mask. The Fourier Filter Interp sub-VI is shown in Fig. B.17.
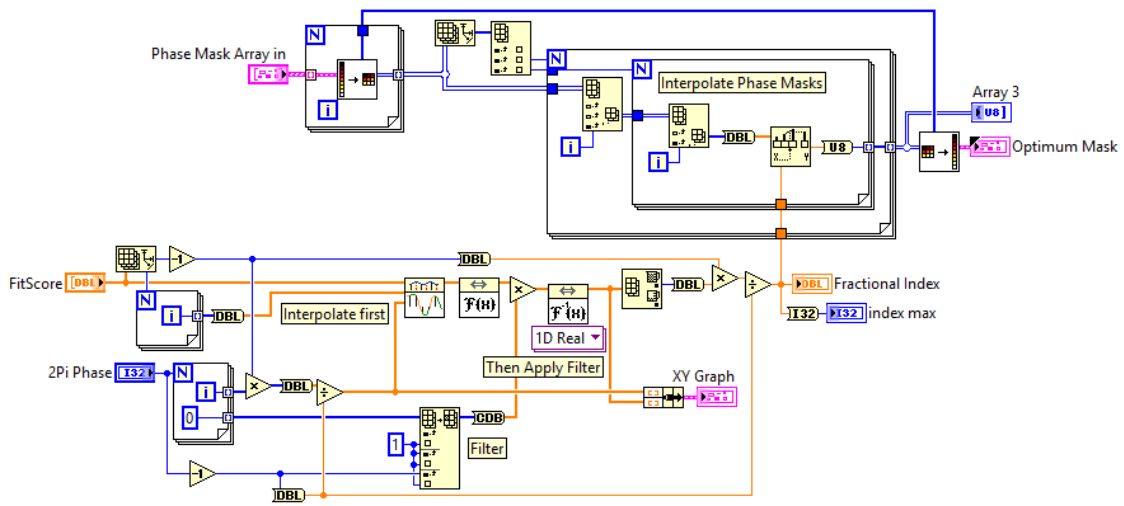
Figure B.17: Fourier Filter Interp sub-VI block diagram. A fourier filter is used to remove noise and interpolate the fitness value array. The phase mask is also interpolated, and the best mask according to the interpolated fitness array is selected.
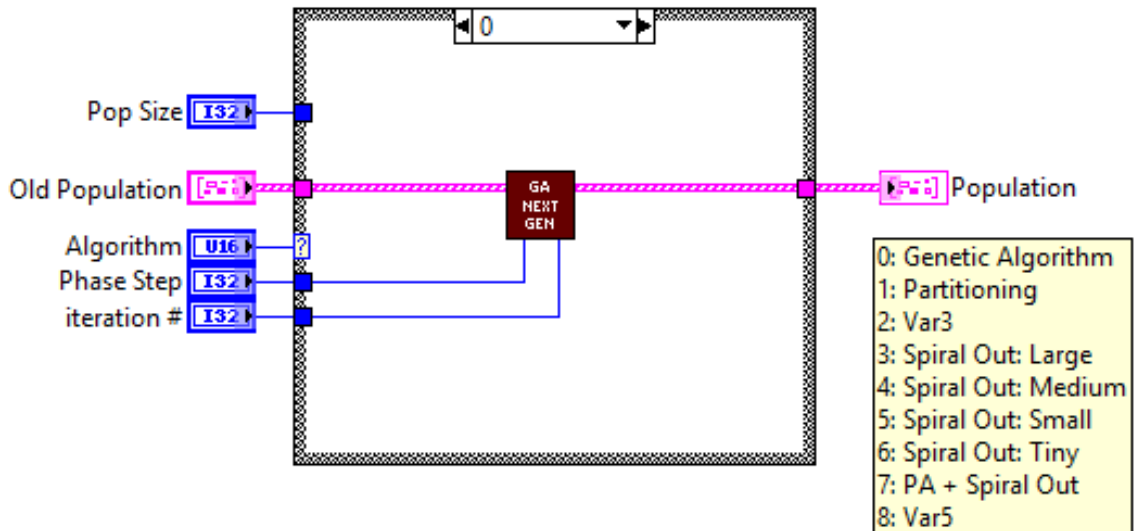
Figure B.18: Pop Next Gen sub-VI block diagram. Case 0 is for the genetic algorithm. It runs the sub-VI GA Next Gen (Figs. B.20, B.21).
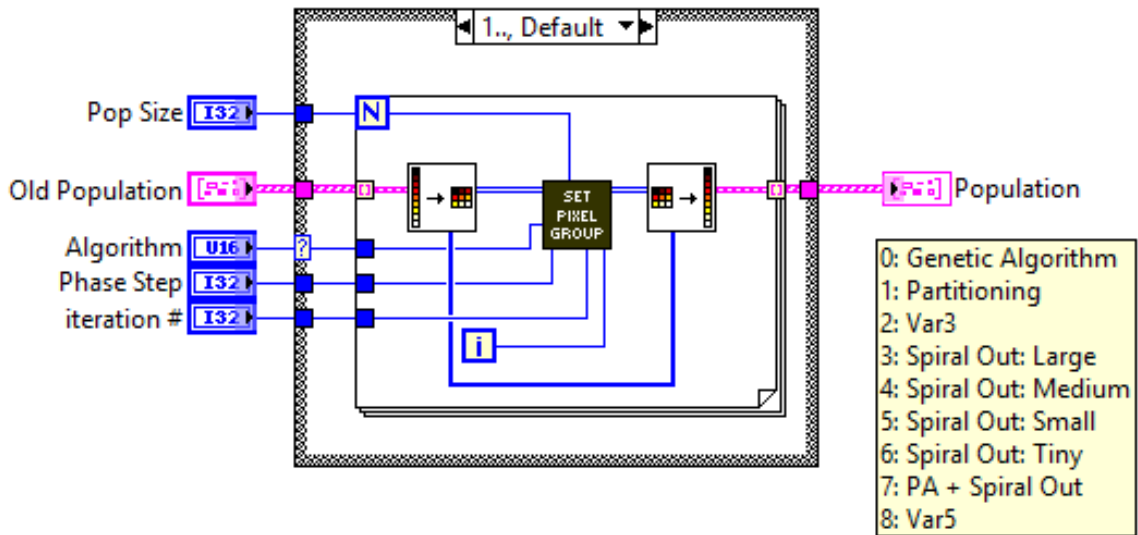
Figure B.19: Pop Next Gen sub-VI block diagram. Case 1 is for all algorithms except the genetic algorithm. This includes the partitioning algorithm, and the continuous sequential algorithm. It runs the sub-VI "Set Pixel Group" (Figs. B.28, B.29, B.30, B.31, B.32, B.33, B.34, B.35, B.36) to facilitate these algorithms.
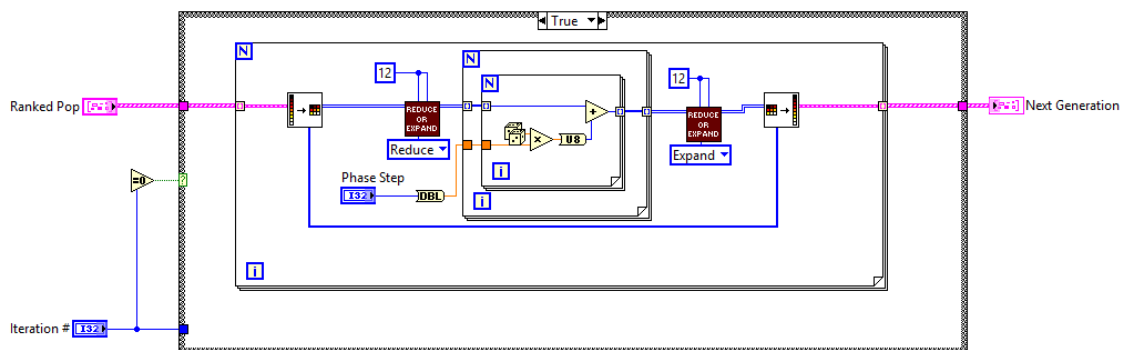
Figure B.20: GA Next Gen sub-VI block diagram. For the first iteration (Case True), each phase mask is populated with an array of randomly selected numbers. The number of phase masks in the population array is controled on the front panel (Population control, see Fig. B.1). The "Reduce or Expand" sub-VI (see Figs. B.25, B.26) makes it possible to treat blocks of neighboring pixels (or pixel groups) as a single pixel.
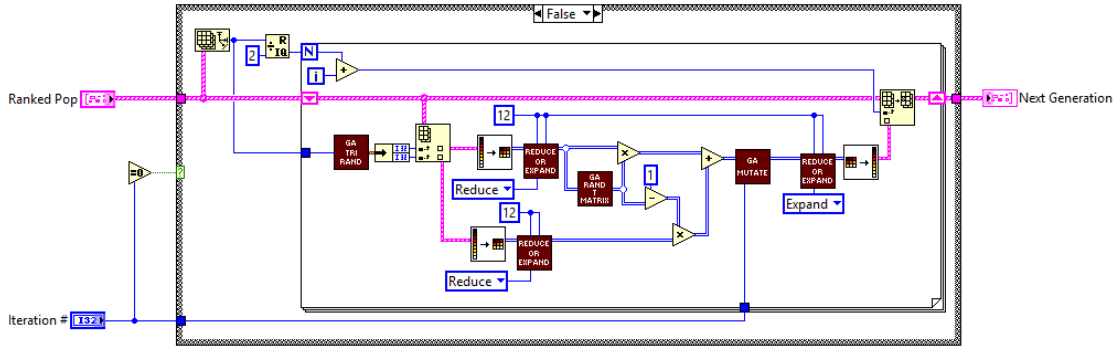
Figure B.21: GA Next Gen sub-VI block diagram. After the first iteration, each next generation phase mask is created by randomly mixing two parent phase masks. The parent phase masks are selected with a triangular probability weighting those masks with better fitness scores with a higher probability. The "GA Tri Rand" sub-VI (Fig. B.22) selects the two parent masks according to the triangular probability. The "Reduce or Expand" sub-VI (Figs. B.25, B.26) enables pixel grouping. The "GA Rand T Matrix" sub-VI (Fig. B.23) generates a random binary mask to fascilitate the random mixing of the two parent masks. The "GA Mutate" sub-VI (Fig. B.24) introduces small mutations to the next generation phase mask.
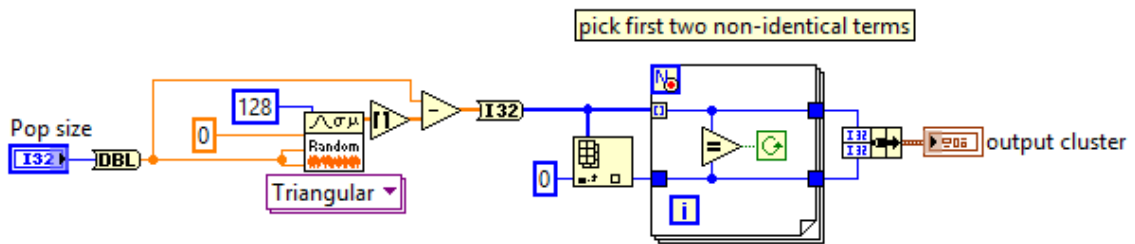
Figure B.22: GA Tri Rand sub-VI block diagram. This sub-VI selects two parent masks according to a triangular probability.

184
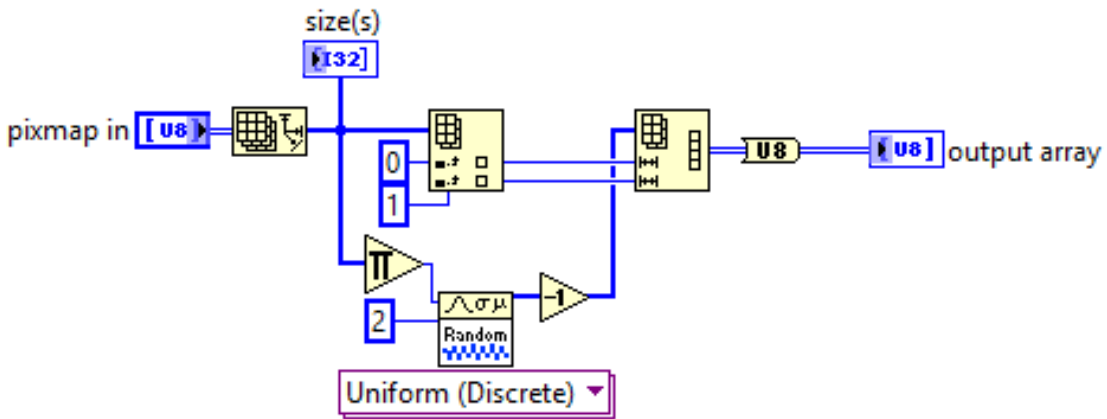
Figure B.23: GA Rand T Matrix sub-VI block diagram. This sub-VI generates a random binary mask to fascilitate the random mixing of the two parent masks.
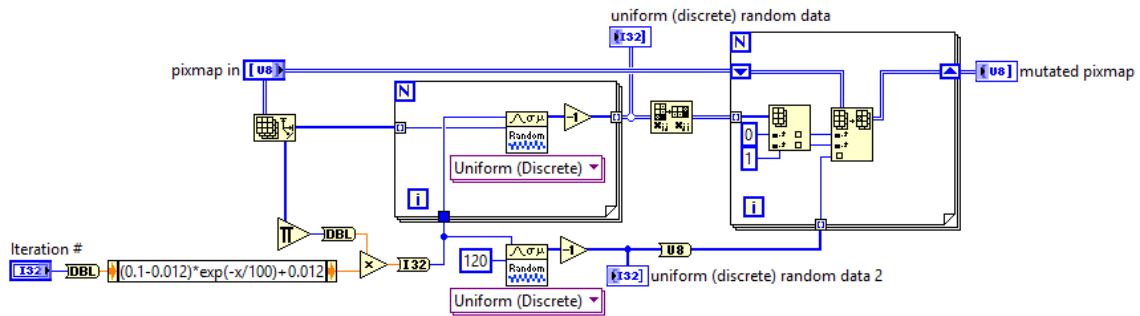
Figure B.24: GA Mutate sub-VI block diagram. This sub-VI introduces small mutations to the next generation phase mask.
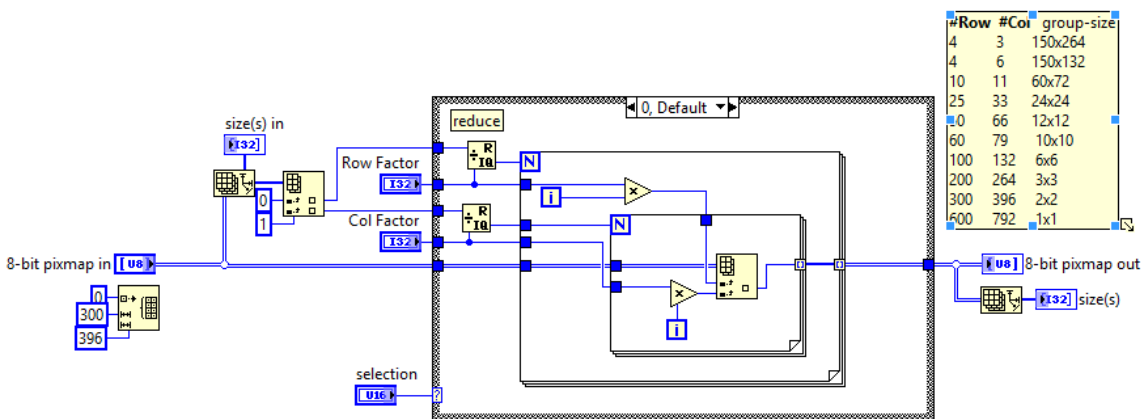
Figure B.25: Reduce or Expand sub-VI block diagram. For case 0, this sub-VI reduces an input matrix by given factors in each dimension. The reduction is such that elements separated by distances equal to the factors are retained in the reduced matrix.
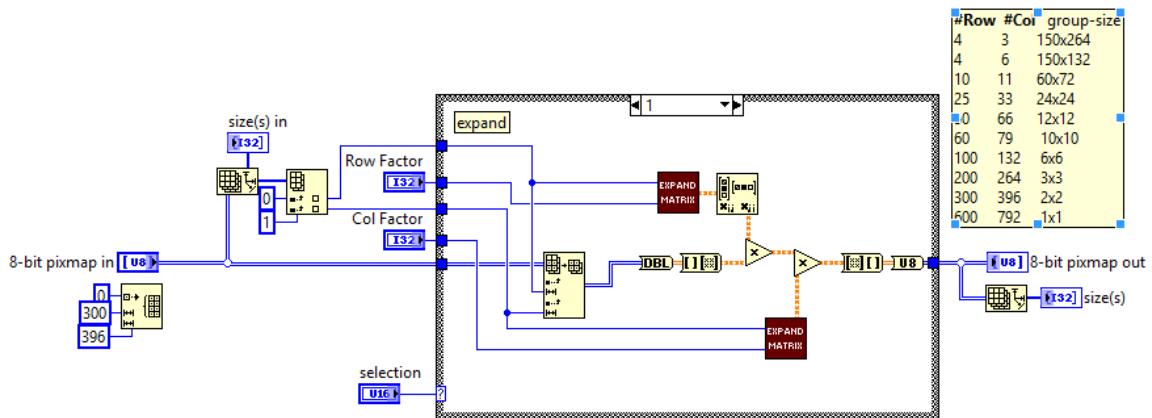
Figure B.26: Reduce or Expand sub-VI block diagram. For case 1, this sub-VI expands an input matrix by given factors in each dimension. The expansion is such that each original element is duplicated to create blocks/groups of neighboring elements with the same values. It makes use of the sub-VI "Expand Matrix" (Fig. B.27), and matrix multiplication.
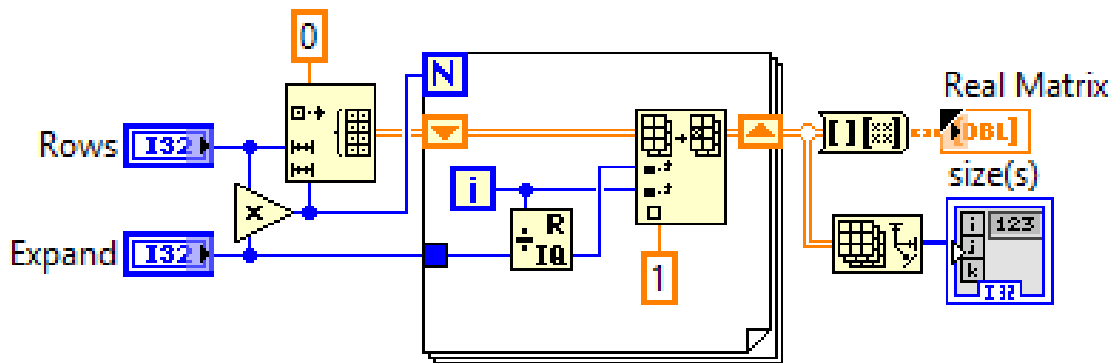
Figure B.27: Expand Matrix sub-VI block diagram. This sub-VI generates a matrix of ones with dimensions dictated by the size of the input matrix and the expansion factor. This matrix is used with matrix multiplication to expand in the input array in Fig. B.26.

186
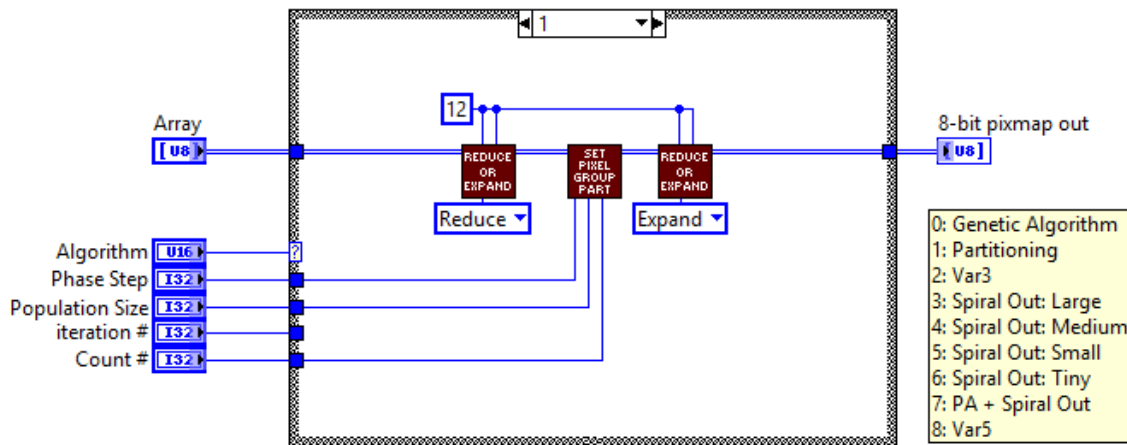
Figure B.28: Set Pixel Group sub-VI block diagram. Case 1 applies the partitioning algorithm via the sub-VI "Set Pixel Group Part" (Figs. B.37, B.38). The "Reduce or Expand" sub-VI (see Figs. B.25, B.26) makes it possible to treat blocks of neighboring pixels (or pixel groups) as a single pixel.
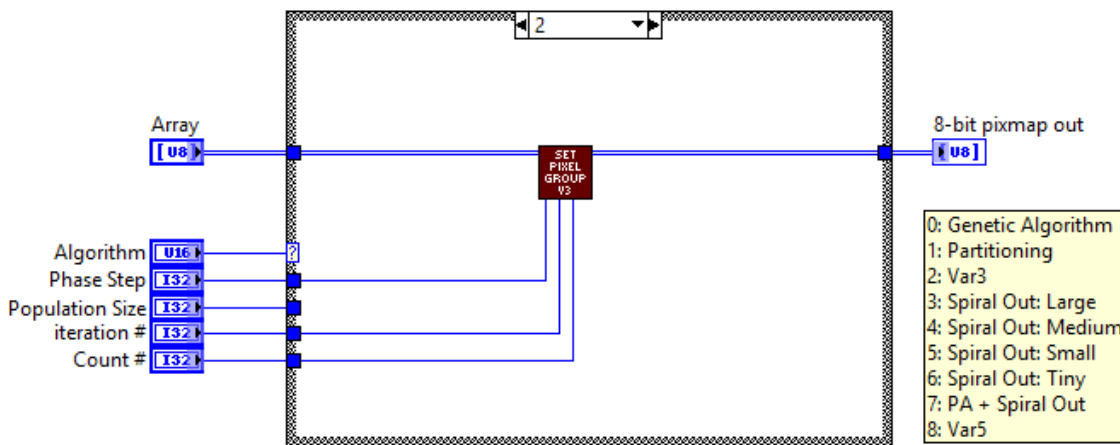
Figure B.29: Set Pixel Group sub-VI block diagram. Case 2 applies the continuous sequential algorithm with 3 varying pixel groups sizes via the sub-VI "Set Pixel Group V3" (Figs. B.39, B.40, B.41). For each pixel group, the pixel selection occurs in a spiraling outward selection order.

187
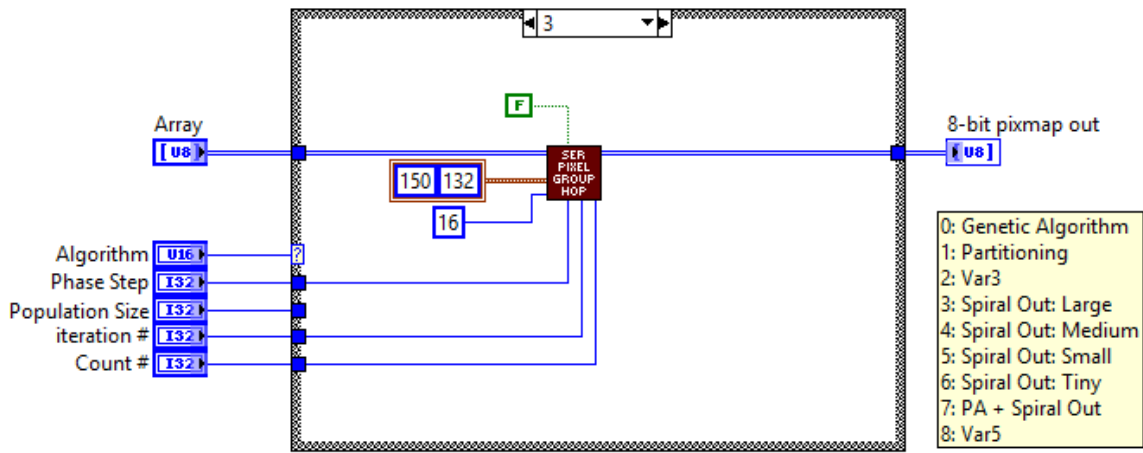
Figure B.30: Set Pixel Group sub-VI block diagram. Case 3 applies the continuous sequential algorithm via the sub-VI "Set Pixel Group Hop" (Fig. B.48). Here, large sized pixel groups are used and selected in a spiraling outward order.
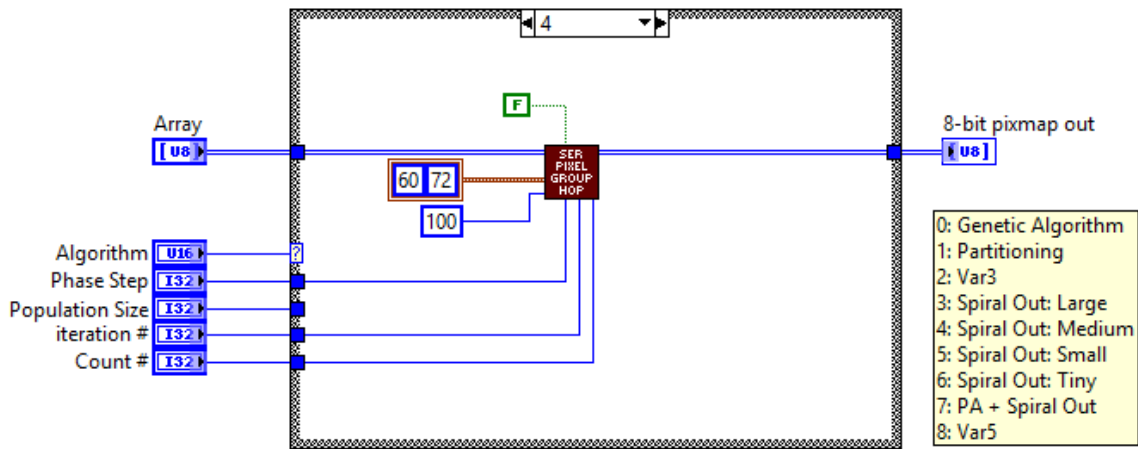
Figure B.31: Set Pixel Group sub-VI block diagram. Case 4 applies the continuous sequential algorithm via the sub-VI "Set Pixel Group Hop" (Fig. B.48). Here, medium sized pixel groups are used and selected in a spiraling outward order.
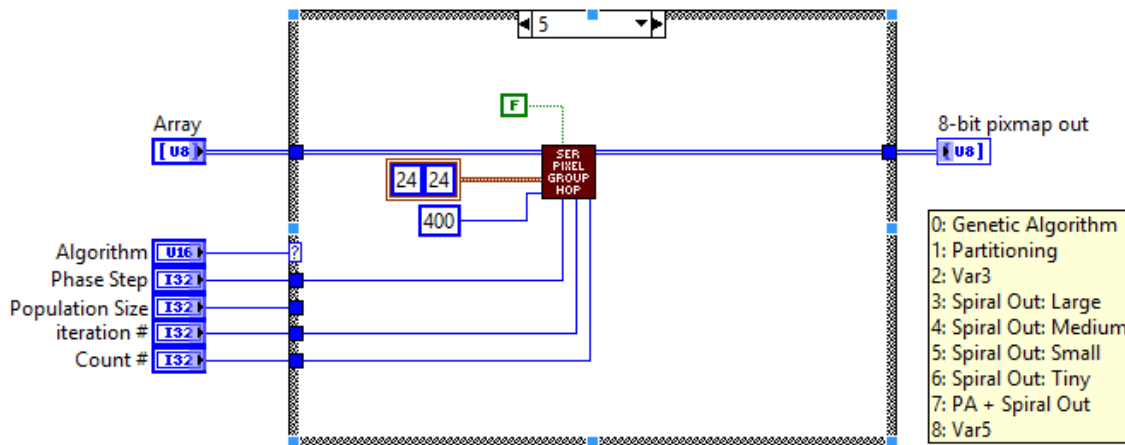
Figure B.32: Set Pixel Group sub-VI block diagram. Case 5 applies the continuous sequential algorithm via the sub-VI "Set Pixel Group Hop" (Fig. B.48). Here, small sized pixel groups are used and selected in a spiraling outward order.
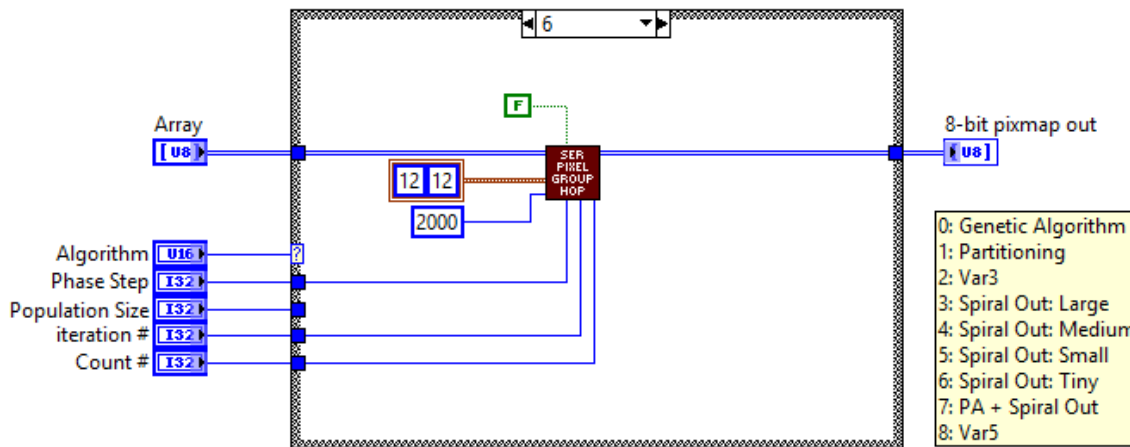
Figure B.33: Set Pixel Group sub-VI block diagram. Case 6 applies the continuous sequential algorithm via the sub-VI "Set Pixel Group Hop" (Fig. B.48). Here, tiny sized pixel groups are used and selected in a spiraling outward order.
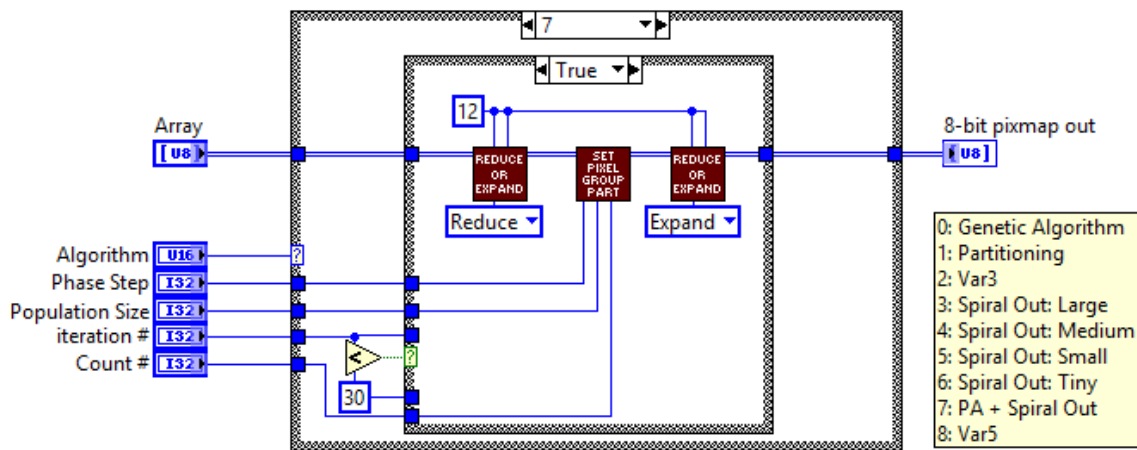
Figure B.34: Set Pixel Group sub-VI block diagram. Case 7 applies a combination of the partitioning and the continuous sequential algorithms. For the first 30 iterations, the partitioning algorithm is run identically to case 1 (Fig. B.28). After 30 iterations the continuous sequential algorithm is used (Fig. B.35).
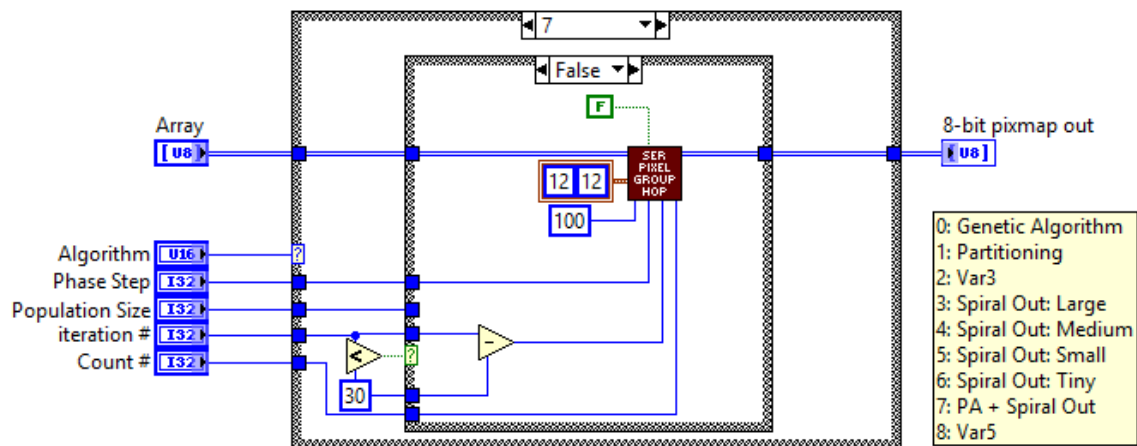
Figure B.35: Set Pixel Group sub-VI block diagram. Case 7 applies a combination of the partitioning and the continuous sequential algorithms. For the first 30 iterations, the partitioning algorithm is run (Fig. B.34. After 30 the continuous sequential algorithm is used as shown here. This is the same continuous sequential algorithm configuration used in case 6 (Fig. B.33), namely, tiny pixel groups in a spiral out orientation.
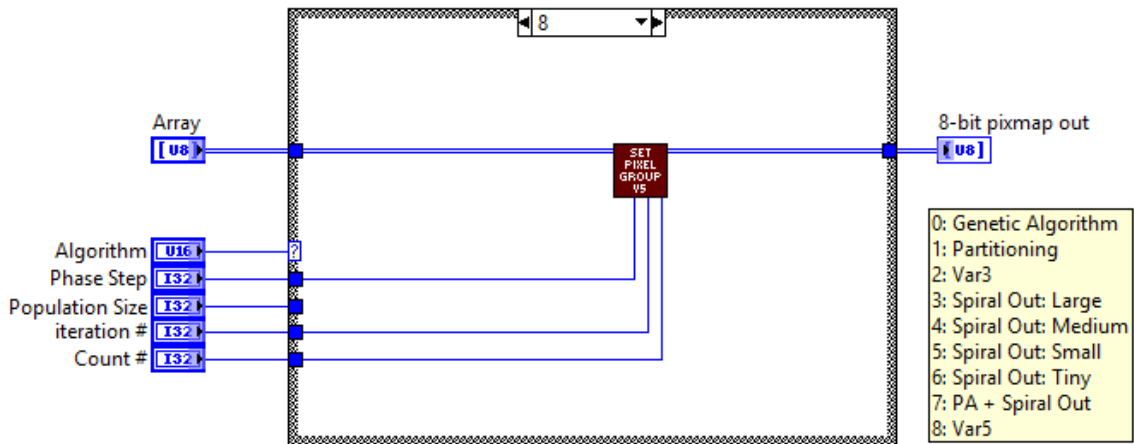
Figure B.36: Set Pixel Group sub-VI block diagram. Case 8 applies the continuous sequential algorithm with 5 varying pixel groups sizes via the sub-VI "Set Pixel Group V5" (Figs. B.49, B.50, B.51, B.52, B.53). For each pixel group, the pixel selection occurs in a spiraling outward selection order.
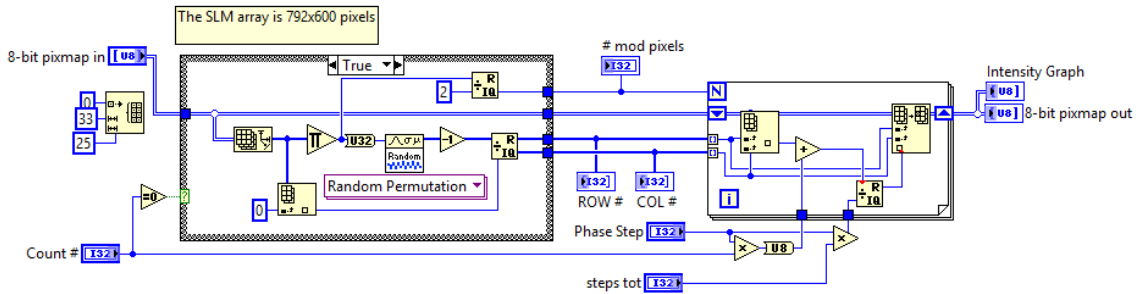
Figure B.37: Set Pixel Group Part sub-VI block diagram. At the start of each iteration (Case True), half of the pixel groups in the array are randomly selected. The phase applied by these pixels is then shifted by a set amount for each step in the iteration.
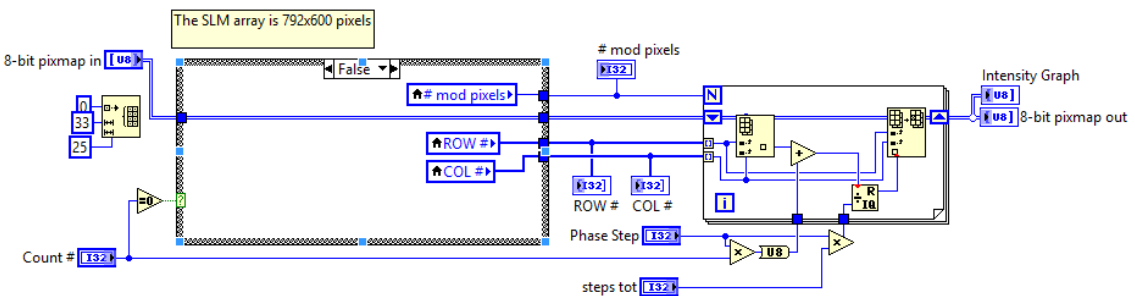
Figure B.38: Set Pixel Group Part sub-VI block diagram. Case false corresponds to the middle of each iteration. Here the pixel group selection is not changed, but the phase applied by the selected pixels is shifted by a set amount for each step in the iteration.

191

Figure B.39: Set Pixel Group V3 sub-VI block diagram. This sub-VI selects pixel groups, starting in the center of the array, and spiraling outward each iteration. Three different pixel group sizes are used, starting with large groups and stepping down to smaller group sizes. This case uses large pixel groups for the first 16 iterations. This sub-VI utilizes the "2D Ones" sub-VI (Fig. B.42) to generate an array populated with a constant value, and the "Square Spiral" sub-VI (Fig. B.43, B.44, B.45, B.46, B.47) to select the pixel group to be modulated based on iteration.

Figure B.40: Set Pixel Group V3 sub-VI block diagram. This sub-VI selects pixel groups, starting in the center of the array, and spiraling outward each iteration. Three different pixel group sizes are used, starting with large groups and stepping down to smaller group sizes. This case uses medium-sized pixel groups for the iteration 16 to iteration 87. This sub-VI utilizes the "2D Ones" sub-VI (Fig. B.42) to generate an array populated with a constant value, and the "Square Spiral" sub-VI (Fig. B.43, B.44, B.45, B.46, B.47) to select the pixel group to be modulated based on iteration.

Figure B.41: Set Pixel Group V3 sub-VI block diagram. This sub-VI selects pixel groups, starting in the center of the array, and spiraling outward each iteration. Three different pixel group sizes are used, starting with large groups and stepping down to smaller group sizes. This case uses small pixel groups for the iteration numbers greater than 87. This sub-VI utilizes the "2D Ones" sub-VI (Fig. B.42) to generate an array populated with a constant value, and the "Square Spiral" sub-VI (Fig. B.43, B.44, B.45, B.46, B.47) to select the pixel group to be modulated based on iteration.
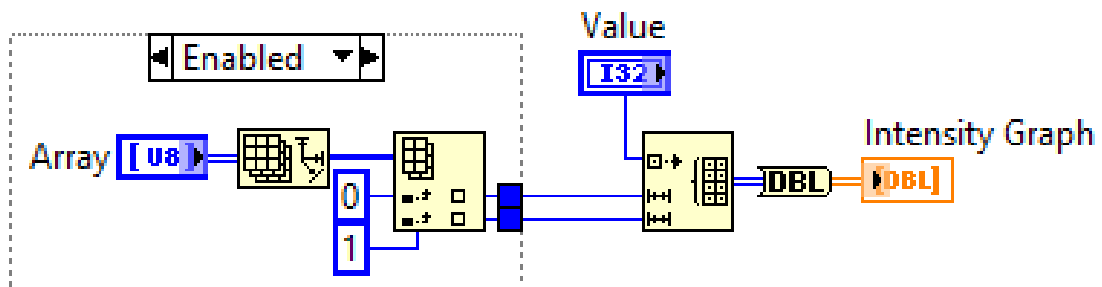
Figure B.42: 2D Ones sub-VI block diagram. This sub-VI generates a 2D array with the same dimensions as the input array, and populated with an input constant value.
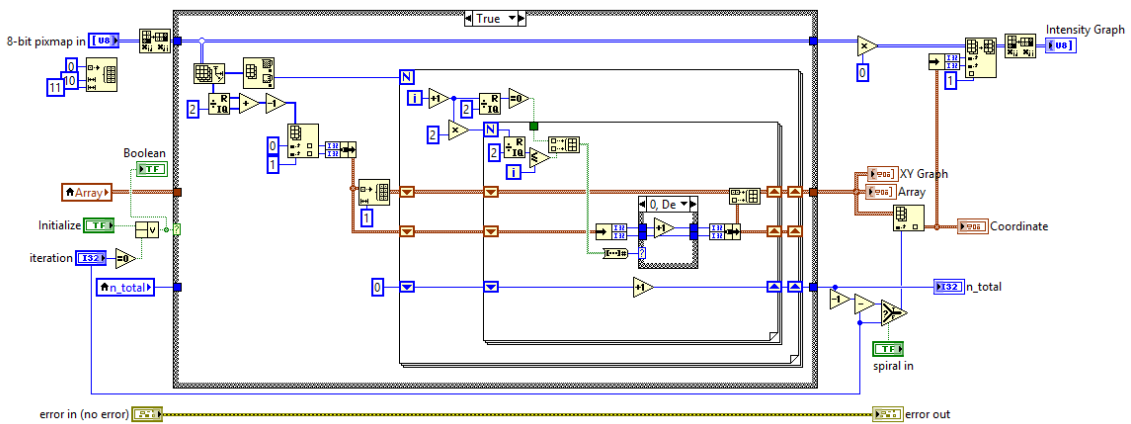
Figure B.43: Square Spiral block diagram. This sub-VI generates and reads a list of 2D array coordinates starting at the center of the array and spiraling outward. For iteration zero, or when triggered through the initialize switch (case True), this sub-VI generates the coordinate list.
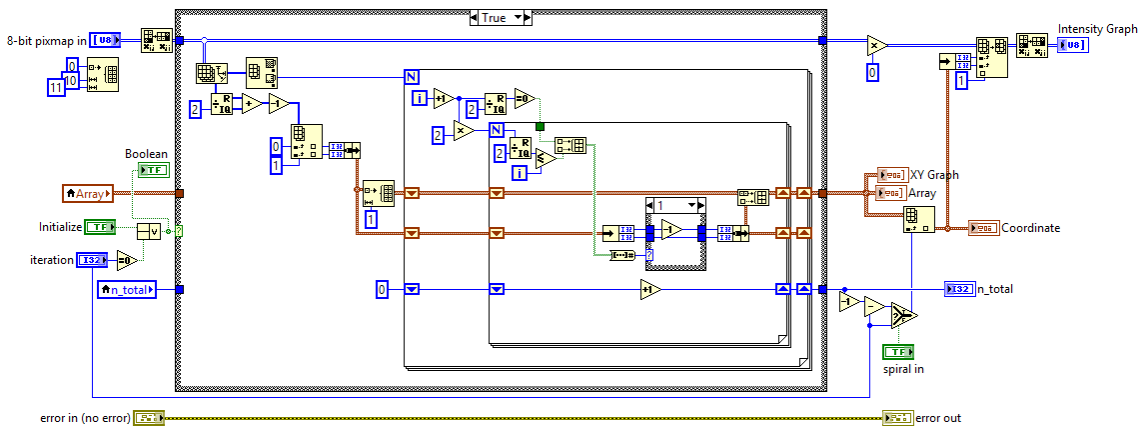
Figure B.44: Square Spiral block diagram. This sub-VI generates and reads a list of 2D array coordinates starting at the center of the array and spiraling outward. For iteration zero, or when triggered through the initialize switch (case True), this sub-VI generates the coordinate list.
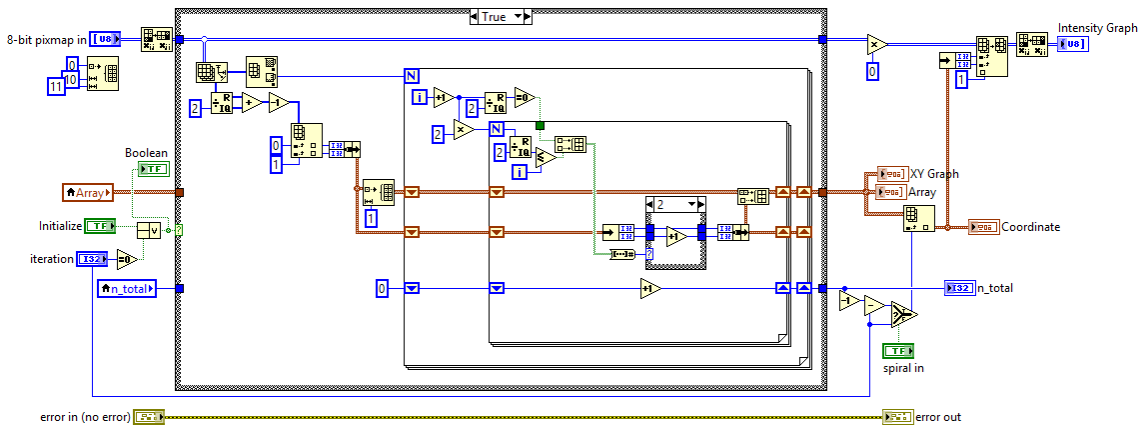
Figure B.45: Square Spiral block diagram. This sub-VI generates and reads a list of 2D array coordinates starting at the center of the array and spiraling outward. For iteration zero, or when triggered through the initialize switch (case True), this sub-VI generates the coordinate list.
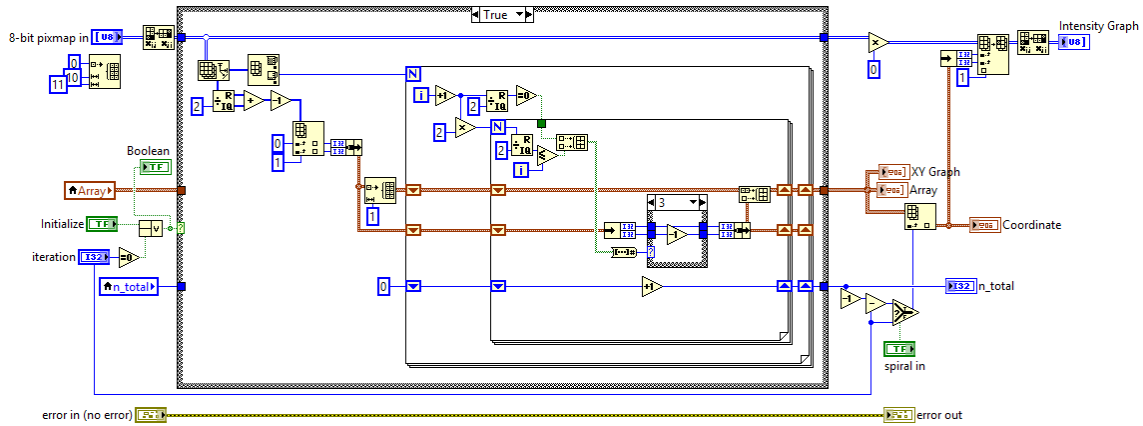
Figure B.46: Square Spiral block diagram. This sub-VI generates and reads a list of 2D array coordinates starting at the center of the array and spiraling outward. For iteration zero, or when triggered through the initialize switch (case True), this sub-VI generates the coordinate list.
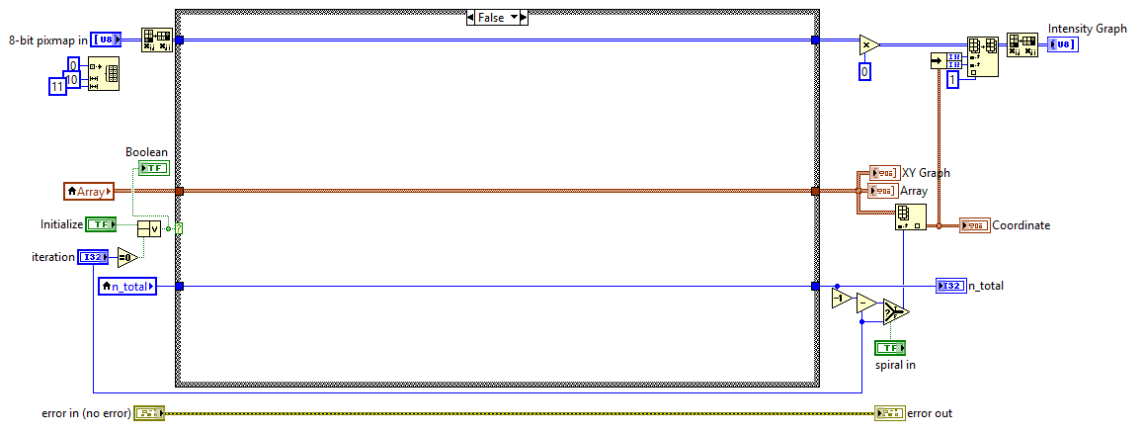
Figure B.47: Square Spiral block diagram. This sub-VI generates and reads a list of 2D array coordinates starting at the center of the array and spiraling outward. When the initialization is not triggered (case False), this sub-VI reads the previously generated coordinate list.
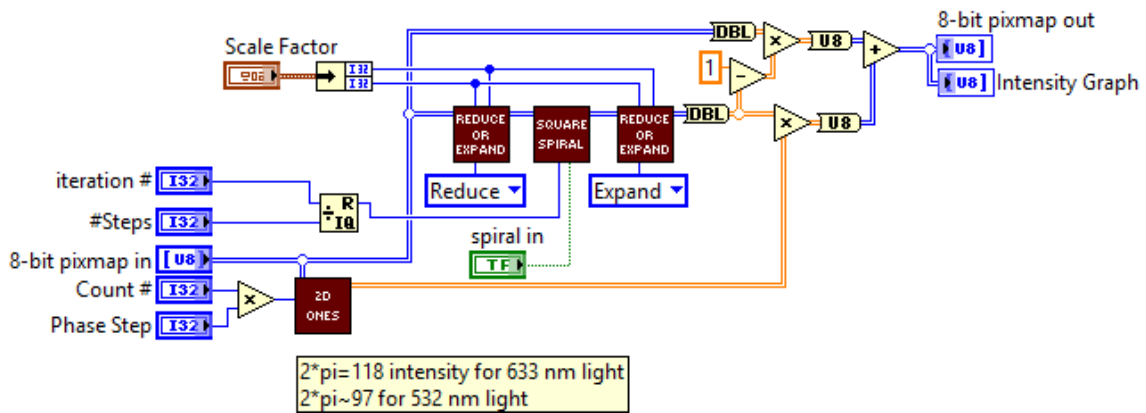
Figure B.48: Set Pixel Group Hop sub-VI block diagram. This sub-VI selects and modifies a pixel group based on algorithm iteration. The selection starts in the center of the phase mask and spirals outward one step each iteration. The "Square Spiral" sub-VI (Fig. B.43, B.44, B.45, B.46, B.47) is used to select the pixel group based on iteration. The "2D Ones" sub-VI (Fig. B.42) to generate an array populated with a constant value, facilitating the modulation of only the selected pixel group.

196
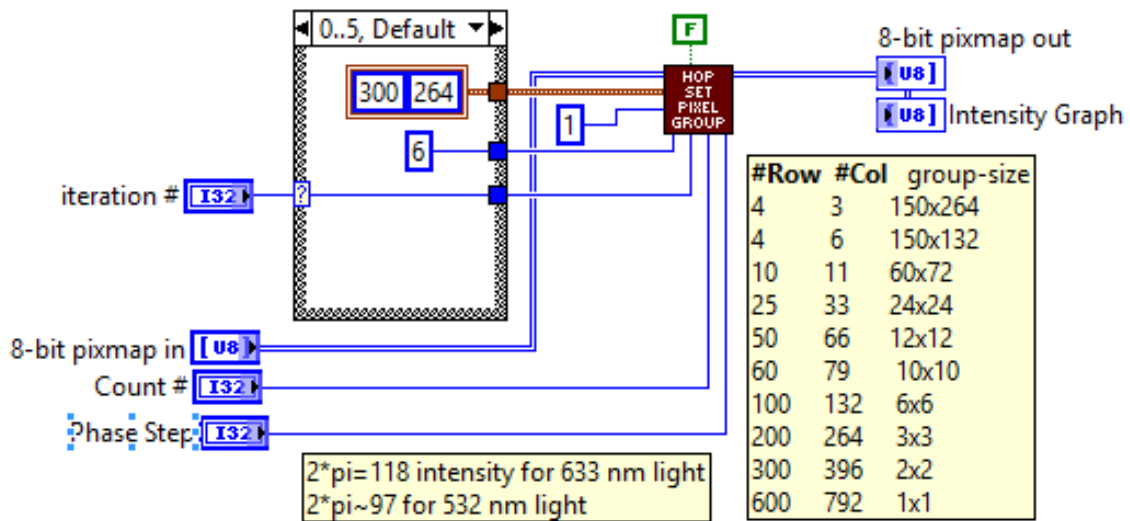
Figure B.49: Set Pixel Group V5 sub-VI block diagram. This sub-VI selects pixel groups, starting in the center of the array, and spiraling outward each iteration. Five different pixel group sizes are used, starting with large groups and stepping down to smaller group sizes. This case uses extra large pixel groups for the first 6 iterations. This sub-VI utilizes the "Hop Set Pixel Group" sub-VI (Figs. B.54, B.55) to select the pixel group elements and modulate them based on iteration number.
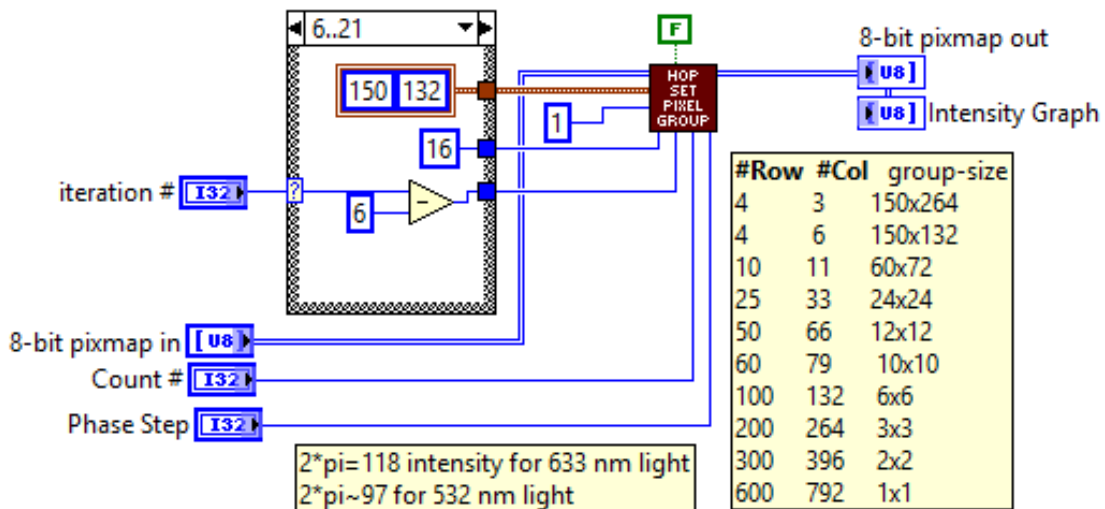
Figure B.50: Set Pixel Group V5 sub-VI block diagram. This sub-VI selects pixel groups, starting in the center of the array, and spiraling outward each iteration. Five different pixel group sizes are used, starting with large groups and stepping down to smaller group sizes. This case uses large pixel groups for iterations 6 through 21. This sub-VI utilizes the "Hop Set Pixel Group" sub-VI (Figs. B.54, B.55) to select the pixel group elements and modulate them based on iteration number.
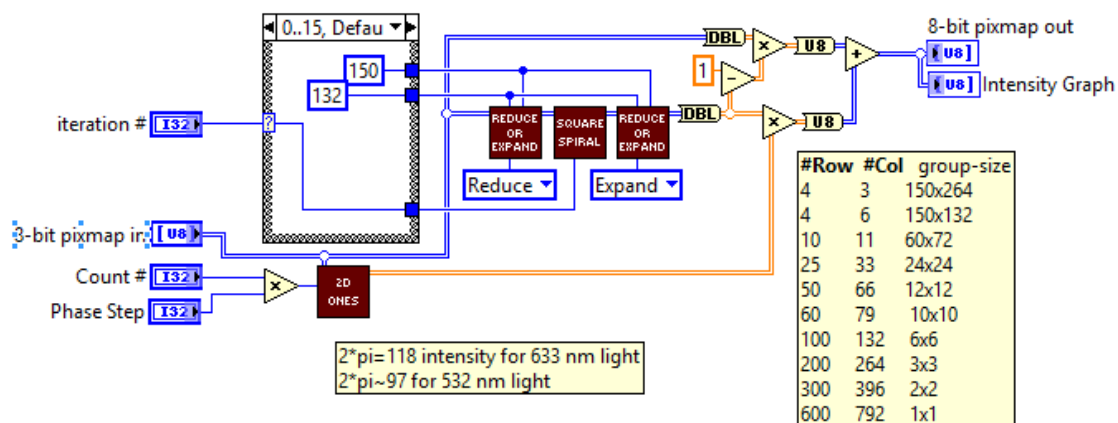
197
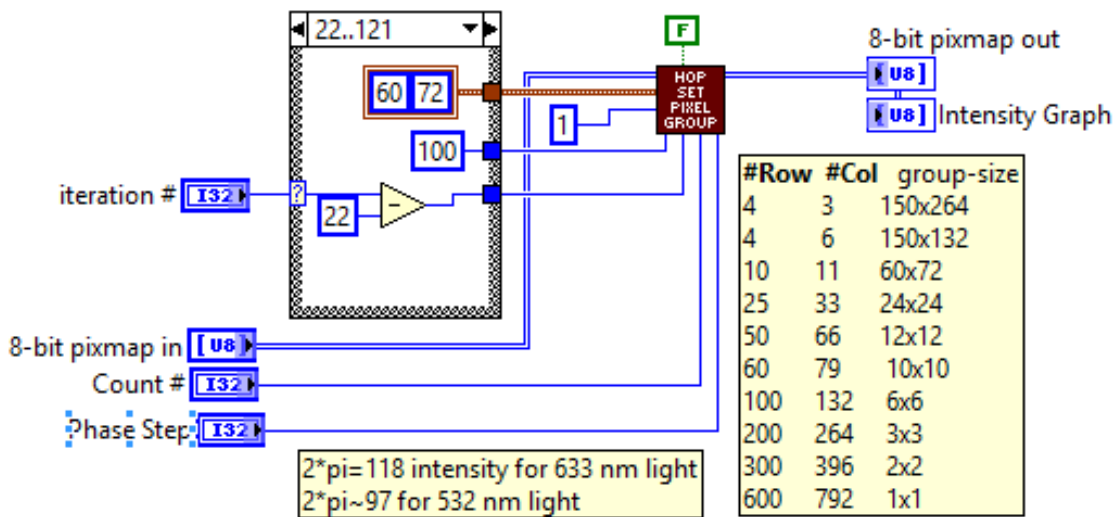
Figure B.51: Set Pixel Group V5 sub-VI block diagram. This sub-VI selects pixel groups, starting in the center of the array, and spiraling outward each iteration. Five different pixel group sizes are used, starting with large groups and stepping down to smaller group sizes. This case uses medium-sized pixel groups for iterations 22 through 121. This sub-VI utilizes the "Hop Set Pixel Group" sub-VI (Figs. B.54, B.55) to select the pixel group elements and modulate them based on iteration number.
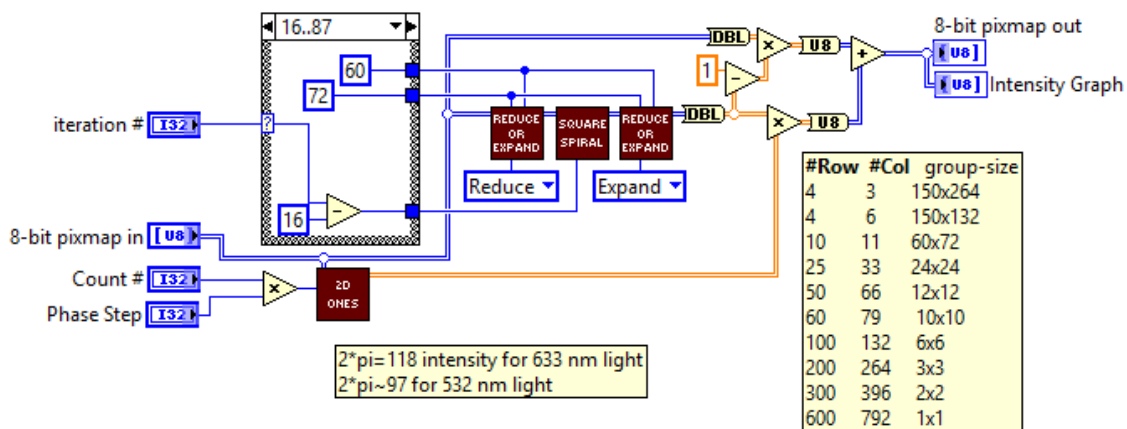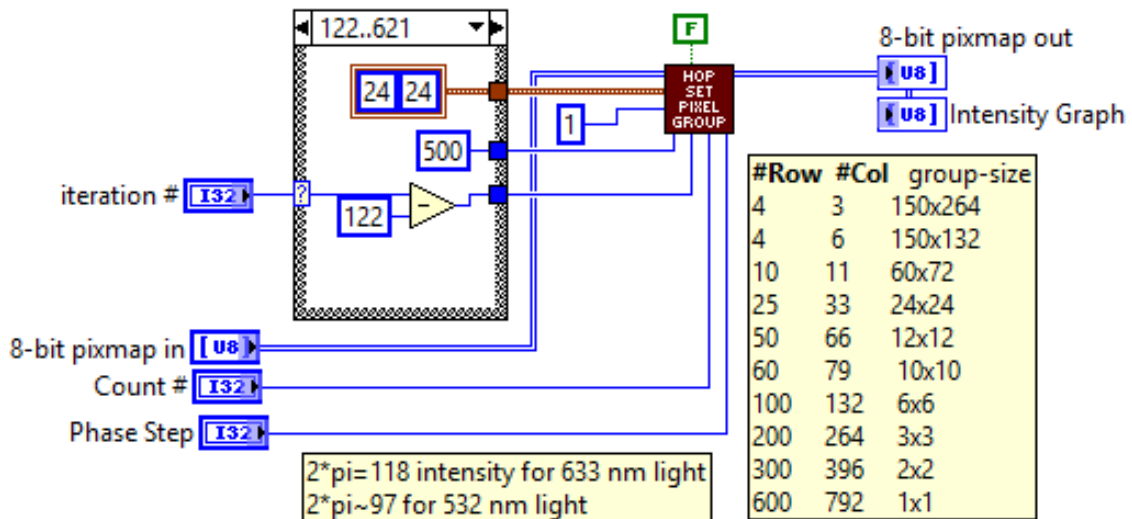

Figure B.52: Set Pixel Group V5 sub-VI block diagram. This sub-VI selects pixel groups, starting in the center of the array, and spiraling outward each iteration. Five different pixel group sizes are used, starting with large groups and stepping down to smaller group sizes. This case uses small pixel groups for iterations 122 through 621. This sub-VI utilizes the "Hop Set Pixel Group" sub-VI (Figs. B.54, B.55) to select the pixel group elements and modulate them based on iteration number.
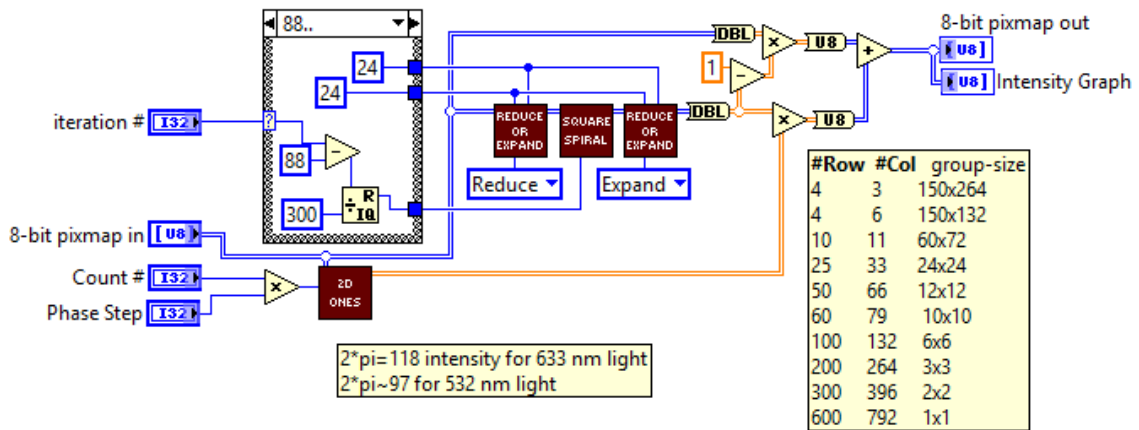
198
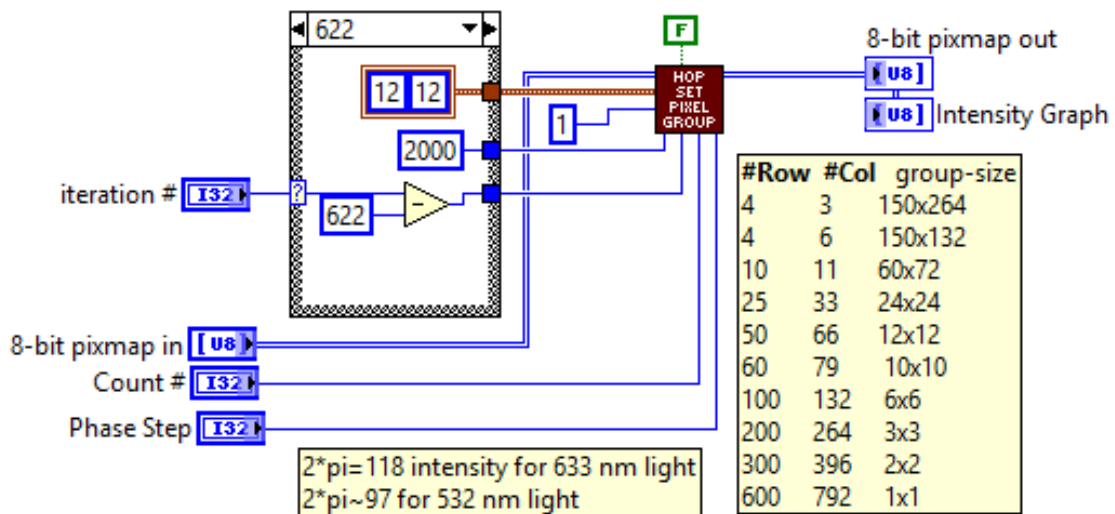
Figure B.53: Set Pixel Group V5 sub-VI block diagram. This sub-VI selects pixel groups, starting in the center of the array, and spiraling outward each iteration. Five different pixel group sizes are used, starting with large groups and stepping down to smaller group sizes. This case uses tiny pixel groups for iteration numbers greater than 621. This sub-VI utilizes the "Hop Set Pixel Group" sub-VI (Figs. B.54, B.55) to select the pixel group elements and modulate them based on iteration number.
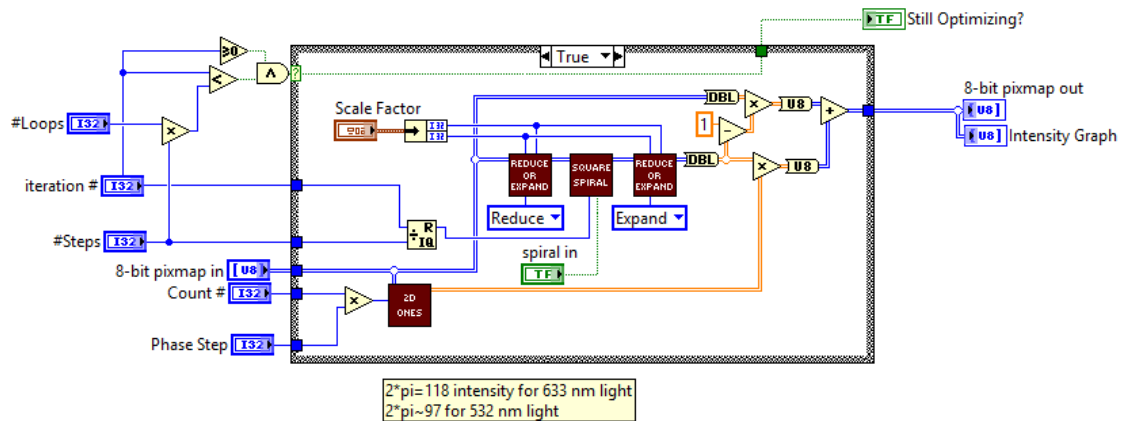
Figure B.54: Hop Set Pixel Group sub-VI block diagram. This sub-VI is nearly identical to the "Set Pixel Group Hop" sub-VI (Fig. B.48). It adds a case structure, which takes into consideration the initializing iteration ($n = -1$) and the total number of iterations. Here, the algorithm selects and modifies a pixel group based on algorithm iteration. The selection starts in the center of the phase mask and spirals outward one step each iteration. The "Square Spiral" sub-VI (Fig. B.43, B.44, B.45, B.46, B.47) is used to select the pixel group based on iteration. The "2D Ones" sub-VI (Fig. B.42) to generate an array populated with a constant value, facilitating the modulation of only the selected pixel group.

199
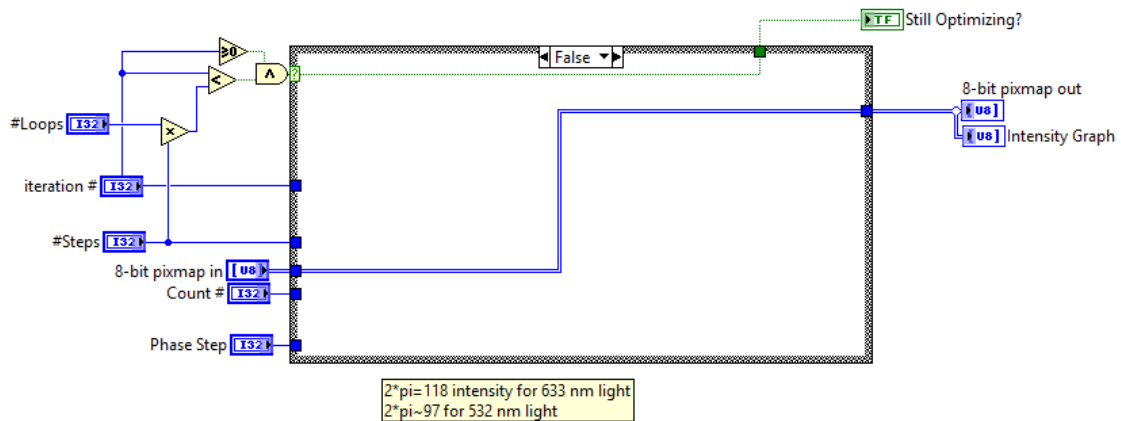
Figure B.55: Hop Set Pixel Group sub-VI block diagram. This sub-VI is nearly identical to the "Set Pixel Group Hop" sub-VI (Fig. B.48). It adds a case structure, which takes into consideration the initializing iteration ($n = -1$) and the total number of iterations. Here, the algorithm is by-passed when the iteration number is outside of the total iteration range.

B.1.2   Save data sub-VI

The Save Data sub-VI controls the saving of both measured data and the applied phase mask. The front panel allows the user to select whether certain types of data are saved on an iteration by iteration basis. However, whenever the optimization algorithm terminates (either by completion or the abort feature), certain data files are always saved. These files contain the optimized phase mask, the detector trace/image, and the enhancement/fitness score as a function of iteration. The save data sub-VI has two parallel case structures. The first controls where the save command comes from. This depends upon the status of the optimization algorithm. The second case is a true/false case that executes the command to save data. The block diagrams for each of these cases are shown in Figs. B.56, B.57, B.58, and B.59. Sub-VI's that support these functions are also shown if Figs. B.60, B.61, B.62, B.63, B.64, B.65, B.66, B.67, & B.68.

Figure B.56: Save Data sub-VI block diagram, for the case when no save command has been received. As is shown, the saving of data is by-passed in this case.

Figure B.57: Save Data sub-VI block diagram. For this case, the optimization algorithm is not running; however, a manual save command has been received. The sub-VIs "Save Matrix" (Figs. B.60, B.61, B.62), "Save Spect" (Figs. B.63, B.64, B.65), and "Save PNG" (Figs. B.66, B.67, B.68) are used to implement saving of the specific data sets.

Figure B.58: Save Data sub-VI block diagram. For this case, the optimization algorithm has been initialize or is running (case 1 or 3). The case structure has been activated to save data, but the specific data sets that will be saved are controled by the save selector cluster. Thus only data sets selected by the user will be saved. The sub-VIs "Save Matrix" (Figs. B.60, B.61, B.62), "Save Spect" (Figs. B.63, B.64, B.65), and "Save PNG" (Figs. B.66, B.67, B.68) are used to implement the saving of specific data sets.
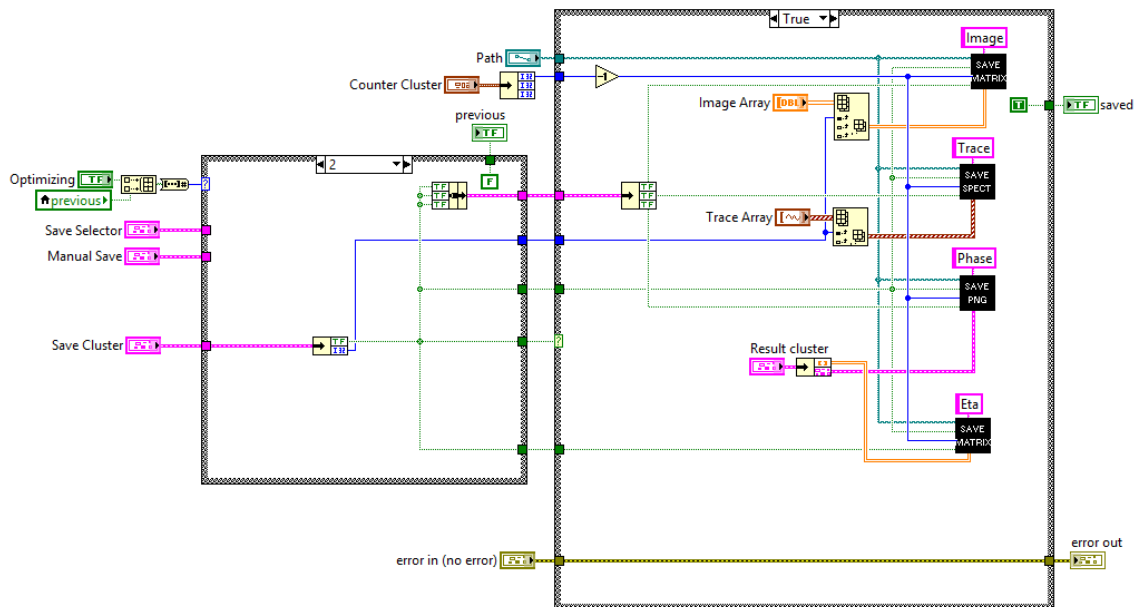
Figure B.59: Save Data sub-VI block diagram. For this case, the optimization algorithm has been terminated (case 2). The case structure has been activated to save data, and the save selector cluster has been overridden so all data sets will be saved. The sub-VIs "Save Matrix" (Figs. B.60, B.61, B.62), "Save Spect" (Figs. B.63, B.64, B.65), and "Save PNG" (Figs. B.66, B.67, B.68) are used to implement the saving of specific data sets.
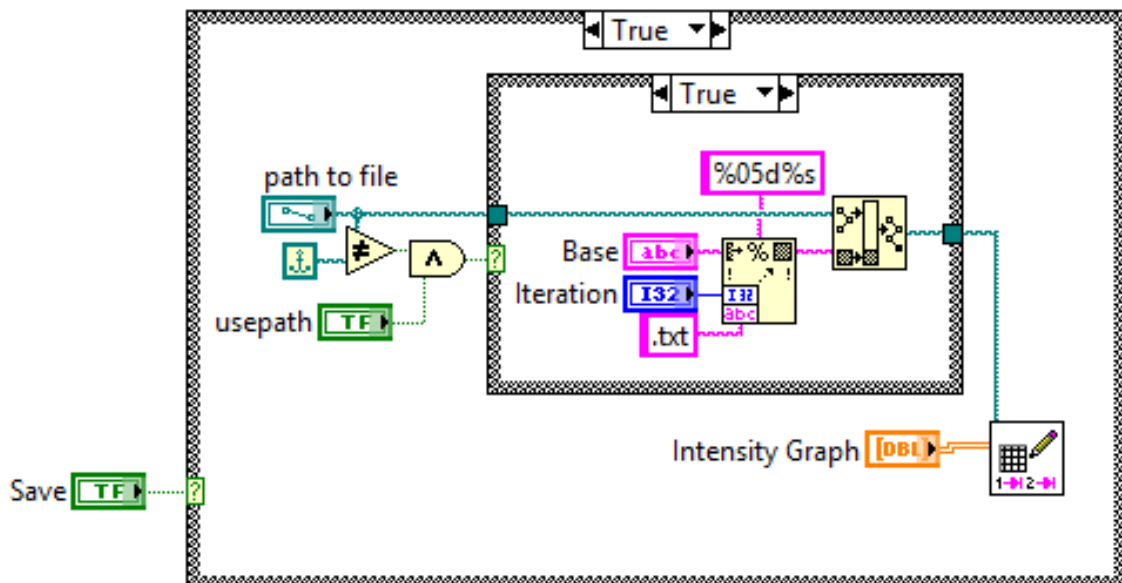
Figure B.60: Save Matrix sub-VI block diagram. When activated, this sub-VI will save data in a spreadsheet (column and row) format at the supplied file location.

203
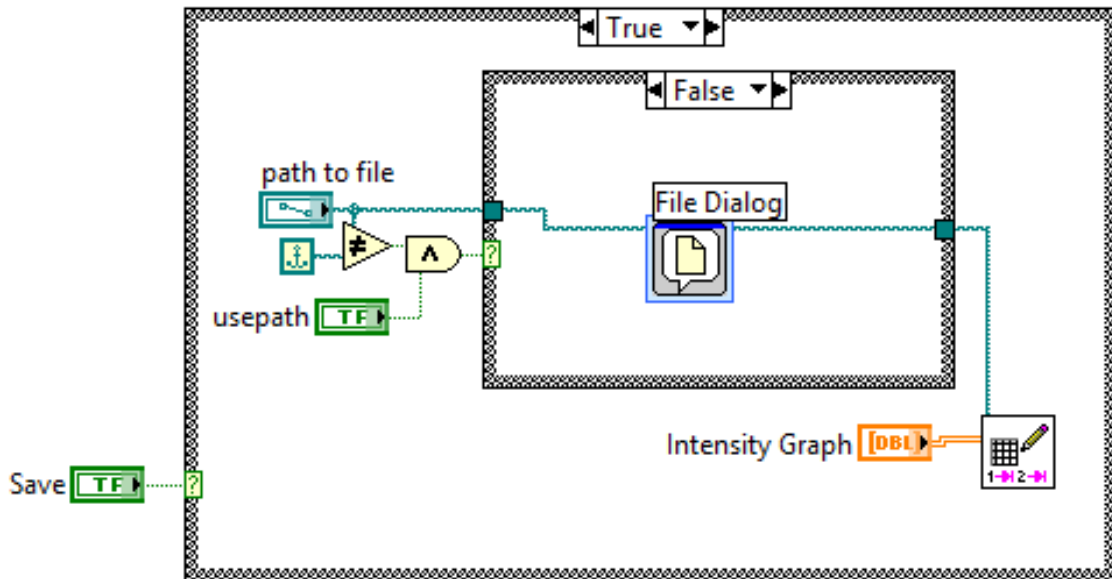
Figure B.61: Save Matrix sub-VI block diagram. When activated, this sub-VI will save data in a spreadsheet (column and row) format. If the file path supplied does not exist, a dialog window will appear.

Figure B.62: Save Matrix sub-VI block diagram. If the save command is false, this sub-VI is by-passed.
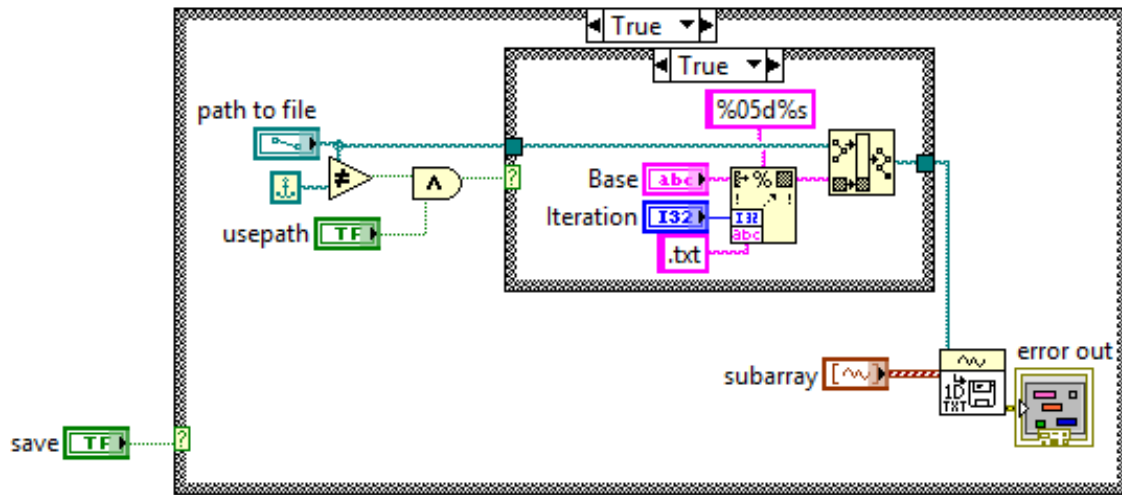
Figure B.63: Save Spect sub-VI block diagram. When activated, this sub-VI will save oscilloscope trace data at the file path supplied.
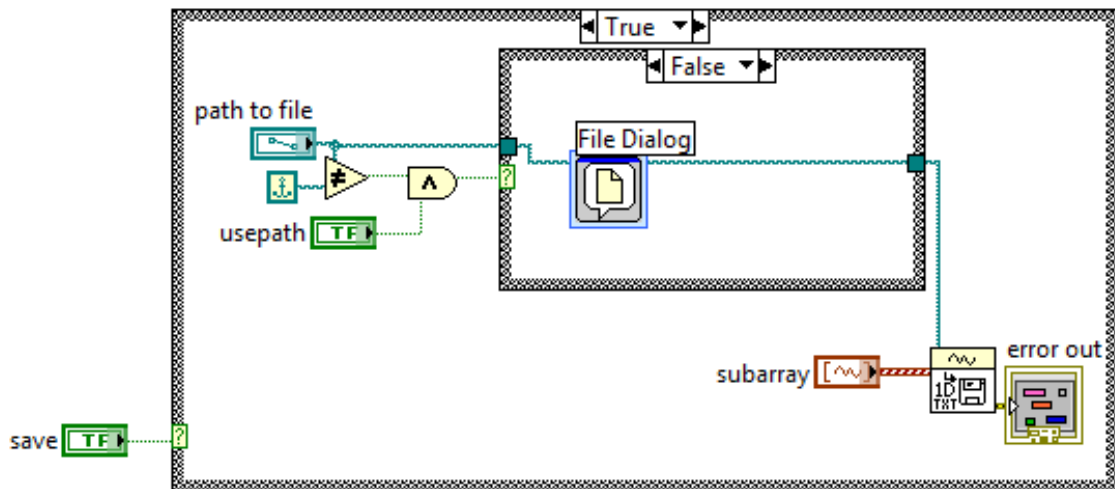
Figure B.64: Save Spect sub-VI block diagram. When activated, this sub-VI will save oscilloscope trace data. If the file path supplied does not exist, a dialog window will appear.
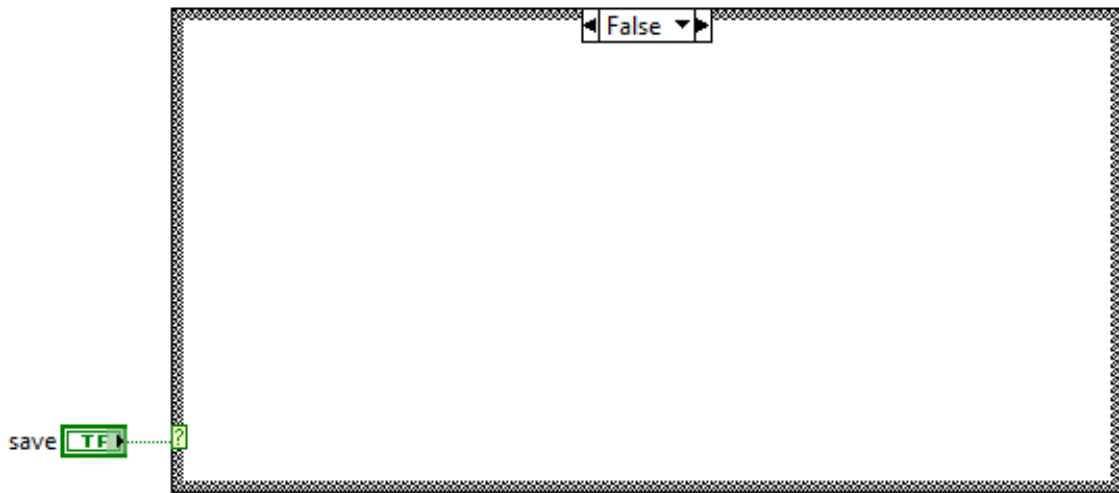
Figure B.65: Save Spect sub-VI block diagram. If the save command is false, this sub-VI is by-passed.
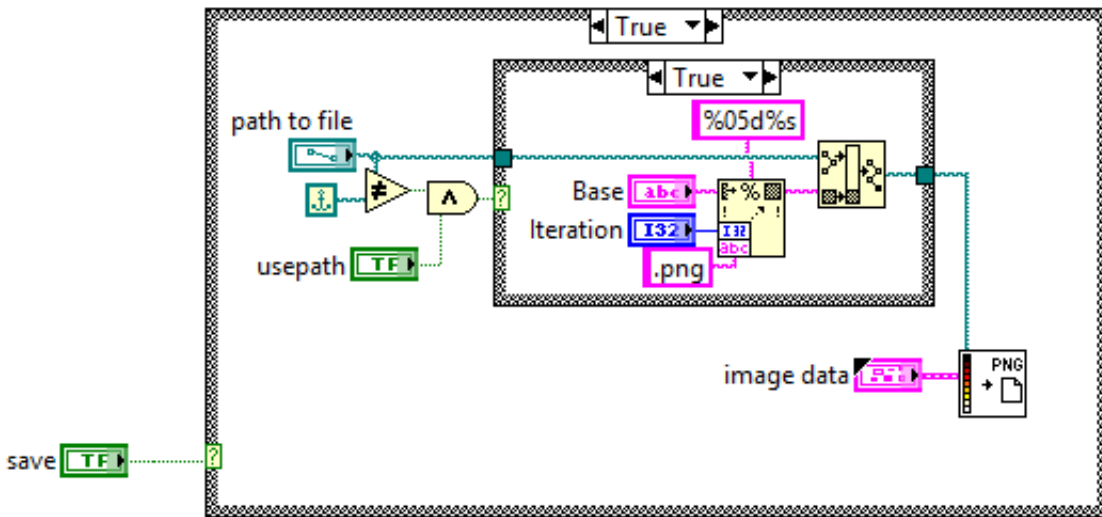
Figure B.66: Save Spect sub-VI block diagram. When activated, this sub-VI will save image data at the file path supplied in the ".png" format.
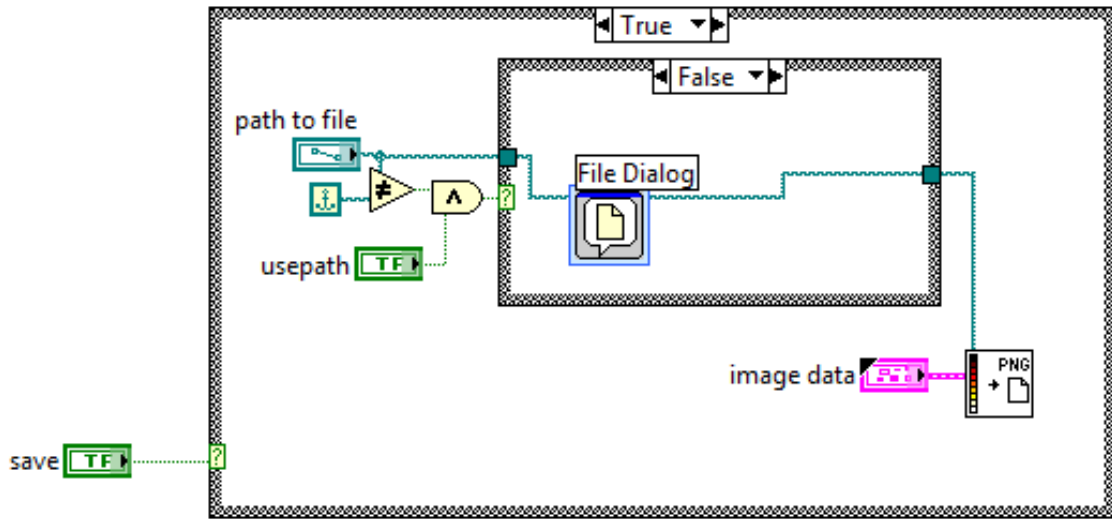
Figure B.67: Save Spect sub-VI block diagram. When activated, this sub-VI will save image data as a ".png" file. If the file path supplied does not exist, a dialog window will appear.
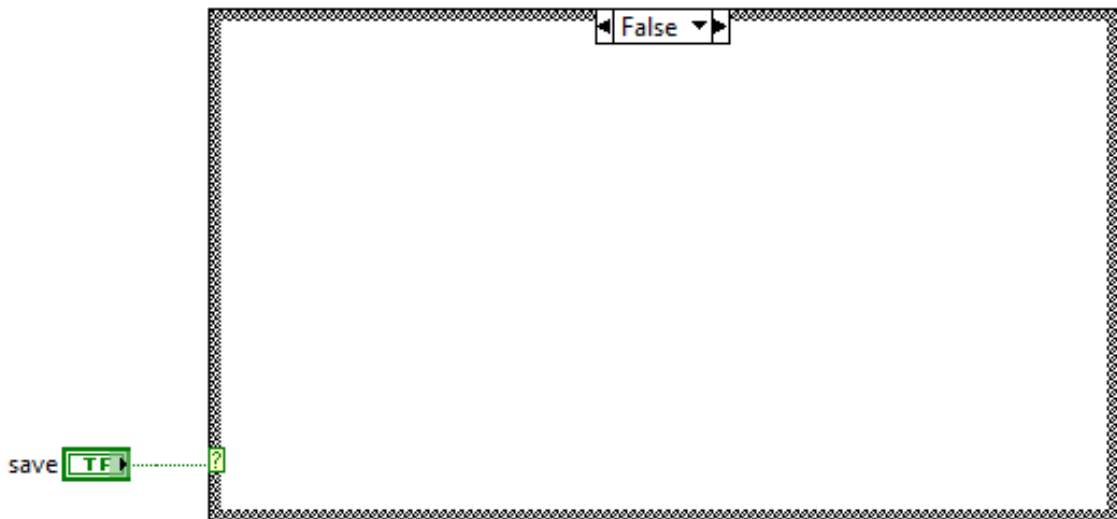
Figure B.68: Save Spect sub-VI block diagram. If the save command is false, this sub-VI is by-passed.

207

B.1.3 SLM phase map sub-VI

The computer treats the Hamamatsu LCOS-SLM as a second monitor. Thus, communication between the computer and the SLM is acheived by displaying the phase mask on a second monitor. This is done with the SLM Phase Map sub-VI, which is shown in Figs. B.69, B.70, B.71, B.72, & B.73. The front panel of this sub-VI (Fig. B.69) was set up to display a picture image. The boarder of the front panel was also fixed to this picture image, so that is all that is displayed. The parameters of the front panel are set in the block diagram, so that when the sub-VI is activated, the front panel is displayed on the second monitor. Thus, the phase mask is sent to the SLM for display.
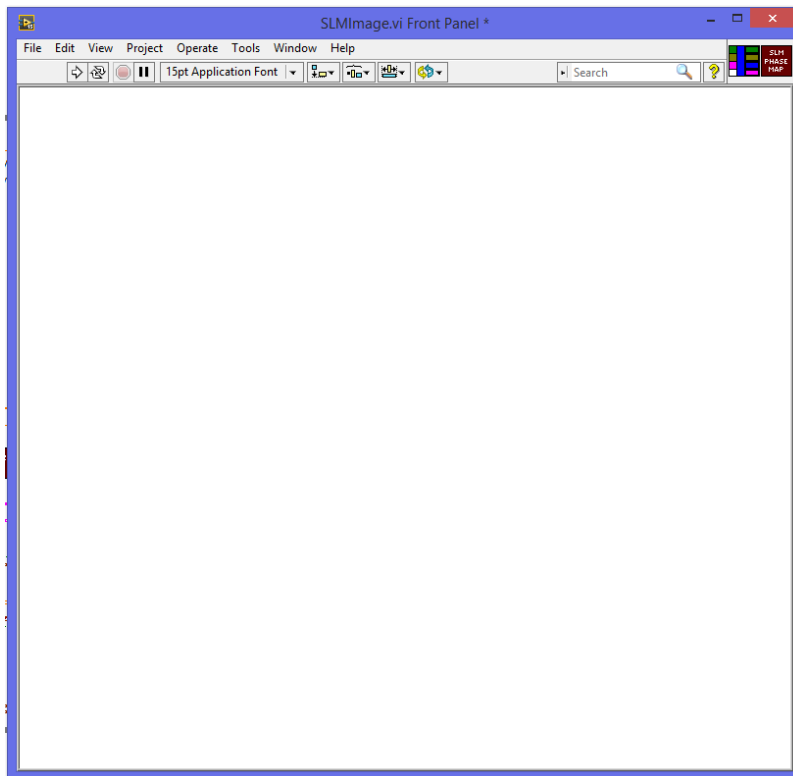
Figure B.69: SLM Phase Map sub-VI front panel. The phase mask is communicated to the SLM by displaying the image as a picture here.
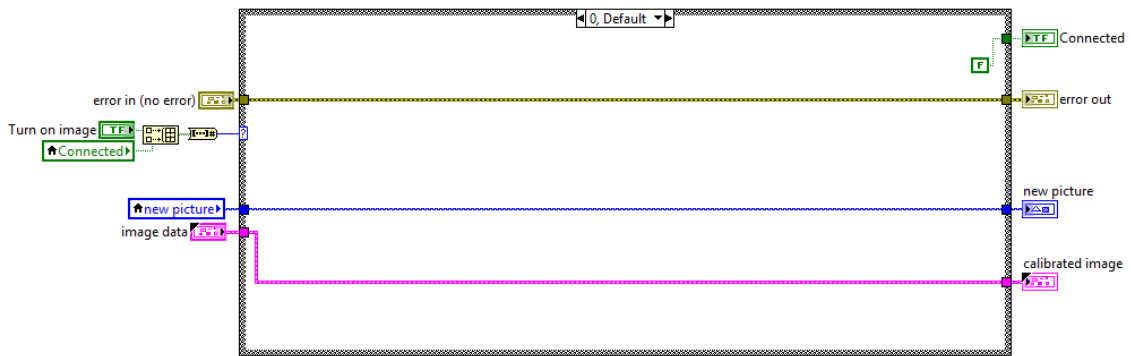
Figure B.70: SLM Phase Map sub-VI block diagram, for the case (case 0) when the SLM is not activated on the front panel of the main VI.
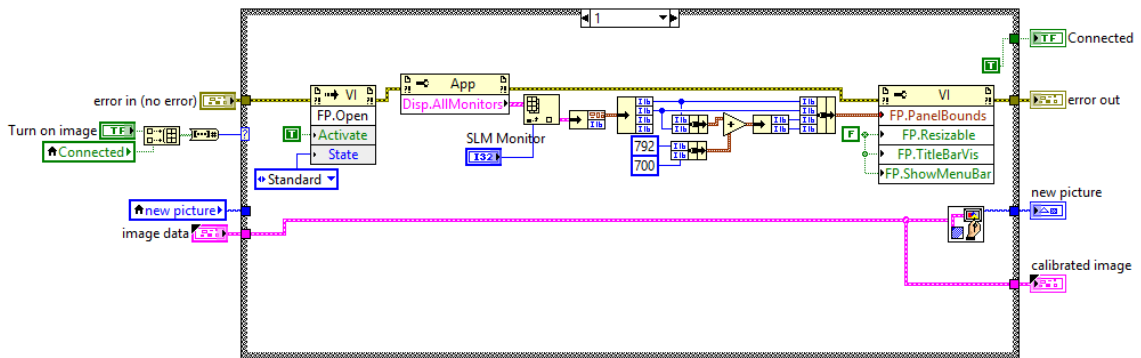
Figure B.71: SLM Phase Map sub-VI block diagram. For this case (case 1), the connection with the SLM has been initialized.
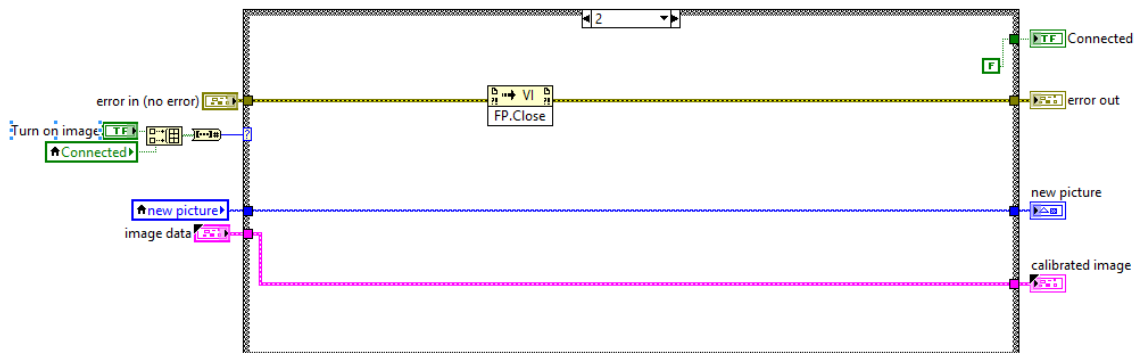
Figure B.72: SLM Phase Map sub-VI block diagram. For this case (case 2), the connection with the SLM has been terminated.
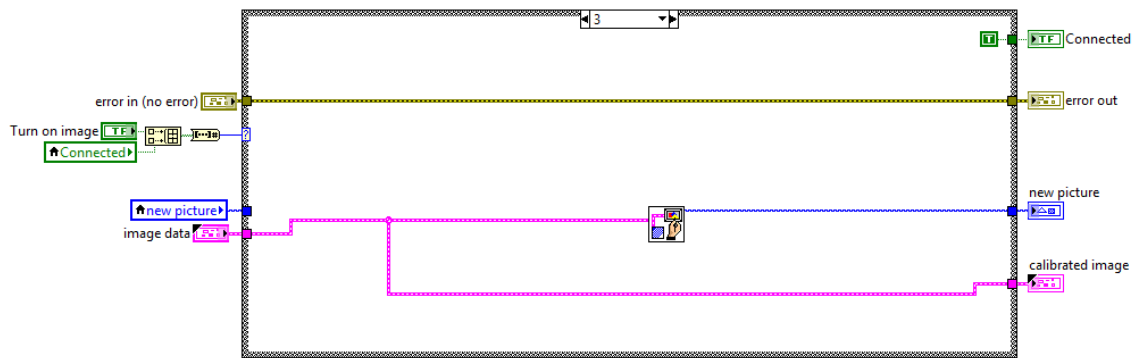
Figure B.73: SLM Phase Map sub-VI block diagram. For this case (case 3), the connection with the SLM is now active, and images displayed in the picture indicator, will appear on the SLM.

B.1.4 Oscope switch sub-VI

Because the LabVIEW communication with oscilloscopes is very similar for different manufacturers, the "Oscope Switch" sub-VI adds the functionality to program connections to different oscilloscopes, and then use a menu to select which device the experiment is using. Here, we have three different devices programmed, and through the selection menu, the user can tell the software which device to gather data from. The switching functionality is contained within this sub-VI, and shown in Figs. B.74, B.75, & B.76. Sub-VI's designed to run Agilent 546XX oscilloscopes are shown in Figs. B.77, B.78, B.79, B.80, & B.81. Sub-VI's designed to run Rigol oscilloscopes are shown in Figs. B.82, B.83, B.84, B.85, & B.86. Sub-VI's designed to run the Agilent 6034A oscilloscope are also shown in Figs. B.87, B.88, B.89, B.90, & B.91.
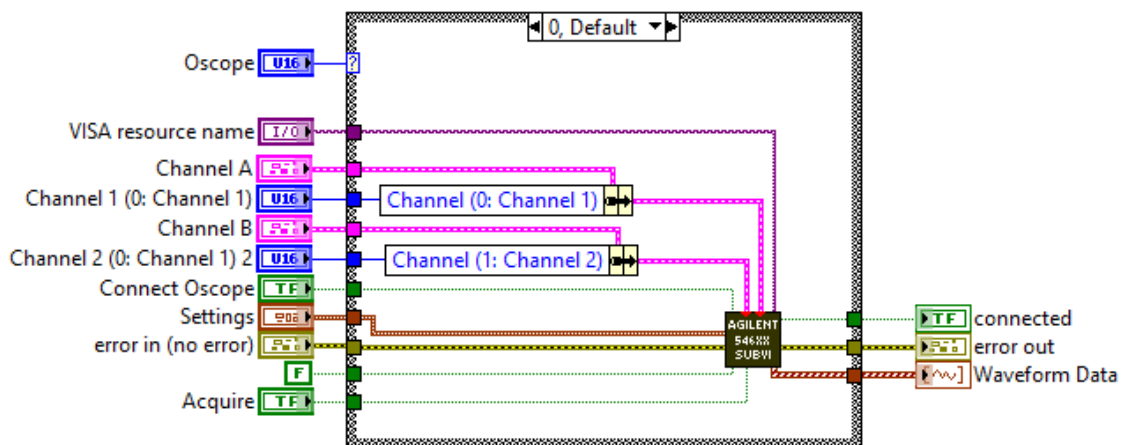
Figure B.74: Oscope Switch sub-VI block diagram. This sub-VI provides a case structure to switch between three different oscilloscopes. More devices can be added by appending new cases to the structure. Case 0, shown here, connects to the Agilent 546XX series of oscilloscopes (Figs. B.77, B.78, B.79, B.80, B.81).
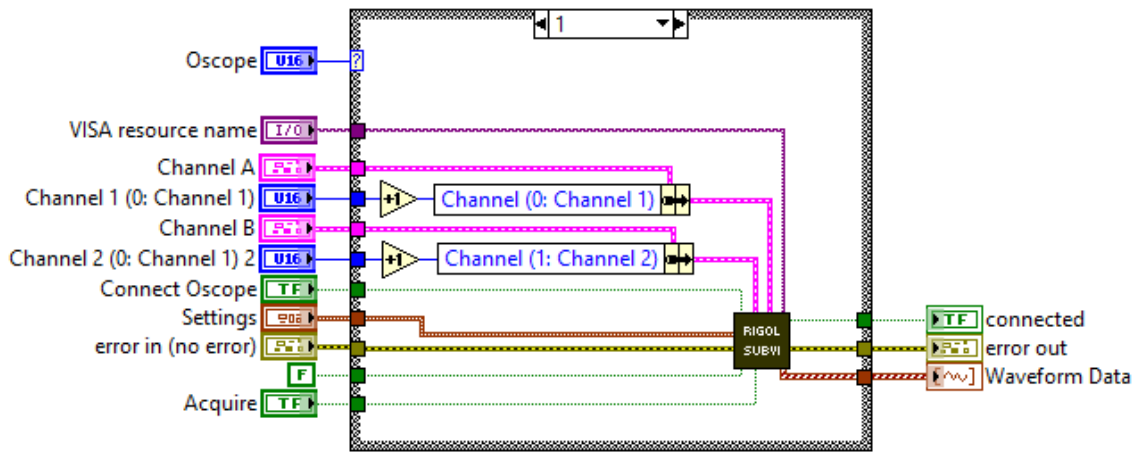
Figure B.75: Oscope Switch sub-VI block diagram. This sub-VI provides a case structure to switch between three different oscilloscopes. More devices can be added by appending new cases to the structure. Case 1, shown here, connects to Rigol oscilloscopes (Figs. B.82, B.83, B.84, B.85, B.86).
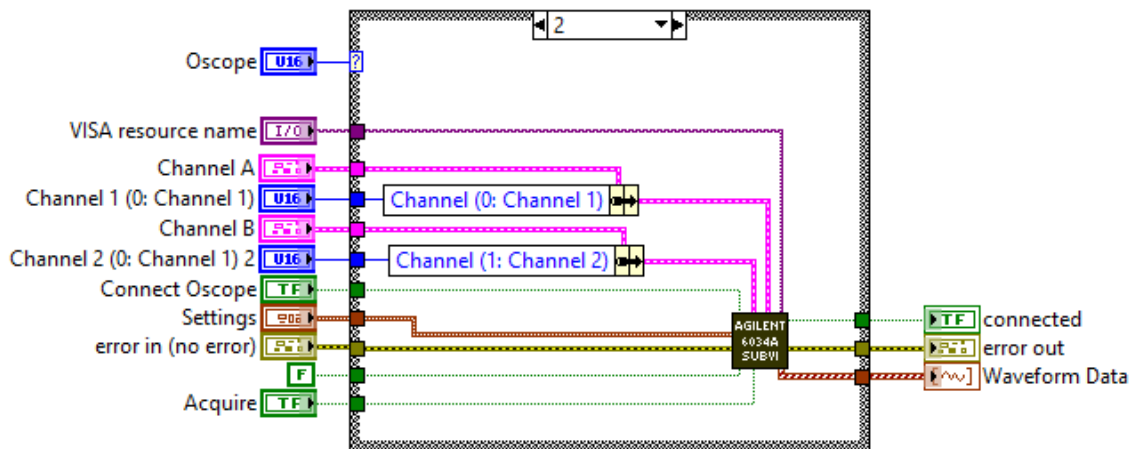
Figure B.76: Oscope Switch sub-VI block diagram. This sub-VI provides a case structure to switch between three different oscilloscopes. More devices can be added by appending new cases to the structure. Case 2, shown here, connects to Agilent 6034A oscilloscopes (Figs. B.87, B.88, B.89, B.90, B.91).
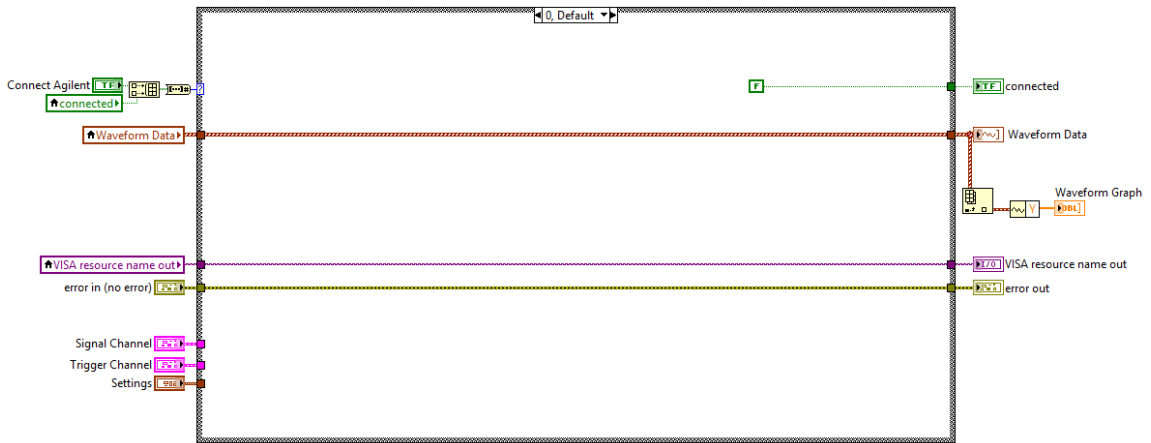
Figure B.77: Agilent 546XX sub-VI block diagram. This sub-VI facilitates the connection and communication with Agilent 546XX series oscilloscopes. Case 0, is the default case, and does nothing.
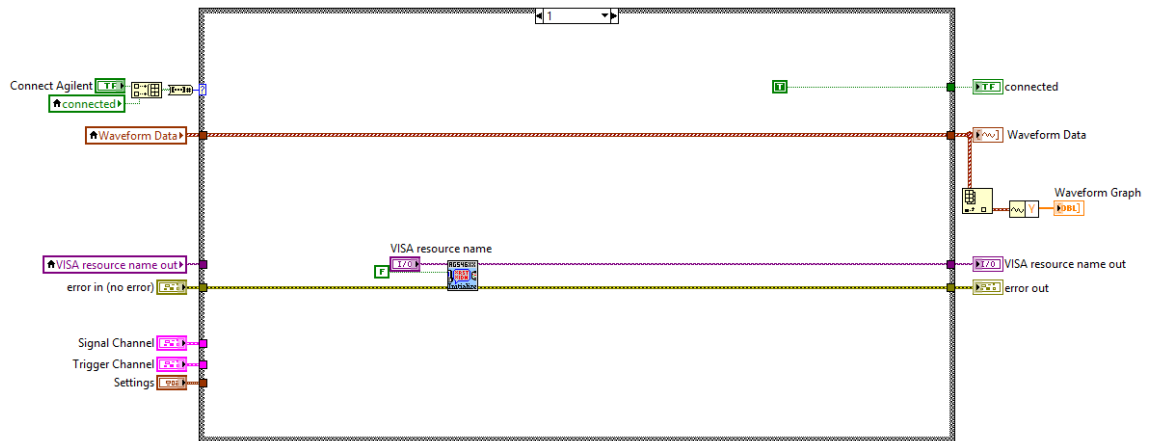
Figure B.78: Agilent 546XX sub-VI block diagram. This sub-VI facilitates the connection and communication with Agilent 546XX series oscilloscopes. Case 1 initializes the connection with the oscilloscope.
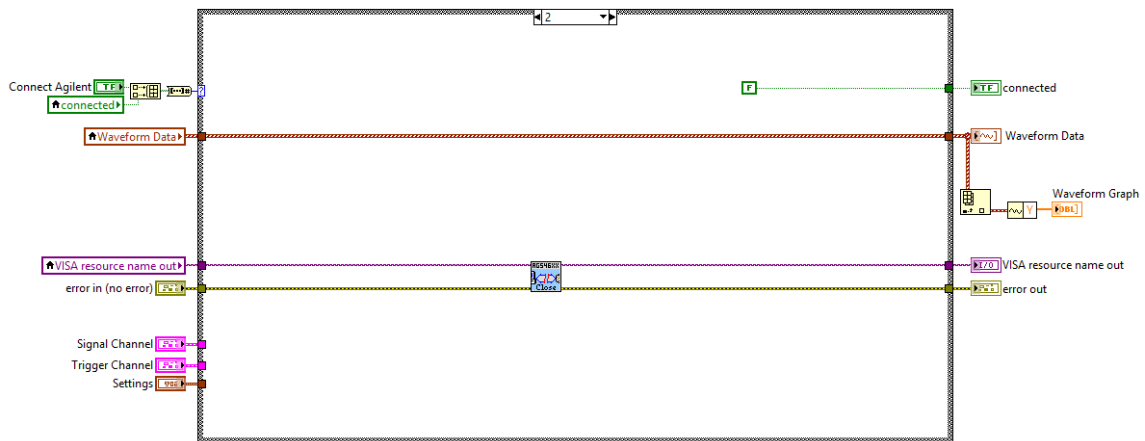
Figure B.79: Agilent 546XX sub-VI block diagram. This sub-VI facilitates the connection and communication with Agilent 546XX series oscilloscopes. Case 2 closes/terminates the connection with the oscilloscope.
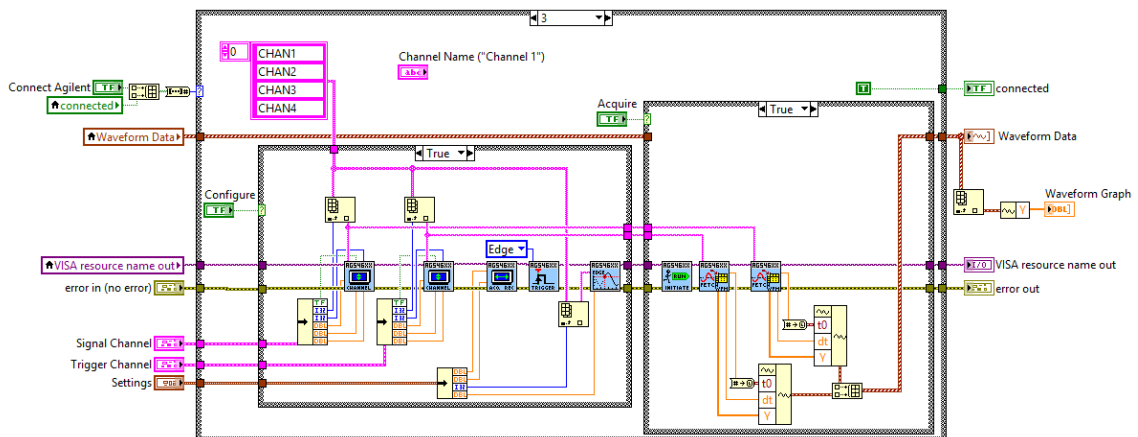
Figure B.80: Agilent 546XX sub-VI block diagram. This sub-VI facilitates the connection and communication with Agilent 546XX series oscilloscopes. Case 3 is chosen when the oscilloscope is actively connected. Two internal case structures allow the user to configure parameters and/or acquire data from the oscilloscope.
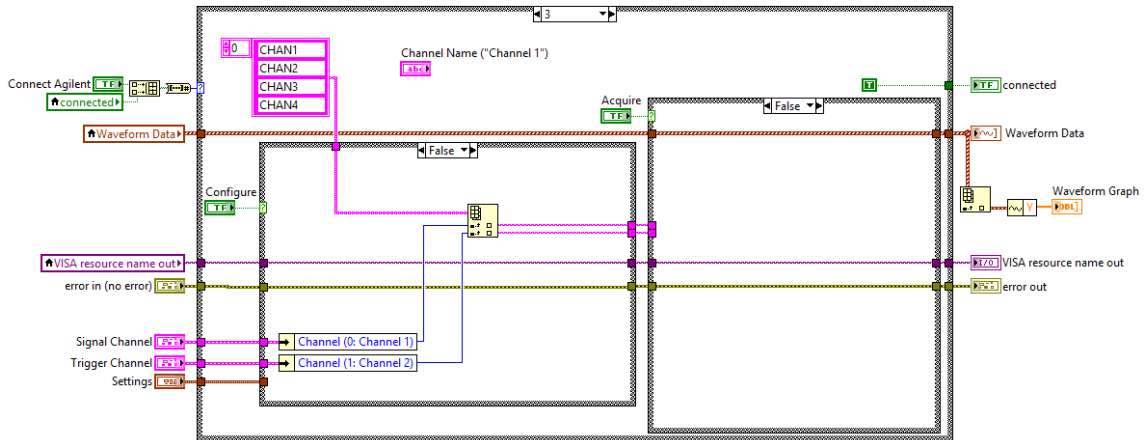
Figure B.81: Agilent 546XX sub-VI block diagram. This sub-VI facilitates the connection and communication with Agilent 546XX series oscilloscopes. Case 3 is chosen when the oscilloscope is actively connected. Two internal case structures allow the user to configure parameters and/or acquire data from the oscilloscope. When neither of these internal case structures are active, the last data set acquired is retained.
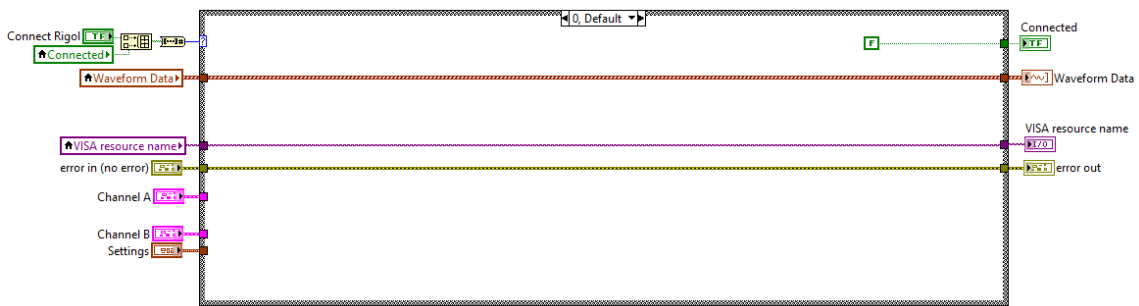
Figure B.82: Rigol sub-VI block diagram. This sub-VI facilitates the connection and communication with Rigol oscilloscopes. Case 0, is the default case, and does nothing.
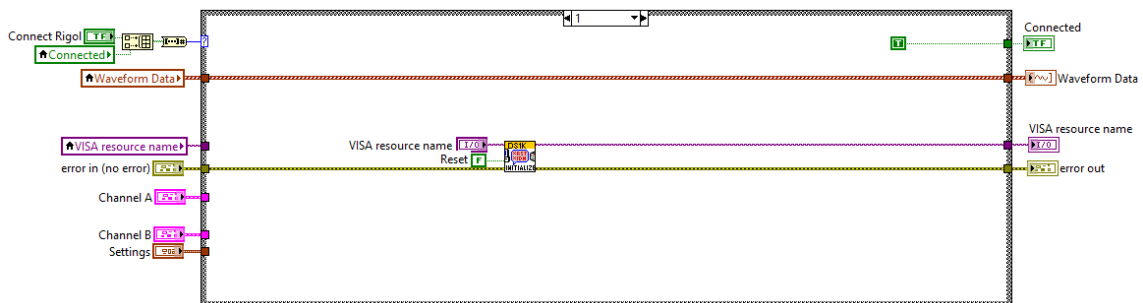
Figure B.83: Rigol sub-VI block diagram. This sub-VI facilitates the connection and communication with Rigol oscilloscopes. Case 1 initializes the connection with the oscilloscope.
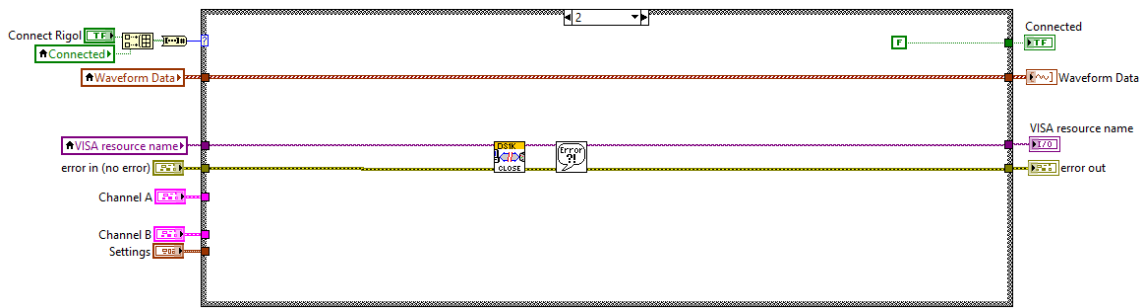
Figure B.84: Rigol sub-VI block diagram. This sub-VI facilitates the connection and communication with Rigol oscilloscopes. Case 2 closes/terminates the connection with the oscilloscope.
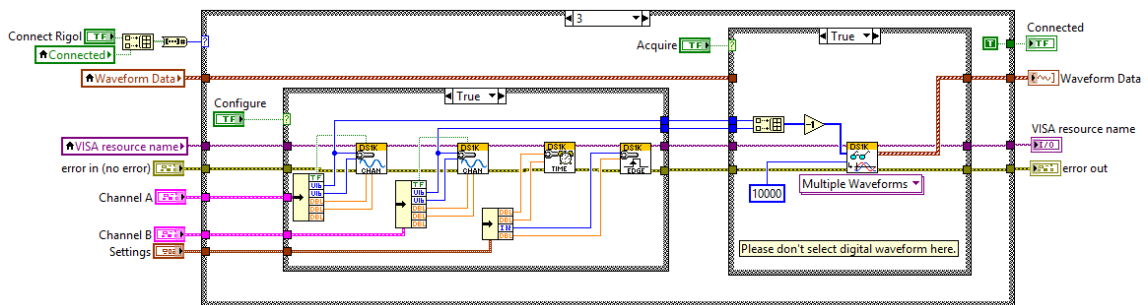
Figure B.85: Rigol sub-VI block diagram. This sub-VI facilitates the connection and communication with Rigol oscilloscopes. Case 3 is chosen when the oscilloscope is actively connected. Two internal case structures allow the user to configure parameters and/or acquire data from the oscilloscope.
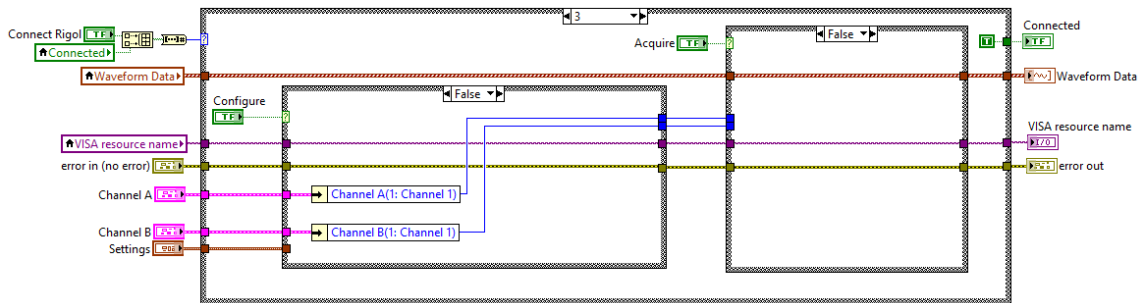
Figure B.86: Rigol sub-VI block diagram. This sub-VI facilitates the connection and communication with Rigol oscilloscopes. Case 3 is chosen when the oscilloscope is actively connected. Two internal case structures allow the user to configure parameters and/or acquire data from the oscilloscope. When neither of these internal case structures are active, the last data set acquired is retained.

216
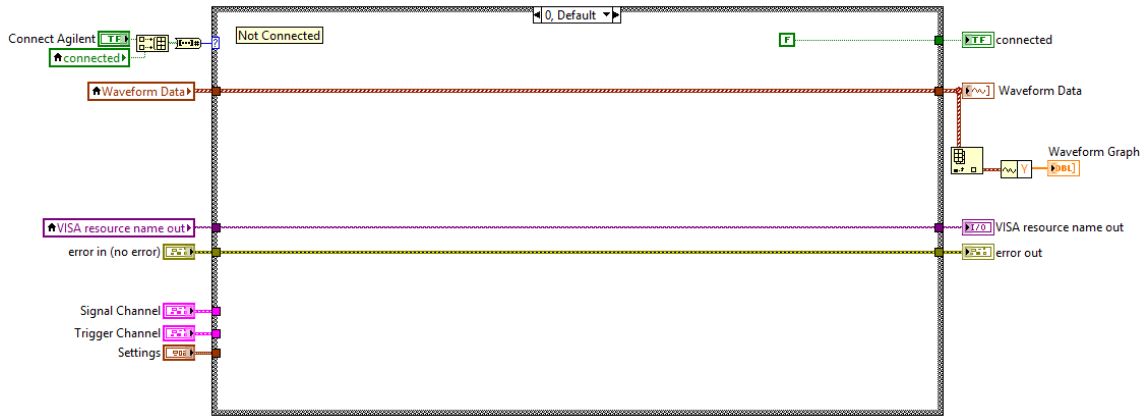
Figure B.87: Agilent 6034A sub-VI block diagram. This sub-VI facilitates the connection and communication with Agilent 6034A series oscilloscopes. Case 0, is the default case, and does nothing.
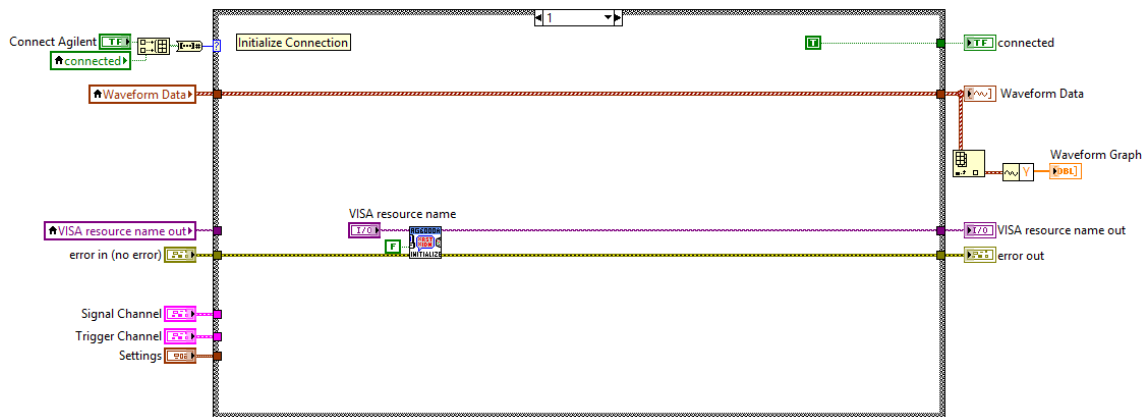
Figure B.88: Agilent 6034A sub-VI block diagram. This sub-VI facilitates the connection and communication with Agilent 6034A series oscilloscopes. Case 1 initializes the connection with the oscilloscope.
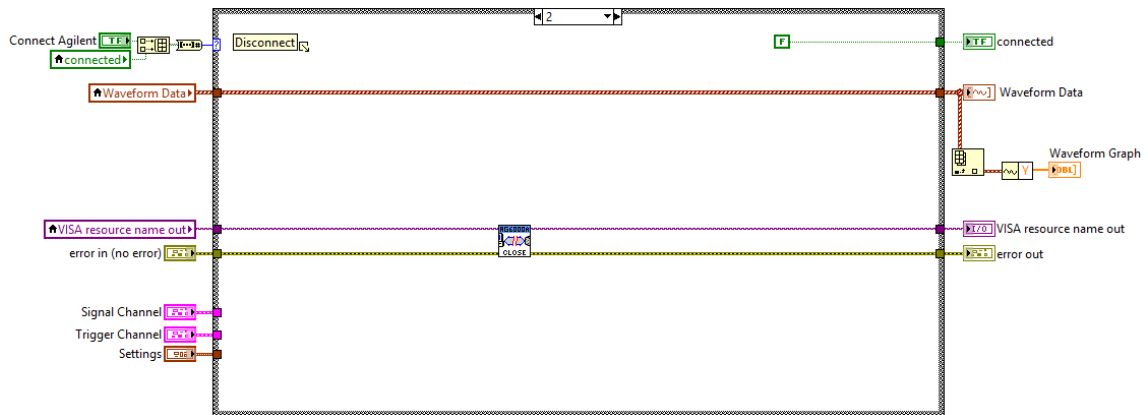
Figure B.89: Agilent 6034A sub-VI block diagram. This sub-VI facilitates the connection and communication with Agilent 6034A series oscilloscopes. Case 2 closes/terminates the connection with the oscilloscope.
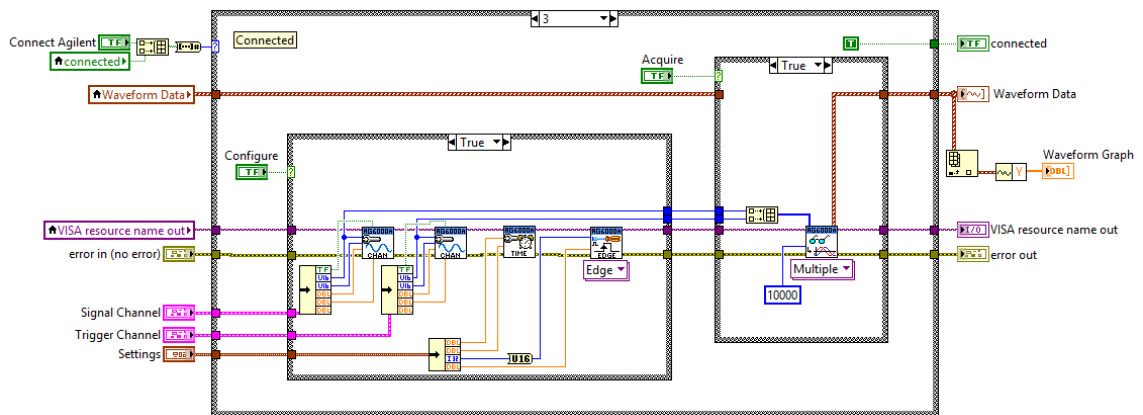
Figure B.90: Agilent 6034A sub-VI block diagram. This sub-VI facilitates the connection and communication with Agilent 6034A series oscilloscopes. Case 3 is chosen when the oscilloscope is actively connected. Two internal case structures allow the user to configure parameters and/or acquire data from the oscilloscope.
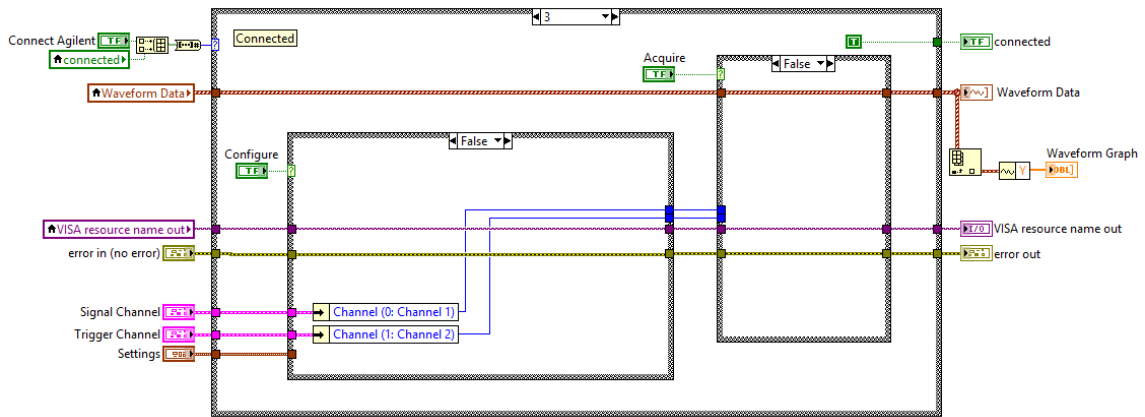
Figure B.91: Agilent 6034A sub-VI block diagram. This sub-VI facilitates the connection and communication with Agilent 6034A series oscilloscopes. Case 3 is chosen when the oscilloscope is actively connected. Two internal case structures allow the user to configure parameters and/or acquire data from the oscilloscope. When neither of these internal case structures are active, the last data set acquired is retained.

B.1.5 Bound sub-VI

The Bounds sub-VI allows the user to control or change the timing bounds on the collected oscilloscope trace. In other words, it sets the region of interest for the trace. This is useful when trying to get better signal to noise ratio by isolating a specific peak from the detector. The sub-VI is shown in Figs. B.92, B.93.
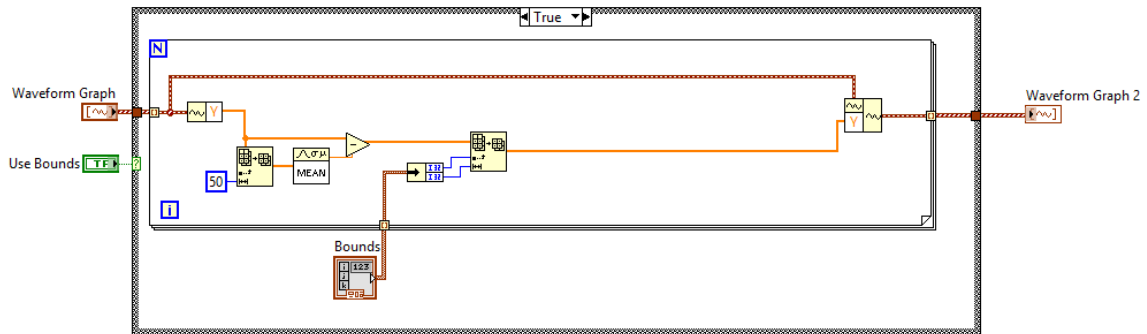
Figure B.92: Bounds sub-VI block diagram. When this sub-VI is activated, it removes the background (first 50 points) from each oscilloscope trace. It then clips the time domain of each trace to the region of interest specified by the user on the front panel.
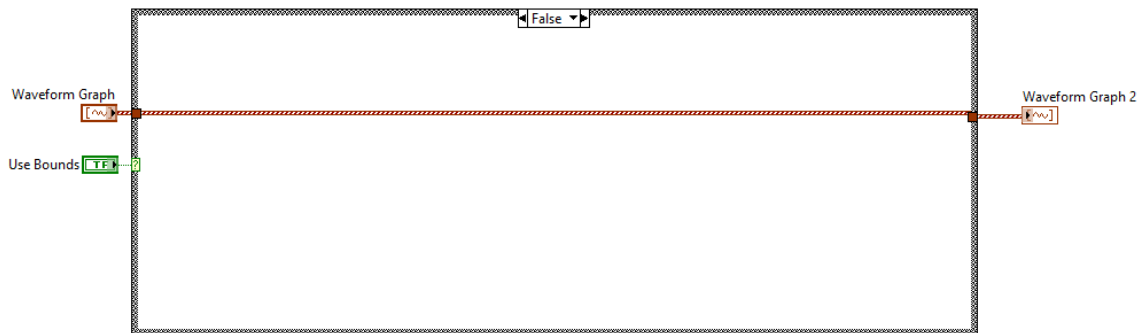
Figure B.93: Bounds sub-VI block diagram. When this sub-VI is not activated, it does nothing.

B.1.6 Mightex camera sub-VI

The Mightex Camera sub-VI facilitates the connection with and data acquisition from the Mightex CGE-B013-U CCD. It was built upon the examples provided by Mightex. Other cameras from Mightex should also work with this sub-VI with minor modification. The sub-VI is shown in Figs. B.94, B.95, B.96, B.97, B.98, B.99 & B.100.
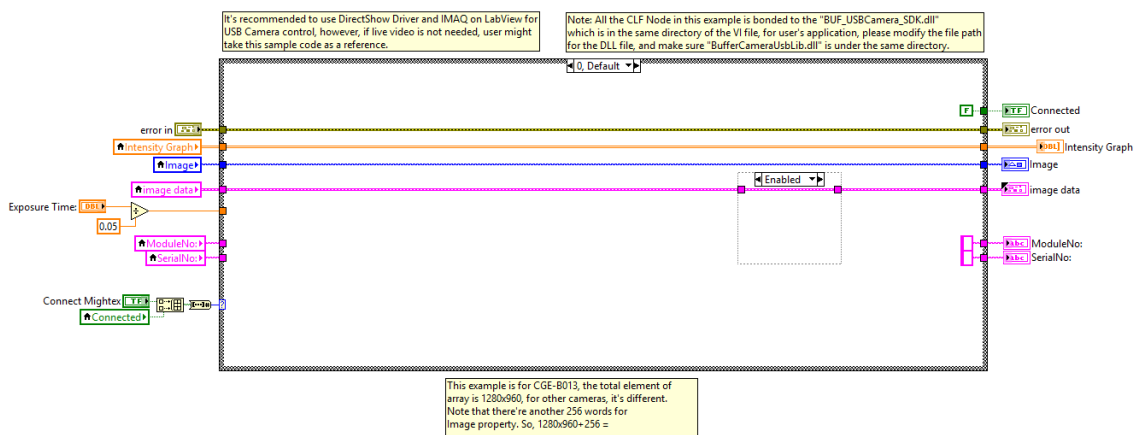
Figure B.94: Mightex Camera sub-VI block diagram. This sub-VI facilitates the connection and communication with Mightex cameras. Case 0, is the default case, and does nothing because the camera is not connected.
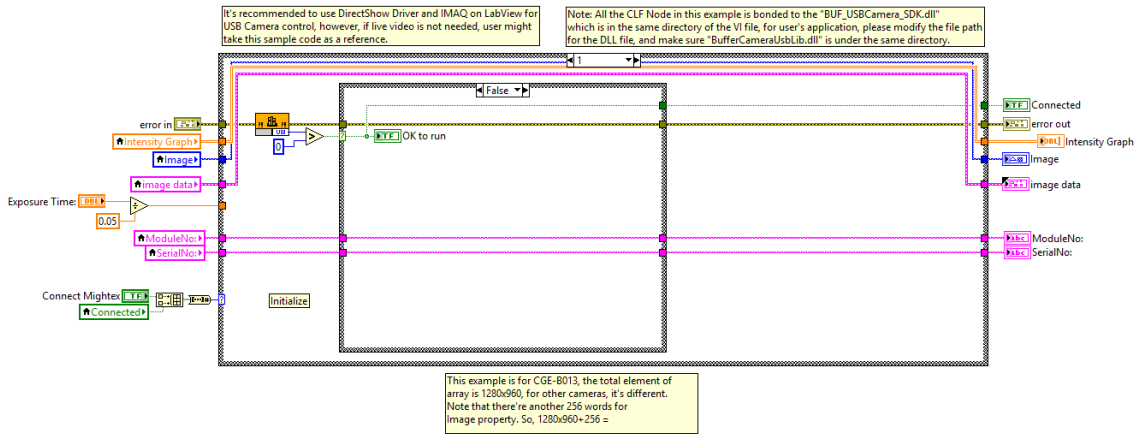
Figure B.95: Mightex Camera sub-VI block diagram. This sub-VI facilitates the connection and communication with Mightex cameras. Case 1 initializes the connection with the CCD; however, if no device is detected by the computer, it will not allow connection as shown here.
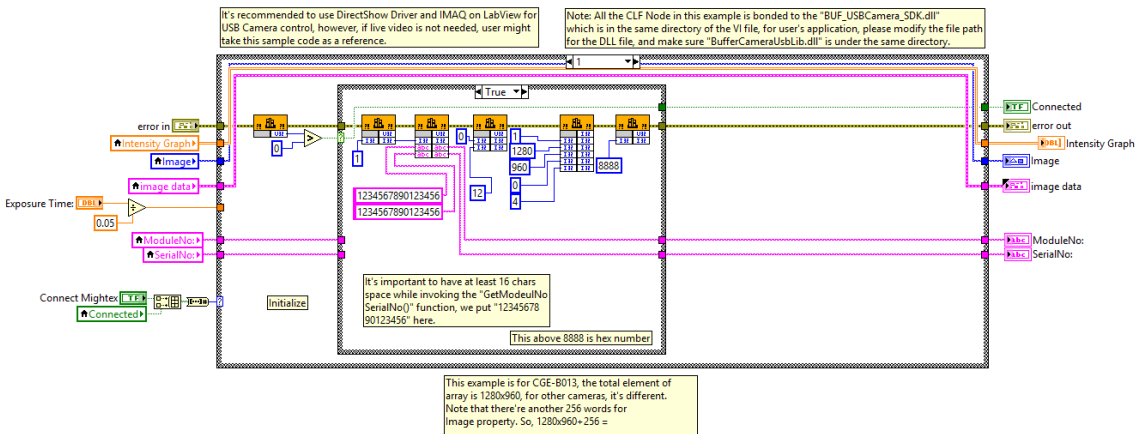
Figure B.96: Mightex Camera sub-VI block diagram. This sub-VI facilitates the connection and communication with Mightex cameras. As shown here, if a device is detected, case 1 completes the initialization and connection with the CCD.

222
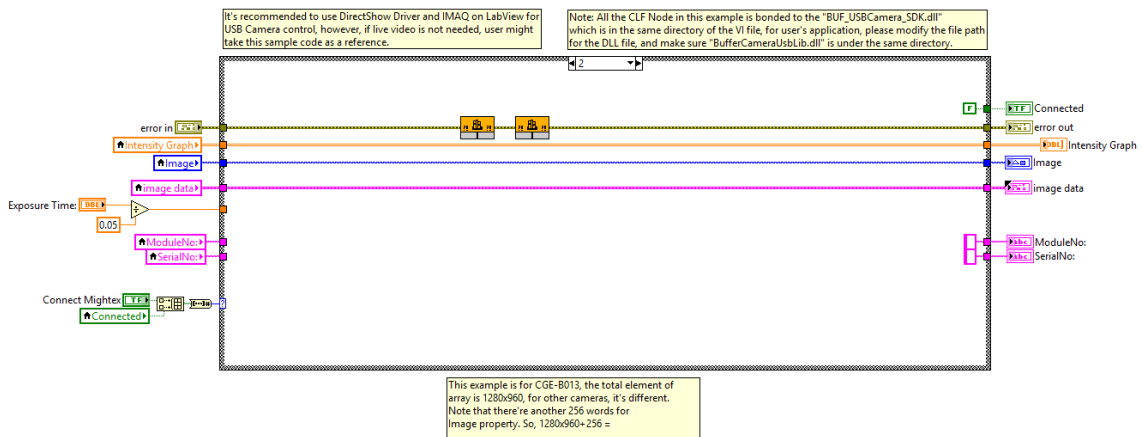
Figure B.97: Mightex Camera sub-VI block diagram. This sub-VI facilitates the connection and communication with Mightex cameras. Case 2 closes/terminates the connection with the CCD.
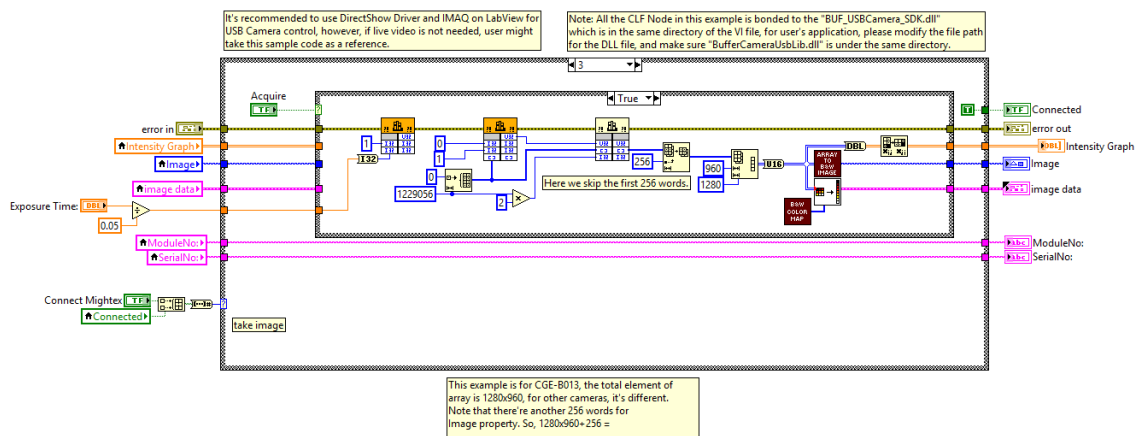
Figure B.98: Mightex Camera sub-VI block diagram. This sub-VI facilitates the connection and communication with Mightex cameras. When the CCD is actively connected, case 3 allows the user or program to acquire images from the camera. The "B&W Color Map" and "Array to B&W Image" sub-VIs are shown in Fig. B.12 and Fig. B.100, respectively. They assist in converting the acquired 2D array into LabVIEW image data.

223
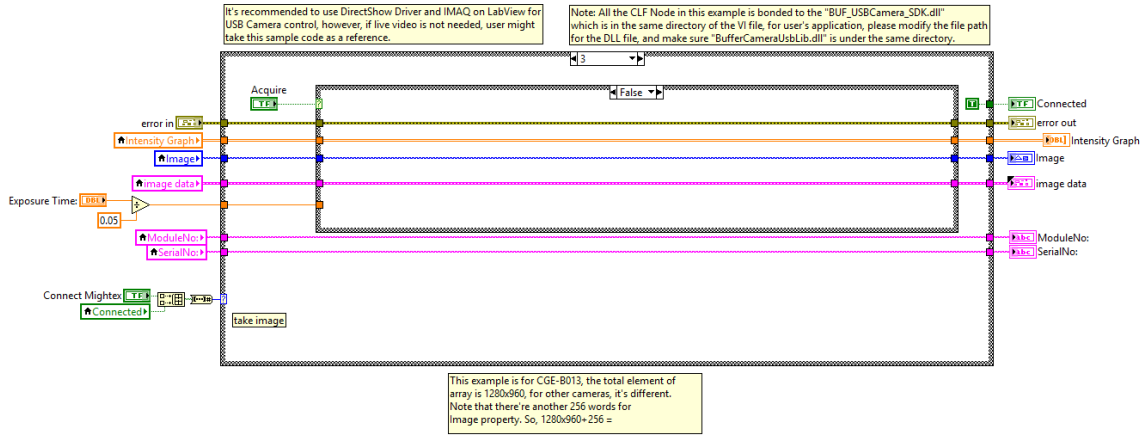
Figure B.99: Mightex Camera sub-VI block diagram. This sub-VI facilitates the connection and communication with Mightex cameras. When the CCD is actively connected, case 3 allows the user or program to acquire images from the camera. If the acquire command/control is not sent, the previously acquired data is not replaced.
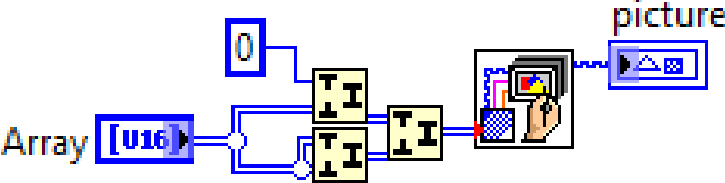
Figure B.100: Array to B&W Imgae sub-VI block diagram. This sub-VI converts a 2D array into a B&W picture.

224

B.1.7 Fitness sub-VI

The Fitness sub-VI uses the data acquired by either the oscilloscope or the camera along with the region of interest set on the front panel to calculate a fitness score for the acquisition. This sub-VI has two outer case structures. The one on the left does the fitness calculation, the one on the right saves the initial fitness score, and computes the enhancement factor, eta, as the optimization algorithm proceeds. The fitness calculations for oscilloscope data are shown in Figs. B.101, B.102, B.103, B.104, B.105, B.106, B.107. The fitness score calculations for camera images are shown in Figs. B.108, B.109. The case structure on the right, which computes the enhancement factor, is shown in Figs. B.101, B.102, B.103. Other device data can be added to this sub-VI by appending new cases into the case structure on the left.
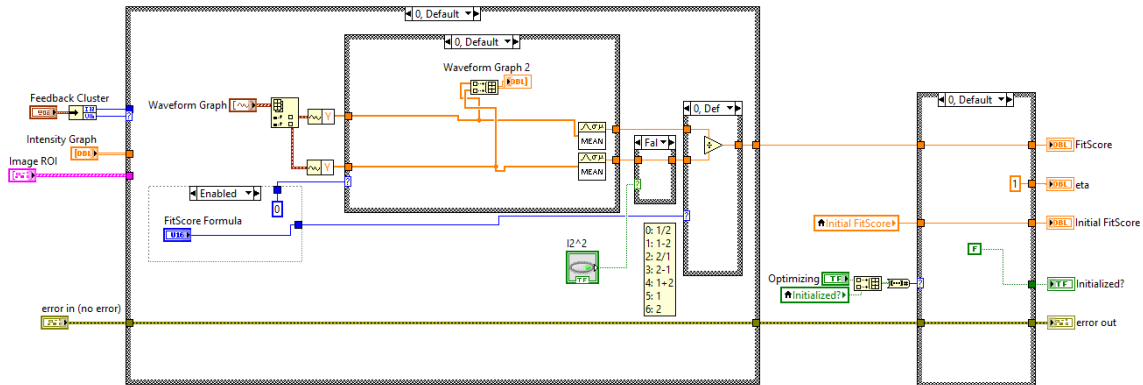
Figure B.101: Fitness sub-VI block diagram. This sub-VI computes the fitness score and enhancement factor of the acquired data in the region of interest. On the left, case 0 corresponds to the oscilloscope data. Inside this structure are three more case structures. The first toggles between averaging (case 0) the data in the ROI, or selecting the maximum value (case 1). The second structure controls whether or not to square the result of the first structure (for trace number 2 only). The third structure computes y_1/y_2 when this calculation is selected on the front panel. The case structure on the right does nothing when the optimization process in not active (case 0).
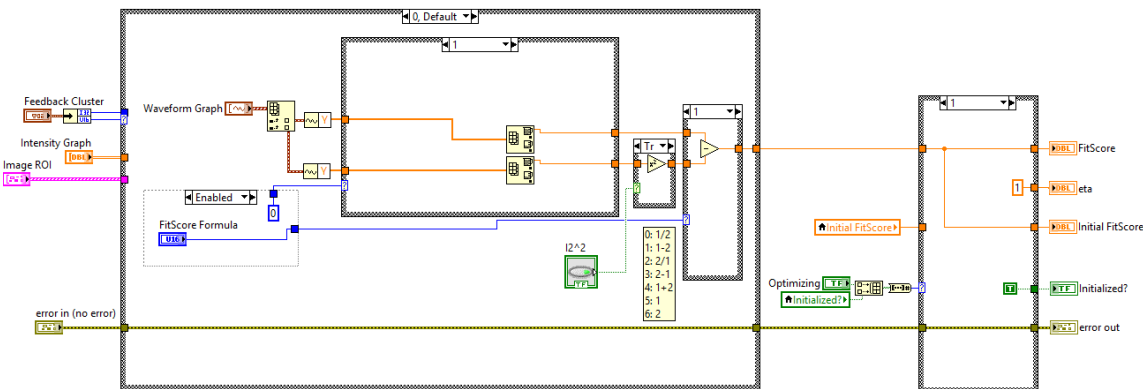
Figure B.102: Fitness sub-VI block diagram. This sub-VI computes the fitness score and enhancement factor of the acquired data in the region of interest. On the left, case 0 corresponds to the oscilloscope data. Inside this structure are three more case structures. The first toggles between averaging (case 0) the data in the ROI, or selecting the maximum value (case 1). The second structure controls whether or not to square the result of the first structure (for trace number 2 only). The third structure computes $y_1 - y_2$ when this calculation is selected on the front panel. The case structure on the right saves the initial fitness score when the optimization algorithm is initialized (case 1).

226
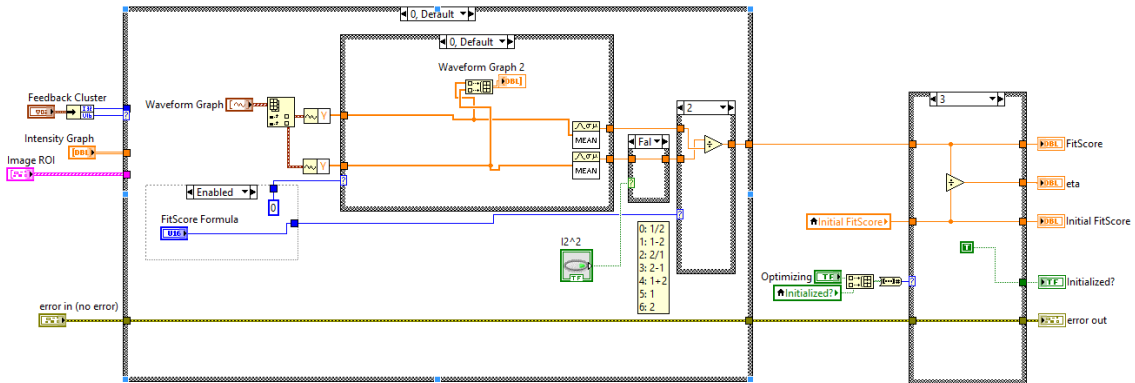
Figure B.103: Fitness sub-VI block diagram. This sub-VI computes the fitness score and enhancement factor of the acquired data in the region of interest. On the left, case 0 corresponds to the oscilloscope data. Inside this structure are three more case structures. The first toggles between averaging (case 0) the data in the ROI, or selecting the maximum value (case 1). The second structure controls whether or not to square the result of the first structure (for trace number 2 only). The third structure computes y_2/y_1 when this calculation is selected on the front panel. The case structure on the right computes the enhancement factor, eta, when the optimization algorithm is running (case 3).
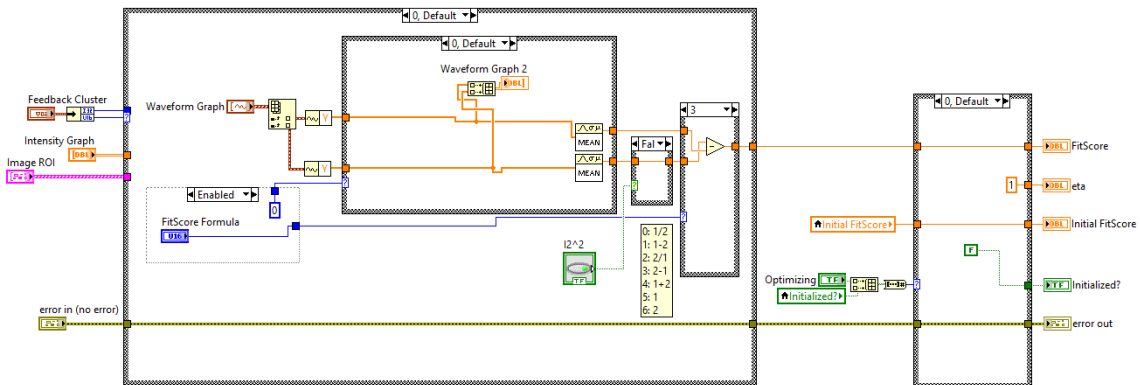
Figure B.104: Fitness sub-VI block diagram. This sub-VI computes the fitness score and enhancement factor of the acquired data in the region of interest. On the left, case 0 corresponds to the oscilloscope data. Inside this structure are three more case structures. The first toggles between averaging (case 0) the data in the ROI, or selecting the maximum value (case 1). The second structure controls whether or not to square the result of the first structure (for trace number 2 only). The third structure computes $y_2 - y_1$ when this calculation is selected on the front panel.
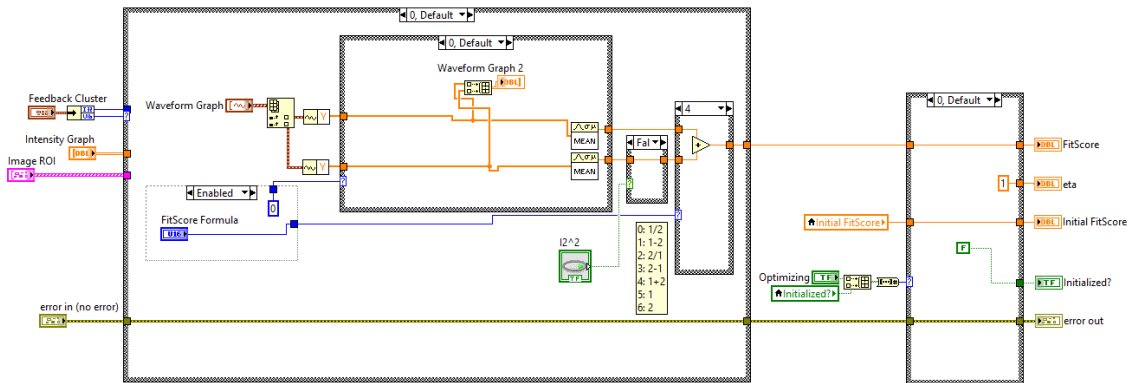
Figure B.105: Fitness sub-VI block diagram. This sub-VI computes the fitness score and enhancement factor of the acquired data in the region of interest. On the left, case 0 corresponds to the oscilloscope data. Inside this structure are three more case structures. The first toggles between averaging (case 0) the data in the ROI, or selecting the maximum value (case 1). The second structure controls whether or not to square the result of the first structure (for trace number 2 only). The third structure computes $y_1 + y_2$ when this calculation is selected on the front panel.
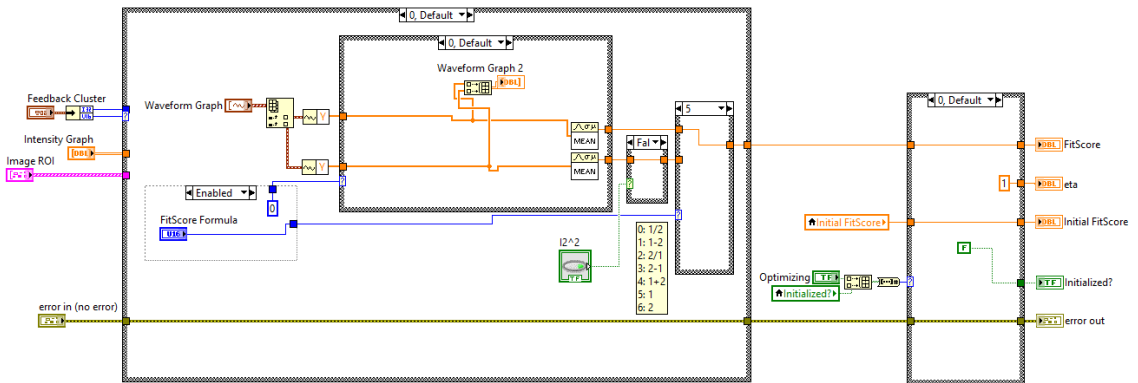
Figure B.106: Fitness sub-VI block diagram. This sub-VI computes the fitness score and enhancement factor of the acquired data in the region of interest. On the left, case 0 corresponds to the oscilloscope data. Inside this structure are three more case structures. The first toggles between averaging (case 0) the data in the ROI, or selecting the maximum value (case 1). The second structure controls whether or not to square the result of the first structure (for trace number 2 only). The third structure selects only y_1 when this calculation is selected on the front panel.

228
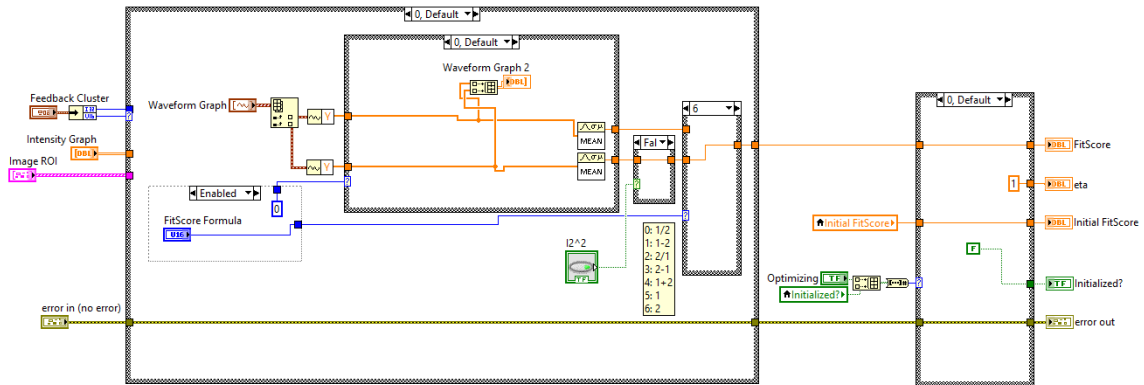
Figure B.107: Fitness sub-VI block diagram. This sub-VI computes the fitness score and enhancement factor of the acquired data in the region of interest. On the left, case 0 corresponds to the oscilloscope data. Inside this structure are three more case structures. The first toggles between averaging (case 0) the data in the ROI, or selecting the maximum value (case 1). The second structure controls whether or not to square the result of the first structure (for trace number 2 only). The third structure selects only y_2 when this calculation is selected on the front panel.
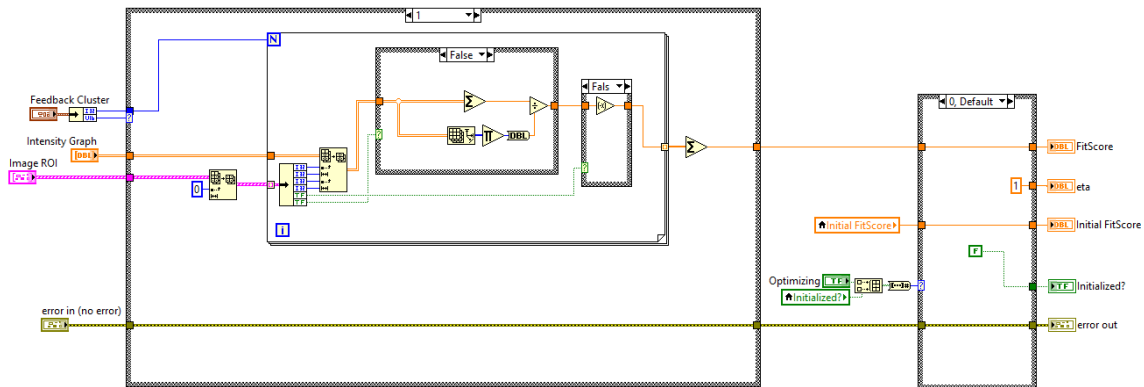
Figure B.108: Fitness sub-VI block diagram. This sub-VI computes the fitness score and enhancement factor of the acquired data in the region of interest. On the left, case 1 corresponds to camera data. Inside this structure are two more case structures. The first toggles between averaging (false) the intensity in each ROI, or selecting the maximum value (true). The second structure controls whether to enhance (true) or suppress (false) the intensity in the region of interest.
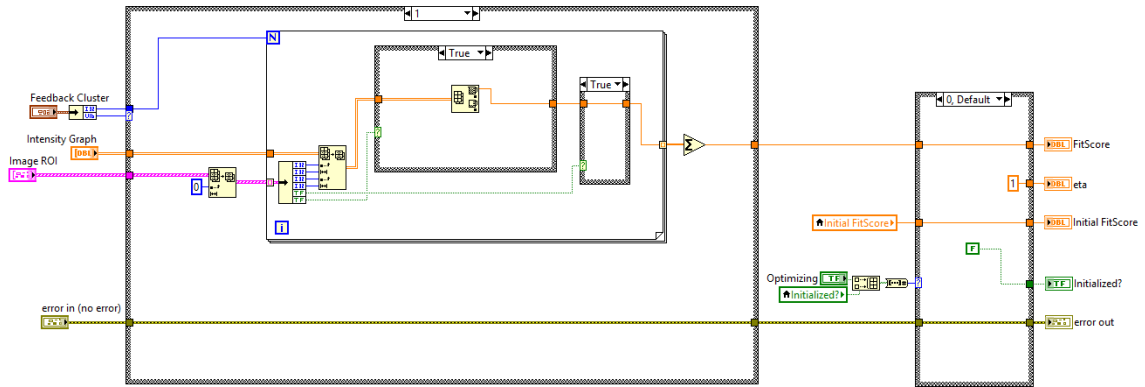
Figure B.109: Fitness sub-VI block diagram. This sub-VI computes the fitness score and enhancement factor of the acquired data in the region of interest. On the left, case 1 corresponds to camera data. Inside this structure are two more case structures. The first toggles between averaging (false) the intensity in each ROI, or selecting the maximum value (true). The second structure controls whether to enhance (true) or suppress (false) the intensity in the region of interest.

B.1.8   Rolling stdv sub-VI

The Rolling Stdv sub-VI (shown in Fig. B.110) computes rolling statistics for the calculated fitness score. This is primarily for diagnostic purposes. Switching the SLM on and off while watching this parameter will give the user a reasonable understanding of the signal to noise of the system with respect to phase modification.
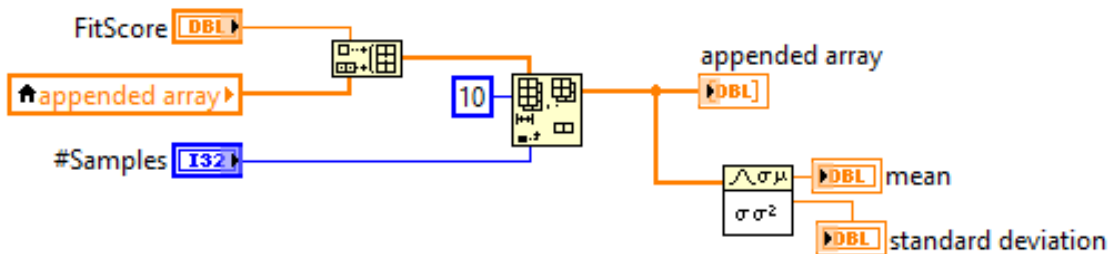
Figure B.110: Rolling StDv block diagram. This sub-VI computes rolling statistics for the computed fitness score. This includes the rolling average and standard deviation. These values are useful for setting up and running experiments as well as diagnostic purposes.

B.1.9 Log trace & image sub-VI

The Log Trace & Image sub-VI, shown in Figs. B.111, B.112, B.113, B.114, B.115, & B.116, saves the oscilloscope traces and CCD images from the current iteration into multidimension arrays. Upon selection of the measurement with the best fitness score, that data can then be saved to file from these arrays. If none of the devices are selected in the save selector on the front panel, this sub-VI does nothing. It is important to remember to check the save selector control if the user wishes to save out the experimental data. This is not always desired, such as in testing situations, so the ability to turn it off was included.
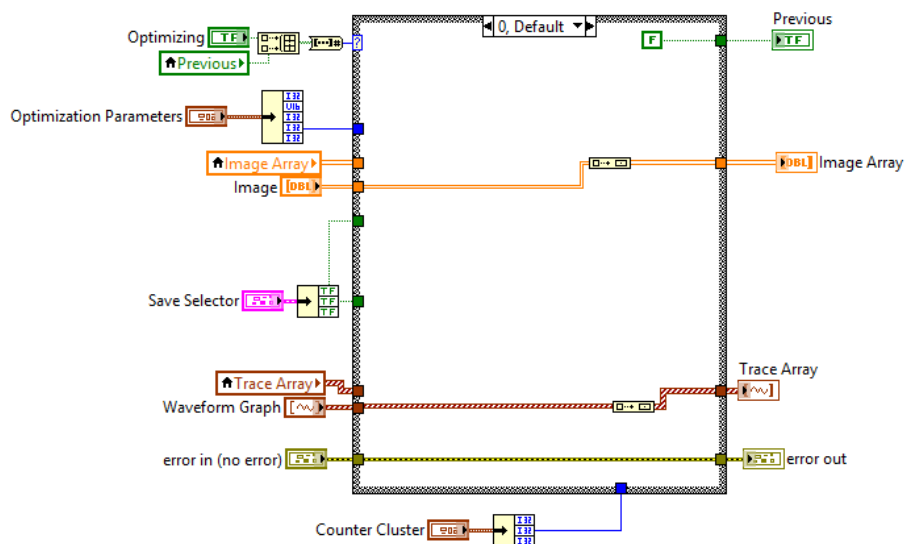
Figure B.111: Log Trace & Image sub-VI block diagram. This sub-VI logs the acquired data from the current iteration into multidimensional arrays. After the iteration completes, the optimal result from these arrays will be saved to file. When the optimization algorithm is not running (case 0), this sub-VI moves each individual acquisition into an array by itself.
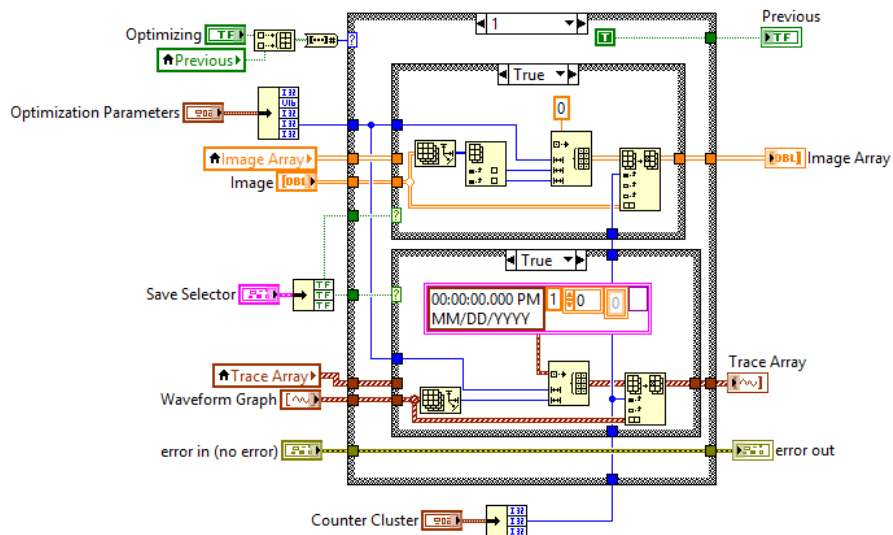
Figure B.112: Log Trace & Image sub-VI block diagram. This sub-VI logs the acquired data from the current iteration into multidimensional arrays. After the iteration completes, the optimal result from these arrays will be saved to file. When the optimization algorithm is initialized (case 1), this sub-VI initializes the data arrays with the appropriate number of elements.

232
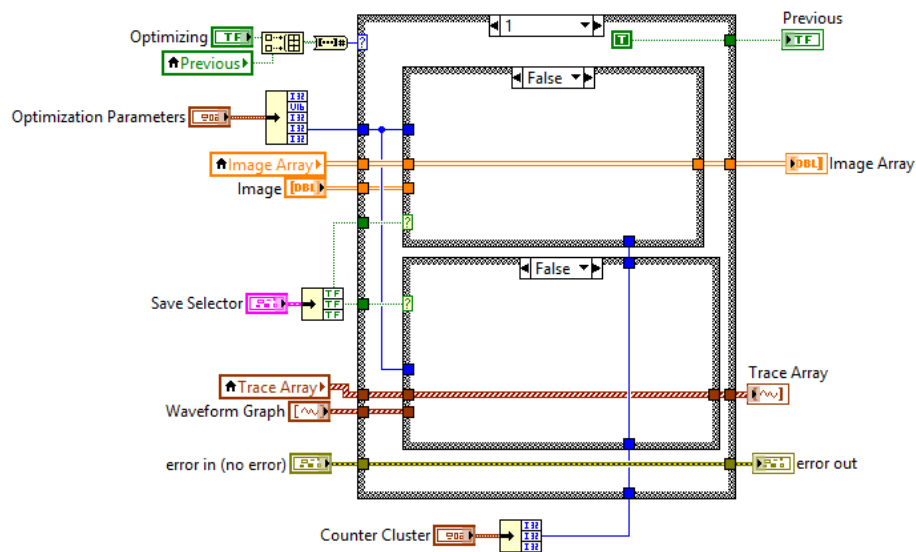
Figure B.113: Log Trace & Image sub-VI block diagram. This sub-VI logs the acquired data from the current iteration into multidimensional arrays. After the iteration completes, the optimal result from these arrays will be saved to file. When the switches in the save selector control are deactivated, this sub-VI does not log that data set, so arrays are not initialized.
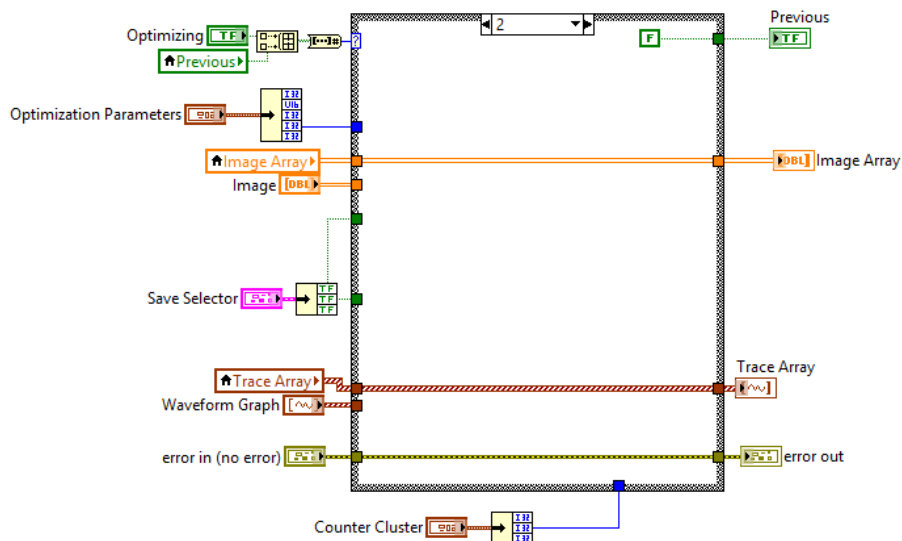
Figure B.114: Log Trace & Image sub-VI block diagram. This sub-VI logs the acquired data from the current iteration into multidimensional arrays. After the iteration completes, the optimal result from these arrays will be saved to file. When the optimization algorithm is terminated (case 2), the logging arrays are not overwritten for one loop of the main algorithm. This allows the save data sub-VI a chance to save the selected data to file.
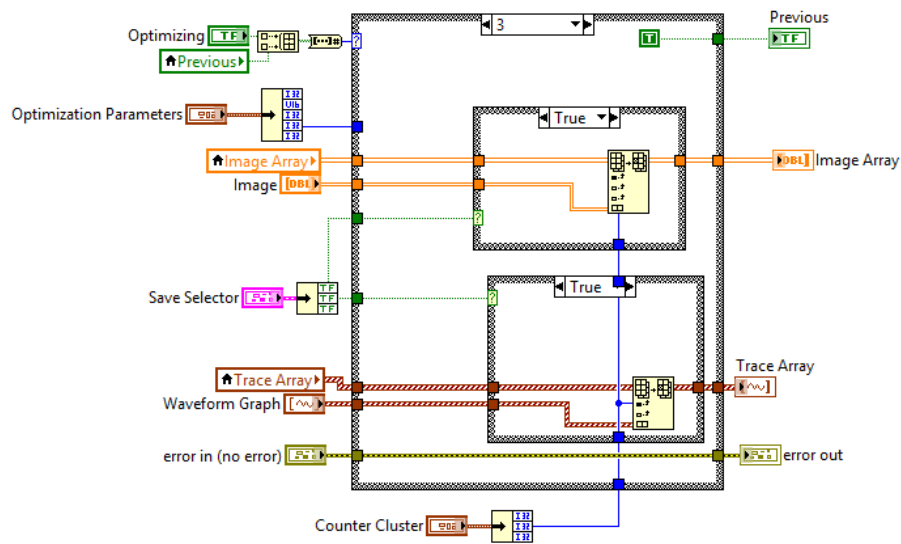
Figure B.115: Log Trace & Image sub-VI block diagram. This sub-VI logs the acquired data from the current iteration into multidimensional arrays. After the iteration completes, the optimal result from these arrays will be saved to file. When the optimization algorithm is running (case 3), this sub-VI places the newly acquired data into the appropriate element of logging array.
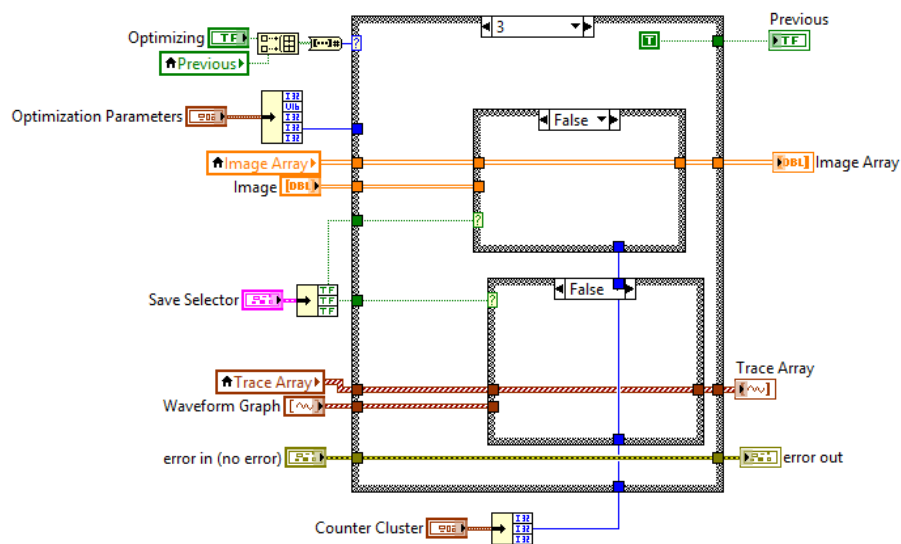
Figure B.116: Log Trace & Image sub-VI block diagram. This sub-VI logs the acquired data from the current iteration into multidimensional arrays. After the iteration completes, the optimal result from these arrays will be saved to file. When the switches in the save selector control are deactivated, this sub-VI does not log the newly acquired data set.

B.2 Wavefront shaping simulation with Python

Numerical simulations of the wavefront shaping optimization were constructed to support the results in chapter 4. This code in particular utilizes and compares the results of three different optimization algorithms: the standard continuous sequential algorithm (CSA), the spiral out algorithm, and a genetic algorithm. In addition to this, functionality was added to modify the parameters of the focusing region of interest. Thus, multiple ROIs could be defined, with adjustable size.

The code is organized as follows. First, external modules are imported, then internal functions are defined. After that, the main script is run, which creates a sample and calls the algorithms to perform the three optimizations. Because the genetic algorithm is used in multiple programs, it was written as an external module, and is documented in section B.3.

```python
#!/bin/python
#==================================================
# Wavefront shaping simulation
# written by Jonathan Thompson
#==================================================
from pylab import *
from progressbar import (ProgressBar, Percentage, ETA, Bar,
                         SimpleProgress)
import GeneticAlgorithm as GA
import os.path


#======================================
# Defined Functions
#======================================
```

```python
def param():
    N=[256,256]              # Grid size
    W=6                      # Speckle Size
    seed(78)                 # Seed Random
    T=(2*pi*random(N))       # Random Transmission Matrix
    seed()                   # Reset Seed
    return N,W,T


def makesample(N,num=10,radius=10,center=True,sd=0):
    '''Create sample with num Raman particles (ROIs),
    each with a radius=radius. Set center to False if
    more that one particle.'''
    if center:
        r0=multiply(0.5,N)*ones((num,2))
    else:
        lmarg=[0.5*radius-0.5,0.5*radius-0.5]
        rmarg=[radius,radius]
        seed(sd)
        r0=add(subtract(N,rmarg)*rand(num,2),lmarg)
        seed()
    m=zeros(append(num,N))
    for i in arange(num):
        m[i]=disk(N,width=radius,center=r0[i])
    return sum(m,axis=0).clip(0,1)
```

```python
# Fitness Function
def R1(Phi,S):
    N,W,T=param()
    Phi=(2*pi/256)*Phi.reshape(N)
    I=Speckle(N,W,(T+Phi))
    R=sum((S*I))/(S.size)
    return R


#==================================================
def normpdf2d(size,FWHM=50,center=None):
    """Return a 2D normal/gaussian probability distribution
        function
    size: Dimensions of distribution, format [ydim,xdim]
    FWHM: Full width half max
    center: Center of distribution, format: [y0,x0]"""
    c=FWHM/2.35482
    if center is None:
        mu=(size[0]/2,size[1]/2)
    else:
        mu=center
    return outer(normpdf(arange(size[0]),mu[0],c),\
                 normpdf(arange(size[1]),mu[1],c))


def square2d(size,width=[1,1],center=None):
    """Return a 2D top hat probability distribution function
```

```python
        size: Dimensions of distribution, format [ydim,xdim]
        width: width of top hat
        center: Center of distribution, format: [y0,x0]"""
    if center is None:
        x0=(size[0]/2,size[1]/2)
    else:
        x0=center
    return outer(tophat(arange(size[0]),width[0],x0[0]),\
                 tophat(arange(size[1]),width[1],x0[1]))


def disk(N,width=10,center=None):
    """Return a 2D disk probability distribution function
    N: Dimensions of distribution, format [ydim,xdim]
    width: width of disk
    center: Center of distribution, format: [y0,x0]"""
    if center is None:
        x0=(N[0]/2,N[1]/2)
    else:
        x0=center
    y,x=meshgrid(arange(N[1]),arange(N[0]))
    return sqrt((x-x0[0])**2+(y-x0[1])**2)<=width


def Spiral(N=[128,128],Outward=False):
    '''Return array coordinates that progress in a spiral
    pattern through the matrix'''
```

```python
    X,Y=meshgrid(arange(N[0]),arange(N[1]))
    x=SpiralMatrix(X,Outward)
    y=SpiralMatrix(Y,Outward)
    return x,y


def SpiralMatrix(N,Out=False):
    '''return array N flattened in spiral order'''
    # or use meshgrid to return array coordinates
    n=N.shape
    num=(n[0]<=n[1])*(n[0]*2-1)+(n[0]>n[1])*(n[1]*2)
    # 2(N.shape[0])-1 if square or fat rectangle
    # 2(N.shape[1]) if tall rectangle
    Y=N[0,:]
    M=N[1:,:].T[::-1]
    for i in range(num):
        Y=append(Y,M[0,:])
        M=M[1:,:].T[::-1]
    if (Out):
        return Y[::-1]
    else:
        return Y


def Speckle(N,spsize,Phi=None):
    '''N: [nx,ny]
    spsize: speckle size in pixels
```

```
    Phi: Phase angle in radians [0,2*pi]'''
    if Phi is None:
        P=exp(2j*pi*random(N))*disk(N,N[0]/(2*spsize))
    else:
        P=exp(1j*Phi)*disk(N,N[0]/(2*spsize))
    return abs(fftshift(fft2(P)))**2


#===================================================
# Optimization Algorithms
#===================================================
def SpOpt(N,num,S,R):
    Phi=zeros(N)
    R0=R(Phi,S)
    eta=zeros(num)
    nx,ny=Spiral(N,True)
    widgets=['_SpO-CSA_Optimization:_', Percentage(),'_',\
            Bar(left='[',right=']'),'_',ETA(),'_']
    pbar=ProgressBar(widgets=widgets)
    for l in pbar(arange(eta.size)):
        Iarr=zeros(8)
        for n in arange(8):
            Phi[nx[l],ny[l]]=n*256/8
            Iarr[n]=R(Phi,S)
        Phi[nx[l],ny[l]]=argmax(Iarr)*256/8
        eta[l]=max(Iarr)
```

```python
        # print(l,m, eta[N[1]*l+m])
    return Phi, eta, R0


#=================================================
def CSA(N,S,R):
    Phi=zeros(N)
    R0=R(Phi,S)
    eta=zeros(product(N))
    nx,ny=meshgrid(arange(N[0]),arange(N[1]))
    nx=nx.ravel();ny=ny.ravel()
    widgets=[' CSA Optimization: ', Percentage(),' ',\
            Bar(left='[',right=']'),' ',ETA(),' ']
    pbar=ProgressBar(widgets=widgets)
    for l in pbar(arange(eta.size)):
        Iarr=zeros(8)
        for n in arange(8):
            Phi[nx[l],ny[l]]=n*256/8
            Iarr[n]=R(Phi,S)
        Phi[nx[l],ny[l]]=argmax(Iarr)*256/8
        eta[l]=max(Iarr)
        # print(l,m, eta[N[1]*l+m])
    return Phi, eta, R0


#=================================================
# Main
```

```python
#===================================================
if __name__ == '__main__':
    N,W,T=param()                    # Parameters
    Phi0=zeros(N)                    # Initial Phase
    I0=Speckle(N,W,(T+Phi0))         # Initial speckle pattern
    num=product(N)//16               # Number of iterations
    S=makesample(N,1,5,True)         # Setup distribution/ROI


    ### Spiral Out ###
    Phi,eta,R0=SpOpt(N,num,S,R1)
    If=Speckle(N,W,(T+(2*pi/256)*Phi))


    ### CSA Standard ###
    Phi1,eta1,R01=CSA(N,S,R1)
    If1=Speckle(N,W,(T+(2*pi/256)*Phi1))


    ### Genetic Algorithm ###
    Iter=product(N)//8
    Popsize=20
    R=lambda Phi: R1(Phi,S)
    Phi2,eta2=GA.GA(Popsize,N,Iter,R,256,0,1)
    If2=Speckle(N,W,(T+(2*pi/256)*Phi2[0]))
```

B.3 Genetic algorithm Python module

A genetic algorithm, as described by [113], was written as a external module named "GeneticAlgorithm.py". It can be imported into Python scripts via the command

```python
import GeneticAlgorithm as GA
```

The module follows the same logic as the genetic algorithm programmed into the experimental LabVIEW control software in section B.1.1.

```python
#!/bin/python
########################################
# Genetic Algorithm for N dimensions
# written in Python3 by Jonathan Thompson
########################################
from pylab import *
from progressbar import (ProgressBar, Percentage, ETA, Bar,
                         SimpleProgress)
from random import choice


########################################
def test_quality(X):
    """X: N-dimensional coordinate"""
    # Spherical function
    # center=arange(X.size)
    return 10-sum((X)**2)


def Initialize_Population(Popsize, N, xupper, xlower):
    return random([Popsize]+N)*(xupper-xlower)+xlower


def Rank_Population(Popsize, Pop, fitness_function, maxmin=-1):
    '''mm: maximize(-1) or minimize(1)'''
```

```python
        cost=zeros(Popsize)
        for i in arange(Popsize):
            cost[i]=fitness_function(Pop[i])
        idx=argsort(cost)[::-1*maxmin]
        return Pop[idx],cost[idx]


def Next_Generation(Popsize,Pop,xup,xlow,Iter):
    N=Pop[0].shape
    m=tril_indices(Popsize)[1] # check with bincount(m)
    for i in arange(Popsize//2):
        ma=choice(m)
        pa=choice(m[where(m!=ma)])
        Template=random_integers(0,1,N)
        Pop[Popsize//2+i]=Mutate(Pop[ma]*Template+Pop[pa]*\
                                (1-Template),xup,xlow,Iter)

    return Pop


def Mutate(X,xup,xlow,Iter):
    R0=0.1
    Rf=0.012
    t=100
    rate=(R0-Rf)*exp(-Iter/t)+Rf
    for i in arange(X.size*rate):
        nx=random_integers(X.shape[0])-1
```

```python
        ny=random_integers(X.shape[1])-1
        X[nx,ny]=random()*(xup-xlow)+xlow
    return X

##################################################

def GA(Popsize,N,Iter,fitness_function,xupper,
        xlower,maxmin=1):
    '''Popsize: Number of individuals in population
    N: Dimensions of genetic code, type list: [Ny,Nx]
    Iter: Number of generations to cycle
    fitness_function: Function handle to compute rankings
    xupper: upper bound on gene value
    xlower: lower bound on gene value
    maxmin: maximize(1) or minimize(-1)'''

    widgets=[' Genetic Alg Optimization: ', Percentage(),\
            ' ',Bar(left='[',right=']'),' ',ETA(),' ']
    pbar=ProgressBar(widgets=widgets)

    Pop=Initialize_Population(Popsize,N,xupper,xlower)
    Pop,fitness=Rank_Population(Popsize,Pop,
                                    fitness_function,maxmin)
    eta=zeros(Iter+1)
    eta[0]=fitness[0]
    for i in pbar(arange(Iter)):
        Pop=Next_Generation(Popsize,Pop,xupper,xlower,i)
```

```
            Pop, fitness=Rank_Population(Popsize,Pop,

                                        fitness_function,maxmin)

        # print(i,fitness[0]);

        eta[i+1]=fitness[0]


    return Pop,eta



#########################################

# Main - Ignore  if  run  as  module

#########################################

if __name__ == '__main__':

    Popsize=30

    N=[64,64]

    xupper=256

    xlower=0

    Iter=5000


    x,y=GA(Popsize,N,Iter,test_quality,xupper,xlower)
```

B.4   Simulation of enhanced second harmonic generation

B.4.1   FORTRAN code to simulate second harmonic generation

A numerical simulation to compute the conversion of 1064 nm light into 532 nm light through second harmonic generation was constructed following the method described in [153]. The results of this simulation are shown in chapter 5. Here, the numerical simulation was coded as subroutines in FORTRAN 90. It was compiled into a Python module (named SHG) using the F2PY package [263] with the following command (from com-

mand line).

```
f2py −c filename.f90 −lfftw3 −I/usr/include −m Modulename
```

The included subroutines were named SHG, SHGcube, gprofile, Intensity, Intensity3d, and Amplitude. It requires the fftw3 code to be installed on your computer.

```fortran
!=================================================
! SUBROUTINES
!=================================================
! by Jonathan Thompson
! compile into python module via
! f2py −c shg3d.f90 −lfftw3 −I/usr/include −m SHG
!
! Follow: Sheng, S. C. & Siegman, A. E.
! Nonlinear−optical calculations using
! fast−transform methods:
! Second−harmonic generation with depletion and
! diffraction. Phys. Rev. A 21, 599âĂŞ606 (1980).
!=================================================
!=================================================
subroutine SHG(Phi,Lz,Lxy,A0,BD,Nz,Ny,Nx,Ip,Is)
  ! Units: cm, W, V
  !==============================
  ! Declarations
  !==============================
  use, intrinsic :: iso_c_binding
  implicit none
```

```fortran
include 'fftw3.f03'

integer, intent(in) :: Nz,Ny,Nx

!A0 should be in Watts,BD:BeamDiameter

real*8, intent(in) :: Lz,A0,BD,Lxy

real*8, dimension(Ny,Nx), intent(in) :: Phi

real*8 :: zq

real*8, dimension(Ny,Nx), intent(out) :: Ip,Is

real*8, dimension(Nx) :: x

real*8, dimension(Ny) :: y

real*8 :: Ly,Lx  ![cm]


real, parameter :: PI=3.14159

real*8, parameter :: lambda1=1064.E-7    ![cm]

real*8, parameter :: lambda2=532.E-7     ![cm]

real*8, parameter :: w1=2*PI*3.e10/lambda1

real*8, parameter :: w2=2*PI*3.e10/lambda2

real*8, parameter :: k1=1.8*w1/3.e10  !k=nw/c,[1/cm]

real*8, parameter :: k2=1.8*w2/3.e10  !k=nw/c,[1/cm]

real*8, parameter :: dk=k2-2*k1                 ![1/cm]

real*8, parameter :: deff=1.4e-9                ![cm/V]

real*8 :: zr                                    ![cm]

complex*16, parameter :: ci=(0.0,1.0)


integer :: l,n,m
```

```fortran
real*8 :: W0          !spot size/resolution  [cm]
real*8 :: dy,dx,dz,s2
real*8, dimension(Ny,Nx) :: I0
real*8, dimension(Nz) :: z


complex*16, dimension(Ny,Nx) :: P,R,A2G,a1
complex*16, dimension(Ny,2*Nx) :: H,G


complex(C_DOUBLE_COMPLEX), dimension(Ny,Nx) :: ff,gg,
complex(C_DOUBLE_COMPLEX), dimension(Ny,Nx) :: Pf,Rf
type(C_PTR) :: planf,planPf,planPb,planRf,planRb
planf=fftw_plan_dft_2d(Ny,Nx,ff,gg,FFTW_FORWARD,&
     FFTW_ESTIMATE)
planPf=fftw_plan_dft_2d(Ny,Nx,P,Pf,FFTW_FORWARD,&
     FFTW_ESTIMATE)
planPb=fftw_plan_dft_2d(Ny,Nx,Pf,P,FFTW_BACKWARD,&
     FFTW_ESTIMATE)
planRf=fftw_plan_dft_2d(Ny,Nx,R,Rf,FFTW_FORWARD,&
     FFTW_ESTIMATE)
planRb=fftw_plan_dft_2d(Ny,Nx,Rf,R,FFTW_BACKWARD,&
     FFTW_ESTIMATE)


zq=k1*(3.e10)**2/(w1**2*deff*A0)    ![cm]
W0=BD
zr=PI*W0**2/lambda1                 ![cm]
```

```fortran
Lx=Lxy
Ly=Lxy


!==============================
! Initial Conditions (Normalized)
!==============================
!==== Coordinates ====
dz=Lz/(Nz*zq)                        ![]
dy=Ly/(Ny*W0)                        ![]
dx=Lx/(Nx*W0)                        ![]
do l=1,Nz
    z(l)=(l-1)*dz
end do
do n=1,Nx
    x(n)=(n-1)*dx-0.5*Lx/W0           !x array
end do
do m=1,Ny
    y(m)=(m-1)*dy-0.5*Ly/W0           !y array
end do
do n=1,Nx
    do m=1,Ny
        s2=(((n-1)-0.5*Nx)/(dx*Nx))**2&
            +(((m-1)-0.5*Ny)/(dy*Ny))**2
        a1(m,n)=-ci*(zq/zr)*PI**2*s2
    end do
```

```fortran
      end  do


      !====  Initial  Field  ====
      call  gprofile (Ny, Nx, dy, dx , A0, BD/W0, I0 )  ! [W/cm**2]
      P=0.0 d0
      R=0.0 d0
      call  Amplitude ( I0 , Ny, Nx, P )               ! [V/cm]
      P=P*exp ( c i *Phi )/A0
      R=R/A0


      !=============================
      ! Iterate  through  z
      !=============================
      A2G=exp(− al *z ( 1 ) )
      do  l =1,Nz−1
         !=== convert  P,R  to  G ===
         call  fftw_execute_dft ( planPf ,P, Pf )
         call  fftw_execute_dft ( planRf ,R, Rf )
         G( : , : Nx)= Pf *(A2G)/(Nx*Ny)
         G( : , Nx+1:)= Rf *(A2G)/(Nx*Ny)


         !=== Construct  H ===
         f f =conjg (P)*R
         call  fftw_execute_dft ( planf , ff , gg )
         H( : , : Nx)=−2* c i *(A2G)*exp ( c i *dk*zq*z ( l ) )* gg / real (Nx*Ny)
```

```fortran
ff=P*P
call fftw_execute_dft(planf,ff,gg)
H(:,Nx+1:)=-2*ci*(A2G)*exp(-ci*dk*zq*z(l))&
        *gg/real(Nx*Ny)


!=== Next z Step ===
G=G+dz*H


!=== Return to new P,R ===
A2G=exp(-al*z(l+1))
Pf=G(:,:Nx)*conjg(A2G)
Rf=G(:,Nx+1:)*conjg(A2G)
call fftw_execute_dft(planPb,Pf,P)
call fftw_execute_dft(planRb,Rf,R)


end do

call intensity(P*A0,Ny,Nx,Ip)
call intensity(R*A0,Ny,Nx,Is)

call fftw_destroy_plan(planf)
call fftw_destroy_plan(planPf)
call fftw_destroy_plan(planPb)
call fftw_destroy_plan(planRf)
call fftw_destroy_plan(planRb)
```

end subroutine SHG


```
!===================================================
subroutine SHGcube(Phi,Lz,Lxy,A0,BD,Nz,Ny,Nx,Ap,As,x,y,zq)
  ! Units: cm, W, V
  !=============================
  ! Declarations
  !=============================
  use, intrinsic :: iso_c_binding
  implicit none
  include 'fftw3.f03'
  integer, intent(in) :: Nz,Ny,Nx
  !A0 should be in Watts,BD:BeamDiam
  real*8, intent(in) :: Lz,A0,BD,Lxy
  real*8, dimension(Ny,Nx), intent(in) :: Phi
  real*8, dimension(Nx), intent(out) :: x
  real*8, dimension(Ny), intent(out) :: y
  complex*16, dimension(Nz,Ny,Nx), intent(out) :: Ap,As
  real*8, intent(out) :: zq
  real*8 :: Ly,Lx ![cm]

  real, parameter :: PI=3.14159
  real*8, parameter :: lambda1=1064.E-7 ![cm]
  real*8, parameter :: lambda2=532.E-7   ![cm]
```

```fortran
real*8, parameter :: w1=2*PI*3.e10/lambda1
real*8, parameter :: w2=2*PI*3.e10/lambda2
real*8, parameter :: k1=1.8*w1/3.e10 !k=nw/c,[1/cm]
real*8, parameter :: k2=1.8*w2/3.e10 !k=nw/c,[1/cm]
real*8, parameter :: dk=k2-2*k1               ![1/cm]
real*8, parameter :: deff=1.4e-9              ![cm/V]
real*8 :: zr                                  ![cm]
complex*16, parameter :: ci=(0.0,1.0)


integer :: l,n,m


real*8 :: W0        !spot size/resolution   [cm]
real*8 :: dy,dx,dz,s2
real*8, dimension(Ny,Nx) :: I0
real*8, dimension(Nz) :: z


complex*16, dimension(Ny,Nx) :: P,R,A2G,a1
complex*16, dimension(Ny,2*Nx) :: H,G


complex(C_DOUBLE_COMPLEX), dimension(Ny,Nx) :: ff,gg
complex(C_DOUBLE_COMPLEX), dimension(Ny,Nx) :: Pf,Rf
type(C_PTR) :: planf,planPf,planPb,planRf,planRb
planf=fftw_plan_dft_2d(Ny,Nx,ff,gg,FFTW_FORWARD,&
      FFTW_ESTIMATE)
planPf=fftw_plan_dft_2d(Ny,Nx,P,Pf,FFTW_FORWARD,&
```

```fortran
        FFTW_ESTIMATE)
planPb=fftw_plan_dft_2d(Ny,Nx,Pf,P,FFTW_BACKWARD,&
        FFTW_ESTIMATE)
planRf=fftw_plan_dft_2d(Ny,Nx,R,Rf,FFTW_FORWARD,&
        FFTW_ESTIMATE)
planRb=fftw_plan_dft_2d(Ny,Nx,Rf,R,FFTW_BACKWARD,&
        FFTW_ESTIMATE)


zq=k1*(3.e10)**2/(w1**2*deff*A0)       ![cm]
W0=BD
zr=PI*W0**2/lambda1                     ![cm]
Lx=Lxy
Ly=Lxy


!============================
! Initial Conditions (Normalized)
!============================
!=== Coordinates ====
dz=Lz/(Nz*zq)                          ![]
dy=Ly/(Ny*W0)                          ![]
dx=Lx/(Nx*W0)                          ![]
do l=1,Nz
    z(l)=(l-1)*dz
end do
do n=1,Nx
```

```fortran
        x(n)=(n-1)*dx-0.5*Lx/W0                !x array
    end do
    do m=1,Ny
        y(m)=(m-1)*dy-0.5*Ly/W0                !y array
    end do
    do n=1,Nx
        do m=1,Ny
            s2=(((n-1)-0.5*Nx)/(dx*Nx))**2&
                +(((m-1)-0.5*Ny)/(dy*Ny))**2
            al(m,n)=-ci*(zq/zr)*PI**2*s2
        end do
    end do


    !==== Initial Field ====
    call gprofile(Ny,Nx,dy,dx,A0,BD/W0,I0)  ![W/cm**2]
    P=0.0d0
    R=0.0d0
    call Amplitude(I0,Ny,Nx,P)                ![V/cm]
    P=P*exp(ci*Phi)/A0
    R=R/A0


    Ap(1,:,:)=P*A0
    As(1,:,:)=R*A0


    !=============================
```

```fortran
! Iterate through z
!=============================
A2G=exp(-al*z(1))
do l=1,Nz-1
    !=== convert P,R to G ===
    call fftw_execute_dft(planPf,P,Pf)
    call fftw_execute_dft(planRf,R,Rf)
    G(:,:Nx)=Pf*(A2G)/(Nx*Ny)
    G(:,Nx+1:)=Rf*(A2G)/(Nx*Ny)


    !=== Construct H ===
    ff=conjg(P)*R
    call fftw_execute_dft(planf,ff,gg)
    H(:,:Nx)=-2*ci*(A2G)*exp(ci*dk*zq*z(l))*gg/real(Nx*Ny)
    ff=P*P
    call fftw_execute_dft(planf,ff,gg)
    H(:,Nx+1:)=-2*ci*(A2G)*exp(-ci*dk*zq*z(l))&
        *gg/real(Nx*Ny)


    !=== Next z Step ===
    G=G+dz*H


    !=== Return to new P,R ===
    A2G=exp(-al*z(l+1))
    Pf=G(:,:Nx)*conjg(A2G)
```

```fortran
      Rf=G(: ,Nx+1:)*conjg(A2G)
       call  fftw_execute_dft(planPb,Pf,P)
       call  fftw_execute_dft(planRb,Rf,R)


      Ap(l+1,:,:)=P*A0
      As(l+1,:,:)=R*A0
   end do


   call  fftw_destroy_plan(planf)
   call  fftw_destroy_plan(planPf)
   call  fftw_destroy_plan(planPb)
   call  fftw_destroy_plan(planRf)
   call  fftw_destroy_plan(planRb)


end subroutine SHGCUBE


!================================================
subroutine  gprofile(Ny,Nx,dy,dx,A0,width,N)  !Ly,Lx,width[cm]
   implicit none
   integer,  intent(in)  :: Nx,Ny
   real*8,  intent(in)  :: dy,dx,  width,A0
   real*8,  dimension(Ny,Nx),  intent(out)  :: N


   integer :: i,j
   real*8 :: c,a
```

```fortran
   c = width/2.35482
   a = A0/(c**2*6.283185307179586)  ![W/cm**2]
   do i=1,Nx
      do j=1,Ny
         N(j,i)=a*exp(-0.5*(((i-0.5*Nx)*dx)**2+ &
            &  ((j-0.5*Ny)*dy)**2)/c**2)
      end do
   end do
end subroutine gprofile


!=================================================
subroutine Intensity(A,Ny,Nx,I)
   ! Return Intensity (W/cm**2) from A [V/cm]
   implicit none
   integer, intent(in) :: Ny,Nx
   complex*16, dimension(Ny,Nx), intent(in) :: A
   real*8, dimension(Ny,Nx), intent(out) :: I

   real, parameter :: n=1.8
   real, parameter :: eps=8.854E-12 ![(s**4)(A**2)/(kg*m**3)]
   real, parameter :: c=3.e8          ![m/s]
   ! W=V*A=Nm/s=kg*m**2/s**3
   ! [(s**3*W**2)/(kg*m**2*cm**2)]=[W/cm**2]
```

```fortran
  I=2*n*eps*c*abs(A)**2
end subroutine INTENSITY


!=================================================
subroutine Intensity3d(A,Nz,Ny,Nx,I)
  ! Return Intensity (W/cm**2) from A [V/cm]
  implicit none
  integer , intent(in) :: Nz,Ny,Nx
  complex*16, dimension(Nz,Ny,Nx), intent(in) :: A
  real*8, dimension(Nz,Ny,Nx), intent(out) :: I

  real , parameter :: n=1.8
  real , parameter :: eps=8.854E-12! [(s**4)(A**2)/(kg*m**3)]
  real , parameter :: c=3.e8          ! [m/s]
  ! W=V*A=Nm/s=kg*m**2/s**3
  ! [(s**3*W**2)/(kg*m**2*cm**2)]=[W/cm**2]

  I=2*n*eps*c*abs(A)**2
end subroutine INTENSITY3d


!=================================================
subroutine Amplitude(I,Ny,Nx,A)
  ! Return Amplitude A [V/cm] from Intensity (W/cm**2)
  implicit none
```

```fortran
    integer , intent(in) :: Ny,Nx
    complex*16, dimension(Ny,Nx), intent(out) :: A
    real*8, dimension(Ny,Nx), intent(in) :: I


    real , parameter :: n=1.8
    real , parameter :: eps=8.854E-12 ![(s**4)(A**2)/(kg*m**3)]
    real , parameter :: c=3.e8           ![m/s]
    ! W=V*A=Nm/s=kg*m**2/s**3
    ![sqrt((W/cm**2)*(kg*m**2/(s**3*A**2)))]=[V/cm]


    A=sqrt(I/(2*n*eps*c))
end subroutine Amplitude

!=================================================
```

B.4.2 Python code to optimize the output of the FORTRAN simulation

A Python script was written to run the genetic algorithm with the second harmonic generation simulation. The FORTRAN simulation was compiled into a Python module, and imported. Here, the code that interfaces between the SHG simulation and the genetic algorithm described in section B.3 is documented.

```python
#!/usr/bin/python
#=================================================
# SHG Optimization via Genetic Algorithm
#   by Jonathan Thompson
# Optimize the phase mask to enhace signal from SHG
#=================================================
from pylab import *
```

```python
from progressbar import (ProgressBar, Percentage, ETA,
                         Bar, SimpleProgress)
import SHG as sg
import GeneticAlgorithm as ga


#=================================================
def SHG_fitness(Phi, frow, fcol, Lz, Lxy, A0, W0, Nz, dxy):
    Ph=expandMat(Phi, frow, fcol)
    PP, PR=sg.shg(Ph, Lz, Lxy, A0, W0, Nz)
    return sum(PR)*dxy


def reduceMat(M, frow, fcol):
    '''Reduce the shape of a matrix by factors fcol
    and frow. Some elements will be lost.'''
    return M[::frow][:,::fcol].copy()


def expandMat(M, frow, fcol):
    '''Expand the shape of a matrix by factors fcol
    and frow. New elements will match the original
    element in that block.'''
    Mx=zeros(multiply((frow, fcol), M.shape))
    nr, nc=M.shape
    for ir in arange(nr):
        for ic in arange(nc):
            Mx[ir*frow:
```

```python
                    ( ir +1)*frow ][: , ic*fcol :( ic +1)* fcol ]=M[ ir , ic ]
    return Mx.copy ()


def Saveall ( ptd , Is , Is0 , Ip , Ip0 , eta , R0, Phi ,W0, x , y , z , dxy ):
    save ( ptd+'Is ' , Is )
    save ( ptd+'Is0 ' , Is0 )
    save ( ptd+'Ip ' , Ip )
    save ( ptd+'Ip0 ' , Ip0 )
    savetxt ( ptd+'eta . txt ' , eta , header="SHG" )
    savetxt ( ptd+'eta_norm . txt ' , eta /R0, header="SHG" )
    savetxt ( ptd+'phase . txt ' , Phi )
    savetxt ( ptd+'F0 . txt ' , Ip0 [ −1])
    savetxt ( ptd+'F1 . txt ' , Ip [ −1])
    savetxt ( ptd+'S0 . txt ' , Is0 [ −1])
    savetxt ( ptd+'S1 . txt ' , Is [ −1])
    savetxt ( ptd+'slice . txt ' , Is [: ,64 ])
    savetxt ( ptd+'slice0 . txt ' , Is0 [: ,64 ])
    savetxt ( ptd+'xslice . txt ' ,
            vstack ((W0*x , Is0 [ −1 ,64], Is [ −1 ,64])).T,
            header='x\tIs0 \tIs ')
    savetxt ( ptd+'xy . txt ' ,W0* vstack ((x , y )).T, header='x\ty ')
    savetxt ( ptd+'zslice . txt ' , vstack ((z , dxy*sum( Is0 ,(1 ,2)) ,
                                    dxy*sum( Is ,(1 ,2)))).T,
            header='z\tIs0 \tIs ')
    savetxt ( ptd+'z . txt ' , z , header='z ')
```

263

```python
        return


#================================================
if __name__ == '__main__':


    #===========================
    # Constant Parameters
    #===========================
    Ny=Nx=2**7
    frow=fcol=2**2
    Lz=0.5                          # cm
    Nz=2**7
    Lxy=0.6                         # cm
    A0=2e6
    W0=0.07                         # cm
    dxy=(Lxy/(Nx*W0))**2
    dxy_cm=(Lxy/Nx)**2


    #===========================
    # Phase Optimization Loop
    #===========================
    #==== Initialize ====
    Phi=zeros((Ny,Nx))


    #==== Initial Intensity ====
```

```python
Ap0,As0,x,y,zq=sg.shgcube(Phi,Lz,Lxy,A0,W0,Nz)
Ip0=sg.intensity3d(Ap0)
Is0=sg.intensity3d(As0)
PP0,PR0=sg.shg(Phi,Lz,Lxy,A0,W0,Nz)
R0=sum(PR0)*dxy


#==== Genetic Algorithm ====
Popsize=20
N=[Ny//frow,Nx//fcol]
Iter=800
xupper=2*pi
xlower=0
fitness_function=lambda x: SHG_fitness(x,frow,fcol,Lz,
                                        Lxy,A0,W0,Nz,dxy)
Pop,eta=ga.GA(Popsize,N,Iter,
              fitness_function,xupper,xlower,1)



z=Lz*arange(Nz)/Nz
Phi=expandMat(Pop[0],frow,fcol)
Ap,As,x,y,zq=sg.shgcube(Phi,Lz,Lxy,A0,W0,Nz)
Ip=sg.intensity3d(Ap)
Is=sg.intensity3d(As)


ptd='output/2016-10-24/5mm-6-2e6/'
```

265

$$Saveall(ptd, Is, Is0, Ip, Ip0, eta, R0, Phi, W0, x, y, z, dxy\_cm)$$

B.5 Diffusion equation calculations in Python

In chapter 7, expressions were derived from the diffusion equation to describe the effects of injecting light into a scattering material. These equations describe the temporal dynamics of light scattered by the material (Eq. 7.1), the average dwell time of light in the medium (Eq. 7.4), and the transmittance and reflectance of the material (Eq 7.9). Because of the complexity of these analytical expressions, Python was used to compute the values based on a handful of inputs. The code developed to do such calculations is documented here.

```python
#!/bin/python
#===================================================
# Dwell Time and Transmission through slab
# Using diffusion theory with extended boundary conditions
#===================================================
from pylab import *
import scipy.integrate as scint


#===================================================
# Defined Functions
#===================================================
def fresnelR(n1,n2,theta):
    temp1 = sqrt(1.0-((n1/n2)*sin(theta))**2)
    temp2 = cos(theta)
    R_s = fabs((n1*temp2-n2*temp1)/(n1*temp2+n2*temp1))**2
    R_p = fabs((n1*temp1-n2*temp2)/(n1*temp1+n2*temp2))**2
```

```python
        R = (R_s + R_p)/2
        return R


def R_eff(n1, n2):
    (R_Phi, error) = scint.quad(
        lambda x: (2.0*sin(x)*cos(x)*
                    fresnelR(n1,n2,x)),0,pi/2)
    (R_J, error) = scint.quad(
        lambda x: (3.0*sin(x)*(cos(x))**2*
                    fresnelR(n1,n2,x)), 0, pi/2)
    return (R_Phi+R_J)/(2.0-R_Phi+R_J)


def mu_eff(mu_a,D):
    return sqrt(mu_a/D)


#==================================================
def time_decay(t,h,Ls,l_t,mu_a,c,R):
    D=l_t/3.
    v0=sqrt((c)/(4*pi*D*t))
    v1=exp(-mu_a*c*t)
    v2=1-exp(-R**2/(4*D*c*t))
    v3=(exp(-(l_t+h)**2/(4*D*c*t))-
        exp(-(2*L_s+l_t+h)**2/(4*D*c*t)))
    return v0*v1*v2*v3
```

```python
def dwell_time(h,Ls,l_t,mu_a,c,R):
    u=sqrt(3*mu_a/l_t)
    k0=u*(h+l_t)
    k1=u*(2*L_s+h+l_t)
    k2=u*sqrt((h+l_t)**2+R**2)
    k3=u*sqrt((2*L_s+h+l_t)**2+R**2)
    return ((1/(2*mu_a*c))*
            (1+(k0*exp(-k0)-k1*exp(-k1)
                -k2*exp(-k2)+k3*exp(-k3))
             /(exp(-k0)-exp(-k1)-exp(-k2)+exp(-k3))))


def Transmittance(d,z0,Ls,l_t,mu_f,R):
    z=z0+l_t
    a=array([d-z,
             d+z+2*Ls,
             d-z+2*Ls,
             d+z+4*Ls,
             3*d-z+4*Ls,
             3*d+z+6*Ls,
             3*d-z+6*Ls,
             3*d+z+8*Ls])
    Ti=zeros(a.shape)
    for j in arange(8):
        Ti[j]=(-1)**j*(exp(-mu_f*a[j])
                       -(a[j]/sqrt(R**2+a[j]**2))
```

```python
                            *exp(-mu_f*sqrt(R**2+a[j]**2)))
    return 0.5*sum(Ti, axis=0)


def Reflectance(d,z0,Ls,l_t,mu_f,R):
    z=z0+l_t
    a=array([z,
             z+2*Ls,
             2*d+z+4*Ls,
             -2*d+z-2*Ls,
             -2*d+z-4*Ls,
             2*d+z+6*Ls])
    Ri=zeros(a.shape)
    for j in arange(6):
        Ri[j]=(exp(-mu_f*a[j])
               -(a[j]/sqrt(R**2+a[j]**2))
               *exp(-mu_f*sqrt(R**2+a[j]**2)))
    return 0.5*sum(Ri, axis=0)


#=================================================
# Main
#=================================================
if __name__ == '__main__':
    # === Defined Parameters ===
    mu_s = 2083.0 # mm^{-1}
    g = 0.6
```

```
mu_a = 0.0001  # mm^{-1}

c = 0.299792458  # mm/ps

n1 = 1.0  # background index

n2 = 1.6  # index of the medium

radius = 0.7  # collection radius into the detector


mu_t = (1.0-g)*mu_s + mu_a  # mm^{-1}

l_t = 1.0/mu_t  # mm

D = 1.0/(3.0*mu_t)  # mm

L_s = 2.0*D*(1.0+R_eff(n1,n2))/(1.0-R_eff(n1,n2))  # mm

mu_f=mu_eff(mu_a,D)


# === Compute Time Decay ===
t=linspace(1,1e4,1e4)  # ps

h=0.3  # mm

P_t=time_decay(t,h,L_s,l_t,mu_a,c,radius)


# === Compute Dwell Time ===
h=linspace(0,.4,2**12)  # mm

t_ave=dwell_time(h,L_s,l_t,mu_a,c,radius)  # ps


# === Compute Transmittance ===
thickness=10  # mm

h=linspace(0,.4,2**12)  # mm

radius=10  # mm (optical collection radius)
```

```python
# Transmittance of slab (T0: control sample)
T0=Transmittance(thickness,0,L_s,l_t,mu_f,radius)
# T1: injected into sample
T1=Transmittance(thickness,h,L_s,l_t,mu_f,radius)
# T2: reduced thickness
T2=Transmittance(thickness-h,0,L_s,l_t,mu_f,radius)


# === Compute Reflectance ===
thickness=10 # mm
h=linspace(0,.4,2**12) # mm
radius=10 # mm
# Transmittance of slab (T0: control sample)
R0=Reflectance(thickness,0,L_s,l_t,mu_f,radius)
# T1: injected into sample
R1=Reflectance(thickness,h,L_s,l_t,mu_f,radius)
# T2: reduced thickness
R2=Reflectance(thickness-h,0,L_s,l_t,mu_f,radius)
```